



**Università
degli Studi
di Palermo**

AREA QUALITÀ, PROGRAMMAZIONE E SUPPORTO STRATEGICO
SETTORE STRATEGIA PER LA RICERCA
U. O. DOTTORATI

Corso di Dottorato di Ricerca in
“Energia e Tecnologie dell’Informazione - curriculum Fisica Tecnica e Ingegneria Nucleare”
Dipartimento di Ingegneria
Settore Scientifico Disciplinare ING-IND/19

**DEVELOPMENT AND APPLICATION OF MULTISCALE
PROCEDURES FOR THE THERMOMECHANICAL
ANALYSIS OF THE DEMO WATER-COOLED
LITHIUM LEAD BREEDING BLANKET**

**IL DOTTORE
ILENIA CATANZARO**

**IL COORDINATORE
CH.MO PROF. MAURIZIO CELLURA**

**IL TUTOR
CH.MO PROF. PIETRO ALESSANDRO DI MAIO**

**I CO TUTOR
DOTT. GAETANO BONGIOVÌ
DOTT. PIERLUIGI CHIOVARO**

Contents

List of Figures	III
List of Tables	XII
List of Acronyms	XIII
List of Symbols	XV
Abstract	XVII
Introduction	1
1 The Breeding Blanket of the DEMO Fusion Reactor	6
1.1 Introduction	6
1.2 Notes on the nuclear fusion reaction	6
1.3 The DEMO fusion reactor.....	13
1.3.1 The HCPB Breeding Blanket concept	16
1.3.2 The WCLL Breeding Blanket concept	18
1.3.3 Eurofer Structural Material	20
1.4 The Thermo-mechanical problem	23
1.4.1 The Finite Element Method	26
1.4.2 The structural assessment as per RCC-MRx	27
1.5 Objective of the study and adopted methodology	33
2 Development of an interpolation procedure for the calculation of a 3D thermal field in a WCLL BB segment	37
2.1 Introduction	37
2.2 Thermal analysis of the WCLL COB segment equatorial region	38
2.2.1 The FEM model	38
2.2.2 Results.....	43
2.3 Interpolation of the calculated thermal field	44
2.4 Structural analysis and comparison of the secondary stress fields	50
2.5 Mesh independence assessment	55
2.6 Secondary stress field on the WCLL COB segment.....	62

3	Global structural analysis of the WCLL Central Outboard Segment and application of the Sub-modelling technique	66
3.1	Introduction	66
3.2	Central Outboard Segment Structural Analysis	67
3.2.1	Loads and Boundary Conditions.....	69
3.2.2	Results.....	72
3.3	The application of the sub-modelling technique	79
3.4	Central, Top and Bottom Cells sub-modelling	80
3.4.1	Loads and Boundary Conditions.....	83
3.4.2	Results.....	85
4	Application of the multiscale design procedure to the thermo-mechanical assessment of the WCLL Central Outboard Segment	102
4.1	Introduction	102
4.2	The adopted methodology	103
4.3	Thermal Analysis of the equatorial radial-toroidal cell of each of the 7 COB poloidal regions.....	106
4.3.1	The reference geometric layout	107
4.3.2	Loads and Boundary Conditions.....	109
4.3.3	Results.....	113
4.4	WCLL COB thermal optimization and determination of its thermal field	115
4.4.1	DWTs and FW channels thermal optimization.....	116
4.4.2	Determination of a thermal field for the whole WCLL COB segment	119
4.5	Structural Analysis of the reference COB segment	121
4.5.1	Loads and Boundary Conditions.....	121
4.5.2	Results.....	123
4.6	Thermo-mechanical analysis adopting the sub-modelling technique of some WCLL COB segment critical regions	130
4.6.1	The FEM models	130
4.6.2	Loads and Boundary Conditions.....	131
4.6.3	Results.....	134
	Conclusion	141
	References	144
5	Appendix 1	149
6	Appendix 2	176
7	Appendix 3	179

List of Figures

Figure 1.1 Average binding energy per nucleon [3].	7
Figure 1.2 Cross section of main nuclear fusion reactions vs. energy for monoenergetic beams [4].	9
Figure 1.3 Schematics of magnetically confined plasmas in tokamaks (left) and stellarator (right) configurations.	11
Figure 1.4 EUROfusion Roadmap [1].	12
Figure 1.5 DEMO tokamak main systems [14].	15
Figure 1.6 DEMO WCLL PHTSs and PCS 3D model [15].	16
Figure 1.7 Reference HCPB for DEMO [16].	17
Figure 1.8 Main WCLL BB layouts [17].	19
Figure 1.9 3D model of Outboard and Inboard BB segments.	20
Figure 1.10 WCLL2018 Elementary cell [17].	20
Figure 1.11 Creep rupture properties at 550°C [26].	22
Figure 1.12 Tensile strengths of 316L(N) and Eurofer [26].	22
Figure 1.13 Yield stress vs. test temperature for Eurofer97 [27].	23
Figure 2.1 WCLL2019.v06 model.	39
Figure 2.2 WCLL2019.v06a DWTs layout.	40
Figure 2.3 WCLL2019.v06 model equipped with 10 FW channels.	40
Figure 2.4 Volumetric density of nuclear heat power field.	43
Figure 2.5 Thermal field arising within SB.	44
Figure 2.6 Interpolation strategies	46
Figure 2.7 Calculated and interpolated thermal fields.	47
Figure 2.8 Radial temperature distributions along the considered paths.	48
Figure 2.9 Contour map of the temperature error [in %] between the calculated thermal field and the “multi-regions” interpolation.	49
Figure 2.10 Statistical distribution of the error on temperature [in %] between the calculated thermal field and the “multi-region” interpolation (histograms) and cumulative curve.	50

Figure 2.11 Boundary conditions.....	51
Figure 2.12 S_x spatial distribution from calculated thermal field (left) and relative error contour map (right) when compared with S_x from interpolated thermal field.....	52
Figure 2.13 S_y spatial distribution from calculated thermal field (left) and relative error contour map (right) when compared with S_y from interpolated thermal field.....	52
Figure 2.14 S_z spatial distribution from calculated thermal field (left) and relative error contour map (right) when compared with S_z from interpolated thermal field.....	53
Figure 2.15 S_{xy} spatial distribution from calculated thermal field (left) and relative error contour map (right) when compared with S_{xy} from interpolated thermal field.	53
Figure 2.16 S_{xz} spatial distribution from calculated thermal field (left) and relative error contour map (right) when compared with S_{xz} from interpolated thermal field.	54
Figure 2.17 S_{yz} spatial distribution from calculated thermal field (left) and relative error contour map (right) when compared with S_{yz} from interpolated thermal field.	54
Figure 2.18 Statistical distribution of the error on S_{ij} between the calculated thermal field and the “multi-region” interpolation (histograms) and cumulative curves.....	55
Figure 2.19 Coarser meshes set-up for the mesh independence study.	56
Figure 2.20 Error on temperature prediction for the coarser meshes 1 and 5.....	57
Figure 2.21 Statistical distribution of the error on S_{ij} between the calculated thermal field and the “multi-region” interpolation (histograms) and cumulative curves.....	58
Figure 2.22 S_x spatial distribution from calculated thermal field (left) and relative error contour map (right) when compared with S_x from interpolated thermal field.	59
Figure 2.23 S_y spatial distribution from calculated thermal field (left) and relative error contour map (right) when compared with S_y from interpolated thermal field.	59
Figure 2.24 S_z spatial distribution from calculated thermal field (left) and relative error contour map (right) when compared with S_z from interpolated thermal field.	60
Figure 2.25 S_{xy} spatial distribution from calculated thermal field (left) and relative error contour map (right) when compared with S_{xy} from interpolated thermal field.	60
Figure 2.26 S_{xz} spatial distribution from calculated thermal field (left) and relative error contour map (right) when compared with S_{xz} from interpolated thermal field.	61
Figure 2.27 S_{yz} spatial distribution from calculated thermal field (left) and relative error contour map (right) when compared with S_{yz} from interpolated thermal field.	61
Figure 2.28 The WCLL COB Segment.	62
Figure 2.29 The “multi-region” interpolated thermal field applied to the whole WCLL COB Segment.	63
Figure 2.30 The attachment system.	63

Figure 2.31 The Von Mises equivalent stress (secondary) calculated.....	64
Figure 2.32 Comparison between secondary stress field in the SPs geometric domain.....	65
Figure 3.1 Central Outboard Segment architecture.	68
Figure 3.2 Central Outboard Segment architecture detail.	68
Figure 3.3 Non-uniform thermal deformation field imposed on the COB segment.....	70
Figure 3.4 Force and moment time behaviour during a UVDE [51] and maximum component (i.e., radial) time-steps.....	71
Figure 3.5 NO Von Mises stress field and Deformed vs. Undeformed Shapes.	73
Figure 3.6 OP Von Mises stress field and Deformed vs. Undeformed Shapes.	73
Figure 3.7 UVDE (t = 11.585 s) Von Mises stress field and Deformed vs. Undeformed shapes.....	74
Figure 3.8 UVDE (t = 11.52 s) Von Mises stress field and Deformed vs. Undeformed shapes.....	74
Figure 3.9 Stress linearization paths in the central cell.	76
Figure 3.10 Stress linearization results under NO loading scenario.....	77
Figure 3.11 Stress linearization results under OP loading scenario.	77
Figure 3.12 Stress linearization results under UVDE - T = 11.52 s loading scenario.....	78
Figure 3.13 Stress linearization results under UVDE - T = 11.585 s loading scenario.....	78
Figure 3.14 Global model and sub-model mesh.	80
Figure 3.15 Three sub-model regions of COB.	81
Figure 3.16 FW channels detail on Central Cells.	82
Figure 3.17 Details of global model and sub-model meshes.....	83
Figure 3.18 Interpolated thermal field imposed on each model.	84
Figure 3.19 Water and breeder wetted surfaces.....	84
Figure 3.20 Displacement field under NO loading scenario on the upper surface of the CC in global model vs. sub-model.....	85
Figure 3.21 Von Mises stress field – NO on sub-models superimposed to global model...	86
Figure 3.22 Von Mises stress field – OP on sub-models superimposed to global model. ..	86
Figure 3.23 Von Mises stress field - UVDE (t=11.585 s) on sub-models superimposed to global model.	87
Figure 3.24 Von Mises stress field - UVDE (t=11.52 s) on sub-models superimposed to global model.	87
Figure 3.25 Total Displacements field – NO on sub-models superimposed to global model.	88

Figure 3.26 Total Displacements field – OP on sub-models superimposed to global model.	88
Figure 3.27 Total Displacements field - UVDE (t=11.585 s) on sub-models superimposed to global model.	89
Figure 3.28 Total Displacements field - UVDE (t=11.52 s) on sub-models superimposed to global model.	89
Figure 3.29 Comparison RCC-MRx criteria on CC - NO.	90
Figure 3.30 Comparison RCC-MRx criteria on CC - OP.	91
Figure 3.31 Comparison RCC-MRx criteria on CC - UVDE (t=11.585 s).	91
Figure 3.32 Comparison RCC-MRx criteria on CC - UVDE (t=11.52 s).	92
Figure 3.33 Comparison RCC-MRx criteria on BC - NO.	92
Figure 3.34 Comparison RCC-MRx criteria on BC - OP.	93
Figure 3.35 Comparison RCC-MRx criteria on BC - UVDE (t=11.585 s).	93
Figure 3.36 Comparison RCC-MRx criteria on BC - UVDE (t=11.52 s).	94
Figure 3.37 Comparison RCC-MRx criteria on TC - NO.	94
Figure 3.38 Comparison RCC-MRx criteria on TC - OP.	95
Figure 3.39 Comparison RCC-MRx criteria on TC - UVDE (t=11.585 s).	95
Figure 3.40 Comparison RCC-MRx criteria along on TC - UVDE (t=11.52 s).	96
Figure 3.41 Paths within FW and SW in CC.	98
Figure 3.42 Stress linearization results under NO loading scenario.	100
Figure 3.43 Stress linearization results under OP loading scenario.	101
Figure 3.44 Stress linearization results under UVDE (t=11.52 s) loading scenario.	101
Figure 3.45 Stress linearization results under UVDE (t=11.585 s) loading scenario.	101
Figure 4.1 Poloidal segmentation and numbering.	104
Figure 4.2 Thermal optimization procedure flowchart.	105
Figure 4.3 COB Segment architecture.	107
Figure 4.4 WCLL v06b DWTs layout and recirculation scheme.	108
Figure 4.5 Models of the two elementary cells equipped with 4 and 6 cooling channels.	109
Figure 4.6 Counter-current flow path on FW-SW cooling channels.	112
Figure 4.7 Thermal field raised within O4 region.	114
Figure 4.8 Thermal field raised within O6 region.	115
Figure 4.9 Alternative DWTs layout.	116
Figure 4.10 Cross-22, cross-24 and cross-26 DWTs layout.	117
Figure 4.11 Thermal field raised in O4 with cross-26 DWTs layout.	118
Figure 4.12 Thermal field raised in O4 with cross-24 DWTs layout.	118

Figure 4.13 Thermal field raised in O4 with cross-22 DWTs layout.	118
Figure 4.14 Thermal field obtained with the interpolation procedure.	120
Figure 4.15 Contour map and statistical distribution of the temperature error [in %] between the calculated and interpolated thermal field and cumulative curve in O1 poloidal region.	121
Figure 4.16 Von Mises stress field under NO e OP loading scenarios.	124
Figure 4.17 Von Mises stress field under UVDE (t=11.52 s and t=11.585 s) loading scenario.	125
Figure 4.18 Deformed vs. Undeformed shapes under NO and OP loading scenarios.	125
Figure 4.19 Deformed vs. Undeformed shapes under UVDE (t=11.52 s and t=11.585 s) loading scenario.	126
Figure 4.20 Paths within SPs grid in the equatorial region.	127
Figure 4.21 Verification of RCC-MRx criteria under NO loading scenario.	128
Figure 4.22 Verification of RCC-MRx criteria under OP loading scenario.	128
Figure 4.23 Verification of RCC-MRx criteria under UVDE - t=11.52 s loading scenario.	129
Figure 4.24 Verification of RCC-MRx criteria under UVDE - t=11.585 s loading scenario.	129
Figure 4.25 Models of Top, Central and Bottom cells	131
Figure 4.26 Mesh of the sub-model vs mesh of the global model in the equatorial region.	131
Figure 4.27 Temperature field onto Top, Central and Bottom models superimposed to the global model.	133
Figure 4.28 Displacement field in global model and sub-model applied in NO scenario to the lower boundary of the central cells sub-model.	133
Figure 4.29 Displacement field in global model and sub-model applied in NO scenario to the upper boundary of the central cells sub-model.	134
Figure 4.30 Von Mises stress field onto Top, Central and Bottom models in NO superimposed to the global model.	135
Figure 4.31 Von Mises stress field onto Top, Central and Bottom models in OP superimposed to the global model.	135
Figure 4.32 Von Mises stress field onto Top, Central and Bottom models in UVDE (t=11.52 s) superimposed to the global model.	136
Figure 4.33 Von Mises stress field onto Top, Central and Bottom models in UVDE (t=11.585 s) superimposed to the global model.	136

Figure 4.34 Paths selected within FW-SW region in TC model.	137
Figure 4.35 RCC-MRx criteria verification in NO loading scenario.	138
Figure 4.36 RCC-MRx criteria verification in OP loading scenario.	138
Figure 4.37 RCC-MRx criteria verification in UVDE (t=11.52 s) loading scenario.....	139
Figure 4.38 RCC-MRx criteria verification in UVDE (t=11.585 s) loading scenario.....	139
Figure 5.1 Error on temperature prediction for the coarser mesh 2.....	149
Figure 5.2 Error on temperature prediction for the coarser mesh 3.....	150
Figure 5.3 Error on temperature prediction for the coarser mesh 4.....	150
Figure 5.4 Paths within FW and SWs.....	151
Figure 5.5 Paths within horizontal and vertical SPs and FW bend.....	151
Figure 5.6 Path FW AB temperature comparison.....	152
Figure 5.7 Path FW CD temperature comparison.....	152
Figure 5.8 Path FW EF temperature comparison.	153
Figure 5.9 Path FW Bend AB temperature comparison.	153
Figure 5.10 Path FW Bend CD temperature comparison.	154
Figure 5.11 Path FW Bend EF temperature comparison.	154
Figure 5.12 Path SW AB temperature comparison.....	155
Figure 5.13 Path SW CD temperature comparison.....	155
Figure 5.14 Path SW EF temperature comparison.	156
Figure 5.15 Path SPh1 temperature comparison.....	156
Figure 5.16 Path SPh2 temperature comparison.....	157
Figure 5.17 Path SPh3 temperature comparison.....	157
Figure 5.18 Path SPv1 temperature comparison.....	158
Figure 5.19 Path SPv2 temperature comparison.....	158
Figure 5.20 Path SPv3 temperature comparison.....	159
Figure 5.21 Statistical distribution of the error on S_{ij} between the calculated thermal field and the “multi-region” interpolation (histograms) and cumulative curves for the “coarse Mesh 1”.....	160
Figure 5.22 Statistical distribution of the error on S_{ij} between the calculated thermal field and the “multi-region” interpolation (histograms) and cumulative curves for the “coarse Mesh 2”.....	161
Figure 5.23 Statistical distribution of the error on S_{ij} between the calculated thermal field and the “multi-region” interpolation (histograms) and cumulative curves for the “coarse Mesh 3”.....	162

Figure 5.24 Statistical distribution of the error on S_{ij} between the calculated thermal field and the “multi-region” interpolation (histograms) and cumulative curves for the “coarse Mesh 4”.....	163
Figure 5.25 S_x spatial distribution from calculated thermal field (left) and relative error contour map (right) when compared with S_x from interpolated thermal field for the “coarse Mesh 1”.....	164
Figure 5.26 S_y spatial distribution from calculated thermal field (left) and relative error contour map (right) when compared with S_x from interpolated thermal field for the “coarse Mesh 1”.....	164
Figure 5.27 S_z spatial distribution from calculated thermal field (left) and relative error contour map (right) when compared with S_x from interpolated thermal field for the “coarse Mesh 1”.....	165
Figure 5.28 S_{xy} spatial distribution from calculated thermal field (left) and relative error contour map (right) when compared with S_x from interpolated thermal field for the “coarse Mesh 1”.....	165
Figure 5.29 S_{xz} spatial distribution from calculated thermal field (left) and relative error contour map (right) when compared with S_x from interpolated thermal field for the “coarse Mesh 1”.....	166
Figure 5.30 S_{yz} spatial distribution from calculated thermal field (left) and relative error contour map (right) when compared with S_x from interpolated thermal field for the “coarse Mesh 1”.....	166
Figure 5.31 S_x spatial distribution from calculated thermal field (left) and relative error contour map (right) when compared with S_x from interpolated thermal field for the “coarse Mesh 2”.....	167
Figure 5.32 S_y spatial distribution from calculated thermal field (left) and relative error contour map (right) when compared with S_x from interpolated thermal field for the “coarse Mesh 2”.....	167
Figure 5.33 S_z spatial distribution from calculated thermal field (left) and relative error contour map (right) when compared with S_x from interpolated thermal field for the “coarse Mesh 2”.....	168
Figure 5.34 S_{xy} spatial distribution from calculated thermal field (left) and relative error contour map (right) when compared with S_x from interpolated thermal field for the “coarse Mesh 2”.....	168

Figure 5.35 S_{xz} spatial distribution from calculated thermal field (left) and relative error contour map (right) when compared with S_x from interpolated thermal field for the “coarse Mesh 2”.....	169
Figure 5.36 S_{yz} spatial distribution from calculated thermal field (left) and relative error contour map (right) when compared with S_x from interpolated thermal field for the “coarse Mesh 2”.....	169
Figure 5.37 S_x spatial distribution from calculated thermal field (left) and relative error contour map (right) when compared with S_x from interpolated thermal field for the “coarse Mesh 3”.....	170
Figure 5.38 S_y spatial distribution from calculated thermal field (left) and relative error contour map (right) when compared with S_x from interpolated thermal field for the “coarse Mesh 3”.....	170
Figure 5.39 S_z spatial distribution from calculated thermal field (left) and relative error contour map (right) when compared with S_x from interpolated thermal field for the “coarse Mesh 3”.....	171
Figure 5.40 S_{xy} spatial distribution from calculated thermal field (left) and relative error contour map (right) when compared with S_x from interpolated thermal field for the “coarse Mesh 3”.....	171
Figure 5.41 S_{xz} spatial distribution from calculated thermal field (left) and relative error contour map (right) when compared with S_x from interpolated thermal field for the “coarse Mesh 3”.....	172
Figure 5.42 S_{yz} spatial distribution from calculated thermal field (left) and relative error contour map (right) when compared with S_x from interpolated thermal field for the “coarse Mesh 3”.....	172
Figure 5.43 S_x spatial distribution from calculated thermal field (left) and relative error contour map (right) when compared with S_x from interpolated thermal field for the “coarse Mesh 4”.....	173
Figure 5.44 S_y spatial distribution from calculated thermal field (left) and relative error contour map (right) when compared with S_x from interpolated thermal field for the “coarse Mesh 4”.....	173
Figure 5.45 S_z spatial distribution from calculated thermal field (left) and relative error contour map (right) when compared with S_x from interpolated thermal field for the “coarse Mesh 4”.....	174

Figure 5.46 S_{xy} spatial distribution from calculated thermal field (left) and relative error contour map (right) when compared with S_x from interpolated thermal field for the “coarse Mesh 4”.....	174
Figure 5.47 S_{xz} spatial distribution from calculated thermal field (left) and relative error contour map (right) when compared with S_x from interpolated thermal field for the “coarse Mesh 4”.....	175
Figure 5.48 S_{yz} spatial distribution from calculated thermal field (left) and relative error contour map (right) when compared with S_x from interpolated thermal field for the “coarse Mesh 4”.....	175
Figure 6.1 Thermal field raised within O1.	176
Figure 6.2 Thermal field raised within O2.	177
Figure 6.3 Thermal field raised within O3.	177
Figure 6.4 Thermal field raised within O4.	177
Figure 6.5 Thermal field raised within O5.	178
Figure 6.6 Thermal field raised within O6.	178
Figure 6.7 Thermal field raised within O7.	178
Figure 7.1 Contour map and statistical distribution of the temperature error [in %] between the calculated and interpolated thermal field and cumulative curve in O2 poloidal region.	180
Figure 7.2 Contour map and statistical distribution of the temperature error [in %] between the calculated and interpolated thermal field and cumulative curve in O3 poloidal region.	181
Figure 7.3 Contour map and statistical distribution of the temperature error [in %] between the calculated and interpolated thermal field and cumulative curve in O4 poloidal region.	182
Figure 7.4 Contour map and statistical distribution of the temperature error [in %] between the calculated and interpolated thermal field and cumulative curve in O5 poloidal region.	183
Figure 7.5 Contour map and statistical distribution of the temperature error [in %] between the calculated and interpolated thermal field and cumulative curve in O6 poloidal region.	184
Figure 7.6 Contour map and statistical distribution of the temperature error [in %] between the calculated and interpolated thermal field and cumulative curve in O7 poloidal region.	185

List of Tables

Table 1.1 Chemical composition of Eurofer steel [23].....	21
Table 1.2 RCC-MRx RB 3200 rules breakdown.....	28
Table 2.1 Mesh parameters.....	39
Table 2.2 Eurofer thermo-physical properties.....	41
Table 2.3 Pb-15.7Li thermo-physical properties.....	41
Table 2.4 Tungsten thermo-physical properties.....	42
Table 2.5 HTC values user for cooling channels and DWTs.....	43
Table 2.6 Features of the coarser meshes set-up and comparison with the original one.....	56
Table 3.1 Summary of the loads and boundary conditions.....	72
Table 3.2 Maximum displacements values in all the assessed scenarios.....	75
Table 3.3 RCC-MRx design criteria [31].....	76
Table 3.4 Sub-model regions mesh detail.....	82
Table 3.5 RCC-MRx criteria percentage errors global model vs sub-model in CC.....	96
Table 3.6 RCC-MRx criteria percentage errors global model vs sub-model in BC.....	97
Table 3.7 RCC-MRx criteria percentage errors global model vs sub-model in BC.....	98
Table 4.1 Eurofer physical properties [56].....	110
Table 4.2 PbLi physical properties [38].....	110
Table 4.3 Tungsten physical properties [57].....	111
Table 4.4 Total Heat Flux and average NWL poloidal distribution.....	112
Table 4.5 HTC values used for cooling channels and DWTs coolant.....	113
Table 4.6 Maximum temperature values for each COB poloidal region equipped with references v06b DWTs layout.....	115
Table 4.7 BZ and FW-SW cooling layout per poloidal region.....	118
Table 4.8 Maximum and minimum displacements values obtained.....	126
Table 4.9 Average temperature within the paths.....	129

List of Acronyms

ASME	American Society of Mechanical Engineers
BB	Breeding Blanket
BC	Bottom Cells
BP	Back Plate
BSS	Back Supporting Structure
BU	Breeder Unit
BZ	Breeder Zone
CB	Ceramic Breeder
CC	Central Cells
COB	Central Outboard Blanket
CS	Central Solenoid
DI	Dipartimento di Ingegneria
DEMO	Demonstration Fusion Reactor
DONES	DEMO Oriented Neutron Source
DWTs	Double Walled Tubes
EFDA	European Fusion Development Agreement
EM	Electro Magnetics
EU	European Union
FEM	Finite Element Method
FPP	Fusion Power Plant
FPR	Fusion Power Reactor
FW	First Wall
HCLL	Helium Cooled Lithium Lead
HCPB	Helium Cooled Pebble Bed
HF	Heat Flux
IB	Inboard Blanket
IED	Immediate Excessive Deformation
IF	Immediate Fracture due to exhaustion of ductility

IFMIF	International Fusion Materials Irradiation Facility
IPFL	Immediate Plastic Flow Localization
IPI	Immediate Plastic Instability
LIB	Left Inboard Blanket
LOB	Left Outboard Blanket
LOCA	Loss Of Coolant Accident
MMS	Multi Module Segmentation
NO	Normal Operation
NWL	Neutron Wall Loading
OB	Outboard Blanket
OP	Over-Pressurization
PFC	Poloidal Field Coil
RAFM	Reduced Activation Ferritic-Martensitic
R&D	Research and Development
RM	Remote Maintenance
SB	Segment Box
SPs	Stiffening Plates
SPh	Horizontal Stiffening Plates
SPv	Vertical Stiffening Plates
SWs	Side Walls
TBM	Test Blanket Module
TBR	Tritium Breeding Ratio
TC	Top Cells
TFC	Toroidal Field Coil
UVDE	Upper Vertical Displacement Event
VV	Vacuum Vessel
WCLL	Water Cooled Lithium Lead
WPBB	Work Package Breeding Blanket

List of Symbols

α	Coefficient of thermal expansion
ΔT	Thermal rise
$\underline{\underline{\epsilon}}$	Strain tensor
ϵ_{ij}	Strain tensor component
ν	Kinematic viscosity
ρ	Density
$\underline{\underline{\sigma}}$	Stress tensor
σ_{ij}	Stress tensor component
τ_{ij}	Shear stress
Φ	Heat flux
c_p	Specific heat
E	Young's modulus
F	Peak stress
HTC	Heat transfer coefficient
k	Thermal conductivity
K_{eff}	Plastic collaboration coefficient
L_m	Additional membrane stress
P	Primary stress
P_b	Primary bending stress tensor
$\overline{P_b}$	Primary bending stress intensity
$P_{des,coolant}$	Coolant design pressure
$P_{des,breeder}$	Breeder design pressure
P_L	Local primary membrane stress tensor
$\overline{P_L}$	Local primary membrane stress intensity
P_m	General primary membrane stress tensor
$\overline{P_m}$	General primary membrane stress intensity
q'''	Volumetric density of heat power
Q	Secondary stress

Q_b	Secondary bending stress tensor
\overline{Q}_b	Secondary bending stress intensity
Q_L	Local secondary membrane stress tensor
\overline{Q}_L	Local secondary membrane stress intensity
Q_m	General secondary membrane stress tensor
\overline{Q}_m	General secondary membrane stress intensity
$R_{p0,2}$	Stress value corresponding to a plastic deformation of 0.2%
$R_{m,min}$	Minimum tensile strength
S_{em}	Maximum allowable primary plus secondary membrane stress
S_{et}	Maximum allowable total stress
S_m	Maximum allowable primary membrane stress intensity
t	Time step
T	Temperature
u	Displacement
U	Creep usage factor
W	Creep rupture factor

Abstract

The Breeding Blanket (BB) is an essential component of the DEMO fusion reactor and its design is one of the pivotal purposes of the DEMO project. Indeed, this component has to withstand severe operating conditions, as it is directly exposed to the plasma, making its design particularly challenging. In particular, the Water-Cooled Lithium-Lead (WCLL) BB concept is one of the candidates currently considered for the conceptual design of the European DEMO reactor, developed under the coordination of the EUROfusion consortium.

The development of a robust BB system is crucial for the design of the whole DEMO reactor and the thermo-mechanical assessment of the whole BB segments is mandatory to allow checking their structural performances in different loading scenarios.

In this dissertation, a multi-scale procedure, allowing to investigate in detail the thermo-mechanical performances of an entire blanket segment, is proposed. In particular, the Central Outboard Blanket (COB) segment has been considered and the results are herewith presented.

Since the current reference design of the WCLL BB is not mature enough to carry out its full thermal-hydraulic analysis and, in any case, it would require a significant modelling effort and a huge computational burden, in the first part of the research activity, an alternative procedure aimed at obtaining a reliable thermal field for the whole segment, which is pivotal for the segment structural analysis, has been developed. In particular, starting from the thermal analysis of an elementary cell representative of a portion of the COB segment, a set of polynomial functions able to reliably reproduce the thermal field arising within it has been searched, exploring its predictive power in terms of temperature and secondary stress. Thanks to this procedure, it is possible to study different design solutions from a mechanical point of view and to select the most promising in order to investigate, in a later phase, its thermal-hydraulic behaviour in detail. Once obtained the thermal field by means of the interpolating procedure, it has been applied onto the entire poloidal length of the segment, the thermo-mechanical analysis of the whole COB segment has been performed and its structural performances have been investigated in view of the RCC-MRx design criteria.

The second step of the multi-scale procedure consists of investigating the structural behaviour of the COB segment by means of the sub-modelling technique, which allows the in-depth study of particular or critical regions of the model. In fact, this technique allows to analyse a portion of an entire segment considering, as boundary conditions, a displacement field derived from the structural analysis of the whole component, to model the selected region with a finer mesh and to add to the local model some structural details not included in the analysis of the global model to reduce the computational effort.

Once set-up the procedure, an update has been also developed and presented. In fact, since in the DEMO WCLL BB the thermal loads strongly vary along the poloidal length of the segment, different elementary cells of the segment, located at 7 different poloidal heights, have been selected and analysed from the thermal point of view. In doing that, different geometric configurations of the cooling layout for each analysed cell have been investigated in order to withstand the corresponding thermal loads and comply with the thermal requirements. Hence, a more detailed thermal field has been obtained for the entire COB segment, stitching together the found 7 sets of polynomial functions obtained from the thermal analyses. The thermo-mechanical analysis of the entire segment has been performed, checking its structural performances against the RCC-MRx structural design rules and, then, investigating more in detail some particular regions by means of the sub-modelling technique.

In conclusion, the developed multi-scale procedure permits to investigate in detail the thermal behaviour of a portion of the entire segment, allowing to select among different possible layouts the most promising configuration and then, thanks to the interpolation procedure, to build-up a set of polynomial functions reproducing the thermal field and to apply it on the entire segment with the aim of performing its structural analysis in different operating conditions. Finally, thanks to the sub-modelling technique, it is possible to study in detail portion of the whole segment with reliable loads and boundary conditions deriving from the complete thermo-mechanical analysis of the whole structure. The developed procedure can also be applied to all the WCLL BB segments and to different blanket concepts, thus, helping the design and the development of the DEMO research activities about the BB. In particular, the obtained analysis procedure downstream the study herewith presented has been adopted within the framework of the DEMO WCLL BB design activities, allowing the evolution of its pre-conceptual geometric configuration towards a more robust conceptual layout able to better satisfy the considered design criteria and requirements.

The assumptions, the methodology and the obtained results are herewith reported and critically discussed.

Introduction

The research of energy sources capable of satisfying a world electricity demand that grows faster and faster as a result of increasing progress in every sector, an even higher standard of life, a strong industrial growth and the emergence of numerous developing countries, is nowadays one of the greatest technological world challenges. At the same time, it is necessary to find an energy source to replace fossil fuels, namely oil, coal, natural gas, etc., with so-called “carbon-free” energy sources, in order to reduce the CO₂ emission and address environmental problems.

In this context, the exploitation of the nuclear fusion reaction for the production of electricity appears to be a promising option to complement renewable energy sources, which cannot satisfy the world’s energy demand by themselves. Therefore, the international scientific community is spending a great deal of financial resources and manpower studying the exploitation of nuclear fusion on large scale, in order to realise nuclear fusion power plants to produce electricity in a continuous and reliable way. Fusion plants do not produce CO₂ during their operational phase, and, unlike nuclear fission power plants, fusion reactors are intrinsically safe, since any deviation from the operating conditions leads to the reactor shutdown. Moreover, the use of the Deuterium-Tritium (D-T) fusion reaction ensures, for a given thermal power amount, significantly less radioactive waste. These main features make the nuclear fusion a very attractive option for the development of future energy supply scenarios.

Therefore, the international scientific community is committed to realizing, by the end of the century, the first Fusion Power Reactor (FPR). To this goal, several research programmes are ongoing worldwide, with the main scope to understand in deep the physical behaviour of a high-power plasma and to study and develop mature enough technological solutions for the realization of the future FPRs components. Indeed, a FPR will have to be capable of producing hundreds of MWs of electrical power to provide the grid in a continuous, safe and reliable way.

In this broad context, the European Commission has issued in 2013 and updated in 2018 the European Roadmap to the Realisation of Fusion Energy, defining the milestones to be

achieved until to the realization in EU, by 2050, of the first electricity production from plasma and, by the end of the century, of the first FPR. According to the agreed work breakdown, the EUROfusion Consortium has been created to carry out the actions envisaged in the roadmap. Finally, these actions have been funding by the framework research programmes Horizon2020 (until 2020) and Horizon Europe (from 2021 onwards).

The European roadmap to the Realisation of Fusion Energy considers the TOKAMAK (toroidal chamber with magnetic coils) concept as the reference technological option toward the realization of the first FPR, whereas the Stellarator option is also studied in parallel as a backup and long-term option. In particular, both the fusion reactor concepts are based on a closed magnetic confinement. The central research facility of the European Fusion Programme is the Joint European Torus (JET), located at the Culham Centre for Fusion Energy in Oxfordshire, UK. The JET reactor, based on the TOKAMAK concept, achieved its first plasma in 1983 and in 1991 realized for the first time in the world a D-T plasma, demonstrating, hence, the scientific feasibility of the controlled nuclear fusion reaction. The JET reactor is still in operation under the EUROfusion umbrella, performing experiments on D-T plasmas to assess in deep the plasma physics in view of the start-up of the ITER fusion reactor. ITER (acronymous of International Thermonuclear Experimental Reactor) is a TOKAMAK reactor under construction in France, thanks to a joint effort of EU, Russian Federation, USA, China, Japan, India and Republic of Korea. The main scopes of ITER, whose first plasma is expected by the 2025, will be to achieve an energy multiplication factor of 10 (namely it has to produce up to 10 times the energy given in input to sustain fusion reactions) and to act as a link between the small-scale experimental fusion devices and the DEMONstration Power Plant (DEMO). In fact, it will house some components' mock-ups to test, in a fully fusion relevant environment, to test the feasibility of Tritium production inside the reactor. In this regard, the EUROfusion Consortium is fully involved in the ITER project for the design, construction and test of the Test Blanket Modules (TBMs), namely the mock-ups of the future DEMO Breeding Blanket (BB). The DEMO reactor, whose EUROfusion is totally in charge of, will be a prototype of a FPR, being able to produce several MWs of net electricity exploiting the D-T reaction without economic purposes. To this goal, one of the DEMO key components will be the BB. Such a component shall be devoted to ensuring the plant Tritium self-sustenance, shielding magnets from radiation and removing the plasma heat power to convey it to the systems for the final conversion in electricity. Currently, the DEMO reactor is approaching the conceptual design phase, after a pre-conceptual design phase concluded in 2020. At this stage, two options are assessed within the EUROfusion Consortium to be selected as a driven blanket for DEMO: the Helium-Cooled Pebble Bed

(HCPB) BB and the Water-Cooled Lithium Lead (WCLL) BB. A final decision will be gone ahead with DEMO design adopting the selected concept as driver blanket and other as test blanket concept.

In this scientific background, the research activity carried out during the XXXIV cycle of the Ph.D. course in Energy and Information Technologies - nuclear engineering and applied physics curriculum, held at the University of Palermo, is framed in the design activities concerning the DEMO nuclear fusion reactor carried out by the EU community, within the Horizon2020 and Horizon Europe framework programmes, supported by the EUROfusion consortium, of which the University of Palermo is a linked third party (now affiliated entity) through ENEA. In particular, the research activity performed in the frame the Ph.D. course has been focussed on the design of the DEMO WCLL BB, in compliance with the work breakdown and the milestones prescribed by the EUROfusion Consortium. The research activity carried out has been mainly aimed at studying the thermo-mechanical performances of an entire Outboard Segment of the DEMO WCLL BB, under different operating loading scenarios, in order to contribute to its pre-conceptual design and allowing to evolve the design in view of the conceptual design phase. In particular, starting from a reference geometric layout, proper design alternatives have been proposed and assessed in order to overcome the arising issues and, to this purpose, an innovative multiscale analysis methodology has been set-up and applied. Hence, a vigorous research campaign has been performed in order to develop a robust geometric configuration for the WCLL BB Central Outboard Segment (COB). In a first phase the multiscale procedure has been developed, then, in a second phase, the procedure has been applied to study the thermal and thermo-mechanical behaviour of the WCLL COB segment.

Given the lack of maturity of the WCLL COB segment reference layout, in the first part of the research activity, a procedure to obtain a realistic thermal field for the COB segment has been set-up and validated. In particular, the procedure consists in predicting the thermal field within a certain region of the segment, then finding out a set of interpolating functions and using them to apply the temperature spatial distribution to the whole segment without performing the thermal-hydraulic assessment of the entire structure, at the moment not possible because of its lack of maturity. Hence, in the first part of the study, the interpolation procedure has been derived and its effectiveness has been assessed both in terms of thermal and secondary stress field prediction. Since the spatial discretization of the region used to calculate the thermal field is typically finer than the whole segment, a mesh independence assessment of the procedure has been performed too. Once obtained the thermal field for the whole segment, it has been assessed from the thermo-mechanical point of view and, then,

using the sub-modelling technique, the local thermo-mechanical behaviour of some regions of interest has been investigated, adopting as boundary conditions the displacement field previously calculated from the structural analysis of the whole segment. The multiscale procedure set-up allows to work in a double direction, going from a local to a global model and vice-versa, permitting an in-depth study of thermo-mechanical behaviour of the WCLL COB segment.

Finally, in a second phase of the research activity performed during the Ph.D. course, the multiscale procedure described above, has been applied to predict the structural behaviour of an up-to-date version of the COB Segment geometric layout, according to the DEMO baseline 2017. In particular, seven poloidal regions have been considered to be, first, optimized from the thermal point of view (namely ensuring that, in each of them, the maximum temperature arising within the structural material was below the suggested limit of 550 °C) and, then, used to calculate the optimized thermal field to be interpolated by means of purposely set-up interpolating functions. In this way, the variation along the poloidal coordinate of the thermal loads the segment undergoes is taken into account. Hence, the seven sets of interpolating functions (one representative of each poloidal region thermally optimized) have been stitched together to obtain a thermal field for the whole WCLL COB segment even more detailed. Thus, the global thermo-mechanical performances of the whole segment have been assessed. Afterwards, the detailed structural behaviour of some region of particular interest has been investigated by means of the adoption of the sub-modelling technique, verifying the fulfilment of the design criteria prescribed by the RCC-MRx structural design code.

The research activity carried out during the Ph.D. course has allowed achieving multiple goals, matching some milestones of the DEMO WCLL BB development expected by the EUROfusion project. Firstly, alternative and innovative methodologies have been set-up and applied to investigate the thermo-mechanical response of a large and detailed structure as the WCLL segment, allowing, on one hand, to speed-up the calculation and, on the other, to perform local assessments that realistically taking into account the influence of the entire structure. Potentially, the developed procedure for the COB segment can be extended for the other BB segments (lateral outboard and inboard ones) and for every blanket concepts. Moreover, a strong contribution towards the achievement of a sound conceptual design of the WCLL COB segment has been given, thermally optimizing it along its poloidal extension and allowing to update the spatial layout of its cooling system. Finally, the drawbacks and the potential showstoppers of the proposed layout, some coming from the interfaces with the

surrounding systems, have been clearly highlighted and detailed, to pave the way for further developments in the design of the whole DEMO reactor.

The whole research activity has been carried out following a theoretical-numerical approach based on the Finite Element Method (FEM) and adopting the commercial FEM code Abaqus v 6.14.

In this dissertation, the whole research activity is presented, showing the adopted methodologies and critically discussing the obtained results.

Chapter 1

1 The Breeding Blanket of the DEMO Fusion Reactor

1.1 Introduction

Nowadays the global electricity demand constantly increasing and it is expected to triple towards the end of the century due to rapid population growth, improved living conditions and progress in developing countries. In this context, the search for energy sources allowing energy production both safe and almost inexhaustible becomes fundamental. So, the exploitation of the nuclear fusion reaction for the electricity production appears as an option to traditional fossil energy sources. In order to allow the nuclear fusion power plants technology achieving the level of maturity necessary to build commercial reactors, worldwide research programmes have been launched with this aim. In this regard, the European Union (EU) is long-time involved in the fusion research and development activities. In particular, the EUROfusion Consortium, on behalf of the European Commission within the framework of HORIZON 2020 research programme, drew up the European Roadmap to the realization of Fusion Energy [1] in order to identify the mayor targets to develop by 2050 a mature technology for the electricity production based on the exploitation of the nuclear fusion reaction.

1.2 Notes on the nuclear fusion reaction

The nuclear fusion is an exergonic reaction in which the nuclei of two light elements interact producing a highly unstable compound nucleus that splits, liberating a huge amount of energy, into a heavier stable nucleus and a nucleon.

The mass of this resulting system is lower that the reactants, so the energy released is associated to the mass difference, defined as “Q-value”:

$$Q = \Delta m \cdot c^2 \tag{Eq. (1.1)}$$

where c is the light speed in vacuum. The Eq. (1.1) is the Einstein Equation and shows that in the fusion reaction, the mass defect is converted into kinetic energy to the produced nuclei, in inverse proportion to their masses, to the conservation of momentum.

The resulting system of products is more stable than that of reactants nuclei. The stability of a nucleus is obtained by the ratio between the binding energy and the total number of nucleons in the nucleus. In fact, this value is the average energy required to remove a nucleon from a nucleus, larger is this ration, more stable is the nucleus. Looking to the graph of the variation of the average binding energy per nucleon with nucleon number (Figure 1.1), light nuclei are less tied, i.e., less stable. So, they can reach a more stable condition moving in the central zone of the graph thanks to the fusion reaction. On the contrary, heaviest elements split into more tightly bound elements due to nuclear fission reaction. Therefore, fusion of light nuclei, with mass numbers much less than ^{56}Fe , and fission of heavy nuclei, with mass numbers greater than ^{56}Fe , are exothermic processes.

At interatomic distances, the two main forces are the strong nuclear force, with an attractive effect on the nucleons, acting over short distance and the electrostatic force acting over longer distances. So, for the fusion reaction to occur, the two reactants must be close enough that the nuclear force overcomes the repulsive electrostatic force, the Coulomb force, acting between positive nuclei.

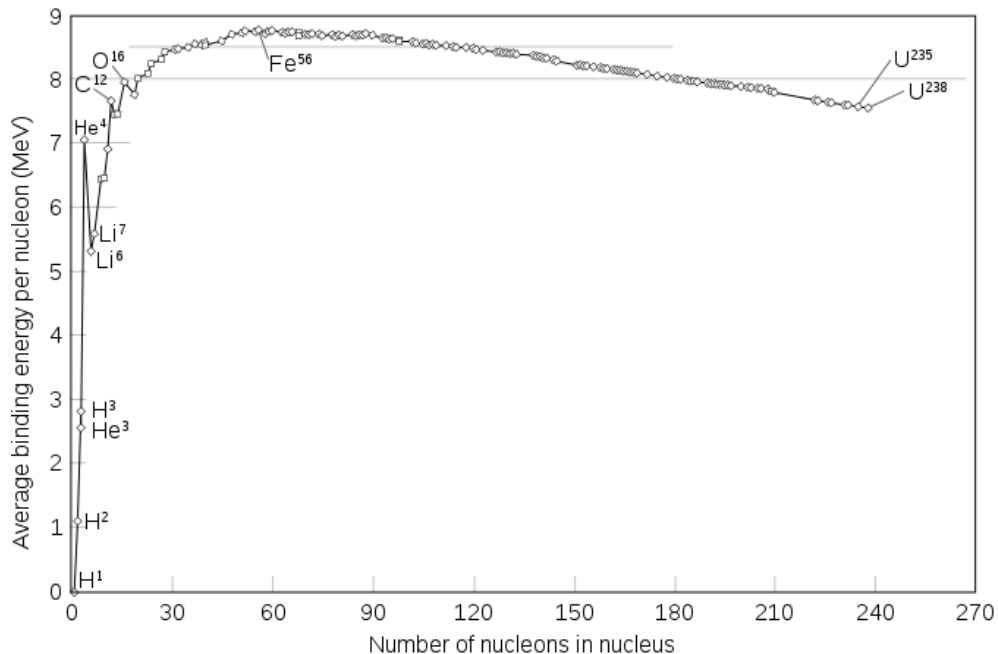
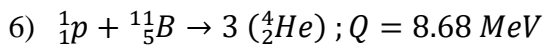
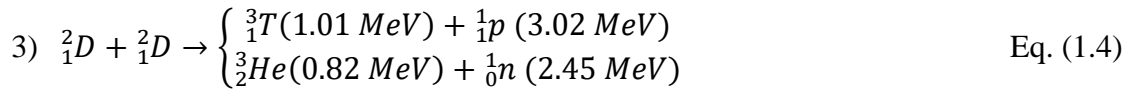
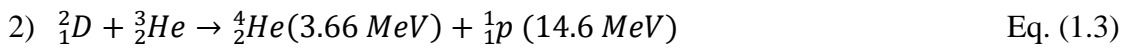
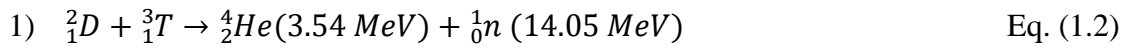


Figure 1.1 Average binding energy per nucleon [3].

To bring nuclei close enough, a distance of order of 10^{-15} m, the nuclei need a certain amount of kinetic energy to overcome the so-called Coulomb barrier, that is directly proportional to the product of the charges and inversely proportional to the square of the

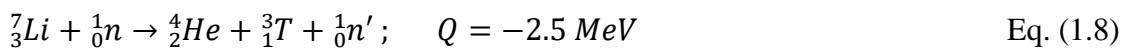
distances between them. However, thanks to the quantum phenomenon known as “tunnel effect”, the threshold energy can be reduced. This phenomenon implies a non-zero probability that two interacting nuclei overcome mutually their electrostatic repulsion, while having a lower energy than the threshold one. So, in order to maximize the tunnel effect, it is necessary to increase the kinetic energy of reacting nuclei.

Different nuclear fusion reactions, releasing energy, have been identified as promising in research and industrial applications. It is possible to compare them thanks to the cross section of fusion reactions. This parameter describes the fusion reaction probability as a function of the relative speed between the two colliding particles. In particular, Figure 1.2 shows the occurrence probability of the most relevant fusion reactions as a function of the incident nucleus energy. Compared to the figure, the following fusion reactions are shown:



Looking at the Figure 1.2, D-T reaction seems the most interesting reaction since it exhibits a high peak value of the cross section of fusion reaction at a lower level of energy than the other reaction showed. Furthermore, among all the other reactions considered, D-T reaction has a fairly low value of Coulomb barrier.

Deuterium is present in nature, available in seawater and rivers, with an isotopic abundance of 0.015%, instead, Tritium is a fast-decaying radioelement and it is practically absent in nature, with the only known inventory of almost 20 kg in the oceans and atmosphere. Therefore, the quantities of Tritium required for a commercial fusion reactor need to be bred on a substantial scale inside the reactor by means of “tritium breeding” reaction. So, tritium can be generated during the fusion reaction thanks to the reaction between the two lithium isotopes, contained in the blanket surrounding the fusion chamber, and the fusion neutrons. The relevant breeding reactions are [5]:



The first is an exothermic reaction and occurs mainly with slow neutrons, so all the fusion neutrons that slow down to thermal energies can generate tritium due to reaction with ${}^6\text{Li}$. Instead, the second one is endothermic and involves fast neutrons. The product neutron of

the latter reaction, n' , has a smaller energy than the incident one, n , and it can be captured on ${}^6\text{Li}$ so forming Tritium. So, it is necessary to select a structural material able to minimize the loss of neutron by absorption or escape from the blanket.

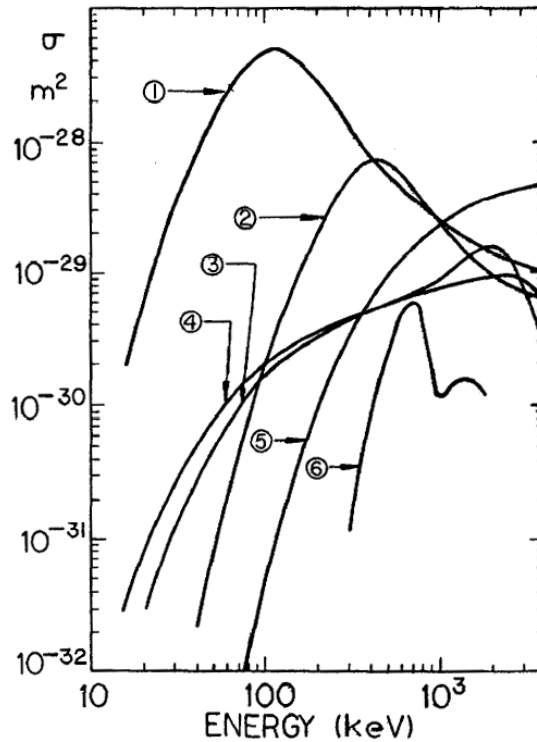
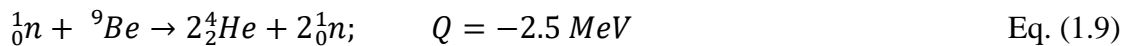


Figure 1.2 Cross section of main nuclear fusion reactions vs. energy for monoenergetic beams [4].

Moreover, the efficiency of the tritium breeding can be increased thanks to adding a neutron multiplier in the lithium blankets, as beryllium or lead. In fact, the most promising $(n, 2n)$ reaction, are [6]:



On the other hand, it is necessary attain a very high number of reactions, in order of 10^{28} reactions per second, to exploit the fusion reaction for large-scale electricity production. So, deuterium and tritium must have a high kinetic energy, that mean temperature in the order of 10^8 K, to overcome the Coulomb barrier and to achieve a good rate of exothermic reactions. Therefore, the high-temperature plasma of colliding particles must be confined in a limited space for a long enough time under the conditions necessary to constantly guarantee the maintenance of the fusion reaction.

While in stars the condition of confinement is obtained due to their gravitational field that creates sufficiently high pressure, that confinement cannot be obtained inside a fusion reactor. Several confinements methods have been studied and the most promising are the

inertial confinement and the magnetic confinement method. Both confinement systems must satisfy two pivotal characteristics for the realization of a viable nuclear fusion reactor: heating and keeping the fuel at high temperature to realize a suitable fusion reaction rate density; and maintaining a sufficiently long confinement time.

In the inertial confinement method, pellets of Deuterium-Tritium fuel are compressed and heated by external driver delivers energy so fast to reach density-temperature condition and fuse together without escaping, because of the fuel inertia. Lasers, particle beams or X-rays can supply the external source of energy.

Instead, the magnetic confinement concept is the most promising approach for prolonged containment of plasma in a nuclear power reactor. This confinement method employs strong magnetic fields, generated by high intensity electric currents, to heat and confine the movement of the Deuterium-Tritium plasma. The charged particles forming the plasma tend to spin around the magnetic lines of force due to the effect of the magnetic field, thus obtaining confinement along the direction perpendicular to the plane of the magnetic field.

Different types of magnetic confinements have been studied over the years, and these may be summarized in: open, namely linear configuration, and closed, i.e., toroidal configuration. The first configuration employs a solenoid providing to establish a straight homogeneous magnetic field to contain the plasma. The disadvantage of this method is the leakage plasma particles from the open ends of the magnetic field. So, increasing the magnetic field at the two ends, charged particles close to these areas slow down and, some of these can be reflected back. This concept is named magnetic mirror confinement. Unfortunately, the fastest particles are usually not stopped.

Therefore, toroidal magnetic confinement offers the advantage of not having particle losses from the terminal regions. In fact, it is possible to form the plasma in a closed shape, a torus, thereby removing the particles loss. The most advanced concepts to realize the closed magnetic confinement of plasma in a nuclear fusion reactor are Tokamak and Stellarator (Figure 1.3).

In a Tokamak machine, the magnetic field is the results of different fields and it has helical force lines that spiral around the torus. A poloidal and a toroidal magnetic field are necessary to confine plasma. In particular, a central solenoid, powered by alternate current, acts as the primary of a transformer which induces in the plasma, acting as the secondary loop of the transformer, a toroidal current. The circulation of this electric toroidal current within the plasma also generates the poloidal magnetic field. Instead, external coils generate the toroidal field. Toroidal and poloidal fields are not able to confine the plasma which tends to expand radially. So, an additional vertical magnetic field, produced by poloidal coils, so-

called stabilizing coils, is added, preventing the expansion of the plasma. This kind of fusion reactors are characterized by a pulsed operating phase.

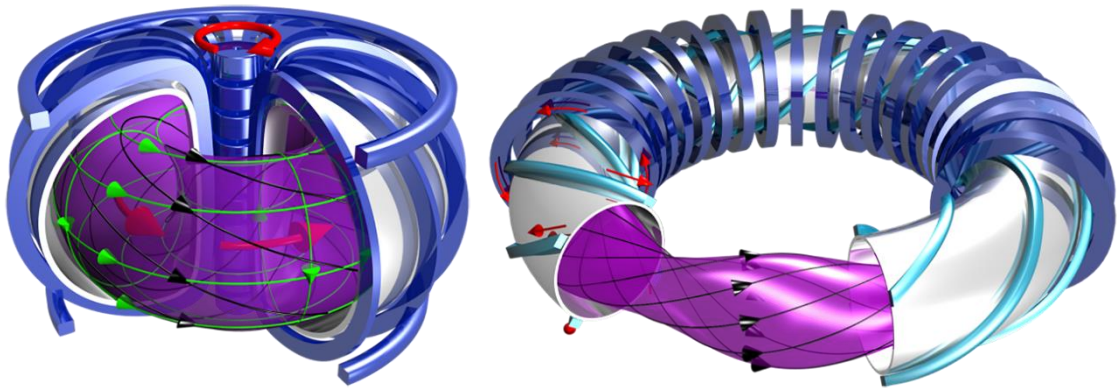


Figure 1.3 Schematics of magnetically confined plasmas in tokamaks (left) and stellarator (right) configurations.

Over the last 60 years, fusion research has been focussed on Tokamak confinement concept and the progress leads to the ITER project [7], the world's largest Tokamak, and its successor, DEMO reactor [8].

In the Stellarator system, instead, the poloidal magnetic field is produced by an external and non-planar toroidal field coil. The Stellarator is toroidally non-axisymmetric while Tokamak is symmetric along the torus. Recently remarkable progresses have been conducted on the Stellarator concept and different experimental projects have been planned across the world. The two major projects are the Wendelstein 7-X reactor [9] (W7-X in short, Greifswald, Germany) and Large Helical Device [10] (LHD in short, Toki, Japan).

Both the reactor lines are studied in the framework of the European Roadmap to the realization of Fusion Energy. In particular, in this document, three separate periods with several objectives can be identified (Figure 1.4):

1. First period (short-term, until 2030): start ITER operation with other parties and complete DEMO conceptual design.
 - Construct and commission ITER;
 - Secure the success of future ITER operation via preparation and early experiments;
 - Prepare the ITER generation of scientists, engineers and operators;
 - Finalise the design and construct a fusion spectrum neutron source (IFMIF-DONES);
 - Lay the foundation of a DEMO fusion power plant;
 - Explore the stellarator as an alternative approach to power plants;

2. Second period (medium-term, 2030-2040): Burning plasma on ITER and DEMO engineering design.
 - Exploit ITER with hydrogen, helium and deuterium to prepare for high performance D-T operation;
 - Optimise ITER performances with operation in D-T plasmas at $Q=10$;
 - Acquire information from ITER to support DEMO design;
 - Exploitation of the IFMIF-DONES fusion material testing facility and collect data for DEMO;
 - Carry out the design of DEMO with industry and prepare for construction;
 - Develop a pre-conceptual design for stellarator power plant;
 - Prepare the DEMO generation of scientists, engineers and operators;
3. Third period (long-term, after 2040): Technology and plasma optimisation on ITER and construction of DEMO.
 - Use ITER to prepare for DEMO and commercial Fusion Power Reactors (FPR);
 - Exploitation of the DONES fusion material testing facility to develop and qualify material for long life in DEMO and commercial power plants;
 - Finalise and then construct DEMO;
 - Demonstrate the electricity generation;
 - Take another step along the stellarator path;
 - Cooperate with industry for the deployment of tokamak or stellarator power plants.

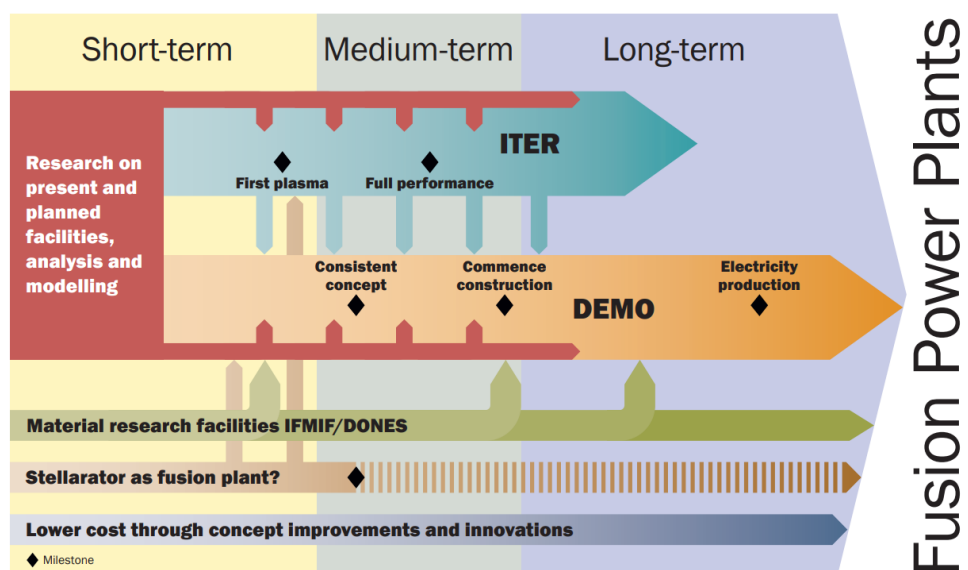


Figure 1.4 EUROfusion Roadmap [1].

The main objectives of the DEMO project [2] are: the conversion of heat into electrical power (~500 MW), achieve tritium self-sufficiency (with a breeding ratio greater than 1), a reasonable availability up to several full-power years and the minimization of radioactive wastes, the extrapolation to a commercial fusion power plant. In particular, producing sufficient tritium to fuel its plasma without requiring supply from external sources is an essential requirement for any next step fusion nuclear plant beyond ITER. For these reasons, one of the key components of the DEMO reactor is the Breeding Blanket (BB) that has several functions including to supply the tritium necessary to the machine self-sustenance and to remove the plasma heat power to be converted in electricity in the dedicated system downstream the BB.

In this context, the research activity carried out during the PhD course has been conducted in the framework of the Research & Development (R&D) activities, promoted by EUROfusion Consortium, concerning the DEMO reactor based on the TOKAMAK concept.

1.3 The DEMO fusion reactor

In accordance with the Roadmap to Fusion Electricity Horizon 2020 [11], the European community began a campaign of research on DEMO fusion reactor, which will have to generate, by mid-century, several hundred MWs of electricity with a closed tritium fuel cycle. In particular, the main DEMO goals are:

- A plasma power of about 2GW to generate 500 MW of net electricity;
- Long plasma pulse (>2h) and minimize dwell time between two pulses
- Achieve tritium self-sufficiency, obtaining a Tritium Breeding Ratio (TBR)>1;
- Several full power years;
- Minimize activation waste, no long-term storage;
- DEMO as a component test facility and pathfinder to a First-of-a-Kind (Foak) Fusion Power Plant (FPP).

Since DEMO is placed between ITER, with the task of develop the fusion technology, and Foak Fusion Power Plant, it is necessary to extrapolate from ITER the mature technologies and regimes of operation, with a design development in parallel to ITER exploitation.

The revised development plan foresees three steps: a Pre-Conceptual Design Phase to investigate different DEMO concept and to analyse system characteristic; a Conceptual Design Phase in order to validate the baseline concept and an Engineering Design Phase to develop the final design. The research activity carried out during the PhD has been developed

in the frame of the Pre-Conceptual Design Phase, which ended in 2020 and underwent a Gate Review process. At the end of this phase, the thermomechanical performances of the WCLL BB, while maintaining the structural material temperature below the suggested limit, have been improved and the neutronic requirement (TBR and components' shielding) have been pursued, different feeding pipes and fluid manifolds have been integrated taking into account the BB interfaces, and a design respecting the limits imposed by the manufacturing process has been developed. Therefore, the obtained results, herewith discussed, represent a starting point for the research activities of the subsequent phase, the Conceptual Design Phase.

The DEMO architecture, based on the Tokamak concept, consists of the main systems listed below and showed in Figure 1.5:

- Vacuum Vessel (VV): is a torus shaped double-walled pressure vessel, necessary to provide and ensure the vacuum, as mechanical support for the plasma facing components and as first barrier for radioactivity;
- Breeding Blanket: covers the inner surfaces of the VV, shielding the vessel itself and the magnets from the plasma heat radiation and additional heat load due to impacting particles, thanks to the First Wall (FW). Neutrons produced from the fusion reactions within the plasma interact with the nuclei of the Blanket's structural material and, as a result most of their energy is transferred to the coolant flowing inside the modules. In fact, inside the BB the cooling system is aimed at removing the thermal power and transfer it to the external system for conversion into electrical energy. So, the removed heat from FW and the breeder units is transferred to the secondary cooling loop by means of water or helium. In addition, one of the main functions of the BB is the internal production of Tritium. Therefore, lithium flows inside the breeder units, constantly cooled, and it is transformed into tritium thanks to fusion neutrons;
- Divertor: located in the lower region of the VV, is a high heat flux component, collects most of the particles and energy exhausted coming from the plasma, ensuring their efficient removal. The Divertor also foresees a cooling circuit to remove the heat due to the radiation;
- Magnet system: is a set of superconducting coils, actively cooled by helium at 4 K, producing the magnetic fields necessary to confine, shape and control the plasma. In particular there are the toroidal and poloidal field coils (TFC and PFC respectively) and the central solenoid (CS);
- Cryostat: is a large steel structure containing the VV and the superconducting magnets. It provides a cryogenic environment at low pressure constitutes an additional

barrier and support the entire tokamak. The Cryostat support system is capable of supporting the superconducting magnet system and the VV and, in addition, of transferring all the loads coming from the machine to the reactor base;

- **Primary Heat Transfer System (PHTS):** is the complex of vessel and in-vessel components cooling pipes transferring the heat generated in the tokamak plasma to the Power Conversion System (PCS). The PHTS system includes the Blanket, Divertor + limiter and VV PHTSs, respectively BB, DIV and VV PHTS Equipment in Figure 1.6.;
- **Power Conversion System:** is the secondary loop to the turbine building or intermediate energy storage building. In fact, the heat removed from the tokamak by the PHTS systems is transferred throughout heat exchangers to the PCS where the steam is generated in order to spin a turbine and to ensure an efficient conversion into electrical power. Two strategies are currently being explored in order to cope with the pulsed nature of the DEMO plasma operation model, the direct configuration, foreseeing a small Energy Storage System (ESS), and an indirect one, adopting an Intermediate Heat Transfer System (IHTS) with an ESS. The direct configuration is the reference one adopted for the DEMO WCLL [12][13] (Figure 1.6).

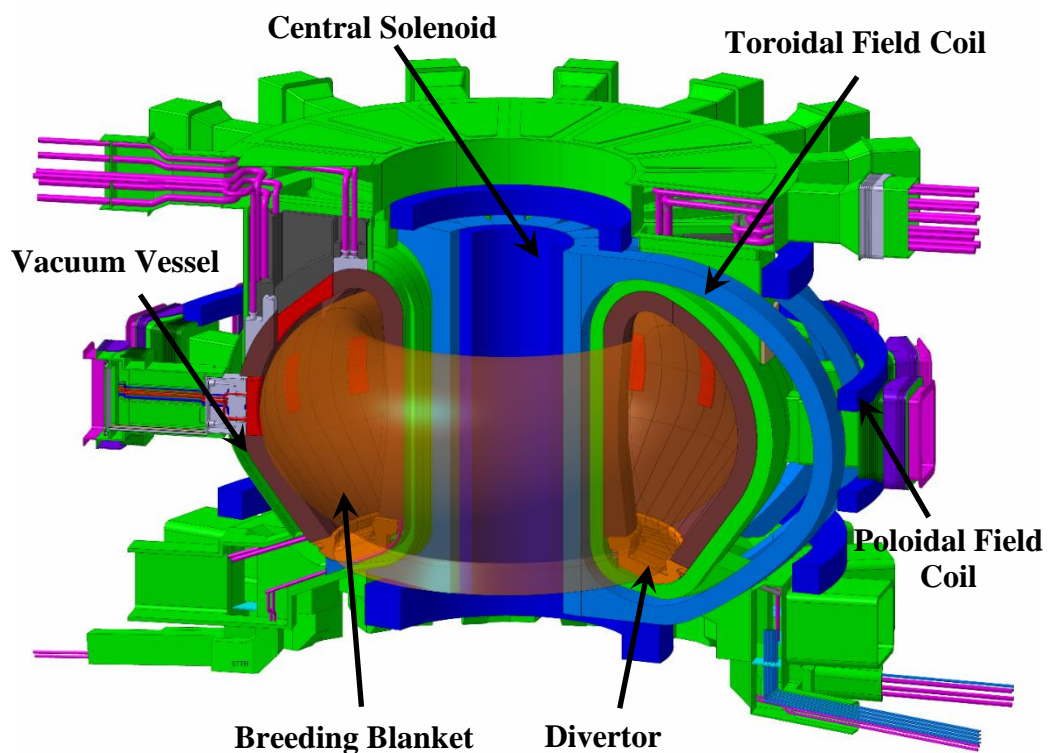


Figure 1.5 DEMO tokamak main systems [14].

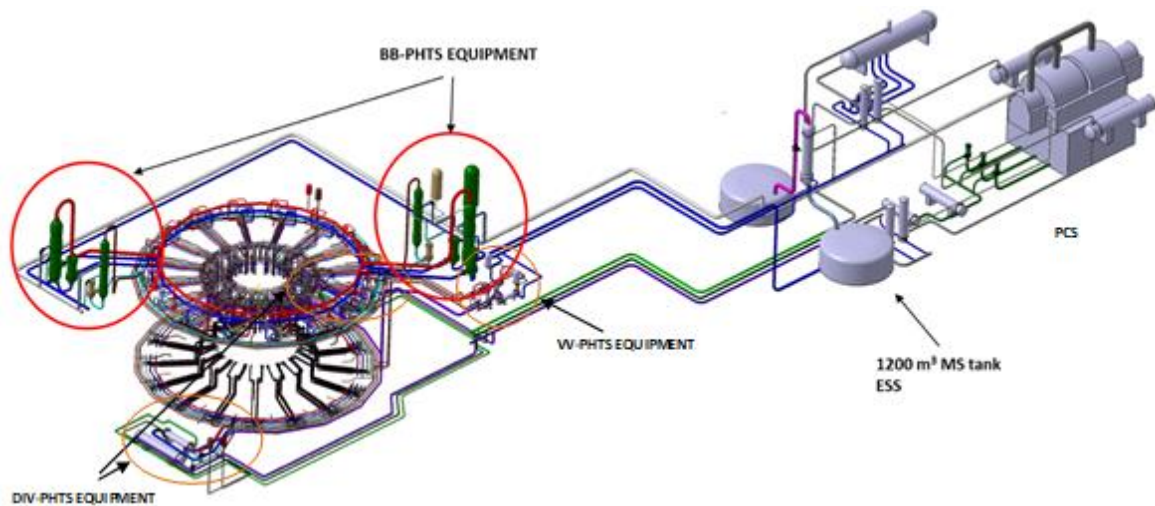


Figure 1.6 DEMO WCLL PHTSs and PCS 3D model [15].

The Breeding Blanket is a crucial component of DEMO fusion reactor, necessary to the Tritium self-sufficiency in the operation phase of the machine that is one of the pivotal objectives of DEMO project. Different BB concepts have been developed during the pre-conceptual phase. The Pre-Conceptual Design phase began with 4 BB concept: the Helium-Cooled Pebble Bed (HCPB), the Helium-Cooled Lithium Lead (HCLL), the Water-Cooled Lithium Lead (WCLL) and the Dual-Cooled Lithium Lead. The DEMO Work Package Breeding Blanket (WPBB) programs in 2017 recommended focussing on the two most promising candidates as driver blanket for the EU DEMO: HCPB and the WCLL concept. Hence, in the following, a brief description of these two candidate concepts is going to be given.

1.3.1 The HCPB Breeding Blanket concept

The HCPB configuration foresees a helium-cooled FW and a ceramic breeder, in particular a mixture of $\text{Li}_4\text{SiO}_4 + 35 \text{ mol } \% \text{ Li}_2\text{TiO}_3$ (60% ^6Li), while Beryllium as neutron multiplier, in form of hexagonal prismatic block of Be_{12}Ti , and helium as coolant and tritium carrier. Helium is used as coolant with a temperature equal to 300/520°C and a pressure of 8 MPa [16] (Figure 1.7). The structural material of all the BB components is Eurofer97, a Reduced Activation Ferritic-Martensitic (RAFM) steel.

The HCPB Blanket is composed by 16 sectors and each sector has a left, central and right outboard segment and a left and right inboard segment. For each segment, two pipes provide the entrance and exit of the coolant and another two pipes are foreseen for the purge gas. The Breeder Zone is composed by a First Wall (FW), in the front, Side Walls (SWs), laterally, and a Back Plate (BP) at the rear part, and it is filled by a hexagonal arrangement

of pressure tubes which connect FW and BP and act as radial stiffeners to support the structure. The so-called fuel-breeder pins are inside the pressure tubes. A pin is a system of two concentric cylinder and the resulting volume in the pin cladding is filled with the Ceramic Breeder (CB), KALOS CB. The neutron multiplier material is in form of prismatic block perforated in the centre to accommodate the corresponding pressure tube, with 1 mm of gap for the gas. The purge gas extracts tritium, produced in both CB and Neutron Multiplier Material (NMM). First, the gas enters in the NMM block and sweep them from top to bottom, then it enters the pins and flush the CB beds from the BP to the front of the pins. The gas is collected into ducts and it is directed to the purge gas outlet manifold as the Back Supporting Structure region, and it exits the segment.

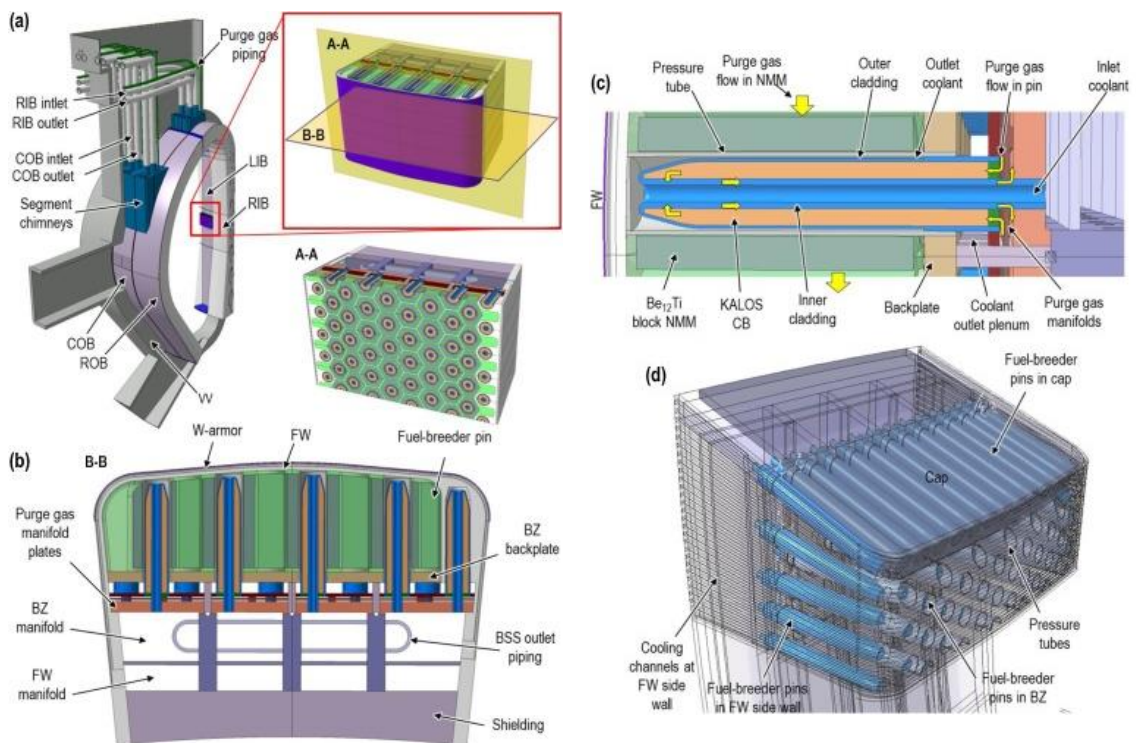


Figure 1.7 Reference HCPB for DEMO [16].

As aforementioned, Helium gas is used as coolant at 8 MPa and with a temperature to 300/520°C. It has a good compatibility with the structural material, Eurofer97, neutronic and chemical inertness, so a good neutron economy. The FW-SW region, subjected to high heat loads, is equipped by internal square cooling channels that cool it down.

With this system, the achievable TBR is approximately equal to 1.20, fulfilling the DEMO requirements with sufficient margin in order to compensate for possible inaccuracies due to the neutronic analysis. Moreover, the thermo-hydraulic analyses demonstrate that the temperature design limits of the BB material. However, several design details need to be fully assessed with future R&D activities.

1.3.2 The WCLL Breeding Blanket concept

In the WCLL concept subcooled pressurized water is used as coolant and liquid metal Pb-15.7Li eutectic alloy as breeder, neutron multiplier and tritium carrier. Segmentation and size of the segments, attachment system, auxiliary system concepts, are similar in both BB concept, instead, the main differences concern breeder and multiplier materials, coolant, manifold and FW configuration and heat load specification [14].

The WCLL BB concept is one of the design solutions foresees for the DEMO blanket. In the framework of EUROfusion R&D activities, since the Pre-Conceptual phase different layouts have been studied, accordingly with the change of the DEMO baseline. In particular, the various versions can be summarised in three main WCLL BB layouts (Figure 1.8) [17]:

- WCLL2014: based on the DEMO2014 Baseline, this design derives from the research conducted in the context of the European Fusion Development Agreement (EFDA) activities [18]. This concept is based on the Multi-Module Segmentation (MMS), so the entire segment is composed of some modules connected through the Back Supporting Structure (BSS). The developed Equatorial Module consists in an external structure called Segment Box (SB), composed of a U-shaped First Wall-Side Wall (FW-SW) region, covered by 2mm of Tungsten and with a wavy surface, closed in the back by a Back Plate (BP) and in the top and bottom region by two caps. The entire structure is internally reinforced by means of Stiffening Plates (SP) located on poloidal-radial and toroidal-poloidal planes. Inside the SB, within the SPs, the PbLi flows, and this region is so-called Breeding Zone (BZ). The coolant has the PWR conditions, pressure of 15.5 MPa and an inlet/outlet temperature equal to 285/325 °C. Water flows in some circular channels located inside the FW-SW region and inside 30 C-shaped Double Walled Tubes (DWT), located in poloidal-radial direction, in order to cooling the BZ.
- WCLL2015 and WCLL2016: in accordance with the DEMO2015 Baseline [19], these two layouts have been developed on the basis of the WCLL2014 configuration. In particular in the WCLL2015 architecture, the coolant inlet and outlet temperature have been turned into 295/328°C respectively. Moreover, the circular channels inside the FW-SW region have been replaced by square channels with a dimension of 7x7 mm². Therefore, toroidal-poloidal SPs have been substituted by toroidal-radial one, while the radial-poloidal, namely vertical SPs, are not connected to the FW. So, the arrangement of the DWTs have been also changed, from poloidal-radial to toroidal radial. Finally, the wavy surface has been removed and changed into a flat one, to

simplifying the manufacturing process. Instead, the WCLL2016 architecture has the same structure of the WCLL2015 one, but is based on the Single Module Segmentation (SMS) concept. The SMS concept foresees that there are only two caps, in the top and bottom part of the segment, while the caps between the various modules are replaced by horizontal SPs.

- WCLL2018: based on the modification introduced by the DEMO2017 Baseline [21]. Studies conducted in [20] have highlighted the better aptitude of the SMS to withstand Electro-Magnetic (EM) loads. Thus, once selected the SMS architecture, different BZ layout have been analysed in order to improve the neutronic, thermo-hydraulic and thermo-mechanical performances of the structure. The selected design is the so-called WCLL2018-t1A and the reference elementary cell the WCLL2018.v0.6.

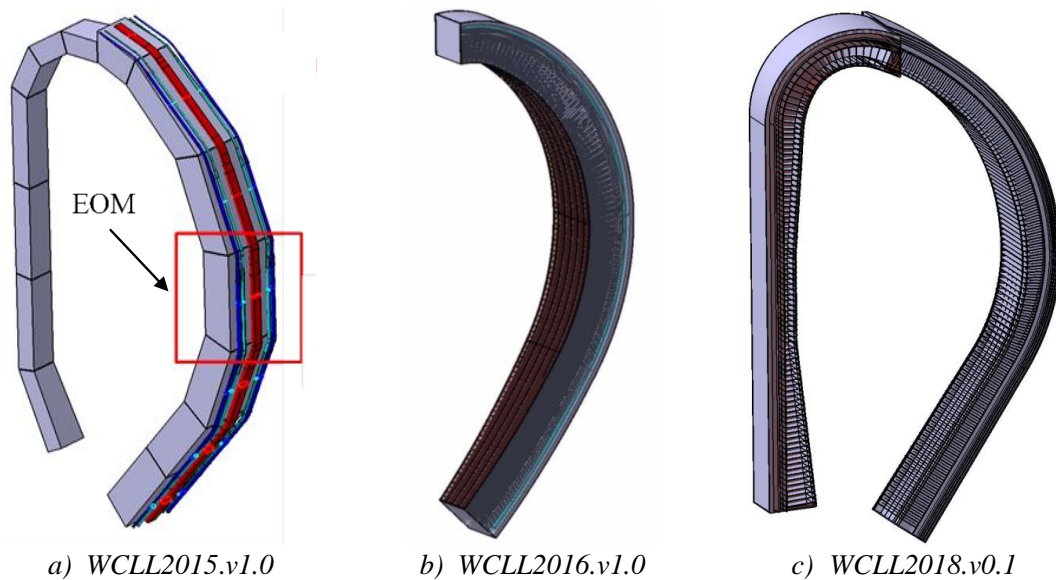


Figure 1.8 Main WCLL BB layouts [17].

The WCLL BB 2018 is subdivided into 16 toroidal sectors (22.5°) in toroidal direction, each one composed by 5 BB segments, two segment make the Inboard Blanket (IB) and three segments the Outboard Blanket (OB). Figure 1.9 shows a sector of DEMO WCLL BB according to the SMS architecture with the identification of its components, Left, Central and Right Outboard Blanket (LOB, COB and ROB) and Left and Right Inboard Blanket (LIB and RIB). Differently from the two lateral Outboard segment (LOB and ROB) which have asymmetric SWs, COB has them parallel, because of the requirements of the Remote Maintenance (RM). Instead, again due to the RM requirements, the two inboard segments are symmetric. Moreover, each segment is separated from the other by 20 mm.

Each segment consists in a single toroidal-radial Breeding Unit (BU), or elementary cell, repeated approximately 100 times, for the entire poloidal length of the segment. The

segments are closed on top and bottom by means of so-called caps [22]. The elementary cell, WCLL2018, with all its components is shown in Figure 1.10, moreover also showing in yellow the breeder path inside the cell.

The selected structural material for WCLL BB, as for the HCPB BB concept, is Eurofer97 RAFM steel, the European reference structural material studied within the framework of the European research activities on the materials.

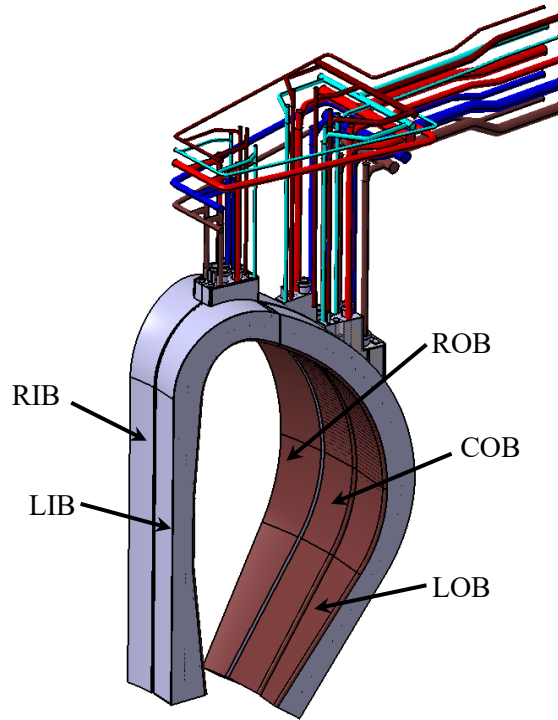


Figure 1.9 3D model of Outboard and Inboard BB segments.

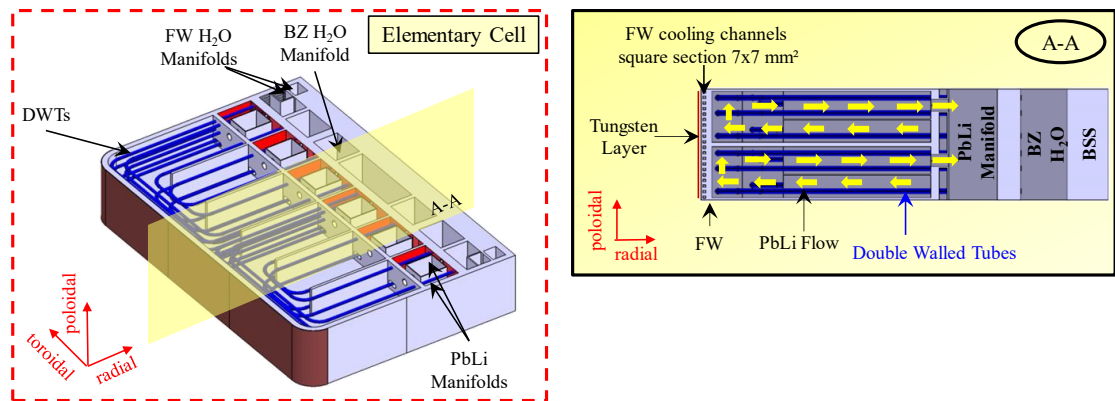


Figure 1.10 WCLL2018 Elementary cell [17].

1.3.3 Eurofer Structural Material

Eurofer97, as above mentioned, is a RAFM steel developed as structural material in fusion power reactor blankets and, in particular, for DEMO power plant. In particular,

Eurofer realized in the framework of the European application driven material development programme, is the European reference structural material for DEMO First Wall and Breeding Blanket. One of the ITER main objective is the installation of Test Blanket Modules (TBMs) representing a portion of DEMO blanket in order to study DEMO technologies and Eurofer97 structural material properties.

RAFM steels derived from the 9Cr-1Mo steel but without the high activation elements (as Molybdenum, Niobium, Nickel, Copper and Nitrogen) replaced with low activation elements as Tungsten, Vanadium and Tantalum. Table 1.1 shows the chemical composition of Eurofer97 steel. This category of steels, with respect to austenitic stainless steels, has an excellent stability (creep and swelling) under neutron irradiation and they exhibit lower values of thermal expansion coefficients and higher thermal conductivities coefficients at high temperature. In RAFM steels properties like the sensibility to radiation damage are kept low by the martensitic transformation thermal cycle design and due to the microstructure refinement.

Cr	8.5-9.5	O₂	<0.01
C	0.09-0.12	W	1.0-1.2
Mn	0.20-0.60	Ta	0.06-0.09
P	<0.005	Ti	<0.01
S	<0.005	Nb	<10 ppm
V	0.15-0.25	Mo	<50 ppm
B	<0.001	Ni	<50 ppm
N₂	0.015-0.045	Cu	<100 ppm
Al	<100 ppm	Si	<500 ppm

Table 1.1 Chemical composition of Eurofer steel [23].

The very high impact issue on the DEMO design is related to the temperature operating range, between 350°C and 550°C. At low-temperature the risk is the embrittlement under fission neutron irradiation. Instead, at the upper limit temperature a drop in properties takes place, in fact, the creep-rupture failure drops below 10⁴ h for stress levels similar to those proposed for fusion reactor (about 100 MPa) [24]. Compared to stainless steel, RAFM steels have a lower creep resistance above 550°C, as reported in Figure 1.11. Further experiments conducted at 550 °C with applied stresses of 285 MPa showed a creep life of two hours. Other European RAFM steels, like the oxide dispersion strengthened (ODS) steels, exhibit significantly higher creep strength than Eurofer97 [25].

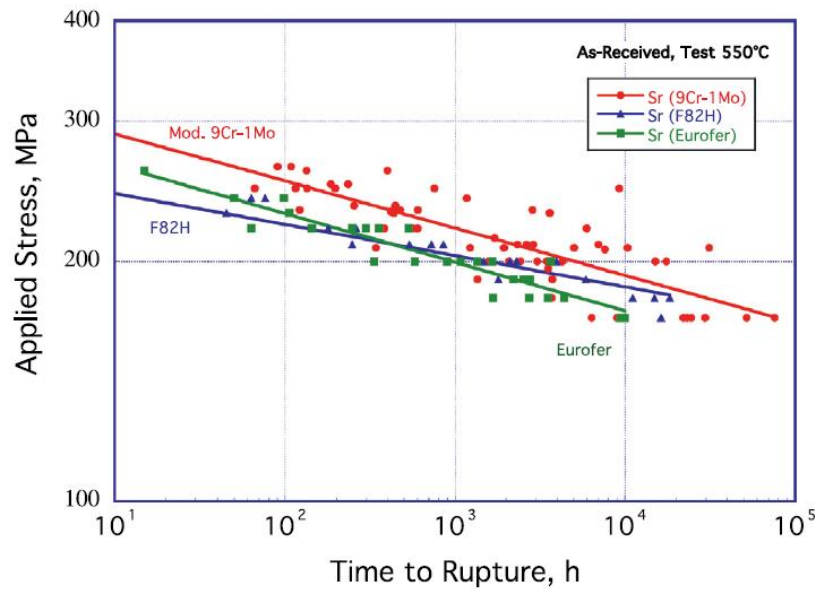


Figure 1.11 Creep rupture properties at 550°C [26].

Comparing Eurofer to the conventional Mod. 9Cr-1Mo, the tensile properties are quite similar while are higher than the SS 316(L) steel when temperature is below 500 °C (Figure 1.12). RAFM steels lose their strength with increasing temperature, and their utilization is recommended up to temperatures of 550°C.

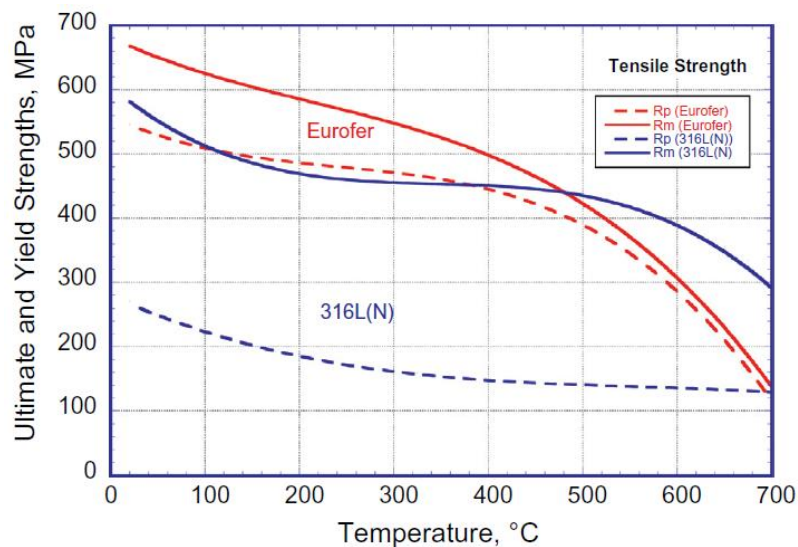


Figure 1.12 Tensile strengths of 316L(N) and Eurofer [26].

Moreover, the Yield stress of RAFM steel increases with the damage dose due to the neutron irradiation and, in particular, the Yield stress increases rapidly at dose below 10 dpa. The Yield stress (R_{p02}) versus test temperature for Eurofer97 in unirradiated condition and after neutron irradiation in different European irradiation programmes is reported in Figure 1.13. The Yield stress increase is linked to the test temperature and this increase is greater at low temperature values.

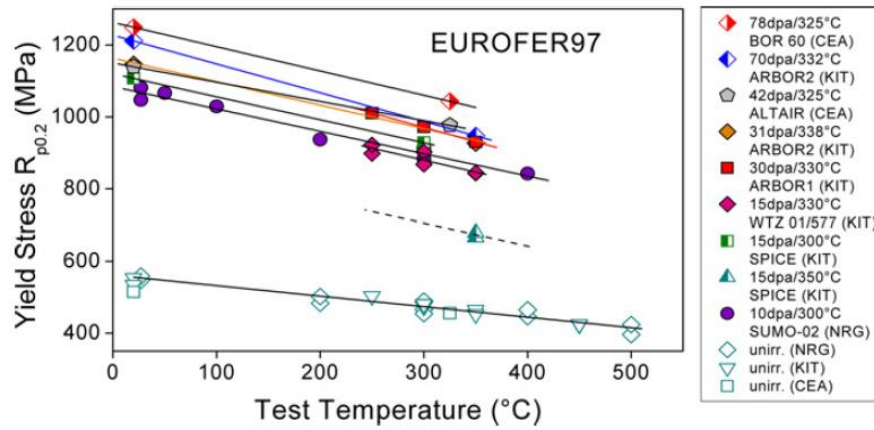


Figure 1.13 Yield stress vs. test temperature for Eurofer97 [27].

Eurofer97 shows a softening behaviour similar to the ferritic-martensitic steels. The total stress range (the difference between positive and negative stress amplitude in a cycle) reaches its peak value during the first cycles and it stabilizes at this value for few cycles. Then, the cyclic stress amplitude rapidly decreases until the specimen failure [28].

Some tests demonstrate that the fatigue behaviour of the material can worsen especially if the fatigue is imposed in conjunction with irradiation. In fact, the irradiation experiments do not consider the fatigue behaviour and how it changes the microstructures of the material. So, further tests are needed to investigate these aspects.

1.4 The Thermo-mechanical problem

The research activity performed during the PhD course in Energy and Information Technologies - nuclear engineering and applied physics curriculum has been specifically intended to numerically investigate the thermomechanical performances of the WCLL COB segment, with the aim of contributing to improve its design in view of the prescribed requirements.

In general, the thermo-mechanical problem of a body, which has certain geometric and physical characteristics and certain thermal and mechanical stresses, consists of studying the thermal stresses, deformations and displacements field.

The laws of heat transfer by conduction govern the temperature distribution within a structure. The thermal field is a scalar function of space-time variables:

$$T = T(x, y, z, t) \quad (\text{Eq. 1.11})$$

The heat balance equation, which states that the heat generated per unit volume and time and that exchanged at the surface must equal the heat accumulated in the volume, is useful to evaluate the variation over time of the temperature in a body. In the hypothesis of

homogeneous and isotropic material, the thermal conductivity remains equal in all directions and, furthermore, approximating that is little dependent on temperature, the balance equation, whose resolution allows to determine the thermal field in the volume studied, can be written:

$$\rho c_p \frac{\delta T}{\delta t} = \lambda \nabla^2 T + q''' \quad (\text{Eq. 1.12})$$

in which ρ is the density of the material of the considered volume, c_p the specific heat, λ the thermal conductivity and q''' the volumetric heat power generation.

As far as the stress field $\sigma(x, y, z, t)$ is concerned, the latter is a second-order tensor with space-time variables:

$$\underline{\sigma}(x, y, z, t) = \begin{pmatrix} \sigma_{xx} & \sigma_{xy} & \sigma_{xz} \\ \sigma_{xy} & \sigma_{yy} & \sigma_{yz} \\ \sigma_{zx} & \sigma_{zy} & \sigma_{zz} \end{pmatrix} \quad (\text{Eq. 1.13})$$

where $\sigma_{ij} = \sigma_{ij}(x, y, z, t)$, with i and j varying between x, y and z , represents the component of the stress along the j axis relative to the plane with normal i . The terms lying on the main diagonal represent the normal stresses, which can be tensile or compressive, while the terms outside the main diagonal are the tangential stresses, which can be indicated as $t_{ij} = t_{ij}(x, y, z, t)$.

Like the stress field, the deformation field is also a second-order tensor function of the space-time variables:

$$\underline{\varepsilon}(x, y, z, t) = \begin{pmatrix} \varepsilon_{xx} & \varepsilon_{xy} & \varepsilon_{xz} \\ \varepsilon_{xy} & \varepsilon_{yy} & \varepsilon_{yz} \\ \varepsilon_{zx} & \varepsilon_{zy} & \varepsilon_{zz} \end{pmatrix} \quad (\text{Eq. 1.14})$$

where $\varepsilon_{ii} = \varepsilon_{ii}(x, y, z, t)$, with i varying between x, y and z , represent the components of the normal deformation, while $\varepsilon_{ij} = \varepsilon_{ij}(x, y, z, t)$, with i varying between x, y and z are the components of the tangential deformation. The deformation field occurs when the body is subjected to both mechanical loads and purely distorting loads, such as a thermal deformation field or due to phenomena such as swelling and creep.

Finally, the displacement field is a trivector function of the space-time variables.

$$\underline{u}(x, y, z, t) = \begin{pmatrix} u_x \\ u_y \\ u_z \end{pmatrix} \quad (\text{Eq. 1.15})$$

The resolution of the fundamental equations of the Elasticity Theory [29] is necessary to determine the distribution of stresses, displacements and deformations within the body, under the assumption of small deformations. The three fundamental equations together produce a system of 21 equations in 21 unknowns (9 components relating to the tensional state, 9 relating to the deformation field and 3 relating to displacement).

The indefinite equilibrium equations represent the equilibrium around a regular section under stationary conditions for translation and rotation:

$$\left\{ \begin{array}{l} \frac{\partial \sigma_x}{\partial x} + \frac{\partial \tau_{yx}}{\partial y} + \frac{\partial \tau_{zx}}{\partial z} + F_x = 0 \\ \frac{\partial \tau_{xy}}{\partial x} + \frac{\partial \sigma_y}{\partial y} + \frac{\partial \tau_{zy}}{\partial z} + F_y = 0 \\ \frac{\partial \tau_{xz}}{\partial x} + \frac{\partial \tau_{yz}}{\partial y} + \frac{\partial \sigma_z}{\partial z} + F_z = 0 \\ \tau_{xy} = \tau_{yx} \\ \tau_{yz} = \tau_{zy} \\ \tau_{xz} = \tau_{zx} \end{array} \right. \quad (\text{Eq. 1.16})$$

with F_x , F_y and F_z being the force components along the x, y and z axes.

The compatibility equations, on the other hand, express the dependence ratio that must exist between the deformation and displacement components, in order to guarantee a response of the structure to external stresses that respects the constraint of continuity without presenting breakages and interpenetrations:

$$\left\{ \begin{array}{l} \varepsilon_x = \frac{\partial u}{\partial x} \\ \varepsilon_y = \frac{\partial v}{\partial y} \\ \varepsilon_z = \frac{\partial w}{\partial z} \\ \gamma_{xy} = \frac{\partial u}{\partial x} + \frac{\partial v}{\partial y} \\ \gamma_{yz} = \frac{\partial v}{\partial y} + \frac{\partial w}{\partial z} \\ \gamma_{zx} = \frac{\partial w}{\partial z} + \frac{\partial u}{\partial x} \end{array} \right. \quad (\text{Eq. 1.16})$$

Finally, the constitutive equations link stresses and deformations, allowing to completely define the problem and its resolution. These take into account the deformation that the structure undergoes when subjected to certain mechanical and thermal loads, as a result of the characteristics of the structural material:

$$\left\{ \begin{array}{l} \varepsilon_x = \frac{1}{E} [\sigma_x - \nu(\sigma_y + \sigma_z)] + \alpha \cdot \Delta T + \varepsilon_{sw} + \varepsilon_{cr} \\ \varepsilon_y = \frac{1}{E} [\sigma_y - \nu(\sigma_x + \sigma_z)] + \alpha \cdot \Delta T + \varepsilon_{sw} + \varepsilon_{cr} \\ \varepsilon_z = \frac{1}{E} [\sigma_z - \nu(\sigma_x + \sigma_y)] + \alpha \cdot \Delta T + \varepsilon_{sw} + \varepsilon_{cr} \\ \gamma_{xy} = \frac{1}{G} \tau_{xy} \\ \gamma_{yz} = \frac{1}{G} \tau_{yz} \\ \gamma_{zx} = \frac{1}{G} \tau_{zx} \end{array} \right. \quad (\text{Eq. 1.17})$$

where, considering the hypothesis of homogeneous, isotropic and linear elastic material, it is possible to express the elastic properties of the body with E, ν and G, called engineering constants, which can be determined experimentally, representing Young's modulus,

Poisson's coefficient and tangential elasticity modulus respectively, while α is the coefficient of thermal expansion and finally the $\Delta T = T - T_0$, is the difference between the operating temperature and the one in which the body is considered not to be deformed due to the effect of temperature. The terms ε_{sw} and ε_{cr} , on the other hand, concern the deformations induced in the body by the two phenomena of swelling and creep.

The system of equations defined is a system of algebraic-differential equation at partial derivatives, linearly independent. By making some substitutions, it is possible to write the indefinite equilibrium equations as a function of the displacements, obtaining the Navier equations, or the compatibility equations as a function of the stresses, obtaining the Mitchell-Beltrami equations; so, the formulations for the displacements and stresses of the elastic problem are obtained. The displacement formulation is expressed with three differential equations having the displacements u , v and w as unknowns:

$$\begin{cases} \frac{E}{2(1+\nu)} \Delta u + \frac{E}{2(1+\nu)(1-2\nu)} \frac{\partial}{\partial x} [div(\bar{u})] - \frac{\alpha}{(1-2\nu)} \frac{\partial \vartheta}{\partial x} + f_x = 0 \\ \frac{E}{2(1+\nu)} \Delta v + \frac{E}{2(1+\nu)(1-2\nu)} \frac{\partial}{\partial y} [div(\bar{v})] - \frac{\alpha}{(1-2\nu)} \frac{\partial \vartheta}{\partial y} + f_y = 0 \\ \frac{E}{2(1+\nu)} \Delta w + \frac{E}{2(1+\nu)(1-2\nu)} \frac{\partial}{\partial z} [div(\bar{w})] - \frac{\alpha}{(1-2\nu)} \frac{\partial \vartheta}{\partial z} + f_z = 0 \end{cases} \quad (\text{Eq. 1.18})$$

The stress formulation, instead, can be summarized by a single expression:

$$\nabla^2 \sigma_{ij} + \frac{1}{1+\nu} \sigma_{kk,ij} = 0 \quad (\text{Eq. 1.19})$$

Using either formulation it is possible to solve the mechanical problem of the body by finding the tension, deformation and displacement fields.

For problems of a complex nature, it is difficult to find a solution in a closed analytical form, and it is therefore necessary to solve them by means of computers and using numerical and computational methods.

1.4.1 The Finite Element Method

Different numerical methods exist for the approximate solution of systems of partial differential equations on a complex domain, created for solving structural, fluid-dynamic, thermal, electromagnetic problems, etc. One of the most common methods is the Finite Element Method (FEM), a method that allows representing the continuum, which has infinite degrees of freedom, by means of a discretization with elements of finite dimensions. Each of these elements is interconnected to the adjacent elements through a finite number of points, named nodes, and the variables of the problem will be evaluated at the nodes. In order to obtain a solution as accurate as possible, it is necessary to carefully evaluate the type of mesh, which is the discretization of the domain, to be adopted for the domain under

examination. Furthermore, it is necessary that the value of the function in each single element is described by means of a shape function, which is able to describe faithfully the real displacement field.

The FEM methodology can be summarized in the following procedure:

1. Modelling of the geometric domain;
2. Representation of the continuum by means of a certain discrete number of finite elements interconnected through nodes at the boundary. This domain discretization procedure is called meshing, and “mesh” indicates the grid of nodes and element dividing the domain. Finer is the discretization, more the solution of the discrete model converges with that of the same continuous model;
3. Assignment of a set of functions to describe the behaviour of each element, the shape of which depends on the element and its number of nodes;
4. Definition of the material properties of the elements, attribution of the boundary conditions at the nodes and of the loads;
5. Solution of the system through appropriate numerical calculation techniques aimed at the derivation of the required variables;
6. Post-processing of the results obtained from the analysis, in order to evaluate the response achieved from the variables and evaluation of the verification criteria, such as those prescribed by the reference code&standards.

Today there are numerous software, both Open Source and Commercial, for finite element analysis; among the software, the most renowned are ABAQUS, ANSYS, etc, and in particular in this thesis work the analyses have been carried out using ABAQUS v. 6.14 [30].

1.4.2 The structural assessment as per RCC-MRx

The structural code currently adopted to design and perform the structural assessment of DEMO Breeding Blanket is the French nuclear standard RCC-MRx [31], concerning the “Design Construction Rules for Mechanical Components in high-temperature structures, experimental reactors and fusion reactors”. At present, it represents the reference code&standard adopted in the frame of the BB design activities carried out under the umbrella of the EUROfusion consortium.

The standard proposes three classes of components (N1Rx, N2Rx, N3Rx), which correspond to decreasing levels of safety demand to support different possible mechanical damage to which the component may be subjected. In particular, the breeding blanket, due

to the high nuclear classification, is classified as N1Rx component and the design-by-analysis rules, RB 3200 in RCC-MRx, must be followed.

The code foresees a different application of the rules based on the operative conditions of the components to be studied, in particular, if creep and/or irradiation effects can be considered negligible or not. The set of criteria to be adopted according to the considered operative condition are shown in Table 1.2. The aim of this rules is to ensure the safety of the components under the various possible mechanical damages.

	Negligible Creep	Significant Creep
Negligible Irradiation	RB 3251.1 (P-type damage)	RB 3252.1 (P-type damage)
	RB 3261.1 (S-type damage)	RB 3262.1 (S-type damage)
Significant Irradiation	RB 3251.2 (P-type damage)	RB 3252.2 (P-type damage)
	RB 3261.2 (S-type damage)	RB 3262.2 (S-type damage)

Table 1.2 RCC-MRx RB 3200 rules breakdown.

P-type and S-type damages are caused by monotonic and cyclic loads, respectively. In particular, the P-type failure modes resulting from the application of a constantly increasing loads, such as excessive deformation, plastic instability and fracture. Instead, the S-type failure modes are those, which could only not result by repeatedly applying loads, such as progressive deformation (i.e., ratcheting) and fatigue.

Moreover, the application of the design rules foresees a stress classification based on the nature of load which has generated it and its position in the structure. In particular, the stress categories [32] are:

- **Primary stress, P.** The primary stress is defined as that portion of the total stress which is required to satisfy equilibrium with the applied loading and which does not diminish after small scale permanent deformation. Small scale deformation is taken to mean deformation which does not lead either to appreciable change in geometry (large displacements) or to significant stretching (large local deformation). If thin-shell form the structure, the stresses can be subdivided into membrane stresses and bending stresses.
 - **General Primary membrane stress (P_m).** The general primary membrane stress is the thickness-averaged value of the primary stress tensor. Each component of the tensor is defined by:

$$(\sigma_{ij})_m = \frac{1}{h} \int_{-h/2}^{+h/2} \sigma_{ij} dx \quad (\text{Eq. 1.20})$$

Where h is the thickness of the wall and x the direction adjacent to the supporting line where the stress is computed through the thickness h.

- **Primary Bending stress (P_b).** Primary bending stress designates the stress distributed linearly through the thickness which has the same moment as the primary stress. It can be obtained applying the following procedure to the primary stress tensor:

$$(\sigma_{ij})_b = \frac{12x}{h^3} \int_{-h/2}^{+h/2} \sigma_{ij} x dx \quad (\text{Eq. 1.21})$$

- **Local Primary membrane stress (P_L).** The local primary membrane stress is defined as the sum of the general primary membrane stress and the additional membrane stress L_m. The latter is an additional membrane stress caused by mechanical loads applied to a gross structural discontinuity or by the presence in the structure of a gross structural discontinuity.

$$P_L = P_m + L_m \quad (\text{Eq. 1.22})$$

Although it does not have all the characteristics of a primary stress, prudence dictates that this stress be classified as a primary stress.

- **Secondary stress, Q.** Secondary stress is that portion of the total stress (minus peak stresses, as defined below), which can be relaxed as a result of small-scale permanent deformation. The basic characteristic of a secondary stress is that it is self-limiting. Local yielding and minor distortions can eliminate the conditions, which cause the stress to occur. The stress classification Q includes only the constant (membrane) and linearly varying (bending) part of the secondary stress. Q is calculated by applying the procedure (Eq. 1.11) and (Eq. 1.12) to the secondary stress tensor and summing the membrane and bending parts. The non-linearly varying part of secondary stress, not included in Q, is classified as peak stress. All thermal stresses, swelling stresses, and stresses due to imposed displacements or deformations are classified as secondary stresses.
- **Peak Stress, F.** Peak stress is the increment of stress which is additive to the primary-plus-secondary stresses by reason of local discontinuities or local thermal stresses including the effects, if any, of stress concentrations. This additional stress, generally very localized and redistributed by plasticity, cannot cause an overall deformation of the structure. For ductile materials, it is objectionable only as a possible source of fatigue cracking or fast fracture damage and, at high temperature, of local cracking damage due to creep or creep-fatigue. The peak stress may be calculated as the non-linearly varying part of the total stress on a cross section

Furthermore, during operation, the component can operate in different loading conditions. These conditions can be classified into several categories on the basis of the probability of occurrence and the consequences of failure. In particular, three criteria levels are considered:

- Level A: this category refers to all the normal operating condition, including start-up, shutdown and incidents of moderate frequency which the components must withstand without repairing damage;
- Level C: is the emergency category, includes events which necessitate the system shutdown and the removal of the component from service for inspection and repair of the damage;
- Level D: this level represents the faulted conditions and considers general deformations with some consequent loss of dimensional stability and damage that require repair and need the removal of the component from service.

Therefore, in order to assess the structural integrity of the considered component, normal and accidental conditions must be considered and the criteria relating to the selected operating condition must be verified. Once individuated the most stressed region of the investigated domain, a linear path along the thickness of those regions is build-up and a stress linearization procedure is performed along each selected path abscissa. In particular, the stress linearization is a technique to decompose the stress tensor araised along the thickness into membrane, bending and peak components. The stress linearization procedure is performed for all primary and secondary stress tensor components' to obtain the stress tensors (namely P_m , P_L , P_b , Q_m , Q_L , Q_b and F) described above. Moreover, it is necessary to calculate a scalar equivalent stress, by means of a resistance criterion, usually Von Mises, to compare the obtained results with the scalar limits prescribed by the RCC-MRx code. Hence, the primary membrane stress intensity $\overline{P_m}$, secondary membrane stress intensity $\overline{Q_m}$, primary bending stress intensity $\overline{P_b}$, and so on, are obtained and these values, or combination of them, are used to check the fulfilment of the RCC-MRx structural criteria [31].

Looking at Table 1.2, the rules for the different operating conditions will be described in the following.

- **Negligible Creep and Negligible Irradiation**

The rules RB 3251.1 (P-type damages) are conceived to assess the structural integrity of the component against two modes of failure directly related to the primary stress intensity in the material: immediate plastic collapse and immediate plastic instability. If a structure is loaded above the yield strength of the material, plastic deformation occurs until the structure collapses because of either excessive deformation or necking. The two criteria concerning the primary stresses are defined by

$$\overline{P_m} \leq S_m \quad (\text{Eq. 1.23})$$

$$\overline{P_L + P_b} \leq 1.5 \cdot S_m \quad (\text{Eq. 1.24})$$

where the overline stands for the equivalent value of the stress tensor (i.e., Von Mises equivalent stress), S_m is the allowable stress intensity of the material and 1.5 is a factor called “plastic collaboration coefficient”. There is no limitation on secondary stresses.

The value S_m , which depends on the structural materials, varies based on the service level. Considering Eurofer RAFM steel as material, for the three levels, the S_m can be calculated as follow:

$$S_m^A = \min \left[\frac{2}{3} R_{p0,2min}(20^\circ C); \frac{2}{3} R_{p0,2min}(\theta); \frac{2}{3} R_{m,min}(20^\circ C); \frac{1}{2.7} R_{m,min}(\theta) \right] \quad (\text{Eq. 1.25})$$

$$S_m^C = \min [1.35 S_m; R_{p0,2min}] \quad (\text{Eq. 1.26})$$

$$S_m^D = \min [2.4 S_m; 0.7 R_{m,min}] \quad (\text{Eq. 1.27})$$

where $R_{p0,2min}$ is the minimum yield strength (conventionally the stress value corresponding to a plastic deformation equal to 0.2%), $R_{m,min}$ is the minimum tensile strength and θ indicate the average temperature in the considered region.

The rules RB 3261.1 (S-type damages) are conceived to assess the structural integrity of the component against failure modes due to cyclic loads. In particular, the rule RB 3261.111 is about the progressive deformation while the rule RB 3261.112 is about fatigue damage.

The ratcheting is the accumulation of plastic deformation in structures subjected to cyclic stress with a non-zero primary stress. When a structure is subjected to cyclic loading, the structure may show signs of permanent deformation at the end of the first cycle. During subsequent cycles, two cases may arise: after a few cycles, the overall permanent deformation is constant and there is no further progressive permanent deformation with cycles; The overall permanent deformation continues to increase with every loading cycle, and the structure gradually changes from its original shape. This is called progressive deformation, or ratcheting. The RCC-MRx provides two different methods to prevent the occurrence of progressive deformation, one based on efficiency diagrams and an alternative rule (RB 3261.1118). As the latter is more conservative, it has been decided to use this criterion, shown below:

$$\max(\overline{P_L + P_b}) + \overline{\Delta Q} \leq 3 \cdot S_m \quad (\text{Eq. 1.28})$$

where either the maximum of the local membrane plus bending primary stress and the range of the total secondary stress are defined inside the cycle.

Instead, fatigue is a damage mode that may appear under cyclic loading. When the loading applied to a structure varies in a cyclic manner and the number of cycles and their amplitudes are sufficiently large, they can cause the material to crack. These cracks or imperfections do

not initially compromise the integrity of the structure but they may grow with repeated cycles, eventually leading to fracture.

The rule RB 3261.112 requires that the fatigue usage factor, $V_A(\overline{\Delta\varepsilon})$ reported below, is lower than one:

$$V_A(\overline{\Delta\varepsilon}) = \sum_i \frac{n_i}{N_i} \quad (\text{Eq. 1.29})$$

where the index i refers to the i th set of cycles of the same loading scenario, n_i are the specified number of cycles the component has to undergo and N_i are the allowable cycles under a fixed strain range $\overline{\Delta\varepsilon}$. The procedure to calculate $\overline{\Delta\varepsilon}$ is widely reported in [31] and, in particular, takes into account the total stress range $\overline{\Delta\sigma_{tot}} = \overline{\Delta(P + Q + F)}$ and different factors describing the effects of plasticity and triaxiality. The rule RB 3261.112 is only applicable if the rules of RB 3261.111 (Progressive deformation) are satisfied.

- **Negligible Creep and Significant Irradiation**

In the event that the creep is negligible but the irradiation effects are not, other rules need to be taken into account. In particular, regarding the P-type damages, the criterion against immediate plastic flow localization is the RB 3251.2121, as follows:

$$\overline{P_m + Q_m} \leq S_{em}^A(\theta_m, G_{tm}) \quad (\text{Eq. 1.30})$$

where $S_{em}^A(\theta_m, G_{tm})$ is the allowable membrane stress, associated with the service level A, as a function of the mean thickness temperature and G_{tm} , a term used to quantify the mean value in the region of the irradiation at the considered time.

Instead, the criterion against the immediate fracture (RB 3251.2122) is:

$$\overline{P_m + P_b + Q + F} \leq S_{et}^A(\theta, G_t) \quad (\text{Eq. 1.31})$$

where $S_{et}^A(\theta, G_t)$ is the allowable membrane stress, associated with the service level A, as a function of the mean thickness temperature and G_t . Both rules above can be used for the three different service levels calculating the S_{em} and S_{et} values as reported in [31].

As for the S-type damages, regarding progressive deformation and fatigue, the rules RB 3261.2 must be checked.

- **Significant Creep and Negligible Irradiation**

When the creep is significant but the irradiation is not negligible, RB 3252.1, and RB 3262.1 must be satisfied.

In particular, the rules for P-type damages are defined in terms of creep usage factor U and creep rupture usage factor W .

$$U_{A,c}(\overline{\Omega P_m}) \leq 1 \quad (\text{Eq. 1.32})$$

$$U_{A,c}(\overline{P_L + \Phi P_b}) \leq 1 \quad (\text{Eq. 1.33})$$

where A and C indicates the service level, Ω and Φ are two coefficients that introduce the effect of the local membrane stresses and multiaxial stress states and of the redistribution of stresses due to relaxation.

Instead, regarding the creep rupture usage factor, the rules are defined as follow:

$$W_{A,C,D}(1.35\Omega\overline{P_m}) \leq 1 \quad (\text{Eq. 1.34})$$

$$W_{A,C,D}(1.35(\overline{P_L} + \Phi\overline{P_b})) \leq 1 \quad (\text{Eq. 1.35})$$

According to the RCC-MRx, the damage resulting from the overlapping of creep effects and fatigue depends on the fatigue usage factor and the creep rupture usage factor and it must be evaluated by means of the creep-fatigue interaction diagram of the material, as reported in [16].

- **Significant Creep and Significant Irradiation**

In case of both creep and irradiation cannot be neglected, rules RB 3252.2 and RB 3262.2 must be followed. For P-type damages, RB 3252.1 must be verified but changing the limits of the U and W factors equal to 0.1 rather than 1. Instead, for S-type damage, only criteria for austenitic steel have been studied and reported in the code.

1.5 Objective of the study and adopted methodology

As widely explained in the previous section, the Breeding Blanket is a crucial system of the DEMO fusion reactor and its design is one of the key steps of the European Roadmap to the Realisation of Fusion Energy. The Blanket is tasked with shielding the out-vessel components from the plasma radiation, slowing down neutrons, converting their kinetic energy into thermal energy and removing it by means of the cooling system. For this reason, the development of a robust geometric configuration of the WCLL BB is one of the pivotal objectives in the DEMO fusion reactor research activities.

Therefore, the research activity carried out during the PhD course has concerned the investigation of the thermo-mechanical behaviour of the whole BB segments to check the segments' structural performances against the RCC-MRx design rules, both in nominal and in accidental loading scenario. In a first part of the activity, an alternative and innovative methodology has been developed and validated in order to investigate in detail the thermo-mechanical behaviour of the WCLL Central Outboard Blanket Segment. Subsequently, the multiscale procedure has been further refined and finally used on the up-to-date model of the segment to improve its design and highlight its criticalities.

The prediction of a realistic and accurate thermal field for the considered BB segments is crucial to perform detailed enough thermo-mechanical analysis. In fact, from the structural

assessments performed during the DEMO BB pre-conceptual phase, emerged that the thermal-induced stress (i. e. the secondary stress) is the main responsible of the failure in the RCC-MRx rules verification. Nevertheless, the full thermal assessment of a whole BB segment requires, firstly, the detailed knowledge of its cooling system layout. Seeing as the current design of the DEMO Water Cooled Lithium Lead (WCLL) BB is not mature enough to allow such a kind of assessment, which would require, in any case, a considerable modelling effort as well as a huge computational burden [33], assumptions and alternative models are necessary to realistically predict the thermal field of a whole WCLL BB segment. Hence, the development of alternative calculation procedures capable of predicting a realistic thermal field for a whole BB segment, without the necessity to directly perform the full thermal analysis of the whole component, can represent an important outcome. Especially in case where the design by analysis strategy is followed, a procedure allowing to easily obtain a realistic and detailed thermal field for the whole BB segment without performing thermal-hydraulic analysis could be helpful to speed up the design. In fact, such a kind of procedure can allow selecting, among a wide range of solutions, the most promising configurations to be studied, in a second step, with dedicated thermal-hydraulic assessments. In particular, the thermal behaviour of an equatorial region of the segment, equipped with the reference cooling system (i.e. DWTs and cooling channels), has been analysed under nominal conditions and the temperature spatial distribution has been obtained. A proper set of polynomial functions in two variables (i.e. radial and toroidal) has been selected in order to realistically reproduce the obtained thermal field and, moreover, its predictive power has been investigated in terms of both temperature and secondary stress.

This interpolating procedure aims to reproduce the thermal field experienced by an entire segment in order to analyse its thermo-mechanical behaviour. The FE model of such a large structure, however, is certainly characterised by a coarser mesh than the equatorial region one. Therefore, a mesh independence procedure has been set up to verify that the interpolating procedure provided the same promising results on coarser meshes.

Afterwards, once predicted the 3D thermal field of the WCLL COB Segment, its structural behaviour has been evaluated under different steady-state loading scenarios to realistically predict its displacement and stress field and investigate its structural behaviour comparing the stress values obtained in some critical regions of the structure with the criteria prescribed by the reference design standard RCC-MRx.

Modelling a structure such as the COB Segment requires a huge computational effort and the meshing procedure is particularly complicated. For this reason, some geometrical details of the Segment have not been modelled and the thermo-mechanical response in these specific

regions could not be evaluated. Therefore, it has been necessary to use the sub-modelling technique, present in ABAQUS, to study more in detail regions of particular interest of the structure. So, from the results of the global model, the COB Segment, it has been possible to study particular regions of the Segment, in particular some elementary cells located at different poloidal heights, and, moreover, to include details which are absent in the whole model analyses. Thanks to this procedure, particular regions of an entire structure can be modelled with a finer mesh, including more defined structural details and, at the same time, using boundary conditions derived from global model analyses. In this way, a more reliable response is obtained. Then, the thermo-mechanical response of these regions has been analysed and critically evaluated comparing the obtained results with the RCC-MRx design criteria.

This multiscale procedure allows to analyse in a detailed way the thermomechanical performance of a large and complex structure. In detail, by means of the first part of the procedure, the interpolating one, from the thermal analysis of a small portion (i.e. elementary cell) of the segment, the global thermal field experienced by the entire structure is obtained, with the aim of performing its thermomechanical analysis. On the other hand, by means of the sub-modelling technique, after conducting the structural analysis of the whole segment, it is possible to study a small portion in detail, maintaining consistent loads and boundary conditions.

The next step of the research activity involved studying the thermo-mechanical performance of the updated WCLL COB BB model with the support of the procedure developed and validated during the first phase the study. Since the BB segment experiences highly variable thermal loads dependent on its poloidal coordinate, unlike the first study in which only the equatorial region of the segment has been analysed, it was necessary to study its thermal behaviour in detail by evaluating different poloidal regions. Then, the segment has been divided into seven poloidal regions each characterized by different thermal loads (heat flux, volumetric density of nuclear heat power, etc.) and for each of them a thermal analysis has been performed equipped with the reference cooling system configuration (i.e. FW channels and DWTs). The results showed that in some regions the reference cooling configuration was not able to properly cool the structure and maintaining the temperature of the structural material (i.e. Eurofer) below the suggested limit of 550°C. Therefore, an optimization procedure of both the cooling channels located in the FW-SW region and the DWTs, aimed at cooling the BZ, has been conducted. Specifically, the number of FW-SW cooling channels has been varied, if necessary, and some alternative configurations of DWTs have been studied with a different spatial distribution of tubes immersed in the breeder. Once

the cooling system layout for each poloidal region of the COB segment has been optimized to keep the temperature of the structure below the aforementioned limit, a thermal analysis has been conducted for each region. Afterwards, the “multi-region” interpolation procedure has been used to reproduce the spatial distribution of temperature for each analysed region and the seven sets of polynomial functions have been stitched together and applied to the whole COB structure in order to realistically reproduce the thermal field which the segment undergoes. The structural analysis of the entire segment under different loading scenarios, both normal and accidental, have been performed and the performances have been checked in view of the RCC-MRx structural design criteria. Finally, the sub-modelling technique has been used to explore in detail the thermomechanical behaviour of some regions located in the upper, equatorial and lower part of the segment enriched with structural details missing in the global model.

Thanks to this dissertation, a complete study of the thermo-mechanical behaviour of the COB Segment, in normal and off-normal conditions, has been performed, thus providing a contribution to the design and the development of this BB concept foreseen for DEMO reactor.

Chapter 2

2 Development of an interpolation procedure for the calculation of a 3D thermal field in a WCLL BB segment

2.1 Introduction

In the framework of the DEMO research activities fostered by the EUROfusion consortium, an intense research campaign has been carried out during the Ph.D. course to develop alternative procedures in support of the thermomechanical analysis of the WCLL BB foreseen for DEMO. In fact, as the DEMO reactor is currently approaching the conceptual design phase, the design of the WCLL BB segments is not sufficiently mature and, therefore, it is not possible to know in detail all the physical variables characterizing it (for example the thermal field it undergoes). It is therefore necessary to find strategies allowing to derive these quantities from the local analysis of a small portion of the segment. Therefore, since it is not possible to perform a full thermal-hydraulic assessment of a BB segment, an alternative procedure aimed at obtaining a thermal field for the whole segment without performing its complete thermal-hydraulic analysis is developed and refined.

In particular, a procedure to obtain a realistic thermal field for the Central Outboard Blanket (COB) segment of the DEMO WCLL BB, starting from the thermal analysis of its equatorial region, is presented. First, a thermal analysis of the COB segment's equatorial region has been performed under nominal conditions to calculate the corresponding thermal field. In particular, the WCLL2019.v06a geometric layout has been adopted for the equatorial region modelling [34]. However, it is important to emphasise that the same procedure can be carried out for any geometric model and any blanket concept, taking into account proper refinements and modifications that could be necessary. Then, a set of polynomial functions of the radial and toroidal variables has been selected in order to interpolate the calculated thermal field and to realistically predict the corresponding

secondary stress field. After that, a mesh independence study has been performed in order to assess the applicability of the found interpolation strategy to coarser mesh, in sight of their use to impose a thermal field to the whole segment. Indeed, in order to save computational resources and time, usually the whole segment is discretized with a lower level of detail with respect to a model reproducing only a local region. Results have allowed concluding a substantial mesh independence of the proposed interpolation procedure, with positive outcomes in sight of its application for the prediction of a realistic thermal field, and of the consequent secondary stress field, within the whole WCLL COB segment. Then, in the end, the found set of interpolation functions has been used to impose a thermal field the WCLL COB segment in order to calculate its secondary stress spatial distribution.

The developed procedure will enable the scientific community involved in the research activities of the BB to exploit a further analysis tool, which provides an accurate response of an entire BB segment without performing its complete fluid-dynamic and thermo-hydraulic analysis.

The models developed, the loads and the boundary conditions assumed to perform the study and the main obtained results are described and critically discussed in this chapter.

2.2 Thermal analysis of the WCLL COB segment equatorial region

In order to obtain a reliable interpolation procedure for the thermal field of the WCLL COB segment, the first step has consisted in the thermal analysis of the most loaded region, namely its equatorial region, under steady state nominal loading conditions. To this purpose, a dedicated FEM model has been set-up and the corresponding analysis has been carried out.

2.2.1 The FEM model

A detailed FEM model reproducing the equatorial region of the reference WCLL2019 COB geometric configuration has been set-up, considering the v06 geometric layout [34]. Figure 2.1 shows the whole model, including the Segment Box (SB) composed by the First Wall (FW), the Side Walls (SWs), the internal Stiffening Plates (SPs), the Back-Plates (BPs), the water and breeder manifolds and the Back Supporting Structures (BSS).

The SB is depicted in Figure 2.1 in two different colours, grey for the structural material Eurofer and green for the Tungsten armour. Moreover, the Double Walled Tubes (DWTs) are reported in blue whereas the PbLi (i. e. the breeder) in yellow. In particular this model is characterized by a thickness of horizontal and vertical SPs equal to 10 mm and 12 mm, respectively, and is endowed with the DWTs layout, reported in Figure 2.2, which foreseen

22 tubes in each poloidal slice, called “v06a”. The Figure 2.2 also show the water path inside the DWTs, where the red arrows indicate the inlet, the green the outlet and the orange the recirculation scheme. Moreover, each slice is endowed with a 10 channel FW, as shown in Figure 2.3.

The typical mesh features usually used for the design analysis of the equatorial region of the WCLL COB segment [35][36] have been used. So, a mesh composed of ~2.5M nodes connected in ~2.7M hexahedral and tetrahedral linear elements has been set up for this geometric model. In Table 2.1 some mesh parameters are reported, where AR is the aspect ratio and AR_{ave} is the average aspect ratio value for each meshed region. The third column represents the percentage of elements having an AR that overcomes the average one.

	AR_{ave}	$AR > AR_{ave}$
Segment Box	9.76	25.10%
DWTs	7.31	30.29%
Breeder	3.26	26.93%

Table 2.1 Mesh parameters.

Concerning the implemented material properties, temperature-dependent thermo-physical properties for Eurofer, Pb-15.7Li and Tungsten have been drawn from [37], [38] and [39], respectively. For Eurofer, PbLi and Tungsten, the set of properties assumed for the analysis have been reported in Table 2.2, Table 2.3 and Table 2.4, respectively. In particular, the breeder, as it flows very slowly, due to the action of buoyancy and magneto-hydrodynamics forces, can be considered as stagnant.

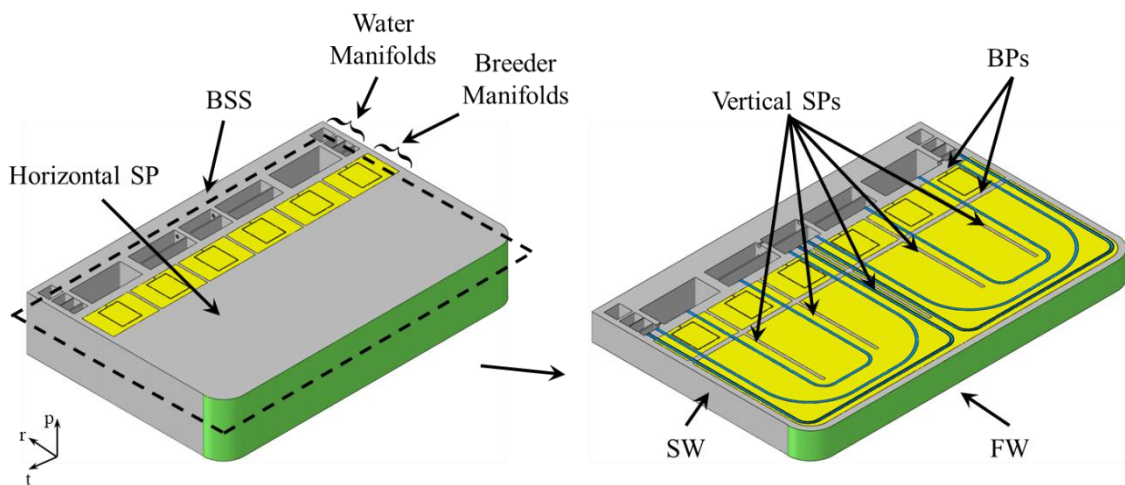


Figure 2.1 WCLL2019.v06 model.

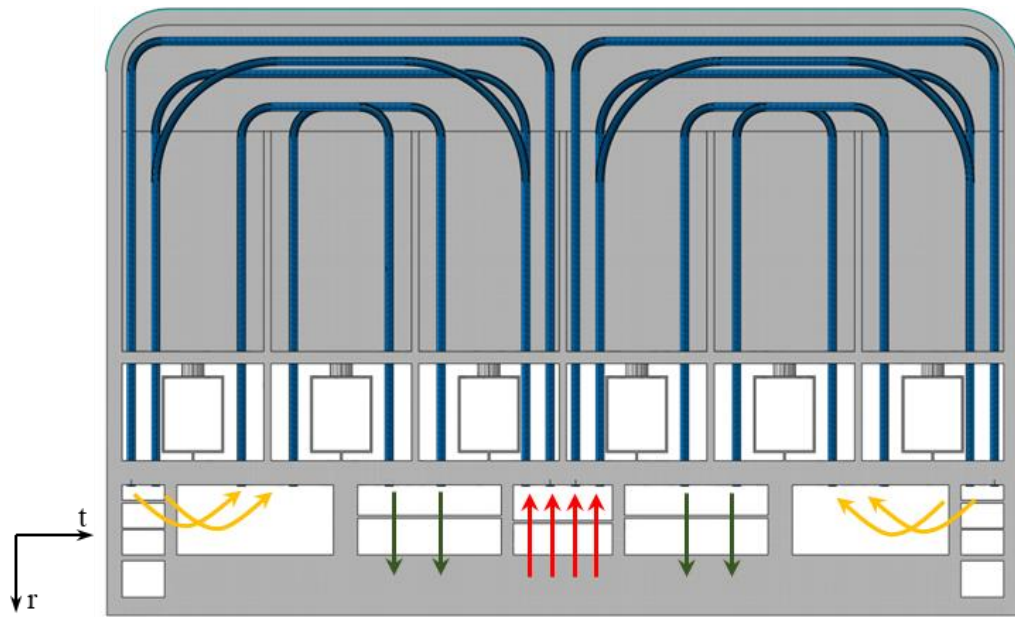


Figure 2.2 WCLL2019.v06a DWTs layout.

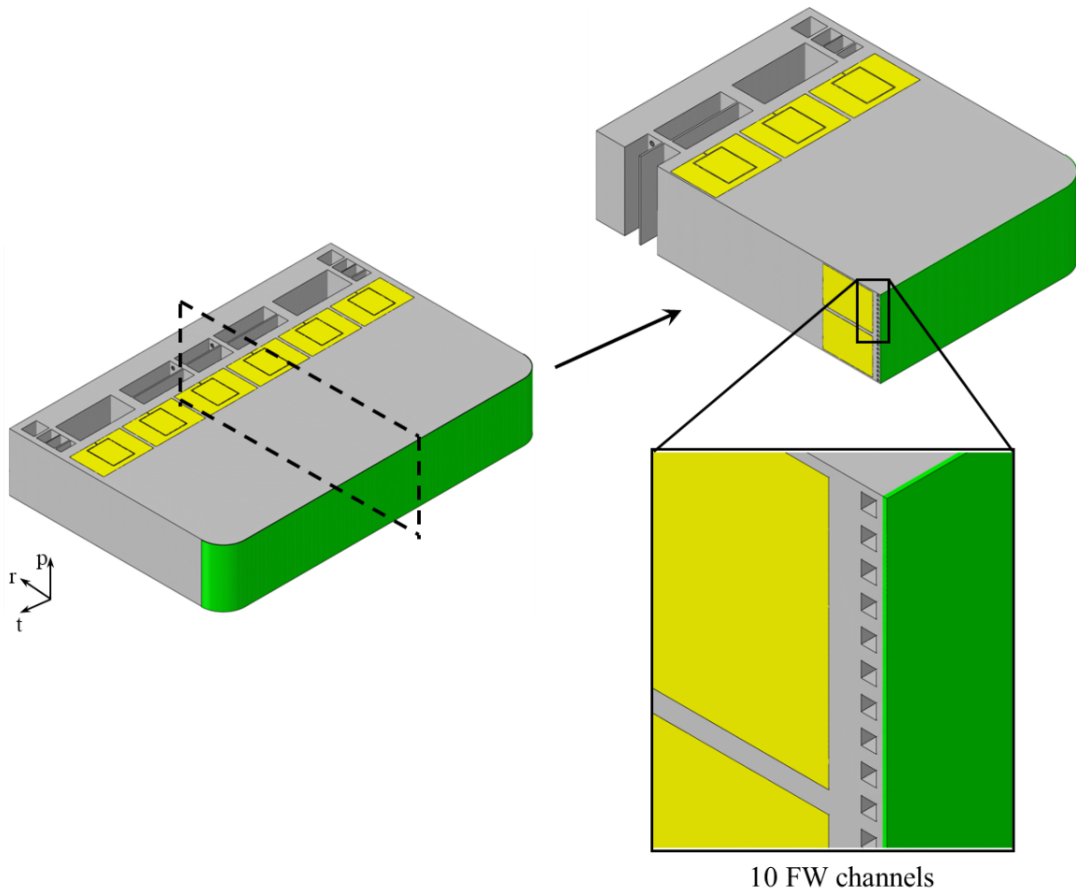


Figure 2.3 WCLL2019.v06 model equipped with 10 FW channels.

T [°C]	ρ [kg/m ³]	k [W/m·°C]	c_p [J/kg·°C]	α [10 ⁻⁶ /°C]	E [GPa]	ν
20	7744	28.08	439	10.4	217	0.3
50	7750	28.86	462	//	//	
100	7740	29.78	490	10.7	212	
200	7723	30.38	523	11.0	207	
300	7691	30.01	546	11.2	203	
400	7657	29.47	584	11.7	197	
500	7625	29.58	660	12.0	189	
600	7592	31.12	800	12.3	178	
700	7559	//	//	12.5	161	

Table 2.2 Eurofer thermo-physical properties.

T [°C]	ρ [kg/m ³]	k [W/m·°C]	c_p [J/kg·°C]	α [10 ⁻⁵ /°C]
20	10172	19.1233	192	11.68
300	9839	20.3993	190	12.10
350	9779	21.3808	189	12.18
400	9720	22.3624	189	12.25
450	9661	23.3439	188	12.33
500	9601	24.3255	188	12.40
550	9542	25.3070	187	12.48
600	9482	26.2886	187	12.55
650	9423	26.2886	187	12.63
700	9363	26.2886	186	14.37

Table 2.3 Pb-15.7Li thermo-physical properties.

T [°C]	ρ [kg/m ³]	k [W/m·°C]	c_p [J/kg·°C]	α [10 ⁻⁶ /°C]	E [GPa]	ν
20	19300	174.91	132.33	5.250	408	0.28
127		159.00	137.00	5.305	404.6	0.28
200		150.12	138.44	5.350	402	0.28
327		137.00	142.00	5.419	396.6	0.28
527		125.00	145.00	5.533	386.4	0.28
600		121.60	146.67	5.550	382	0.29
727		118.00	148.00	5.656	374.3	0.29

Table 2.4 Tungsten thermo-physical properties.

In order to predict the steady state thermal response of the assessed WCLL COB equatorial region, the following set of loads and boundary conditions has been imposed:

- non-uniform heat flux onto the tungsten armour's plasma facing surface, characterised by a maximum value of 0.32 MW/m² [40];
- non-uniform volumetric density of nuclear heat power, calculated in-house at the University of Palermo by means a fully heterogenous neutronic model (Figure 2.4);
- forced convective heat transfer onto water-wetted surfaces, simulated adopting a simplified method, imposing a sink temperature of 311.5 °C (the average between the inlet and outlet coolant temperature [17]) and a uniform convective Heat Transfer Coefficient (HTC) purposely calculated by means of an iterative procedure. In particular, in the first analysis of the iterative procedure the HTC values calculated by means of the Dittus&Bölder correlation [41] have been used, subsequently, the new HTC values have been calculated from the power extracted on the coolant wetted surfaces (i.e. cooling channels and DWTs internal surfaces) and the new mass flow rates values evaluated in the previous analysis, considering a coolant thermal rise of 33 °C. The HTC values calculated using the iterative procedure described above and adopted in the last iteration for the complex of cooling channels and DWTs are reported in Table 2.5, where HTC_{cc} , HTC_{DWTs} and $HTC_{DWTs,rec}$ indicate the values used for the cooling channels, first group and recirculation DWTs;
- water manifolds surfaces temperature equal to 311.5 °C;
- thermal contact model between breeder geometric domain and breeder-wetted surfaces (namely the inner SB surfaces and DWTs outer surfaces) characterized by a

thermal conductance of $100 \text{ kW/m}^2 \text{ }^\circ\text{C}$ [17], in order to reproduce the very low (\sim) contact thermal resistance between the breeder and the Eurofer;

- periodic thermal boundary condition, applying a thermal coupling between the radial-toroidal upper face and the radial-toroidal lower face, in order to simulate the thermal effect of the rest of the segment.

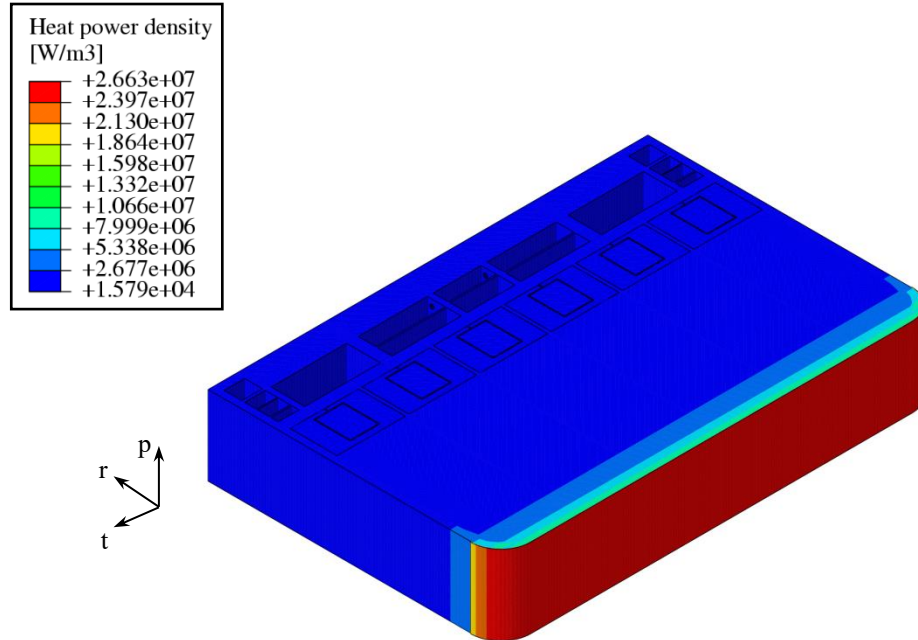


Figure 2.4 Volumetric density of nuclear heat power field.

HTC_{cc} [$\text{W/m}^2\cdot\text{K}$]	20480
HTC_{DWTs} [$\text{W/m}^2\cdot\text{K}$]	19274
HTC_{DWTs,rec} [$\text{W/m}^2\cdot\text{K}$]	30159

Table 2.5 HTC values user for cooling channels and DWTs.

2.2.2 Results

Adopting the FEM model described above, steady state thermal analysis has been performed. Results have shown that temperature values predicted within the SB remain below the Eurofer maximum allowable value of $550 \text{ }^\circ\text{C}$, and the maximum value of $539.5 \text{ }^\circ\text{C}$ is reached within the horizontal SPs, as shown in Figure 2.5. As expected, the predicted thermal field show an accentuated dependence on the radial and toroidal direction. Hence, in sight of the search for the interpolating functions, this double dependence must be taken into account.

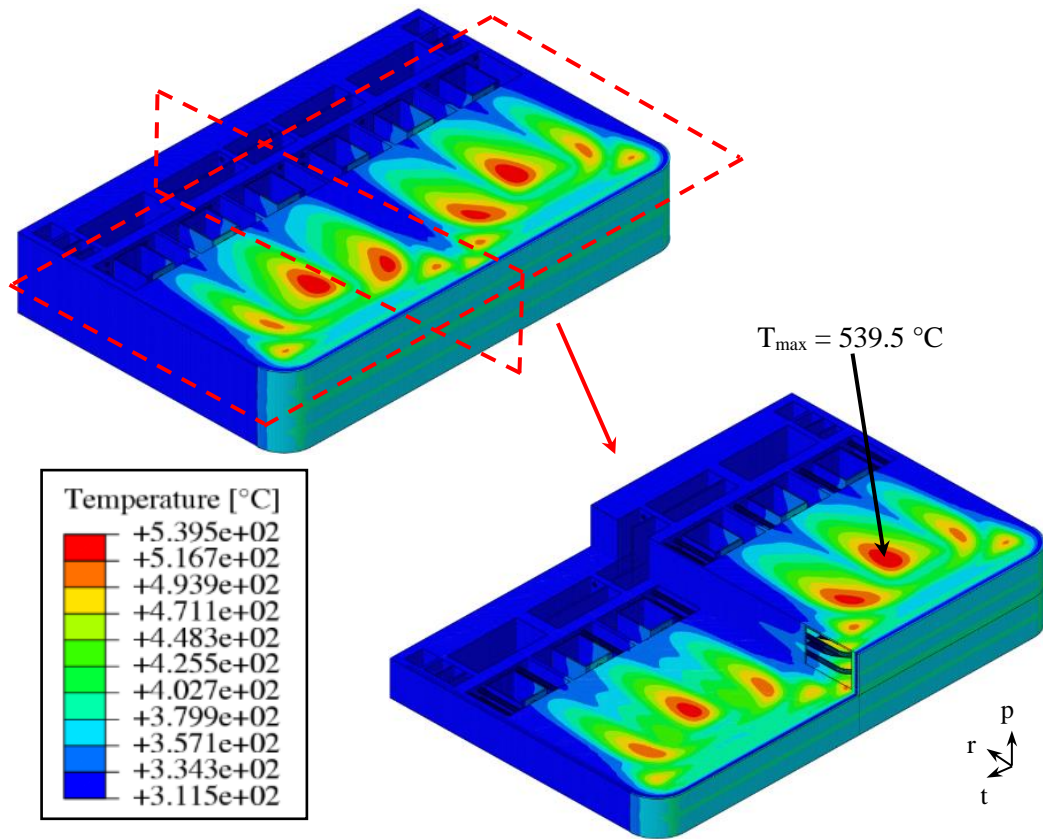


Figure 2.5 Thermal field arising within SB.

2.3 Interpolation of the calculated thermal field

Once calculated the thermal field arising within the equatorial region of the WCLL COB SB, its application to the whole segment is not straightforward. Hence, observing that the thermal field calculated within the equatorial region mainly depends on radial and toroidal variables, an interpolation procedure has been performed to attain a set of polynomial functions capable of best reproducing it. Then, in order to introduce the dependence on the poloidal variable so to apply the thermal field to the whole segment, in the Abaqus environment a user subroutine has been properly coded using the Fortran programming language.

To this end, after a preliminary phase (here not depicted for the sake of brevity) aimed at calibrating the interpolation procedure, the two most reliable interpolation strategies, obtained by dividing the assessed domain in regions, are herewith presented. Following this approach, it may be possible obtaining, with a certain region, an interpolating function of only one variable as well as both the radial and toroidal variable. In fact, decomposing the calculation domain in circumscribed regions, the dependence of the temperature on one direction may be neglected with respect to the other. Then, assembling the different functions, the radial and toroidal dependence of the thermal field in the whole calculation

domain can be recovered. To this end, particular attention has to be paid to the behaviour of the obtained interpolating functions at the boundary of the considered regions. In fact, functions derived from adjacent regions should return equal (or, at least, very similar) values at the shared border of the domains.

On this basis, the first interpolation strategy, named “two-region”, has been obtained subdividing the structure in only two regions (Figure 2.6): the SW-FW-SW region and a single region for SPs, BPs, BSS and manifolds. For both the regions, a polynomial function of one variable, i.e., the radial direction, has been searched. The subdivision into these two regions, on the one hand, allows to not overestimate the temperature of the SWs but, on the other hand, causes inaccuracies in the region in contact with the horizontal SPs.

Instead, a “multi-region” interpolation strategy has been pursued, dividing the assessed domain in several regions: SW-FW-SW region (in green in Figure 2.6), 6 different regions for the toroidal-radial (i. e. horizontal) SPs (in grey in Figure 2.6, each delimited by a vertical SP), 5 different regions for the vertical SPs (in blue in Figure 2.6) and, lastly, a manifolds region (in orange in Figure 2.6). Hence, in total, the calculation domain has been divided in 13 different regions and a polynomial function of one or two variables (i. e. only radial or radial and toroidal) has been searched for each region in order to best reproduce the original (i.e. the calculated) thermal field. In particular, the following interpolating functions have been found to best reproduced the thermal field:

- SW-FW-SW region: 14th degree polynomial function of the radial and toroidal variables;
- manifolds region: 9th degree polynomial function of the radial variable;
- SPh regions: six different 8th-10th degree polynomial functions of the radial and toroidal variables, one per region;
- SPv regions: five different 12th degree polynomial functions of the radial variable, one per region.

Hence, in the “multi-region” interpolation strategy, the 13 different polynomial functions selected allow a particularly accurate representation of the calculated thermal field, as it can be seen qualitatively in Figure 2.7. As can be seen from the Figure 2.7, the thermal field obtained through the “multi-region” interpolation strategy is much more accurate than that obtained with the “two-region” strategy, showing temperature peaks that are present in the calculated thermal field.

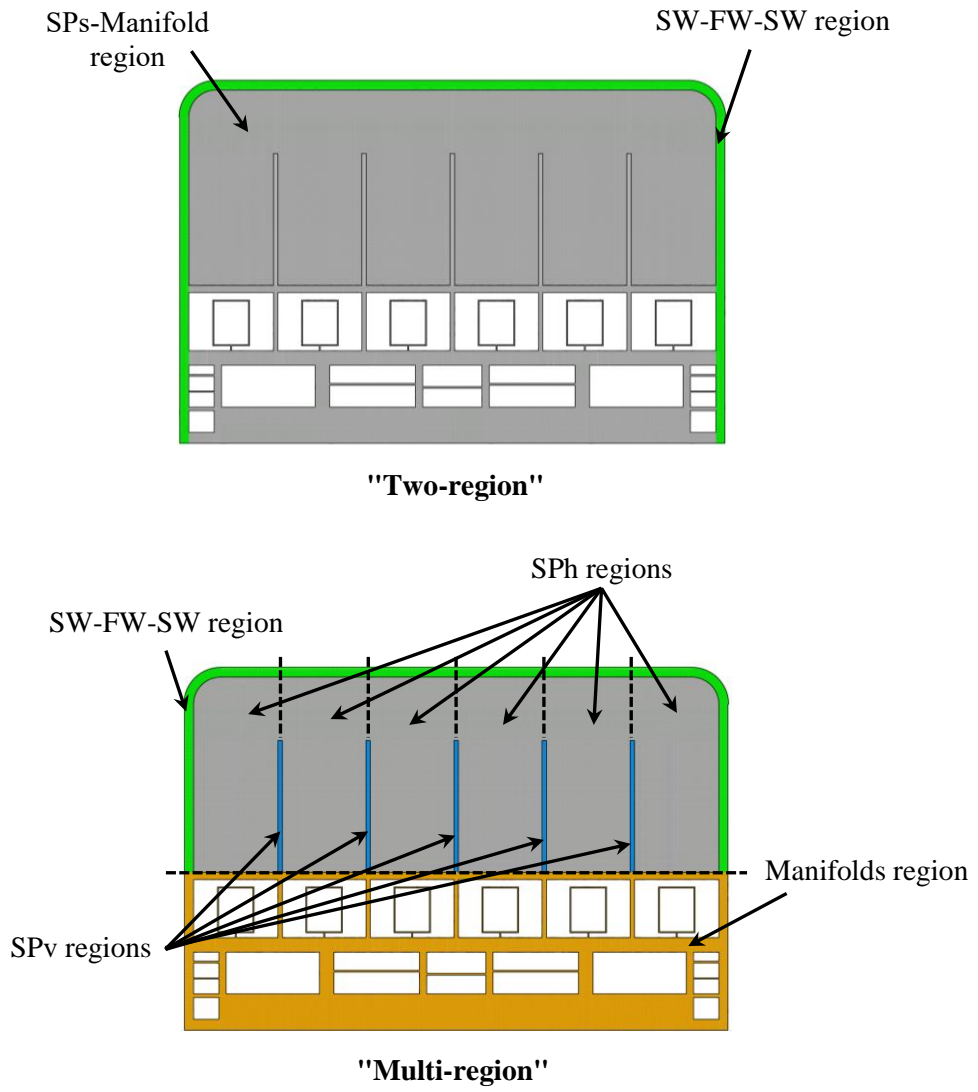


Figure 2.6 Interpolation strategies

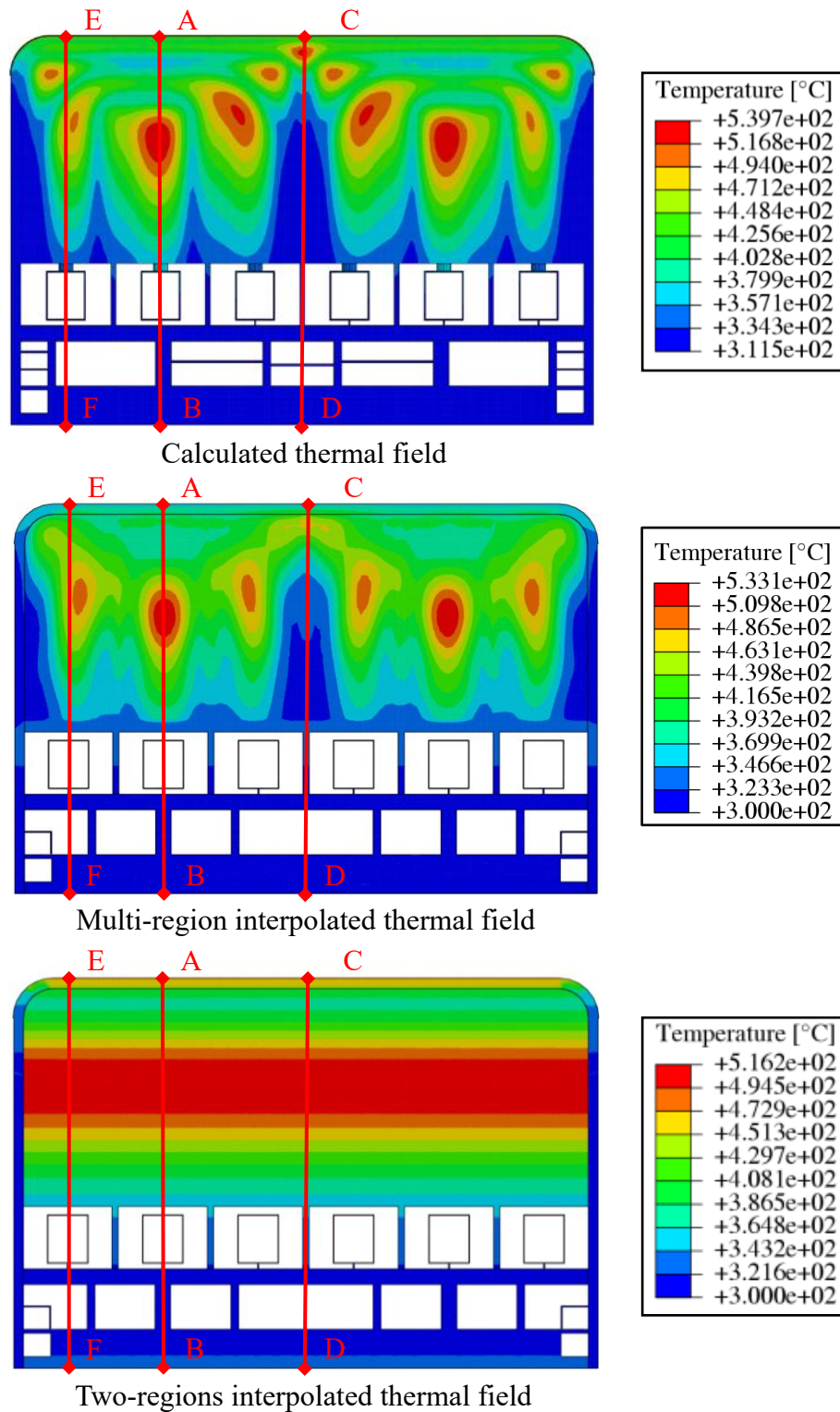


Figure 2.7 Calculated and interpolated thermal fields.

Moreover, in order to have a semi-quantitative comparison between the three thermal fields (namely that calculated and those obtained from the two interpolation strategies), the temperature radial distributions obtained by the two interpolation strategies have been compared to the calculated one, along the radial paths AB, CD and EF reported in Figure 2.7. The outcomes of this comparison, reported in Figure 2.8, allow confirming that in the

considered paths, the “multi-region” approach shows a more accurate trend than the other interpolation strategy and, moreover, shows a very good agreement with the calculated values. So, the “two-region” interpolation strategy has been discarded and subsequent studies have been carried out adopting the “multi-region” only.

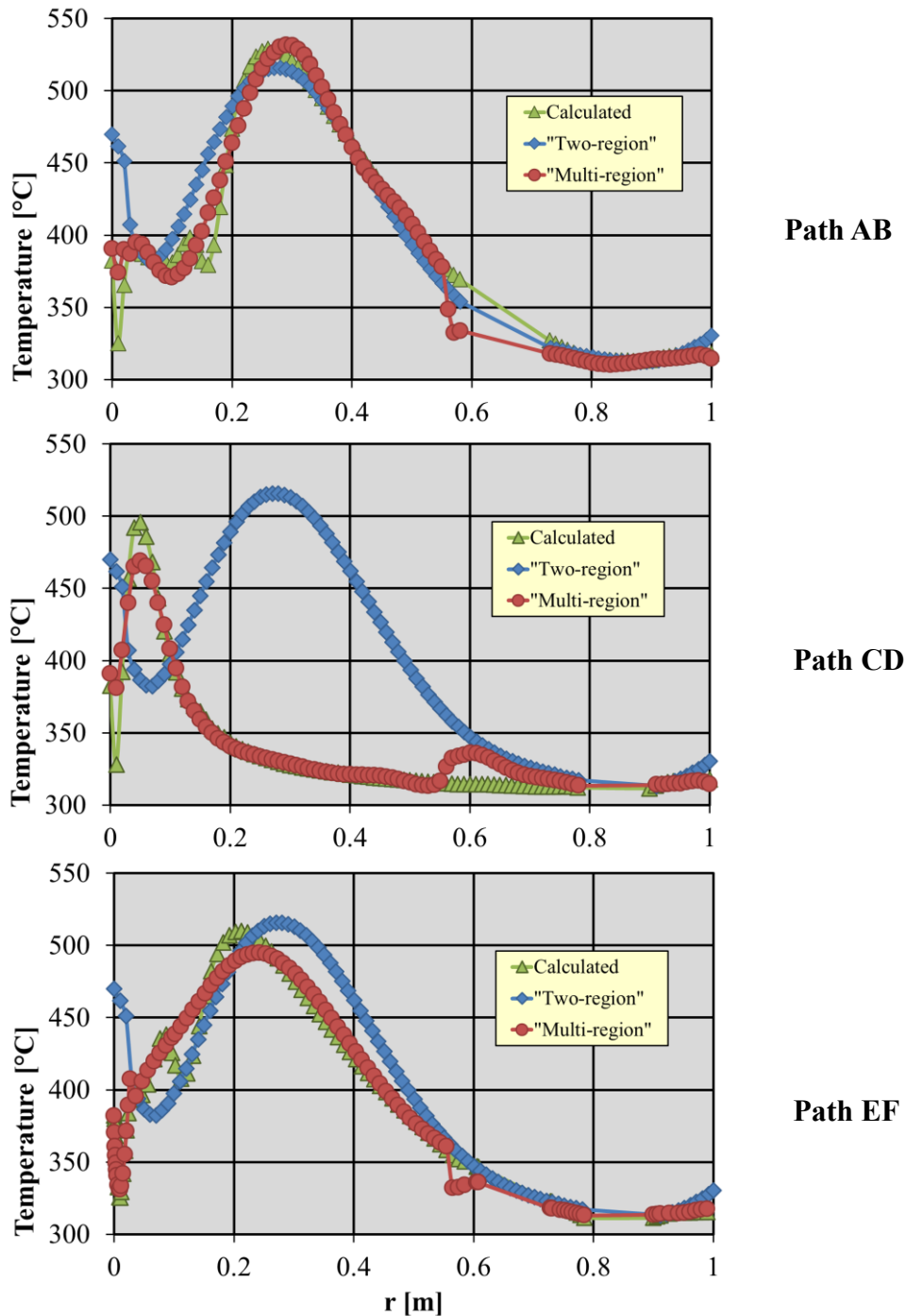


Figure 2.8 Radial temperature distributions along the considered paths.

In order to get a further confirmation of the predictive capabilities of the selected “multi-region” interpolation strategy, a quantitative comparison between the calculated thermal field and that interpolated has been performed. To this purpose, the contour map of the

relative error, defined as the difference between the calculated temperature and the interpolated one divided by the calculated value, is shown in Figure 2.9. Moreover, the relative error statistical distribution is depicted in Figure 2.10 together with the associated cumulative curve.

As it can be observed, the highest relative error is predicted in the manifold region, where the temperature values are the lowest (and strongly influenced by the imposed thermal boundary condition), and in between the BZ cooling tubes, where the three-dimensional distribution is more pronounced. In any case, as the latter regions are very localised, this loss of detail can be considered acceptable.

Moreover, the statistical distribution of the calculated relative error (i.e. histograms and the cumulative curve in Figure 2.10) shows that most of the error values stays within the range $\pm 4\%$, with a peak around 0. Indeed, looking at the cumulative curve, more than the 90 % of the relative error values stay within this range.

These outcomes allow concluding that the “multi-region” interpolation strategy is capable of matching the calculated thermal field with a very good agreement with the calculated data.

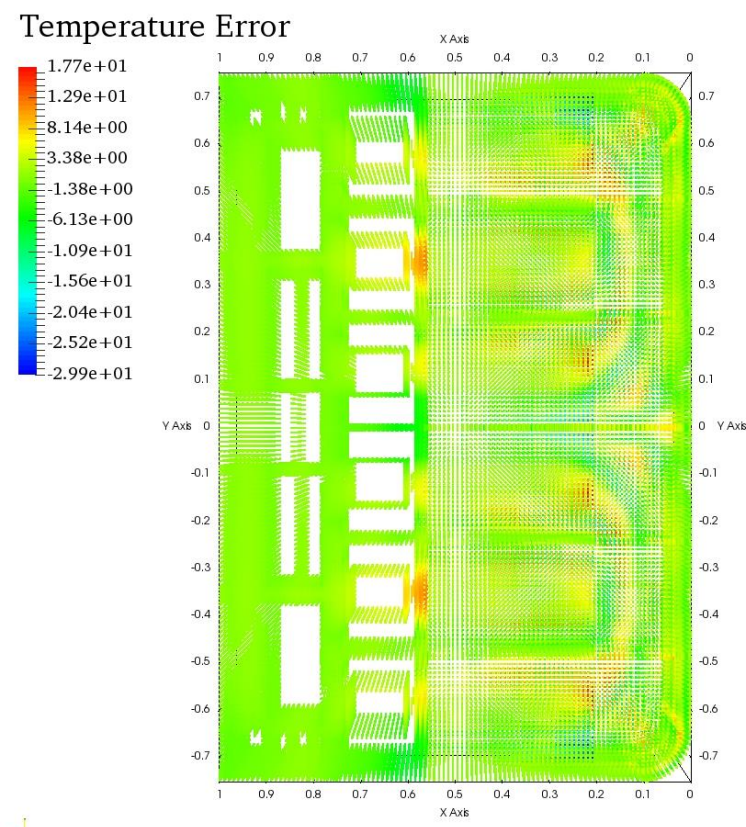


Figure 2.9 Contour map of the temperature error [in %] between the calculated thermal field and the “multi-regions” interpolation.

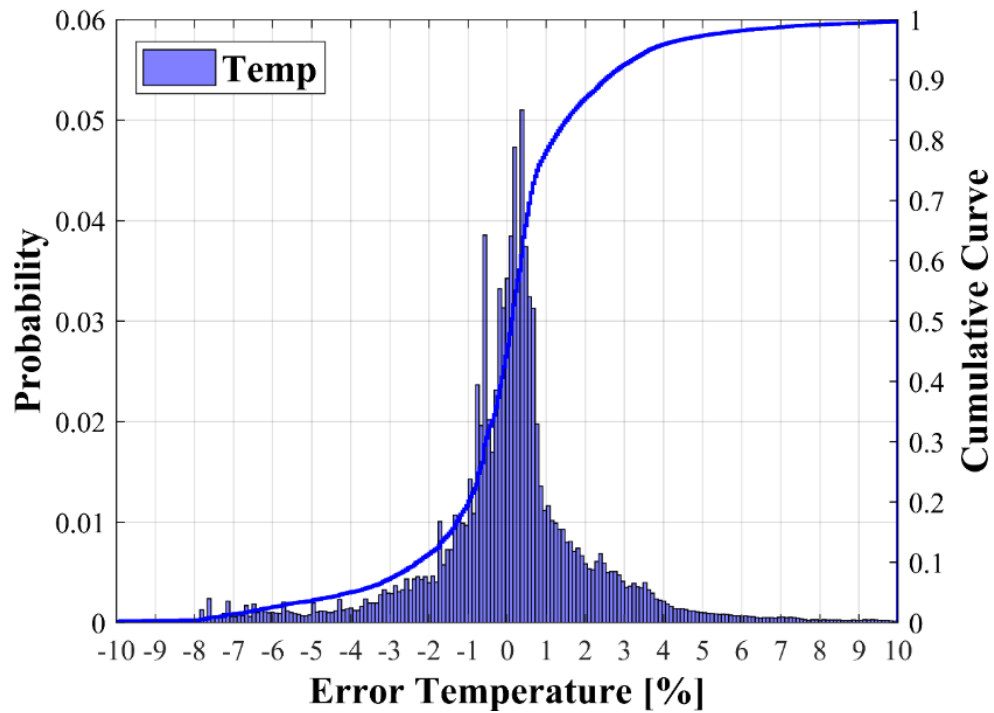


Figure 2.10 Statistical distribution of the error on temperature [in %] between the calculated thermal field and the “multi-region” interpolation (histograms) and cumulative curve.

2.4 Structural analysis and comparison of the secondary stress fields

Once assessed the capability of the “multi-region” interpolation strategy of matching the calculated temperature field on a given spatial discretization grid, a quantitative comparison between the secondary stress fields originated by the calculated and the interpolated thermal fields has been performed.

To this purpose, a FEM model has been set-up on the same mesh already adopted for the thermal analysis. In particular, the set of mechanical boundary conditions shown in Figure 2.11 has been imposed in order to simulate the poloidal continuity of the assessed region as well as to reproduce the action of the WCLL BB attachment system devoted to mechanically connect the BB to the Vacuum Vessel. To this end, displacement of nodes lying onto the red and blue lines of Figure 2.11 has been prevented along radial and toroidal directions, respectively. Moreover, a symmetry condition along the vertical direction has been imposed to the nodes lying onto the lower radial-toroidal face, whereas a plane strain condition along the same direction has been assumed for the nodes lying onto the upper radial-toroidal face.

Since the scope of this comparison is to assess the secondary stress, no pressure load has been taken into account in the model. Hence, uniquely the thermal fields (calculated and interpolated) have been imposed as load for the steady state mechanical analysis.

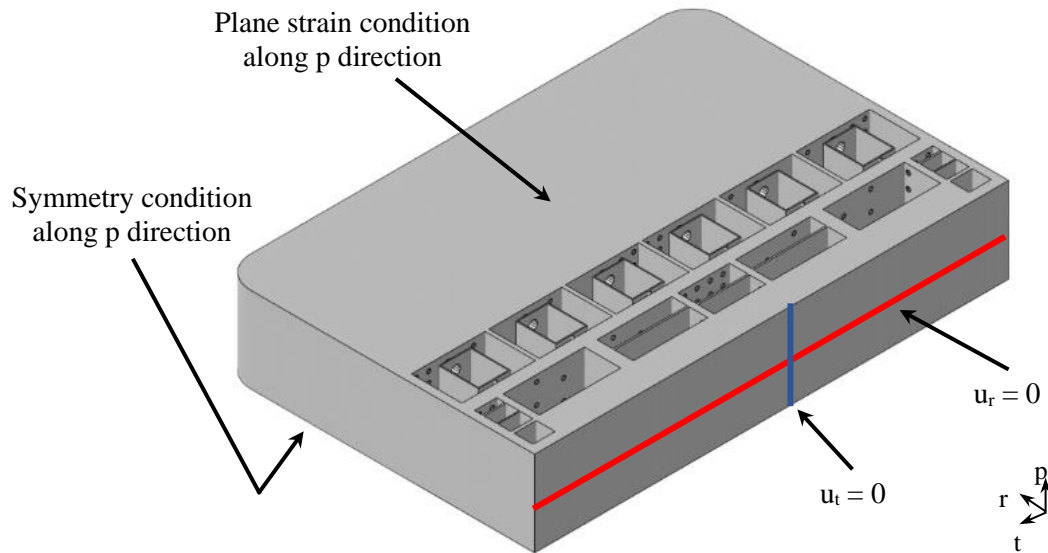


Figure 2.11 Boundary conditions.

Then, in order to compare the secondary stress arising within the central region of the WCLL COB segment as effect of the calculated and interpolated thermal fields, the spatial distributions of the stress tensor components S_{ij} have been considered. In particular, from Figure 2.12 to Figure 2.17, the S_{ij} spatial distributions predicted assuming the calculated thermal field are shown together with the spatial distribution of the relative error arising from the comparison between the S_{ij} values obtained from the calculated thermal field and those predicted assuming the interpolated temperature spatial distribution. The reported point to point comparison allows observing, as general remark, that the absolute value of the error is the highest (i.e., the error is greater than 50% or lower than -50 %, namely red and blue dots in figures from Figure 2.12 to Figure 2.17) where stress values are the lowest. Hence, it can be concluded that the interpolated thermal field allow predicting stress values with a good degree of reliability if compared with the analogous stress obtained from the calculated temperature spatial distribution. As a further demonstration, the statistical distributions of the error on stress prediction are reported in Figure 2.18. Here, it can be seen that error distributions present a peak near to 10-20 %, which can be considered acceptable error. Moreover, looking at the reported cumulative curves, it can be observed that, as to the normal stress components, about the 50 % of the relative error values stay within the range $\pm 20\%$ whereas regarding the shear stress components about the 60 % of the relative error values stay within the same range. In addition, looking at the range $\pm 50\%$, one can see from the cumulative curves that it includes about the 80 % of the relative error values on the normal stress components and about the 90 % of the errors on the shear stress components.

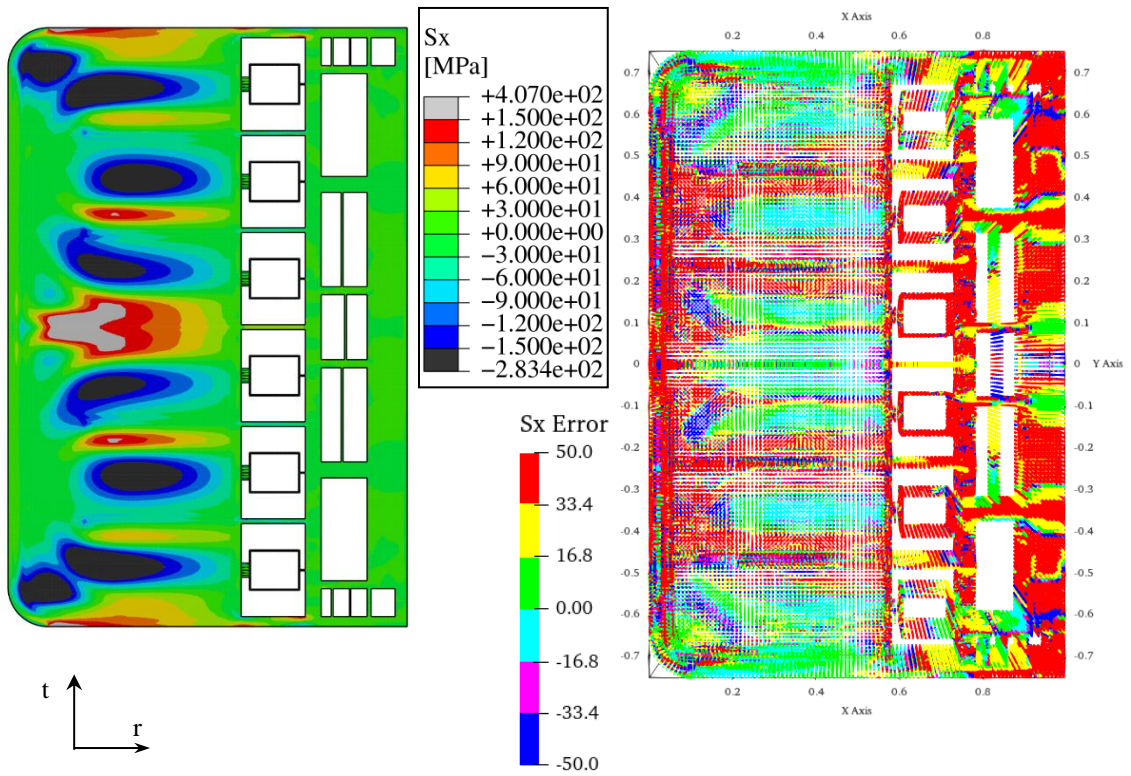


Figure 2.12 S_x spatial distribution from calculated thermal field (left) and relative error contour map (right) when compared with S_x from interpolated thermal field.

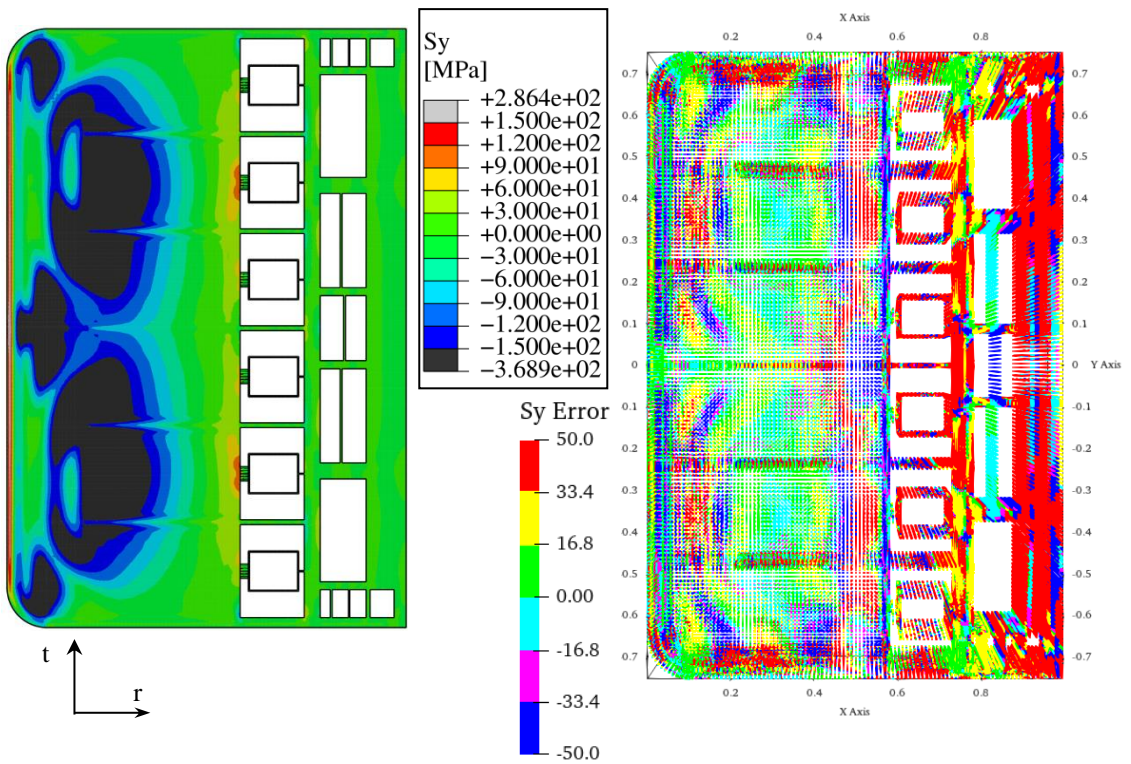


Figure 2.13 S_y spatial distribution from calculated thermal field (left) and relative error contour map (right) when compared with S_y from interpolated thermal field.

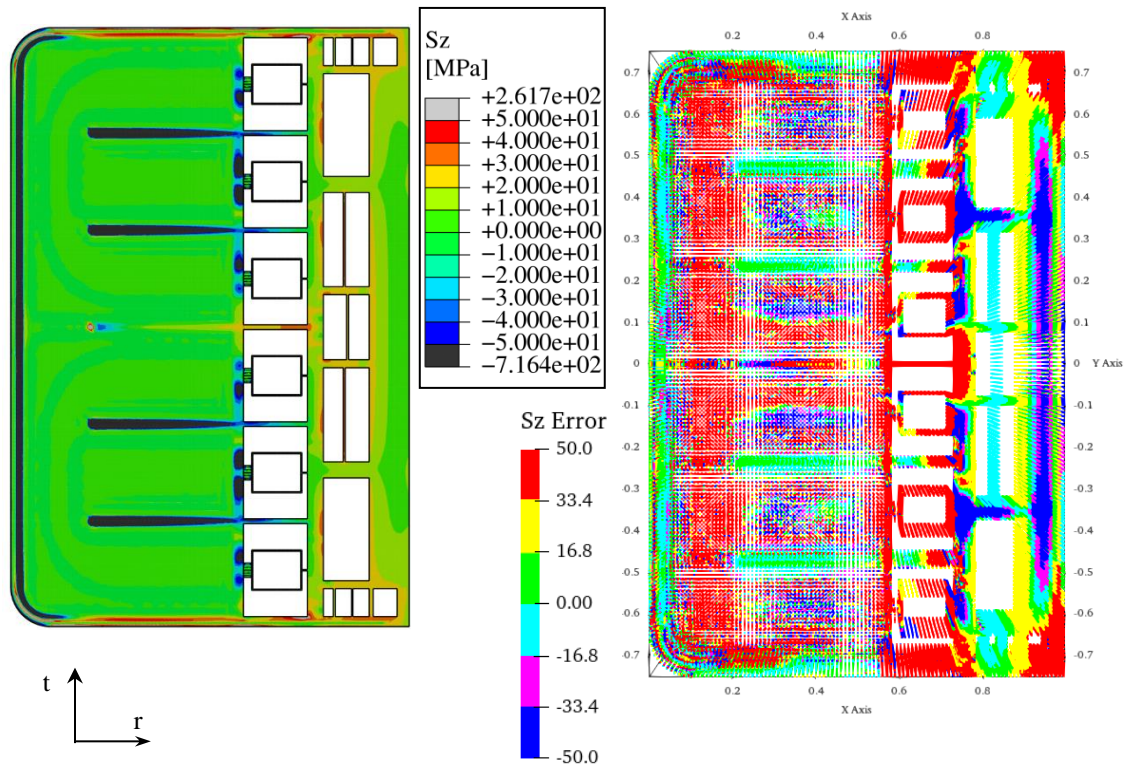


Figure 2.14 S_z spatial distribution from calculated thermal field (left) and relative error contour map (right) when compared with S_z from interpolated thermal field.

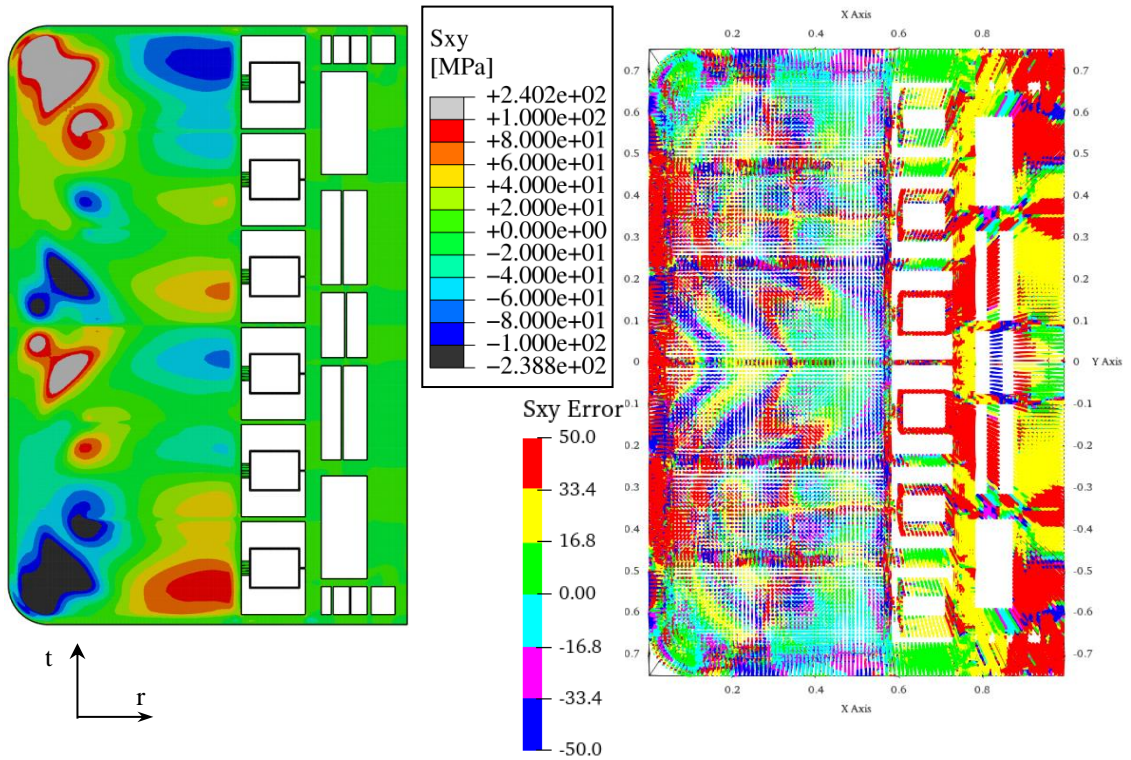


Figure 2.15 S_{xy} spatial distribution from calculated thermal field (left) and relative error contour map (right) when compared with S_{xy} from interpolated thermal field.

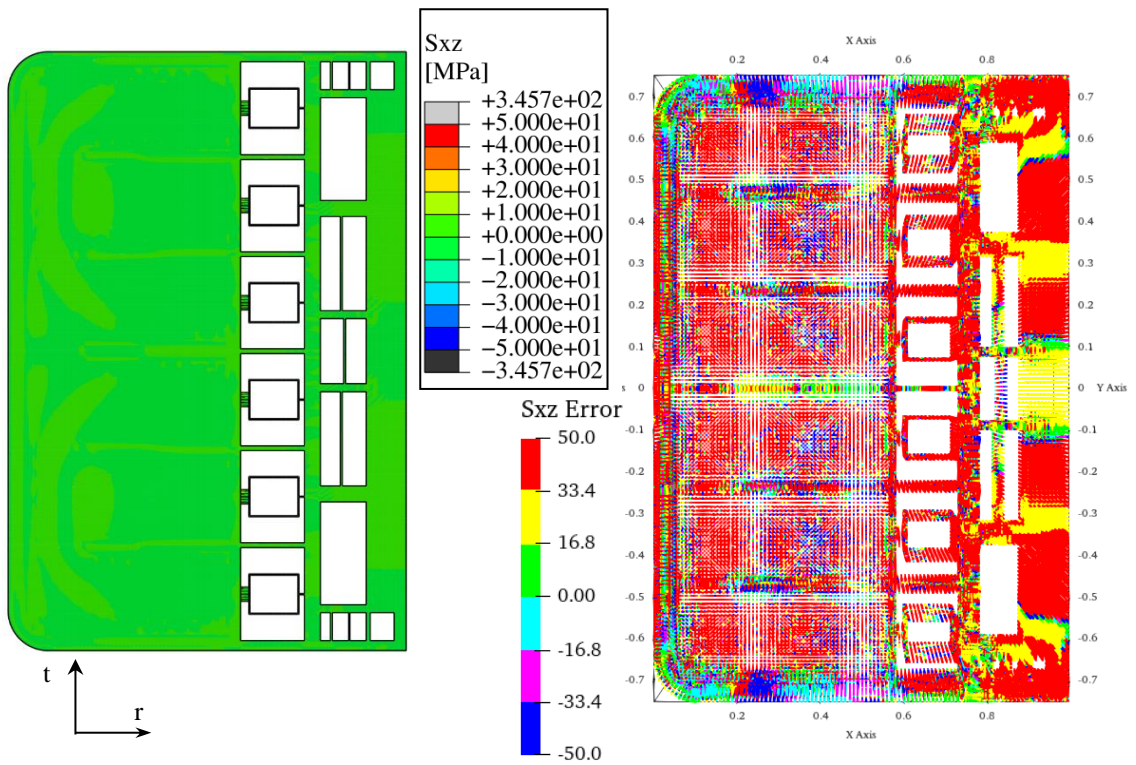


Figure 2.16 S_{xz} spatial distribution from calculated thermal field (left) and relative error contour map (right) when compared with S_{xz} from interpolated thermal field.

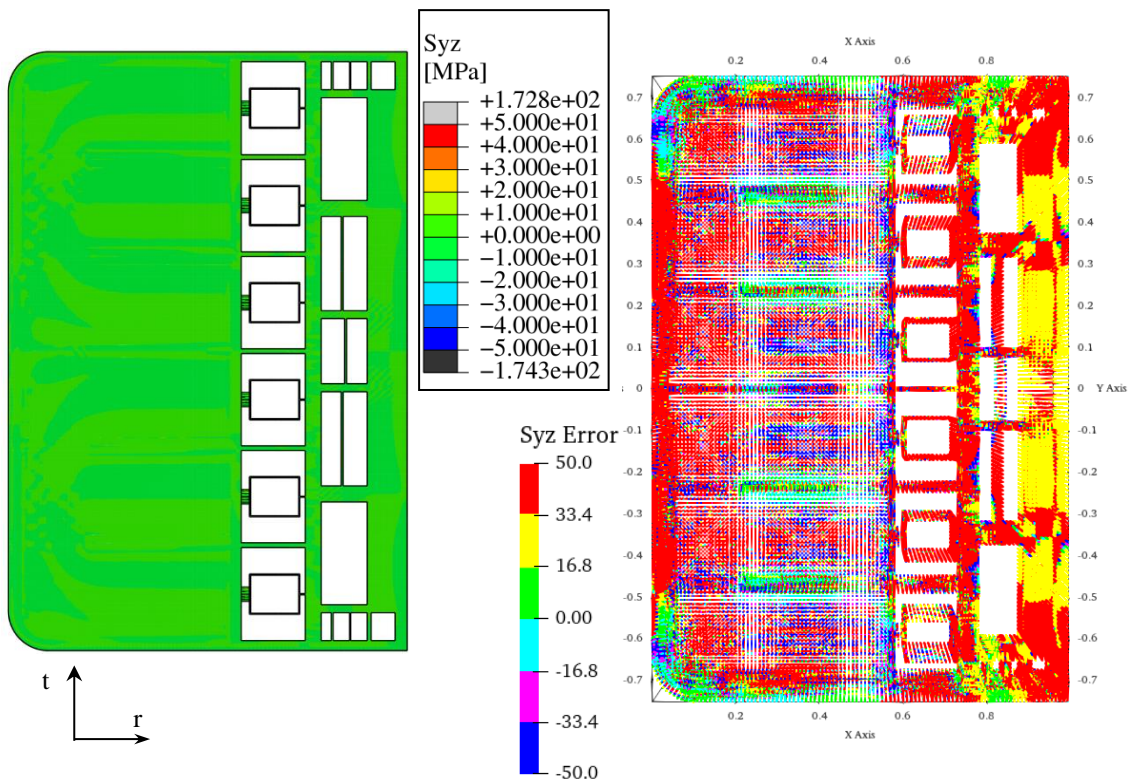


Figure 2.17 S_{yz} spatial distribution from calculated thermal field (left) and relative error contour map (right) when compared with S_{yz} from interpolated thermal field.

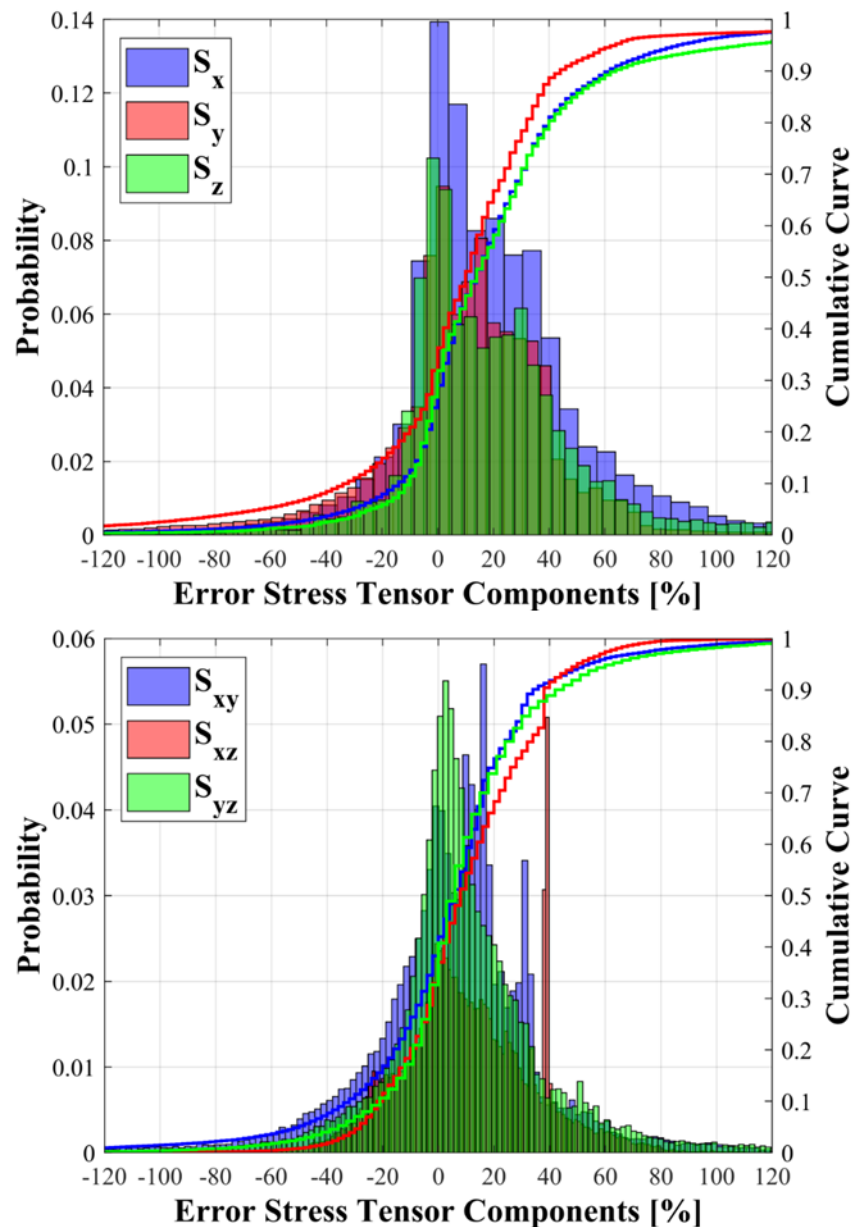


Figure 2.18 Statistical distribution of the error on S_{ij} between the calculated thermal field and the “multi-region” interpolation (histograms) and cumulative curves.

2.5 Mesh independence assessment

Once proved the predictive power of the set of interpolating functions both in terms of temperature calculation and secondary stress prediction, a mesh independence assessment has been performed in order to verify that the promising outcomes obtained so far are still valid for coarser meshes. Indeed, in sight of the application of the interpolated thermal field to a whole WCLL BB segment, a very coarse mesh is expected. To this purpose, five alternative meshes (Figure 2.19) have been set-up and their features are summarized in Table 2.6 together with the original mesh adopted so far.

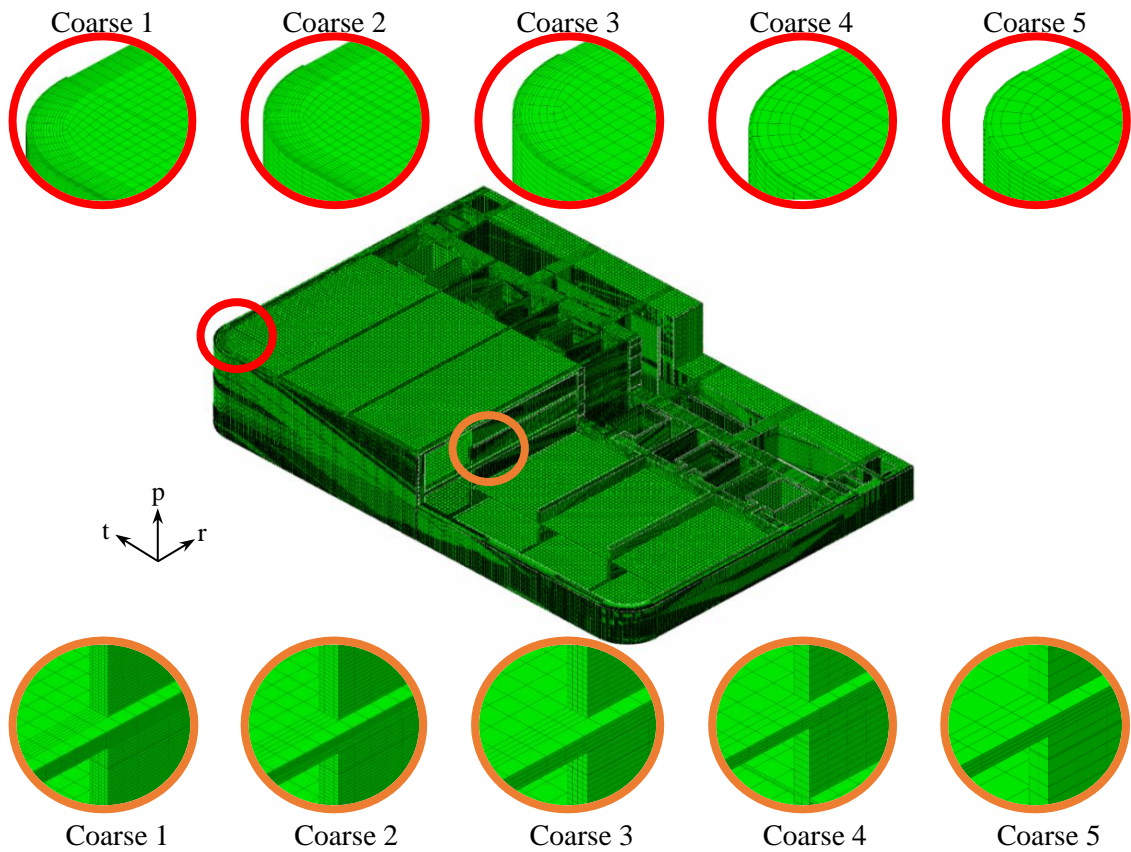


Figure 2.19 Coarser meshes set-up for the mesh independence study.

	Nodes	Elements	Nodes % decrease	AR_{ave}	AR>AR_{ave}
Original mesh	1'948580	1'627'736	/	9.76	25.10%
Mesh 1	1'556'139	1'303'312	~20%	6.06	21.05%
Mesh 2	1'037'463	826'294	~45%	4.07	24.22%
Mesh 3	715'984	561'616	~65%	3.89	46.27%
Mesh 4	312'738	224'328	~85%	4.53	38.66%
Mesh 5	211'753	142'108	~90%	7.60	21.61%

Table 2.6 Features of the coarser meshes set-up and comparison with the original one.

As a first comparison, the set of 13 polynomial functions has been applied to each of the 5 coarser mesh in order to reproduce the thermal field on them and, afterwards, to calculate the secondary stress field originated by the interpolated temperature distribution. After that, a proper thermal and thermo-mechanical analysis has been performed for each of the 5 coarse mesh. Then, each calculated thermal field has been compared with the “multi-region” interpolation field obtained on the same mesh and, in addition, each calculated secondary stress field has been compared to the stress field originated by the interpolated temperature distribution on the same mesh. About the thermal comparison, for the sake of brevity results

concerning coarse meshes 1 and 5 are reported in Figure 2.20. Further details of thermal comparisons of the other coarser meshes are reported in Appendix 1.

As it can be seen, the statistical distribution of the percentage error is peaked on 0 %, with most of the error ranging from -5% to 5% as indicated from the cumulative curves (in particular, about the 95-90 % of the error values stay within this range for Coarse Mesh 1 and 5, respectively). In addition, it can be observed from the error contour maps that the highest errors are concentrated in the manifold regions, where the temperatures are low and strongly depending on the boundary condition, and in between the DWTs, in very localized spots, where the 3D behaviour is more pronounced. Hence, this is a further proof of the high predictive power, in terms of temperature spatial distribution, of the “multi-region” interpolation procedure set-up regardless of the mesh it is applied to.

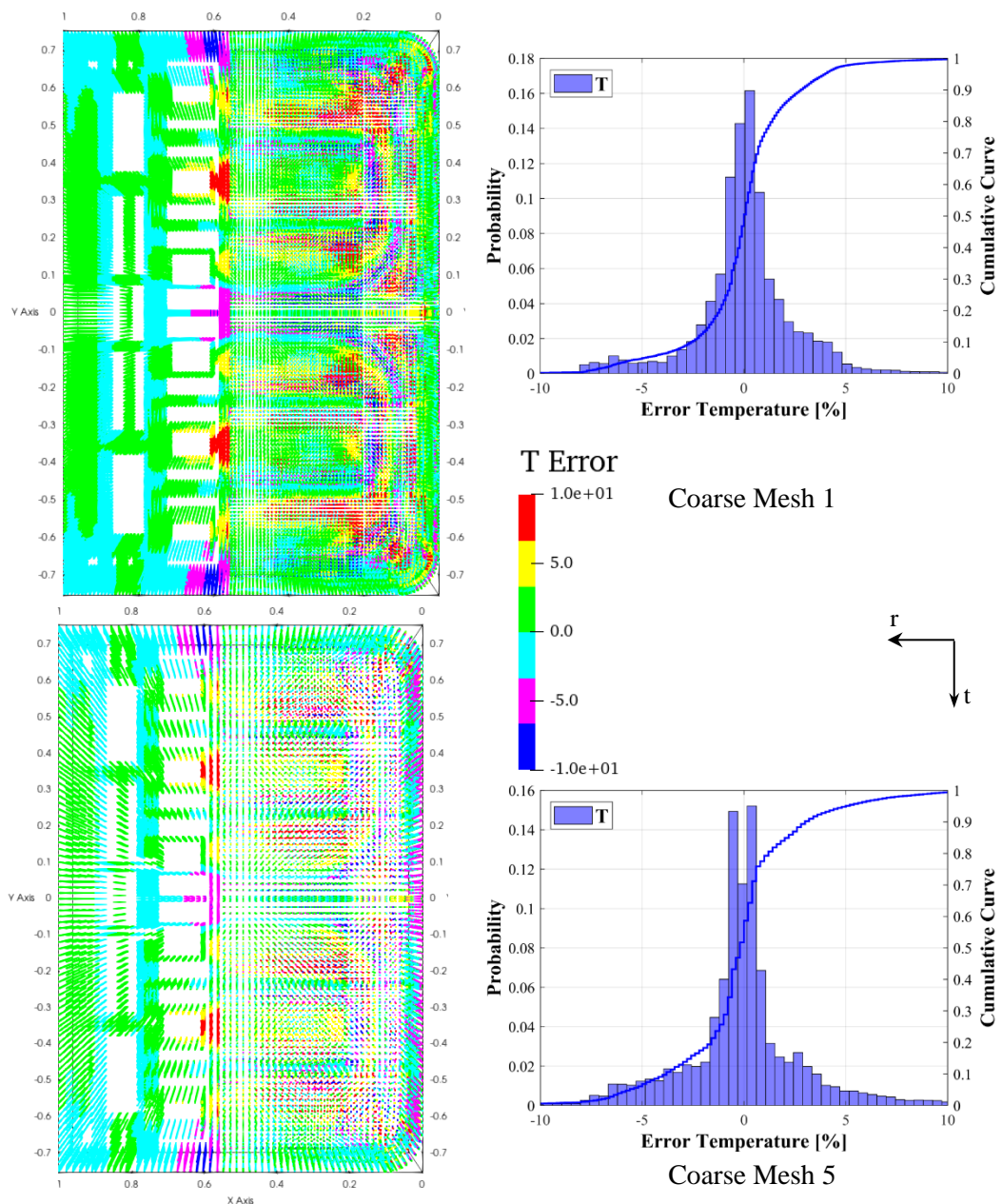


Figure 2.20 Error on temperature prediction for the coarser meshes 1 and 5.

Regarding the comparison between the secondary stress fields, results qualitatively similar to those already shown in figures from Figure 2.12 to Figure 2.17 are obtained for each of the 5 coarser meshes. As an example, results concerning the coarse Mesh 5 are reported from Figure 2.21 to Figure 2.27. The comparison between the secondary stress fields of the other coarser meshes are reported in Appendix 1. Also in this case, the highest percentage error resulting from the comparison between the calculated thermal stress and that coming from the interpolated temperature arise where the stresses are the lowest. In addition, looking at the error statistical distributions and the associated cumulative curves, it can be seen that most of the error values ($\sim 80\%$) stay within the range $\pm 50\%$ with peaks in between $\pm 20\%$. Hence, in principle, this allow concluding that the proposed procedure is viable for coarser meshes even from a mechanical standpoint.

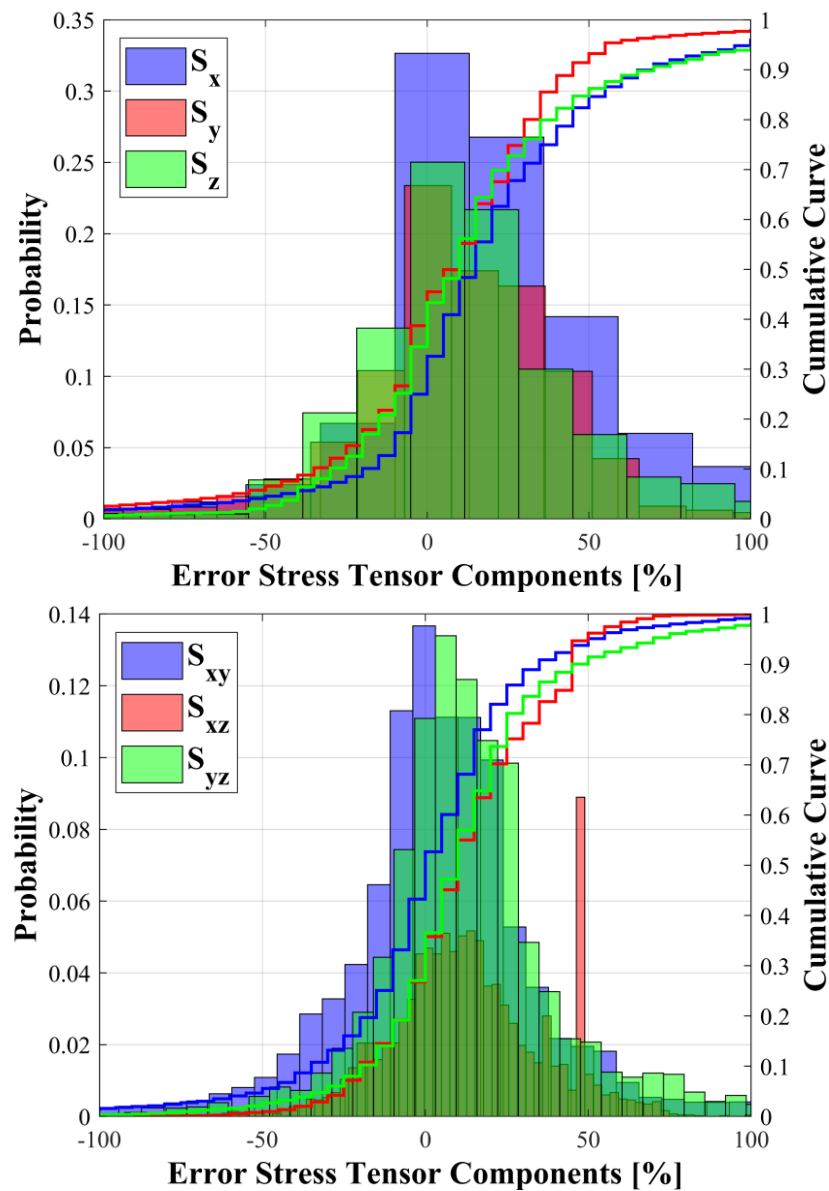


Figure 2.21 Statistical distribution of the error on S_{ij} between the calculated thermal field and the “multi-region” interpolation (histograms) and cumulative curves.

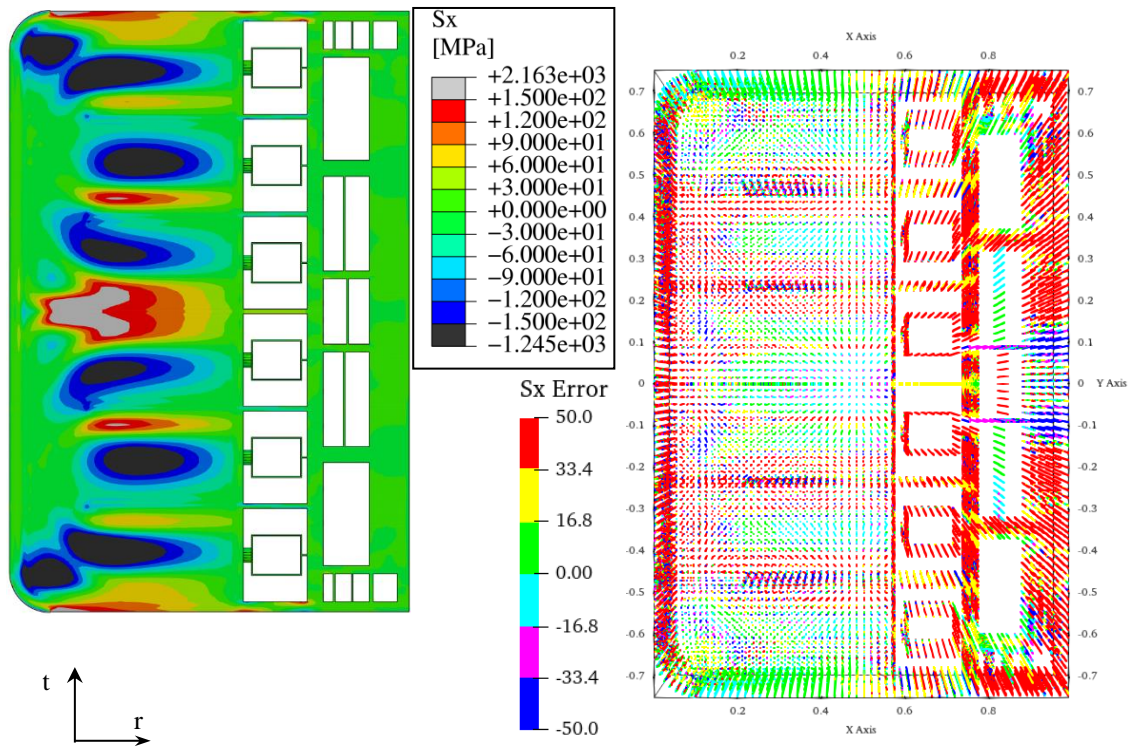


Figure 2.22 S_x spatial distribution from calculated thermal field (left) and relative error contour map (right) when compared with S_x from interpolated thermal field.

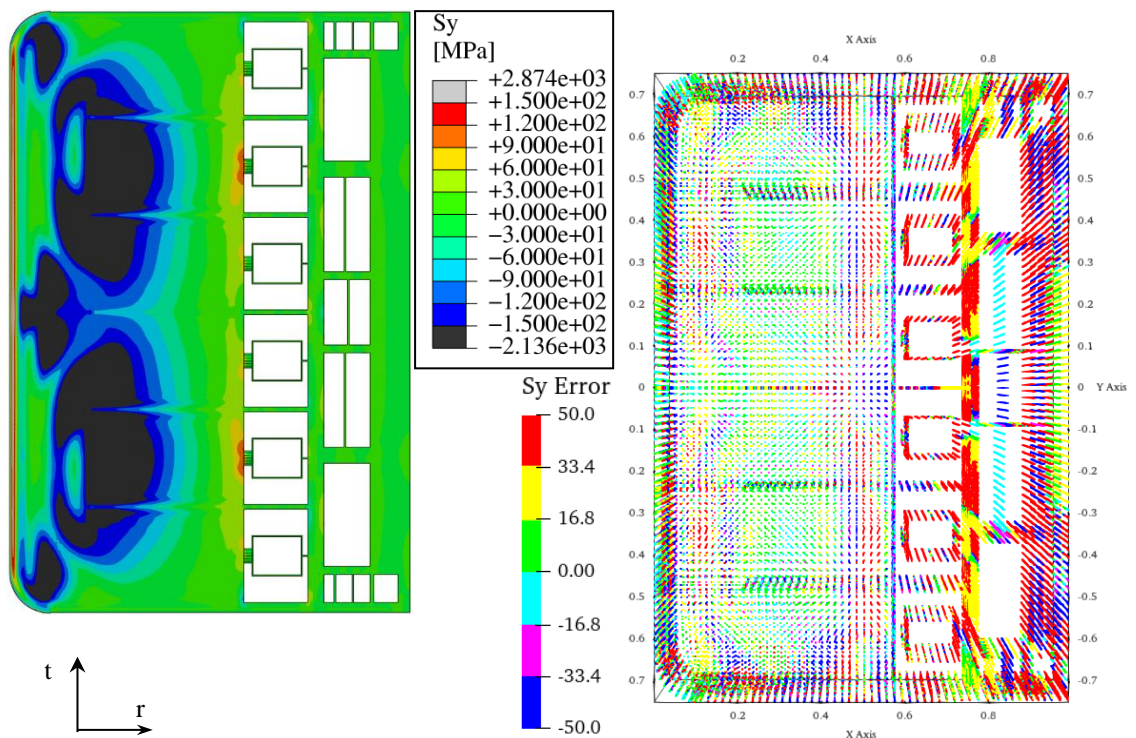


Figure 2.23 S_y spatial distribution from calculated thermal field (left) and relative error contour map (right) when compared with S_y from interpolated thermal field.

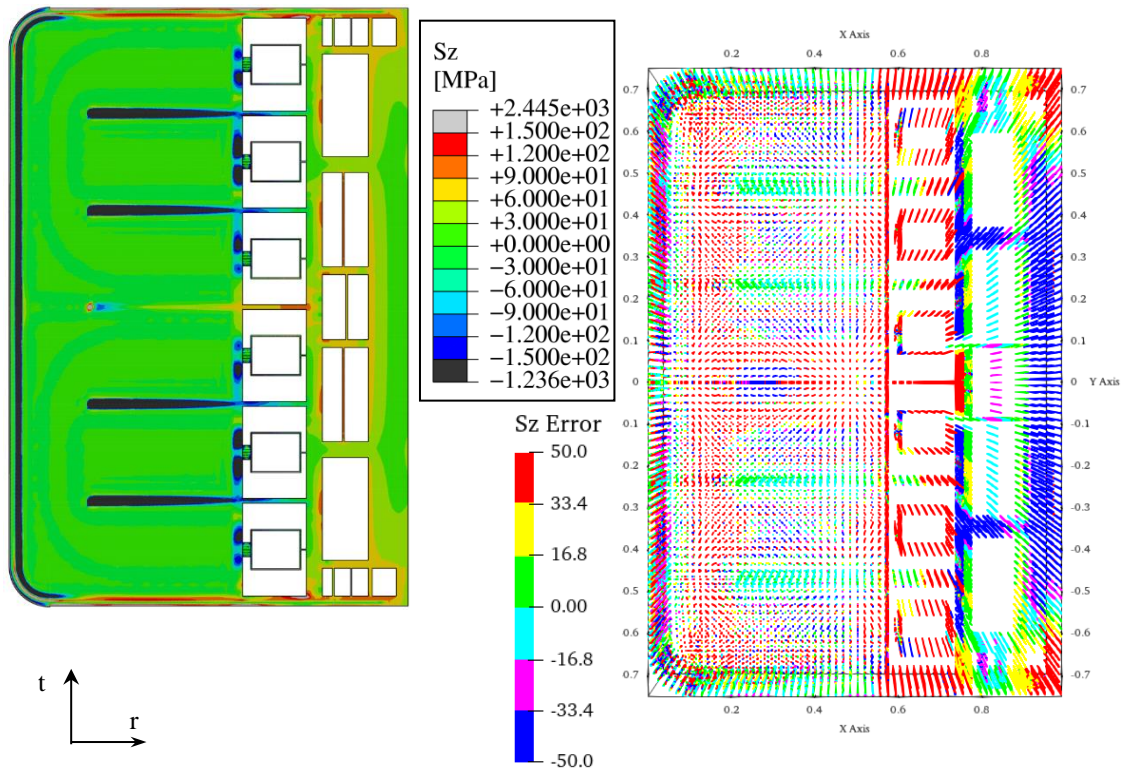


Figure 2.24 S_z spatial distribution from calculated thermal field (left) and relative error contour map (right) when compared with S_z from interpolated thermal field.

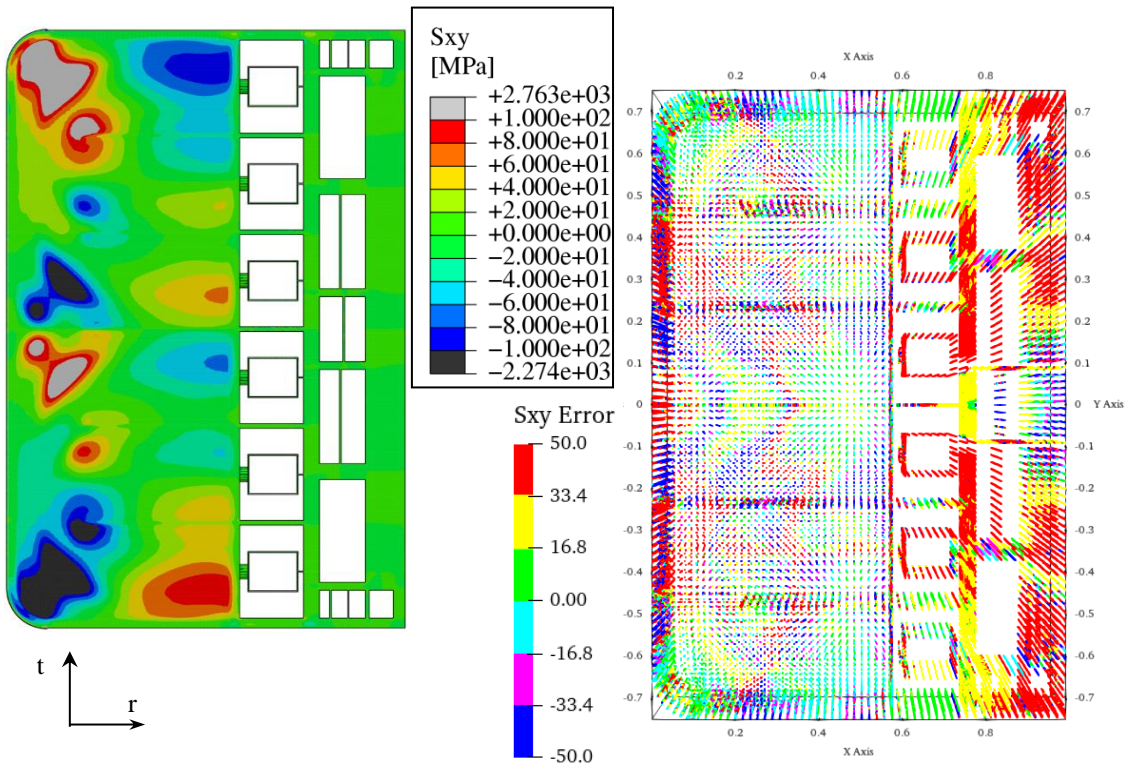


Figure 2.25 S_{xy} spatial distribution from calculated thermal field (left) and relative error contour map (right) when compared with S_{xy} from interpolated thermal field.

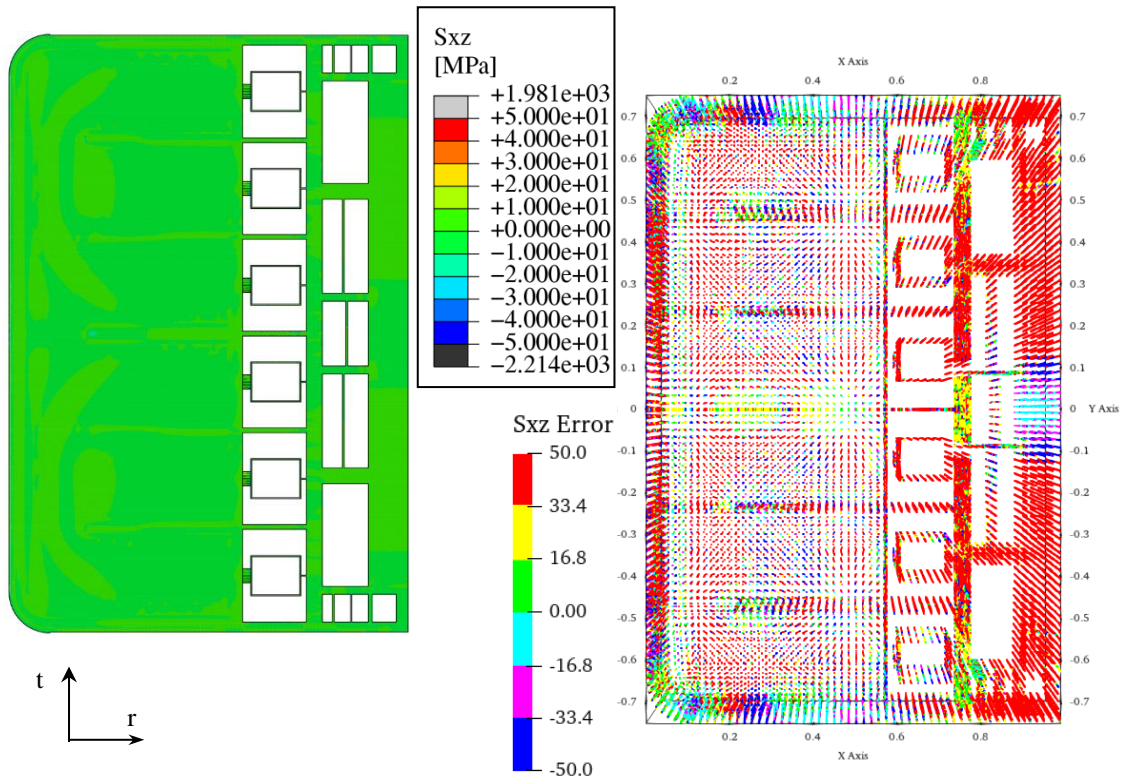


Figure 2.26 S_{xz} spatial distribution from calculated thermal field (left) and relative error contour map (right) when compared with S_{xz} from interpolated thermal field.

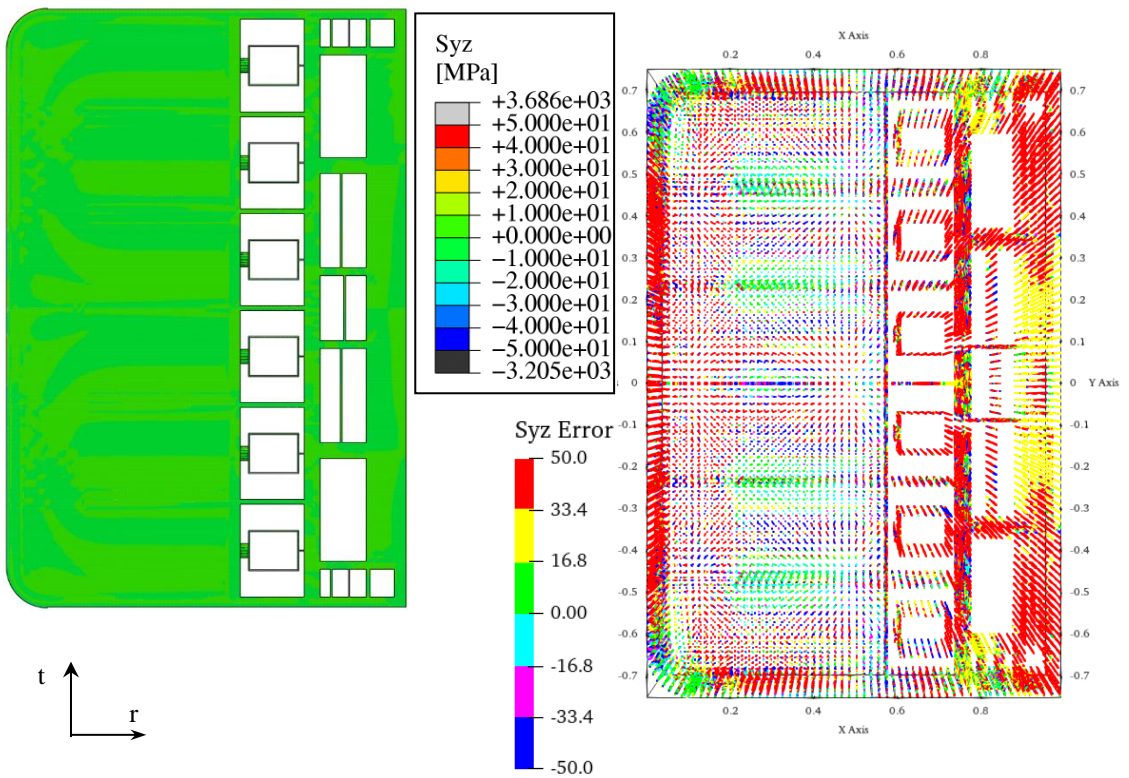


Figure 2.27 S_{yz} spatial distribution from calculated thermal field (left) and relative error contour map (right) when compared with S_{yz} from interpolated thermal field.

2.6 Secondary stress field on the WCLL COB segment

Once assessed the predictive power of the “multi region” interpolation strategy, either in terms of temperature and secondary stress values prediction, the set of polynomial functions has been used for the thermo-mechanical analysis of the whole WCLL COB segment. The geometric layout of the considered segment is depicted in Figure 2.28, where the attachment system devoted to connecting the BB segment to the vacuum vessel is shown too. The reference attachment system configuration consists of a set of mechanical keys able to ensure the connection between BB and vacuum vessel, without using screws and/or bolts in order to simplify the remote maintenance operations.

In order to assess its thermo-mechanical performances, a mesh composed of ~2.3M nodes connected in ~4.6M tetrahedral and hexahedral linear elements has been set-up. Since the scope of this analysis was to predict the secondary stress field arising within the WCLL COB, the thermal field obtained using the “multi-region” interpolation field has been applied (Figure 2.29).

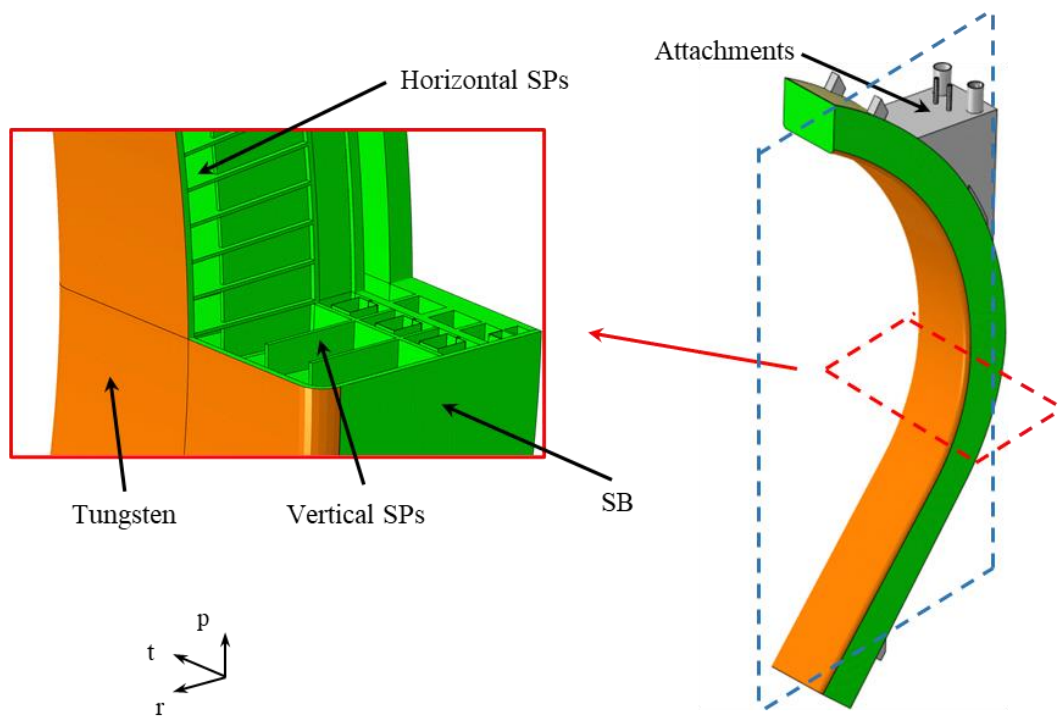


Figure 2.28 The WCLL COB Segment.

As to mechanical restraints, in Figure 2.30 the regions highlighted in red represent the areas of the attachments in contact with the VV, each working along the direction indicated by the arrows in the figure. In particular, in the FEM model, their actions have been simulated by means of special spring elements with axis oriented along the specific working

direction. Their elastic constants have been calculated in order to correctly simulate the connection between BB and VV, as reported in [42].

Then, the secondary stress field has been calculated by means of a steady state structural analysis. The predicted Von Mises equivalent stress field is reported in Figure 2.31.

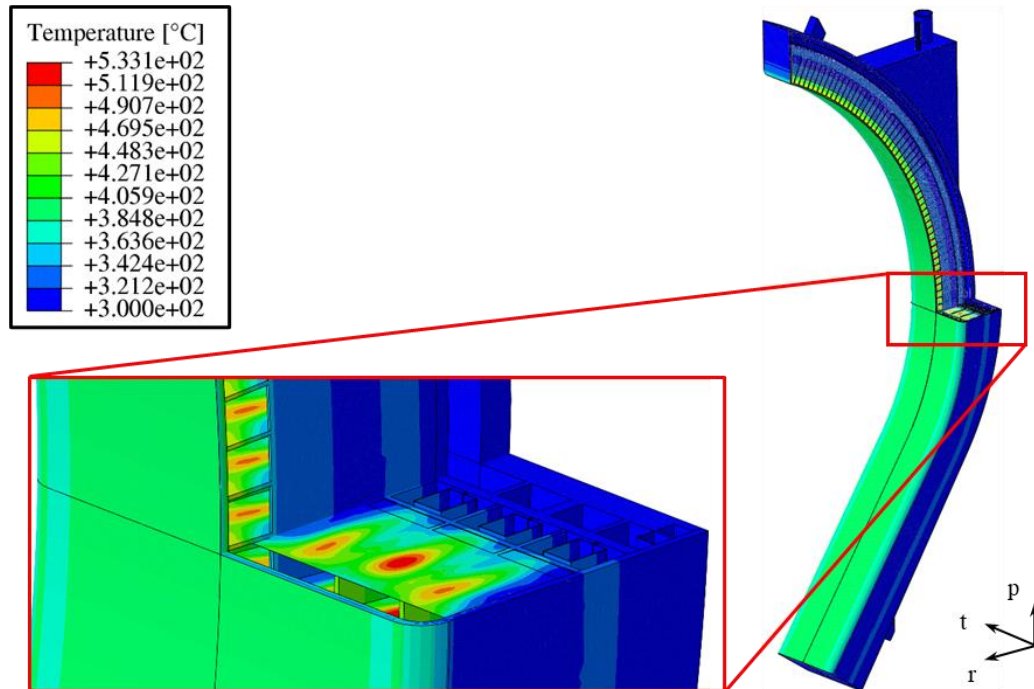


Figure 2.29 The “multi-region” interpolated thermal field applied to the whole WCLL COB Segment.

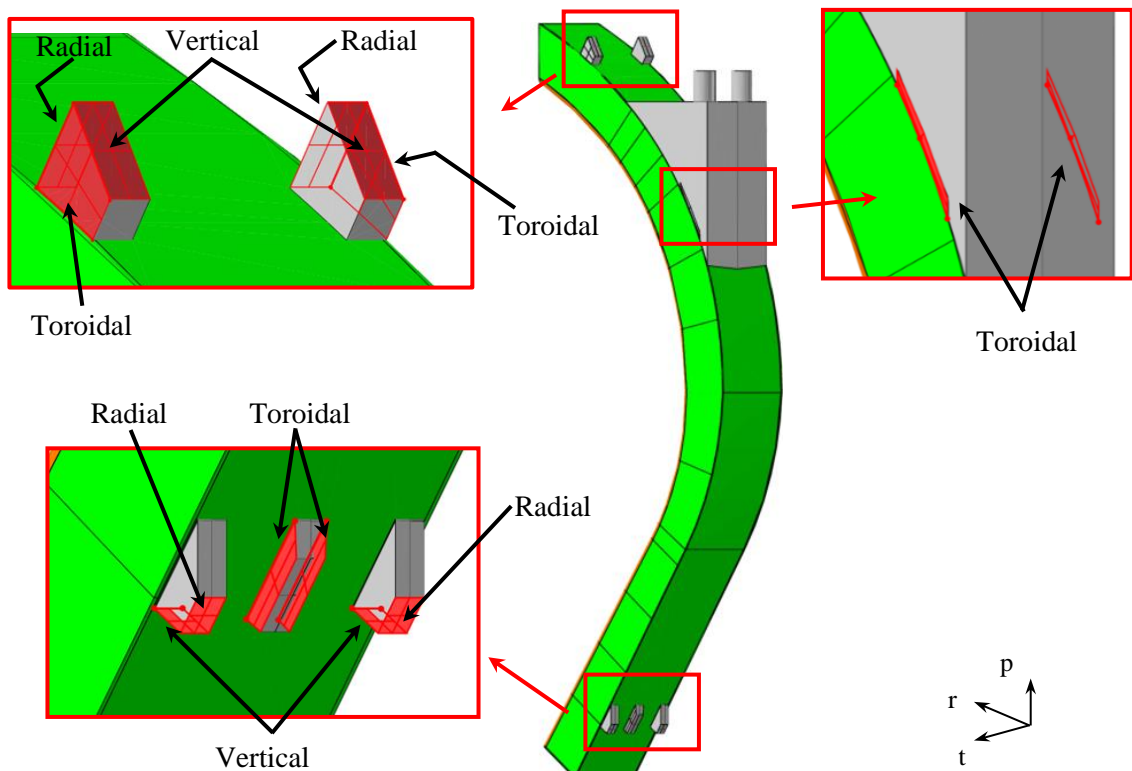


Figure 2.30 The attachment system.

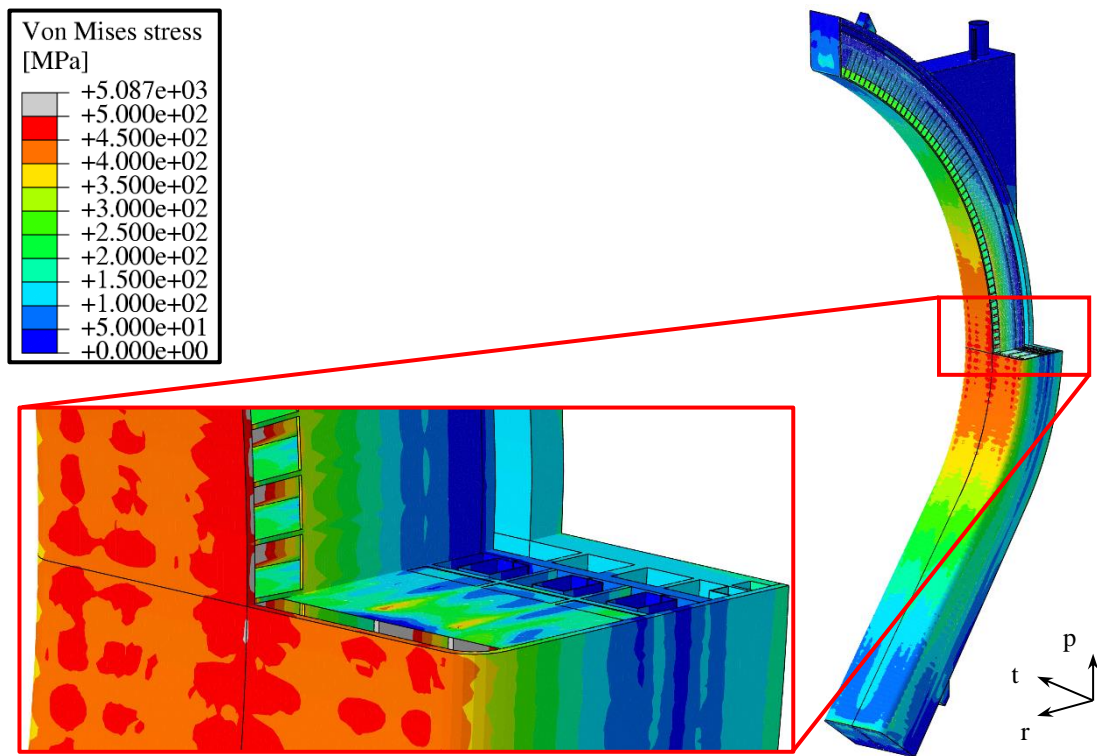


Figure 2.31 The Von Mises equivalent stress (secondary) calculated.

Adopting the procedure herein presented, it is possible obtaining a remarkable level of detail in the stress field, otherwise not predictable in the whole segment unless it was studied from thermal-hydraulic and mechanical standpoints. For instance, it is possible considering the effect of the SB cooling channels even though they are not currently present in the WCLL COB segment geometric layout, since the assumed thermal field is derived from a local model endowed with the detailed FW channels layout. Moreover, as depicted in Figure 2.32, a remarkable difference in the stress spatial distribution within SPs can be observed comparing the obtained stress field (originated from the “multi-region” interpolation approach) with a different secondary stress field originated by a purely radial temperature profile given by a unique polynomial function, adopted so far in the WCLL BB design activities. In particular, as shown in figure, an increased stress toroidal dependence can be observed adopting the “multi-region” interpolation strategy for the thermal field.

In any case, the adoption of the interpolation strategy, regardless of its level of detail, allows predicting results more reliably than in the past where the thermal field arising within the BB segments was assumed on the basis of rough considerations [43] or estimated averaging results of local analysis [20].

It is important to notice that thanks to this procedure, developed and refined in the framework of the Ph.D. course, a new tool in support of thermomechanical analysis has been built-up and is now available to the entire scientific community. This procedure permit to

study the structural performances of a such detailed structure as is a WCLL segment from local analyses of portion of it.

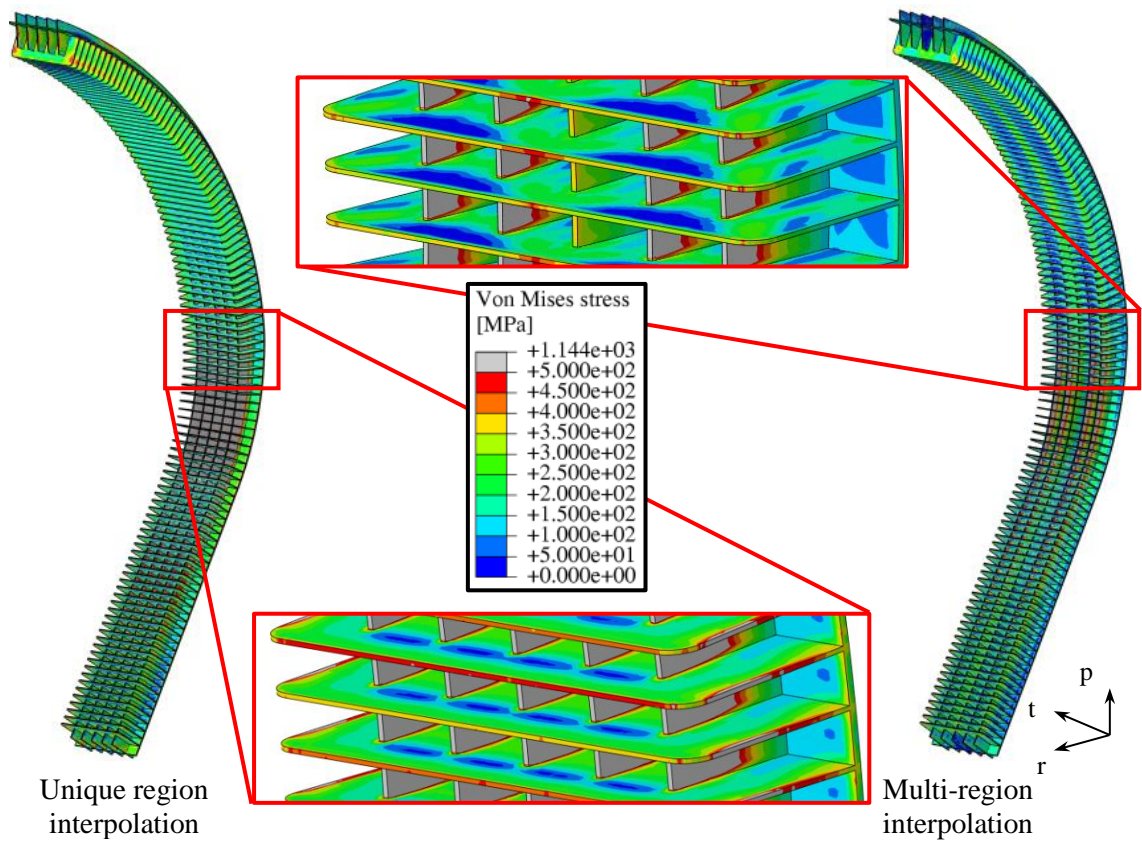


Figure 2.32 Comparison between secondary stress field in the SPs geometric domain.

Chapter 3

3 Global structural analysis of the WCLL Central Outboard Segment and application of the Sub-modelling technique

3.1 Introduction

The study of the structural behaviour of an entire segment of WCLL BB is one of the major challenges in the framework of the DEMO research activities. The thermal analysis of an entire segment, however, is quite time-consuming and computationally intensive, requiring detailed modelling of the structure and a complex set of loads and boundary conditions concerning the thermal-hydraulic state of the whole segment. In addition, the current level of maturity of the WCLL COB segment design would not allow a straightforward thermal-hydraulic analysis, mainly because the manifolds are at early design state and the Segment Box cooling channels are not designed in the reference geometric layout of the WCLL COB segment, since their poloidal distribution has not been defined yet. Hence, an alternative procedure aimed at obtaining a realistic, although approximated, 3D thermal field for the whole segment has been presented in the last chapter. In particular, a thermal analysis of a reference cell, representing the equatorial region of the segment, has been carried out and, from the obtained results, the point-by-point temperature values have been extrapolated. Then, a set of polynomial functions has been determined to achieve an interpolated thermal field. The non-uniform temperature spatial distribution found has been imposed to the whole COB structure in order to obtain the corresponding non-uniform thermal deformation field and to perform the structural analysis of the segment under a realistic thermal field. Hence, in this chapter, the structural assessment of the whole WCLL COB segment is presented. Moreover, some local regions of interest have been assessed more in detail, from the structural standpoint, thanks to the application of the sub-modelling technique. This further assessment is reported in the present chapter too, in order to provide

a detailed investigation of the thermo-mechanical performances of the WCLL COB segment in some regions of interest.

A 3D FEM model reproducing the whole WCLL COB segment, obtained by removing components that do not play any significant structural role (e.g., baffle plates and DWTs) has been set up. Then, the thermomechanical analyses of the COB segment under Normal Operation (NO), Over-Pressurization (OP) and Upper Vertical Displacement Event (UVDE) steady state scenarios have been performed in order to predict the displacement and stress fields, comparing the obtained results with the reference RCC-MRx code. Once the overall structural response of the COB segment has been obtained, certain interesting regions have been studied in detail, by means of the sub-modelling technique, including structural details missing in the global model within proper local 3D FEM models. In particular, the Segment Box cooling channels have been purposely designed in the local models, in order to realistically assess its structural performances. Thanks to this technique, it is possible to obtain a realistic and complete thermo-mechanical response of the WCLL COB segment, being able to study in detail small portions of a system while maintaining continuity with its overall structural response.

3.2 Central Outboard Segment Structural Analysis

According to the DEMO baseline 2017 [21], 16 identical toroidal sectors are envisaged within the machine. The COB segment (Figure 3.1) is mainly constituted by an external steel structure named Segment Box (SB). It is composed by First Wall (FW) and Side Walls (SWs), and it is closed vertically by upper and lower Caps. The SB is internally reinforced by a system of SPs [44]. In particular, the COB segment analysed foresees a thickness of 12 mm and 16 mm for SP_h and SP_v respectively, according to a preliminary version of the COB segment [45]. Moreover, a 2 mm-thick Tungsten armour coats the FW and an attachment system is devoted to mechanically connect the SB to the Vacuum Vessel (VV). The SB encloses the Breeder Zone (BZ) in which the Lithium-Lead (PbLi), a liquid metal eutectic alloy acting as breeder and neutron multiplier, flows in poloidal direction throughout the SPs, following the path highlighted in yellow in Figure 3.2. The SB internals, i.e., the BZ, are cooled by means of bundles of DWTs [46][47] whereas FW, SWs and Caps are endowed with square section cooling channels. Subcooled water, at the operational pressure of 15.5 MPa, flows inside both DWTs and channels. In order to save computational resources and speed-up calculations, the model developed for this study has been simplified removing DWTs (Figure 3.2), but their effect on the thermal field has been purposely considered.

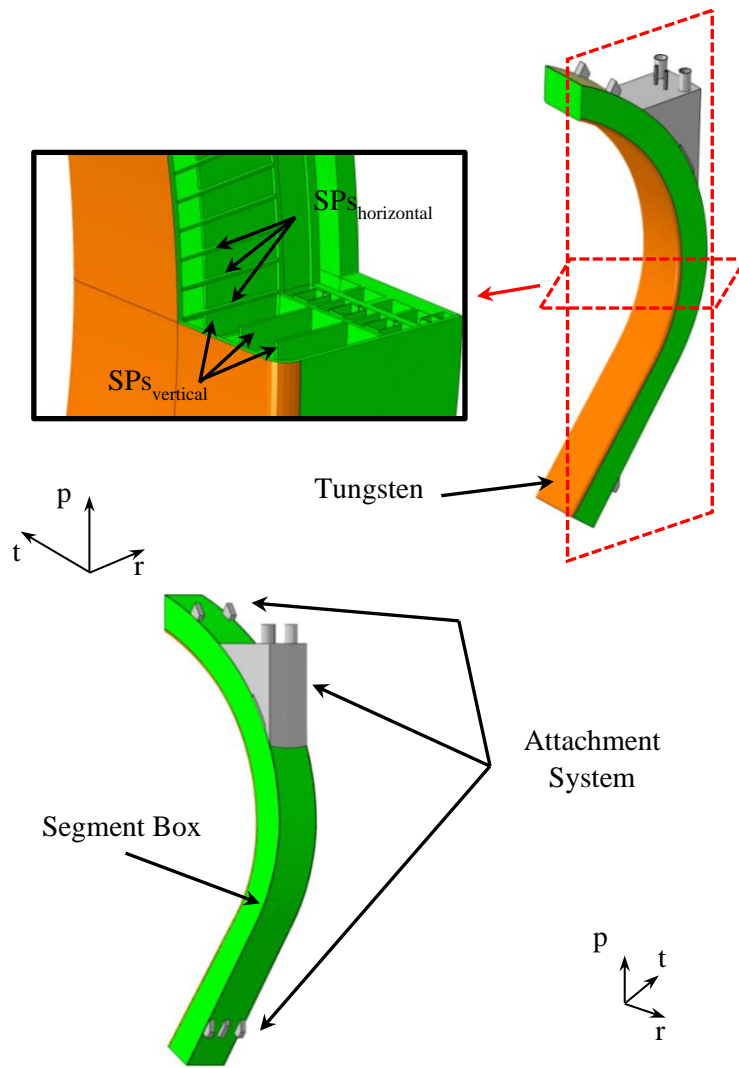


Figure 3.1 Central Outboard Segment architecture.

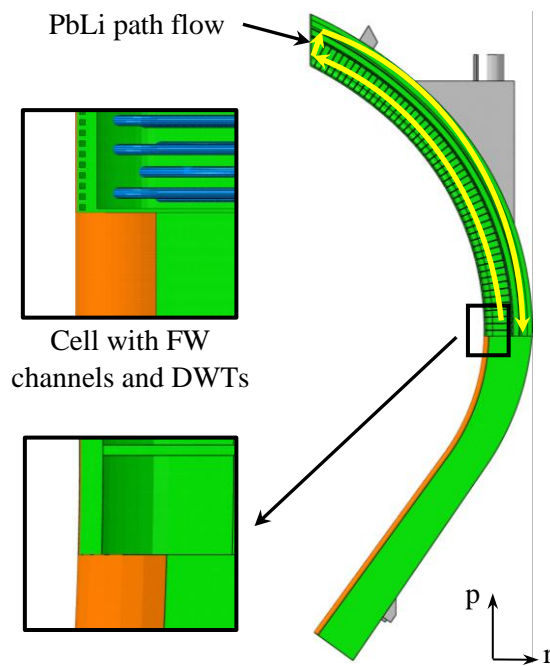


Figure 3.2 Central Outboard Segment architecture detail.

A FEM model composed of ~2.3M nodes connected in ~4.6M tetrahedral and hexahedral linear elements has been set-up. Water and breeder have not been modelled but their effects on the thermo-mechanical behaviour have been simulated considering proper loads and boundary conditions.

3.2.1 Loads and Boundary Conditions

The thermo-mechanical performances of the WCLL COB segment have been investigated under purposely selected steady state loading scenarios. First, the NO scenario has been considered. It takes into account the thermomechanical loads arising under the nominal operating condition and therefore it is considered as Level A scenario in RCC-MRx structural design code [31][50]. Then, analysis under the UVDE scenario have been performed. Such scenario refers to an off-normal event due to a vertical plasma disruption, being classified as Level C. Lastly, the OP loading scenario has been considered. It refers to a severe accidental condition, relevant to a coolant leak within the segment, which ultimately entails the loss of the component. It is hence classified under Level D in RCC-MRx structural design code. In order to correctly reproduce the NO, OP and UVDE loading scenarios, a proper set of loads and boundary conditions has been implemented [48][49].

In particular, the following loads and boundary conditions have been taken into account:

- Non-uniform thermal deformation field;
- Pressure load;
- Gravity load;
- Electro-Magnetic loads;
- Mechanical restraints.

The Reduced Activation Ferritic/Martensitic (RAFM) Eurofer steel has been considered as SB structural material, covered by a thin Tungsten layer. Water and breeder have not been modelled, so, in order to simulate their presence in terms of weight force, an Eurofer equivalent density has been calculated, assumption already adopted in previous analyses [20]. In particular, this value has been calculated considering the percentage of steel, breeder and water inside an equatorial cell.

Temperature-dependent properties of Eurofer [37] and Tungsten [39] have been adopted and considered in the analysis, properly modifying the Eurofer density, as afore mentioned. So, the acceleration of gravity value has been imposed on the whole structure.

The non-uniform temperature spatial distribution has been imposed to the COB structure, using the set of functions described in the previous chapter, in order to obtain the corresponding non-uniform thermal deformation field, as drawn in Figure 3.3.

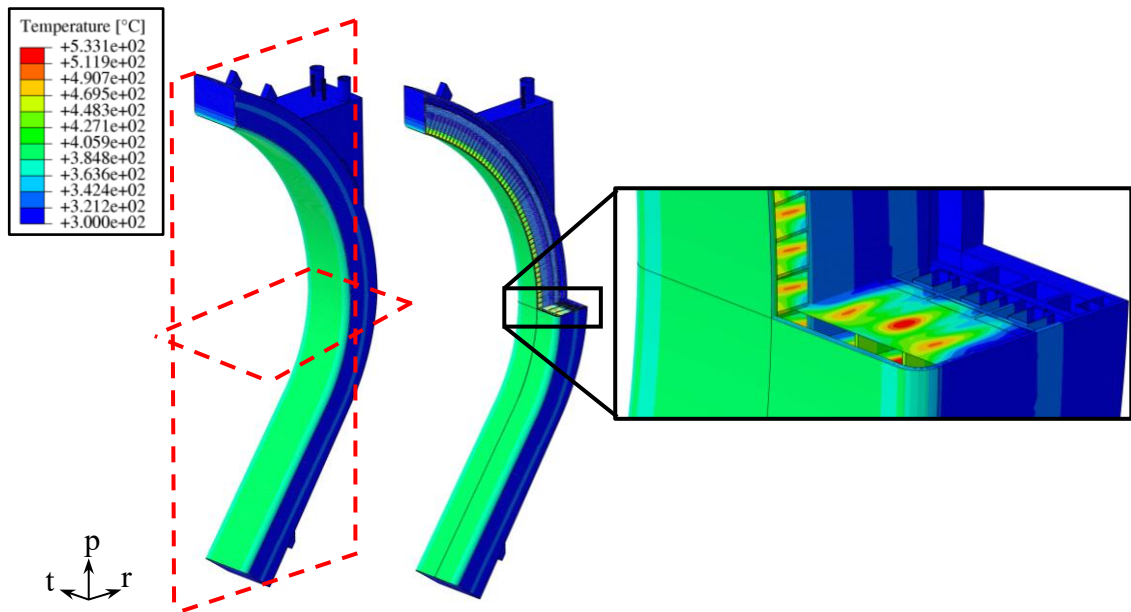


Figure 3.3 Non-uniform thermal deformation field imposed on the COB segment.

During both normal and off-normal operations, EM loads arise and act within the structure. In particular, during the NO loading scenario, according with the assumption that the Lorentz's forces due to the variation of the poloidal field coils during the flat-top is negligible [51], only the contribution given by the ferromagnetic loads has been considered. According to [48][49], the same EM loads have been used for the OP loading scenario. On the contrary, during the considered UVDE loading scenario, the impact of Lorentz's forces is not negligible and must be taken into account. Since EM loads related to a plasma disruption undergo great variations [52], a selection of the most demanding timesteps has been made and respective equivalent static analyses (neglecting dynamic effects) have been launched. In particular, looking at the time behaviour of the force and moment components acting on the COB segment (Figure 3.4), the time-steps corresponding to the maximum of the radial force ($t = 11.52$ s) and moment ($t = 11.585$ s) have been considered for the structural analyses. Hence, two different UVDE scenarios have been set-up, differing each other for the EM leads spatial distribution.

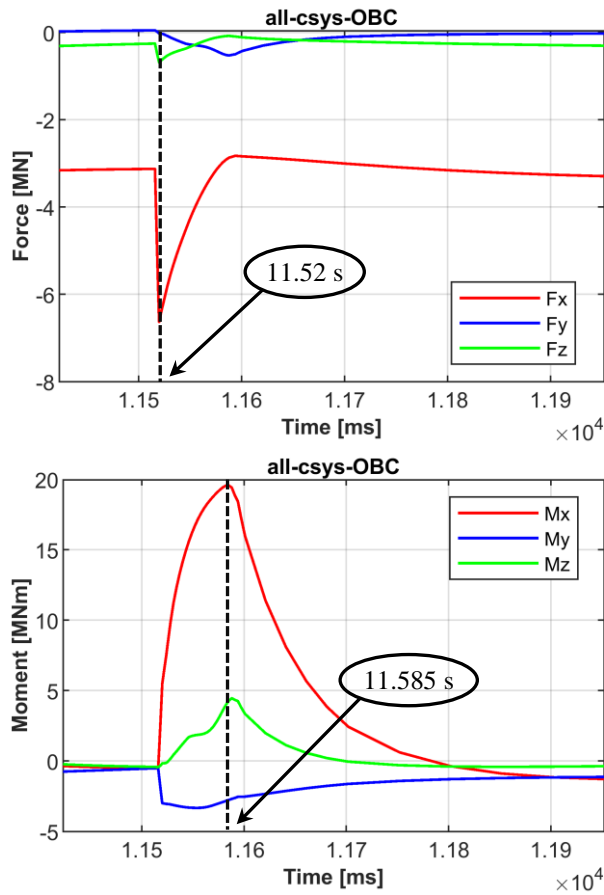


Figure 3.4 Force and moment time behaviour during a UVDE [51] and maximum component (i.e., radial) time-steps.

As prescribed in [48][49], the design pressures, calculated as the nominal pressure multiplied by a safety factor of 1.15, have been adopted for this study. Therefore, a coolant design pressure ($P_{\text{des,coolant}}$) of 17.825 MPa and a breeder design pressure ($P_{\text{des,breeder}}$) of 0.575 MPa have been set. Concerning NO and UVDE scenarios, $P_{\text{des,coolant}}$ has been imposed onto all the coolant wetted surfaces while $P_{\text{des,breeder}}$ has been assumed acting on the breeder-wetted surfaces. Instead, for OP loading scenario, $P_{\text{des,coolant}}$ has been considered for both coolant and breeder-wetted surfaces as this scenario represents the over-pressurization conditions due to an in-box LOCA event.

Lastly, in order to reproduce the mechanical action of the COB attachment system to the VV, a set of mechanical restraints has been imposed. In particular, a set of springs has been located in correspondence of each blanket support structure, highlighted in red in Figure 2.30, and acting in the direction indicated in figure, with different stiffness values as reported in [42].

A summary of the loads and boundary conditions (BCs) considered for each analysed loading scenarios is reported in Table 3.1.

Loads and BCs	NO	OP	UVDE (t=11.52 s)	UVDE (t=11.585 s)
Thermal Field	Set of interpolating functions			
Water-wetted surfaces	p=17.825 MPa	p=17.825 MPa	p=17.825 MPa	p=17.825 MPa
Breeder-wetted surfaces	p=0.575 MPa	p=17.825 MPa	p=0.575 MPa	p=0.575 MPa
EM loads	Ferromagnetic loads	Ferromagnetic loads	Ferromagnetic loads + Lorentz's forces (t=11.52 s)	Ferromagnetic loads + Lorentz's forces (t=11.585 s)
Restraints	Set of springs reproducing the attachment systems			

Table 3.1 Summary of the loads and boundary conditions.

3.2.2 Results

Steady state analyses have been launched in order to assess the thermo-mechanical behaviour of the WCLL COB segment under the selected loading scenarios.

Von Mises equivalent stress field (primary + secondary stress) obtained for the different assessed scenarios and the deformed (with an isotropic deformation amplification factor equal to 30) vs. undeformed shapes, also showing the total displacement fields, are shown in Figure 3.5, Figure 3.6, Figure 3.7 and Figure 3.8. For all four loading operative scenarios, it is possible to observe that the most of the investigated domain experiences stress values lower than 500 MPa. The maximum displacement values obtained along the three directions (radial, toroidal and poloidal) have been reported in Table 3.2.

In particular, the deformation field is almost the same in all the assessed scenarios with a maximum displacement along the radial direction, value obtained in the NO loading scenario equal to 46.63 mm. On the other hand, only small displacements occur in toroidal direction, quite symmetrically. Moreover, in the UVDE loading scenario, considering the loads combination reproducing the time-step corresponding to the maximum of the radial moment (t = 11.585 s), higher displacements than the other scenarios are predicted along the toroidal direction.

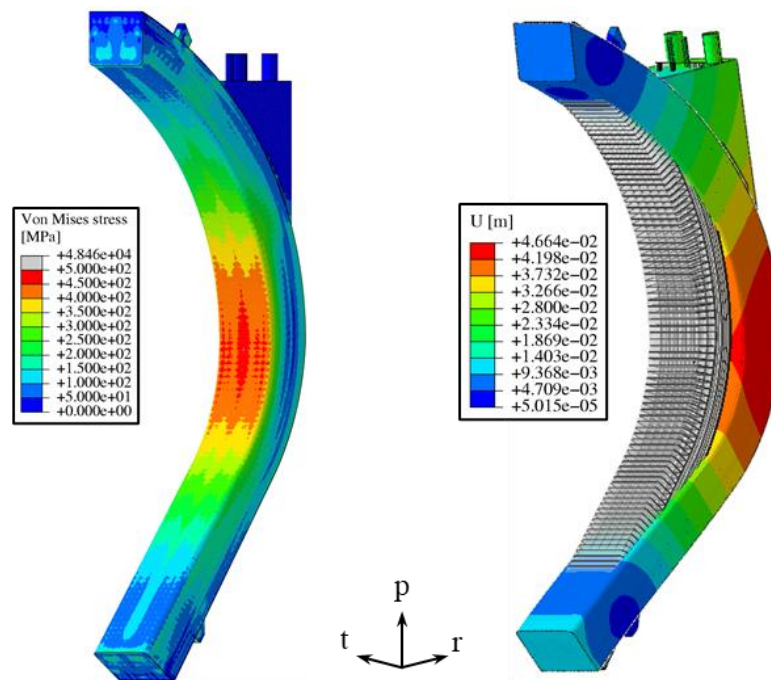


Figure 3.5 NO Von Mises stress field and Deformed vs. Undeformed Shapes.

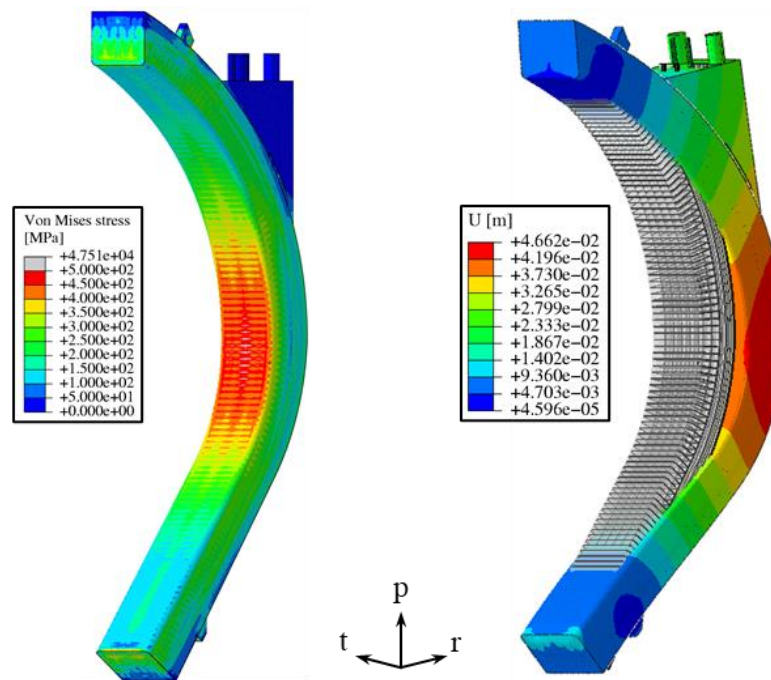


Figure 3.6 OP Von Mises stress field and Deformed vs. Undeformed Shapes.

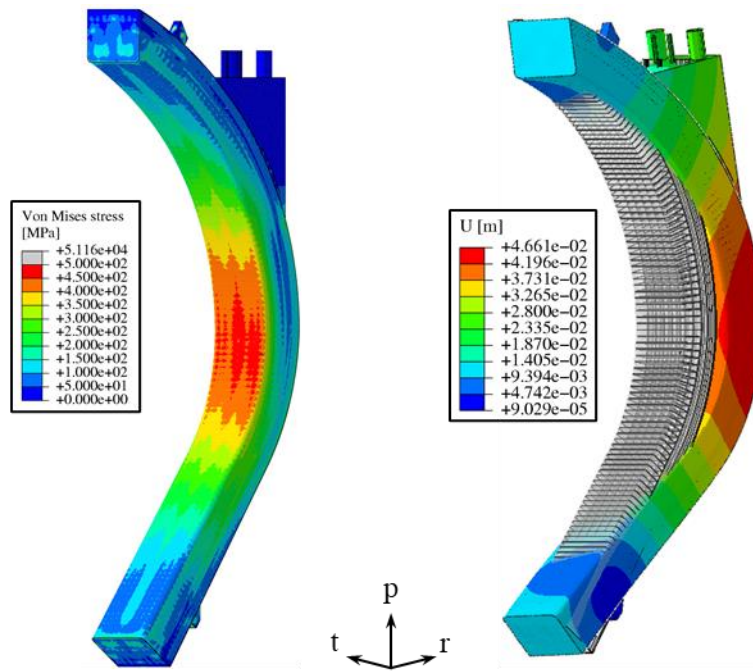


Figure 3.7 UVDE ($t = 11.585$ s) Von Mises stress field and Deformed vs. Undeformed shapes.

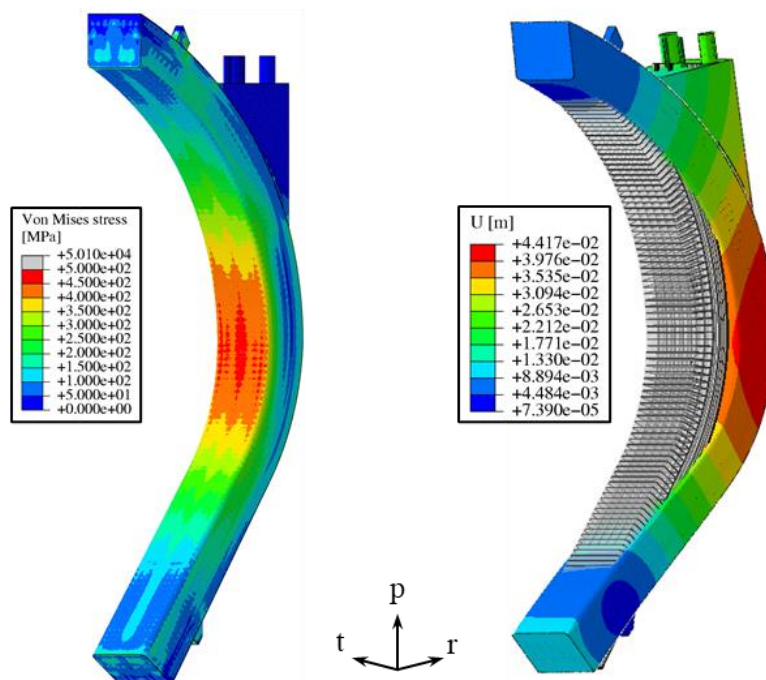


Figure 3.8 UVDE ($t = 11.52$ s) Von Mises stress field and Deformed vs. Undeformed shapes.

	NO	OP	UVDE t=11.52s	UVDE t=11.585s
Ur, max [mm]	46.63	46.61	44.13	46.58
Ur, min [mm]	-9.81	-9.56	-10.01	-10.92
Ut, max [mm]	3.84	4.18	5.08	7.67
Ut, min [mm]	-4.41	-4.44	-5.23	-12.74
Up, max [mm]	21.77	22.16	22.15	22.06
Up, min [mm]	-7.85	-8.17	-7.14	-8.06

Table 3.2 Maximum displacements values in all the assessed scenarios.

In order to evaluate the thermo-mechanical behaviour of COB in view of the reference RCC-MRx code in the different scenarios taken into account, a stress linearization procedure has been carried out within the most critical regions individuated.

In particular, the most stressed regions have been identified within the poloidal-radial and toroidal-radial SPs and proper paths have been built. No paths have been considered along the SW-FW-SW region due to the absence of the cooling channels. In particular, four paths have been considered for a single elementary cell, two throughout vertical SPs and two throughout horizontal SP, as depicted in Figure 3.9. Paths located in the same position as the central cell have also been identified in other two cells located in the upper part and in lower part of the COB, indicated in red in Figure 3.9.

After the stress linearization procedure was performed, the RCC-MRx structural design criteria have been checked in order to verify the structural integrity of the component. In particular, P-type failure, resulting from applying a constantly increasing load, have been considered. The rules taken into account are: Immediate Excessive Deformation (IED), Immediate Plastic Instability (IPI), Immediate Plastic Flow Localization (IPFL) and Immediate Fracture due to exhaustion of ductility (IF) criteria. In Table 3.3 the criteria are reported, where S_m is the maximum allowable primary membrane stress intensity of the material, S_{em} is the maximum allowable primary plus secondary membrane stress, function of temperature and irradiation, S_{et} is the maximum allowable total stress, also function of temperature and irradiation, and, finally, K_{eff} is a factor called “plastic collaboration coefficient”, equal to 1.5 for rectangular sections. Temperature-dependent values of S_m , S_{em} and S_{et} [53] have been differently calculated for Level A, C or D according to the structural material Eurofer. In this study, the stress limit values have been calculated at the path average temperature.

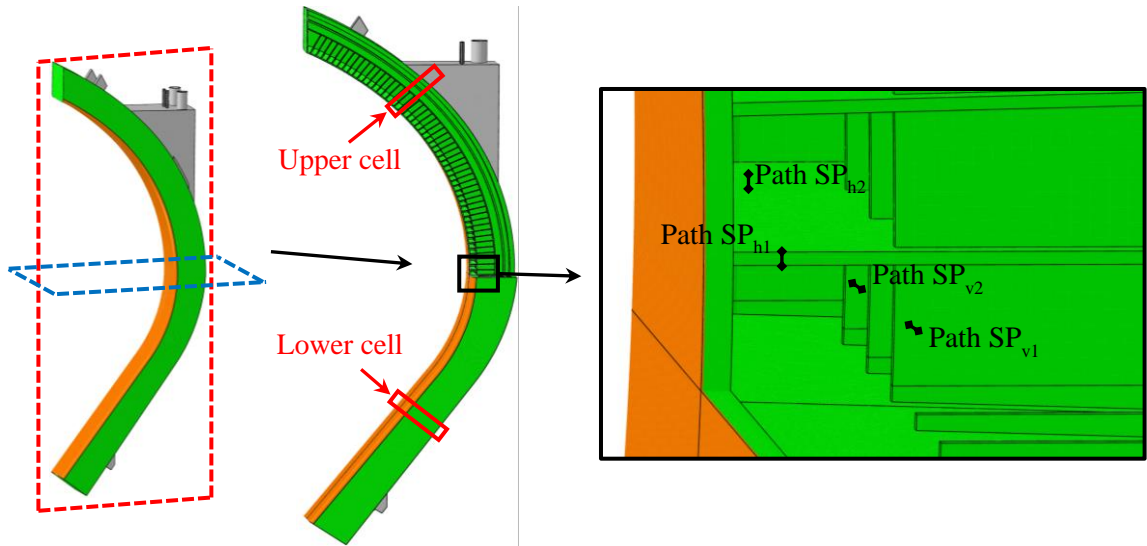


Figure 3.9 Stress linearization paths in the central cell.

	Criteria
Immediate Excessive Deformation (IED)	$\frac{P_m}{S_{m,A-C-D}} < 1$
Immediate Plastic Instability (IPI)	$\frac{P_m + P_b}{K_{eff} \cdot S_{m,A-C-D}} < 1$
Immediate Plastic Flow Localization (IPFL)	$\frac{P_m + Q_m}{S_{em,A-C-D}} < 1$
Immediate Fracture due to exhaustion of ductility (IF)	$\frac{P_m + P_b + Q + F}{S_{et,A-C-D}} < 1$

Table 3.3 RCC-MRx design criteria [31].

In NO and OP loading scenarios (Figure 3.10 and Figure 3.11) IED, IPI and IF criteria are fulfilled along all paths, while the IPFL criterion is not. In particular, looking at the results obtained in the NO loading scenario, in the equatorial region both the paths individuated within the vertical SPs does not fulfil the IPFL criterion, instead in the upper and lower region, both paths located within the horizontal SPs do not fulfil the same criterion. During the OP loading scenario, the IPFL criterion evaluated within both SP_h paths in the upper and lower regions exceeds or reaches a critical value (>0.8). The IPFL criterion, evaluated during all the assessed loading scenarios, overcomes the limit in the “SP_{v2}” path within the central region of the segment.

Moreover, during both UVDE loading scenarios assessed (Figure 3.12 and Figure 3.13), IED IPI and IF criteria are widely fulfilled within all the paths taken into account. Instead,

the paths located along both SPv (namely SPv1 and SPv2), located in the equatorial region, does not fulfil the IPFL criterion.

Globally, the two paths identified within the vertical SPs in the equatorial region of the COB segment far exceed the limit value (>1) of the IPFL criterion, almost doubling this value in a path in the NO loading scenario. This behaviour allows to confirm the equatorial region as the most stressed of the segment.

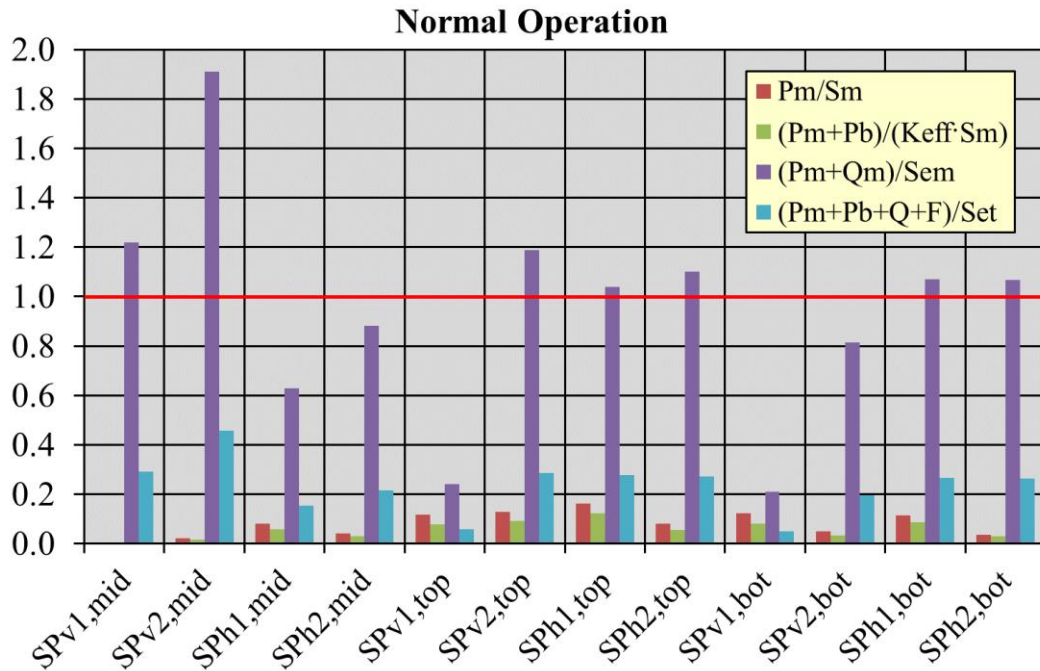


Figure 3.10 Stress linearization results under NO loading scenario.

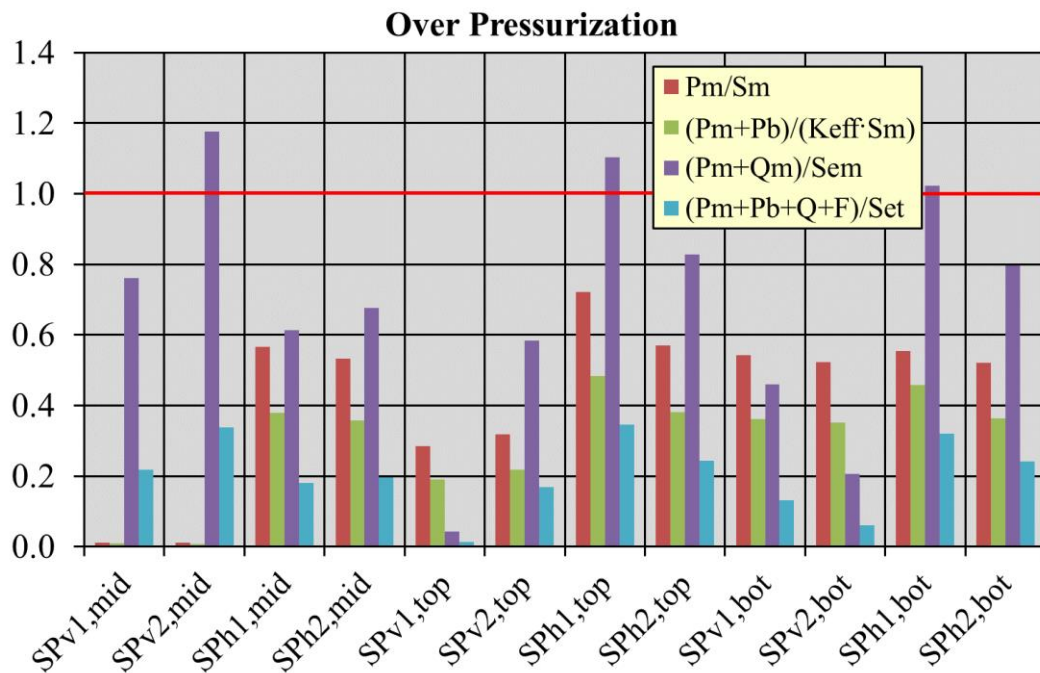


Figure 3.11 Stress linearization results under OP loading scenario.

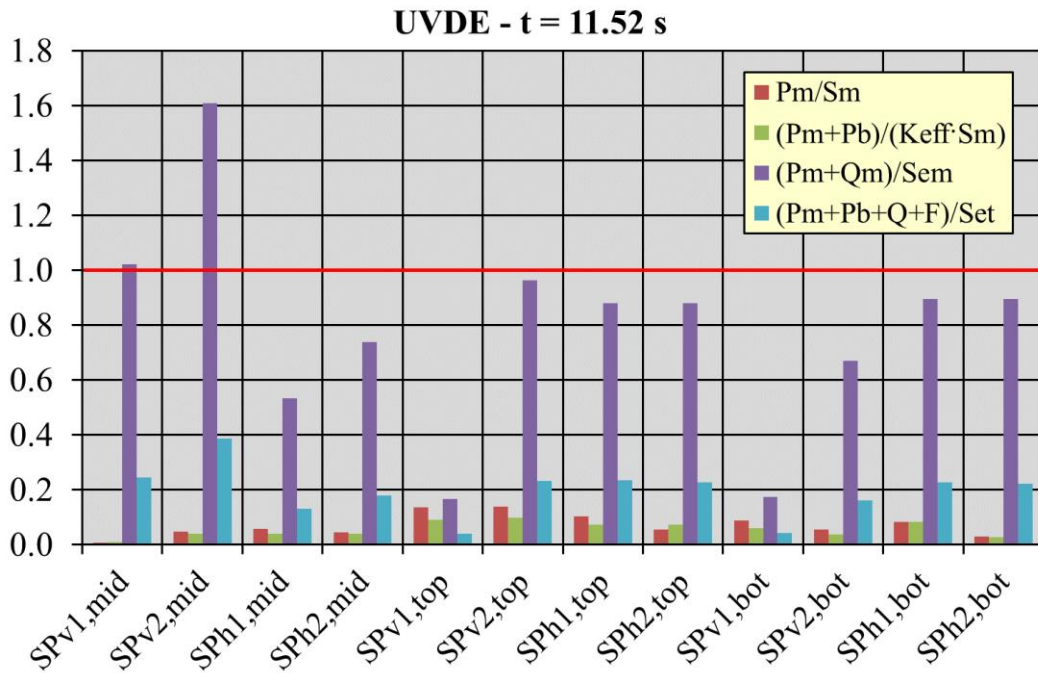


Figure 3.12 Stress linearization results under UVDE - T = 11.52 s loading scenario.

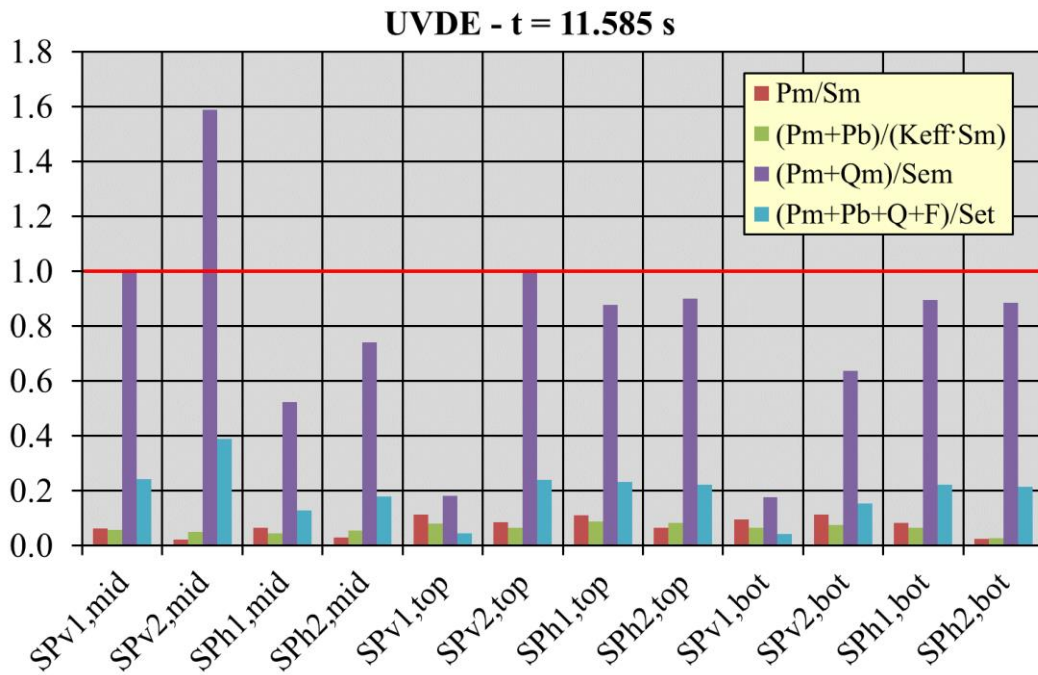


Figure 3.13 Stress linearization results under UVDE - T = 11.585 s loading scenario.

Results obtained highlight that, globally, not all criteria are fulfilled along the paths taken into account and, in particular, paths considered within the poloidal-radial SPs are the most stressed. Furthermore, none of the cases fully verified the IPFL criterion, which takes into account secondary stresses. The displacement field is similar in all of the assessed loading scenarios. However, a remarkable displacement along the radial direction has been observed. This common trend probably can be due to the fact that the attachment system does not

foresee any support in the equatorial region to prevent the radial displacement of the segment, thus showing a very large deformation.

Analysis results have shown that further studies need to be carried out. In particular, the COB supporting system needs to be reviewed in order to avoid too large displacements and improve its thermomechanical behaviour. Moreover, the structural performances of the Segment Box need to be investigated. To this purpose, the sub-modelling technique has been applied purposely adding the cooling channels in those regions selected to be assessed in detail. Moreover, the local assessment will allow confirming the results obtained from the analysis of the whole segment in the SPs domain.

3.3 The application of the sub-modelling technique

In some cases, the overall behaviour of a structure is of interest as much as the detailed behaviour of one of its parts. In order to study in detail a specific part of an entire model, it is possible to realize a fine mesh in that exact region, but this can be challenging, require a temporal effort and high computational burden. Moreover, it is usually not immediately clear which region of an entire structure requires a more detailed study. Sometimes, it is not possible to know in advance the boundary conditions that characterise one part of a more complex model. In still other cases, the whole model has certain structural details that would require a high level of computational effort and make the meshing operation complex. In these cases, the sub-modelling technique is used.

The sub-modelling is a technique to study a smaller local part of a complete model with a refined mesh, based on the interpolation of the solution from an initial model on the boundary regions of the sub-model, which represents a cut through the larger complete model (Figure 3.14). So, the boundary conditions of the local region are defined by the response of the global model and these, together with the loads and the other condition applied onto the sub-model, determines its solution.

In Abaqus [30], two forms of the sub-modelling technique are implemented: node-based and surface-based technique. With the node-based option, node-located solution variables from global model, usually displacements, are interpolated and transferred to the sub-model. Instead, for the surface-based technique, the global stress field is interpolated to obtain a surface traction that is applied to the boundary regions of the sub-model. In Abaqus, with the node-based sub-modelling a boundary condition is obtained, while, with the surface-based a load is defined. The most commonly used technique is the node-based, which also allows large displacements and rotations to be transmitted more accurately.

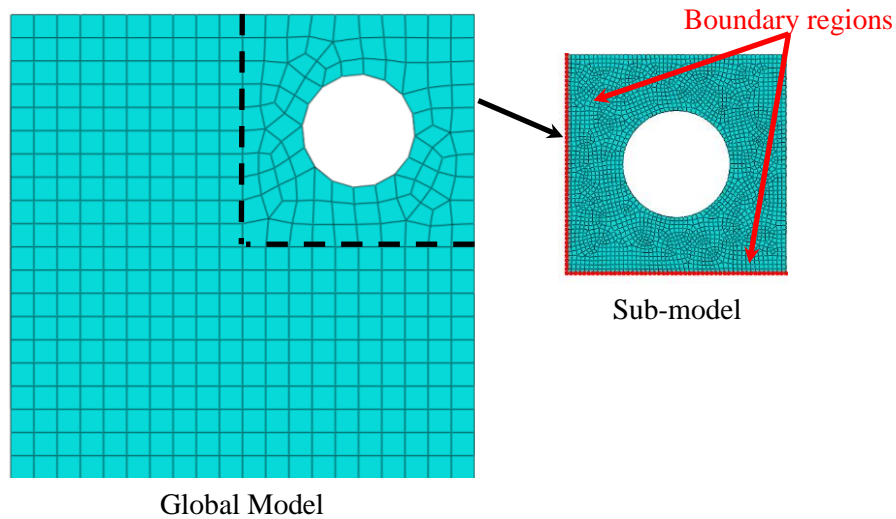


Figure 3.14 Global model and sub-model mesh.

Initially, the complete model, usually called “global model”, is analysed and the results are critically evaluated to identify the regions that need a more accurate analysis. A not-too-fine mesh is usually used for the global model. This corresponds to the structural assessment of the whole WCLL COB segment reported above.

Once the global analysis is complete, the sub-model can be obtained by cutting the model and removing the remaining parts. This ensures that the region to be analysed is in the exact position as it is in the global model, a necessary condition for carrying out a sub-modelling analysis. Then it is possible to add to the smaller model any structural details not present in the global model (namely holes, bolts, supports, etc.) that is intended to study. In this case, the Segment Box cooling channels have been added to the local models, as they are not present in the reference geometric layout of the WCLL COB segment previously assessed. This is possible because Abaqus with this technique only identifies regions of the sub-model where boundary conditions (by means of node-based or surface-based techniques) are applied, which therefore must not be modified with respect to the original model.

Finally, it is necessary to develop a denser mesh (“sub-model” in Figure 3.14) and apply all the loads and conditions to which the structure is subjected, as well as, of course, the boundary conditions due to the sub-modelling technique. The latter are directly drawn from the global model analysis results. Then the local analysis can run and the results can be critically evaluated.

3.4 Central, Top and Bottom Cells sub-modelling

In the analysed WCLL COB segment, as previously mentioned, the SB channels have not been modelled as their poloidal layout has not been defined yet. So, in order to in-depth

study the structural response in those regions and to have a more accurate response in the most critical regions (e.g., stiffening plates), three regions of the segment at different poloidal height have been selected and analysed by means of the sub-modelling technique. Therefore, two central cells, two in the upper part and two in the lower part of the COB segment have been individuated and studied under the assessed loading scenarios considered in the structural assessment of the entire structure.

The three selected regions are shown (highlighted in orange) in Figure 3.15 superimposed to the entire structure of the COB segment, depicted in grey. In particular, these three regions have been obtained by cutting the COB segment by means of planes parallel to the middle of the horizontal SPs delimiting each couple of cells.

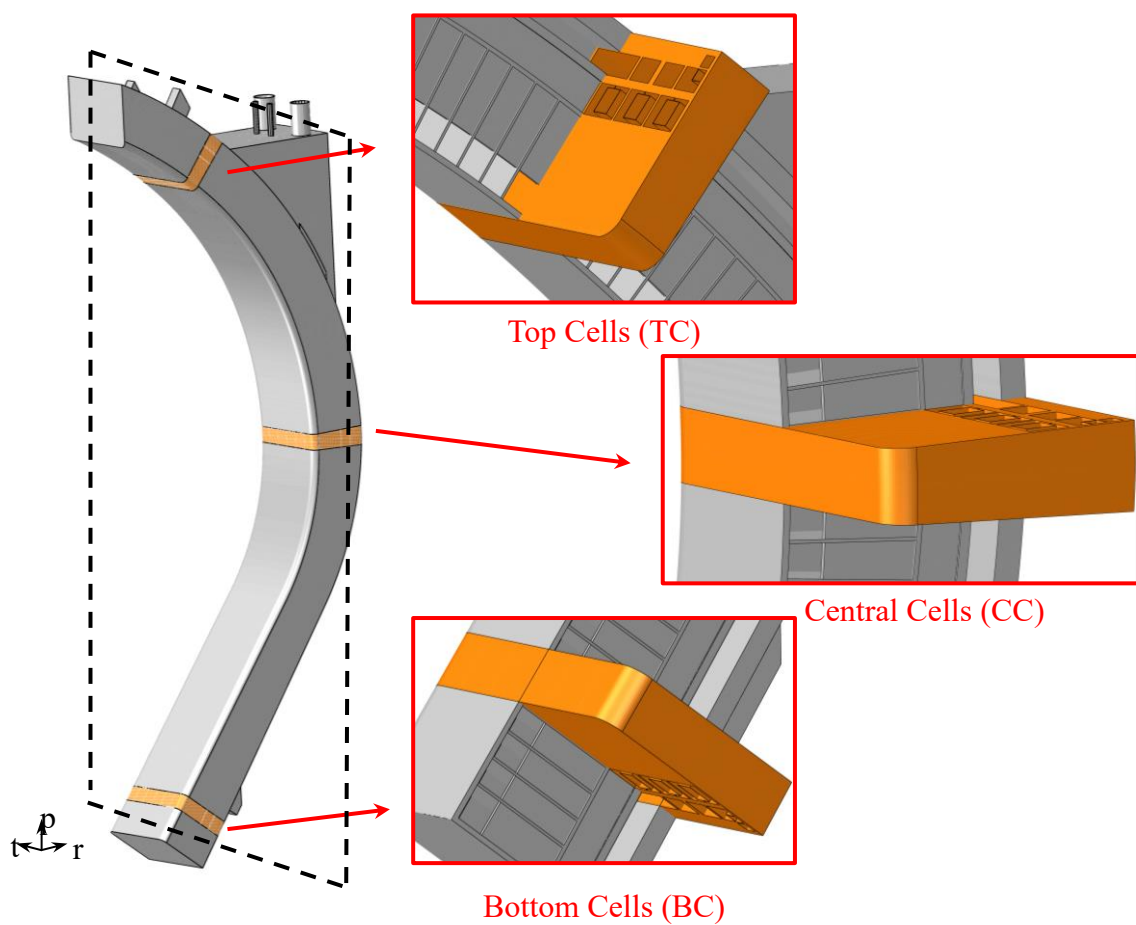


Figure 3.15 Three sub-model regions of COB.

The geometric models of these regions of the COB segment have been modified with respect to the reference configuration, being equipped with 10 cooling channels per slice in the SW-FW-SW region (as showed in Figure 3.16 for the Central Cells), in order to investigate their influence on the overall structural response and to analyse in detail the FW-SWs region. The DWTs and the baffle plate, instead, have not been modelled since they do

not have any significant structural function. In particular, the baffle plates have the task of guiding the PbLi in its poloidal path within the segment.

Hence, three different 3D FEM models have been set-up. The three meshes set-up for each FEM model have similar features, and, concerning the element type, hexahedral linear elements, foreseen by the ABAQUS FEM code elements library, have been adopted. The number of nodes and elements characterizing each mesh has reported in Table 3.4. It is important to note that the meshes of the three local models are much finer compared to the same regions in the global model, as depicted in Figure 3.17. For example, within the vertical and horizontal SPs thickness in the global model a number of elements equal to 1 and 2 are used respectively, instead, in the sub-models 6 and 8 elements are used within the same thicknesses.

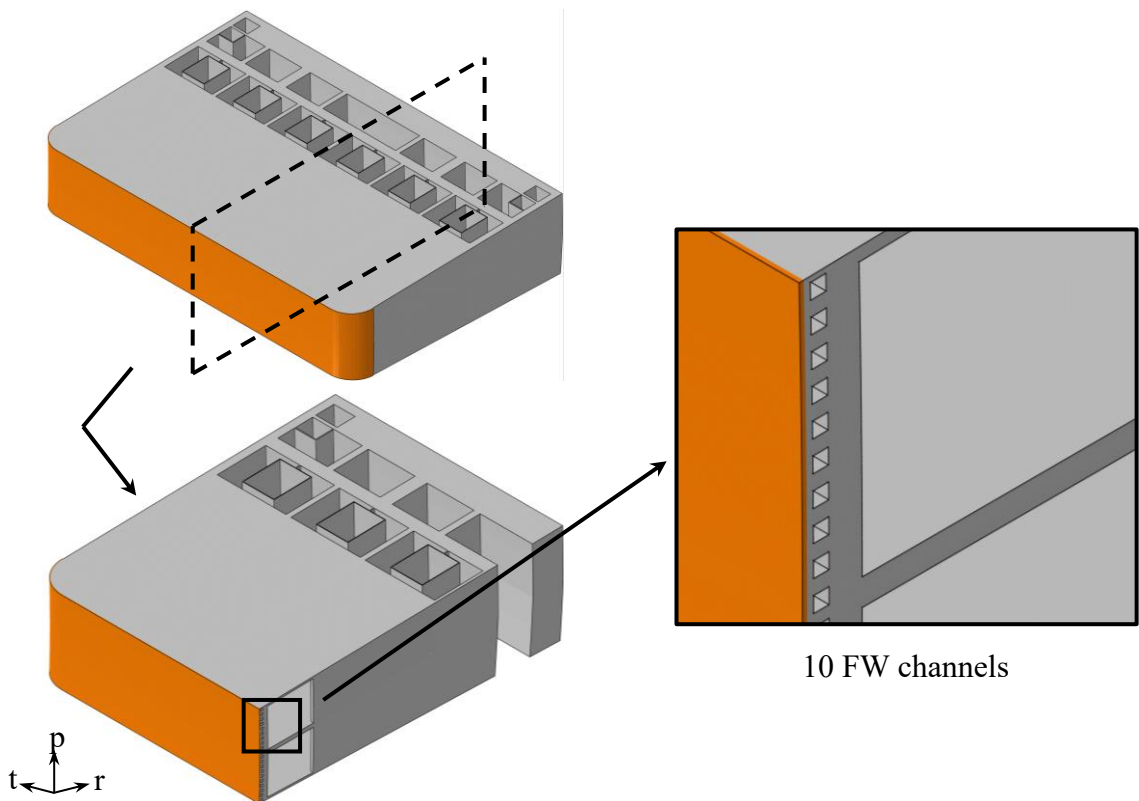


Figure 3.16 FW channels detail on Central Cells.

	Nodes	Elements
Central Cells	2473169	2135992
Bottom Cells	2142812	1833972
Top Cells	2831823	2458156

Table 3.4 Sub-model regions mesh detail.

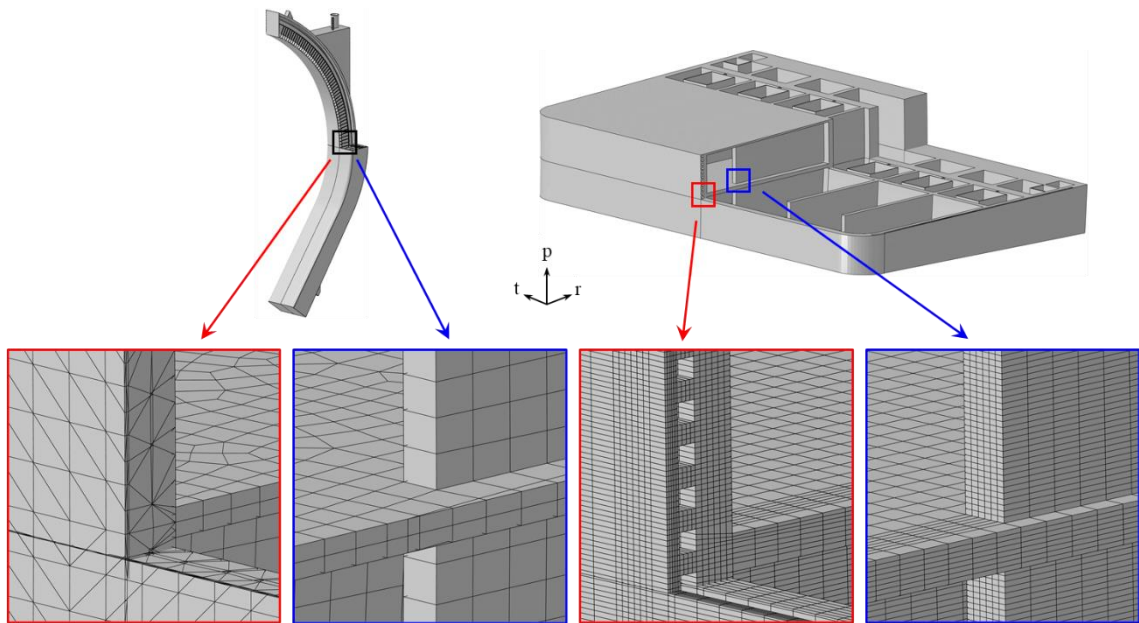


Figure 3.17 Details of global model and sub-model meshes.

3.4.1 Loads and Boundary Conditions

Mechanical loads and boundary conditions have been applied according to NO, OP and UVDE loading scenario investigated.

The non-uniform thermal deformation field arising within the model as a consequence of its thermal field (obtained by the interpolation procedure) and its isotropic thermal expansion tensor, has been implemented for each model (Figure 3.18).

Furthermore, during the NO and the UVDE scenarios, in order to simulate the action of the water flowing inside the FW channels and the manifolds water, a pressure equal to 17.825 MPa ($P_{des,coolant}$) have been imposed onto all the water-wetted surfaces, instead all the surfaces wetted by the breeder, a pressure of 0.575 MPa ($P_{des,breeder}$) have been set. Instead, concerning the OP loading scenario, representing an incidental scenario following an in-box Loss Of Coolant Accident, a pressure value of 17.825 MPa has been selected for all the aforementioned surfaces (Figure 3.19).

Additionally, in the same way as in the global model, EM loads have been considered for all the assessed scenarios. During the NO and OP scenarios, only the ferromagnetic loads have been taken into account. Instead, during the UVDE loading scenario both Lorentz's forces and ferromagnetic loads must be considered. So, the same two time-steps selected in the previous global analyses, corresponding to the maximum radial force and the maximum moment ($t = 11.52$ s and $t = 11.585$ s), have been chosen for the structural analysis of each sub-model.

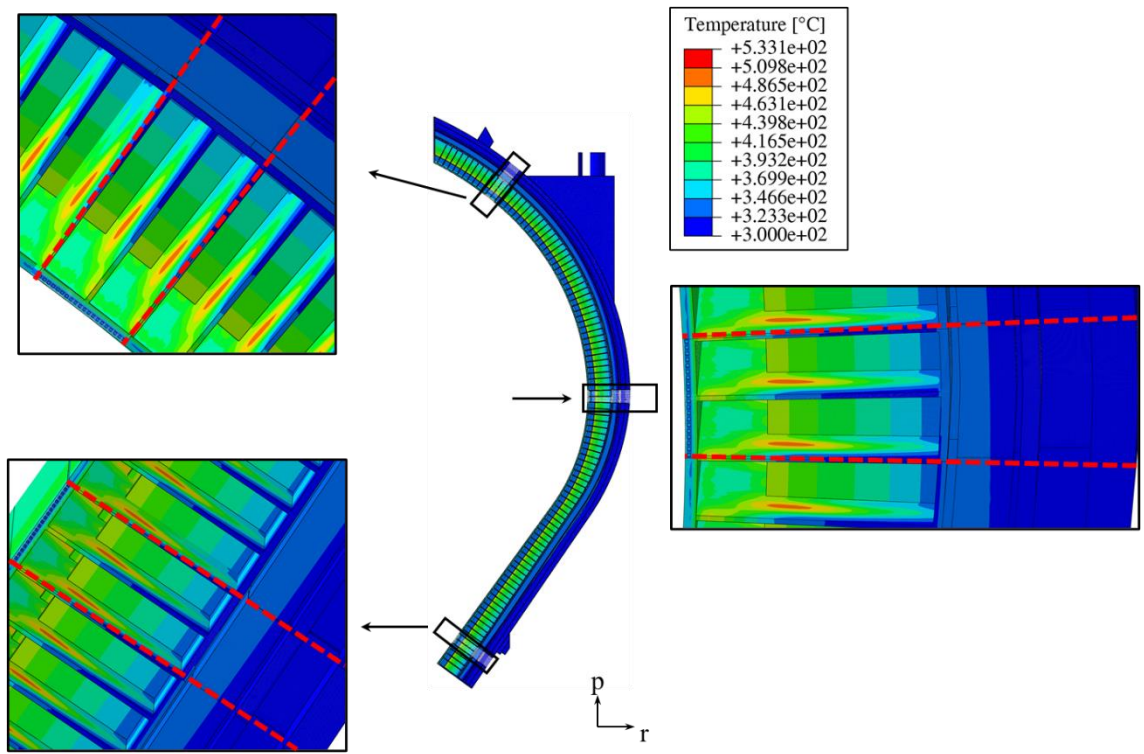


Figure 3.18 Interpolated thermal field imposed on each model.

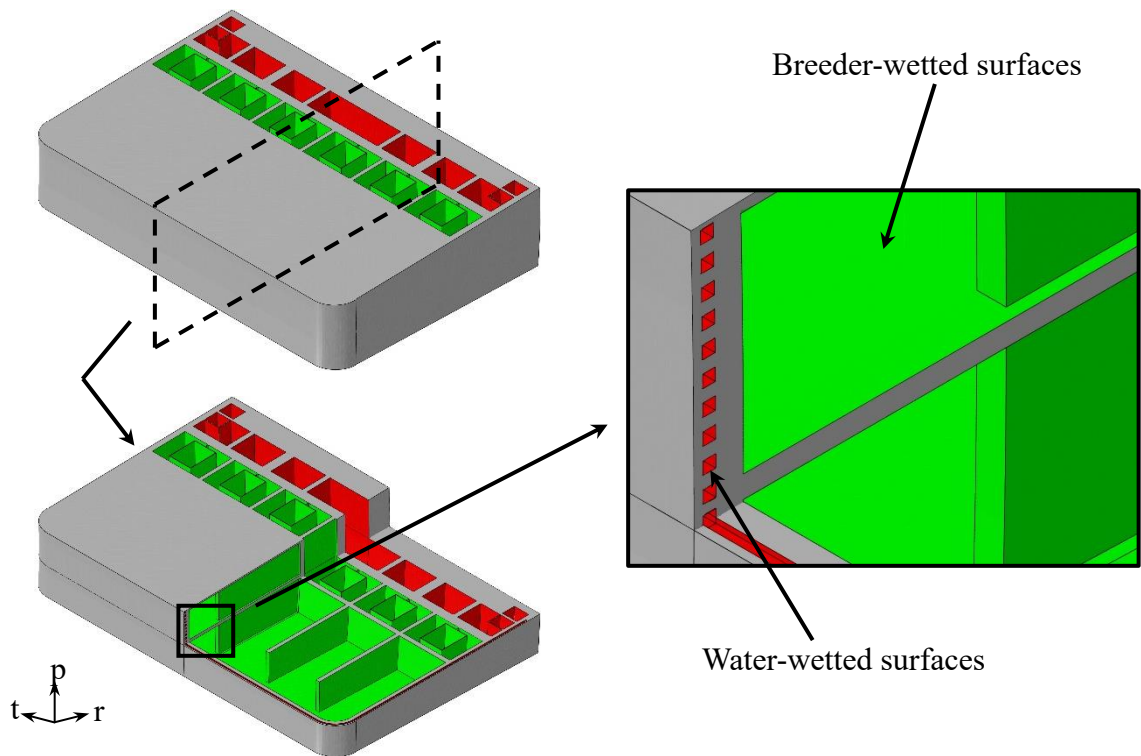


Figure 3.19 Water and breeder wetted surfaces.

The RAFM Eurofer steel has been assumed as the structural material, except for the 2 mm of Tungsten covered the FW (highlighted in orange in Fig. 3.12). For both materials, except for the tungsten density assumed constant and equal to 19300 kg/m^3 , their thermomechanical properties have been assumed temperature-dependent. As already done

for the COB segment, an Eurofer equivalent density has been calculated to simulate the presence of water and breeder inside the SB. So, the acceleration of gravity value has been imposed on the whole structure.

Finally, the sub-model boundary condition has been applied onto the nodes lying on the cutting surfaces of each local model. In this manner, all three degrees of freedom, that in a structural analysis are the three components of the displacement vector (U_x , U_y and U_z), are driven by the global model. As an example, in Figure 3.20, the displacement field imposed on the upper surface of the Central Cells sub-model in comparison to that obtained in the same region of the global model under NO loading condition is reported.

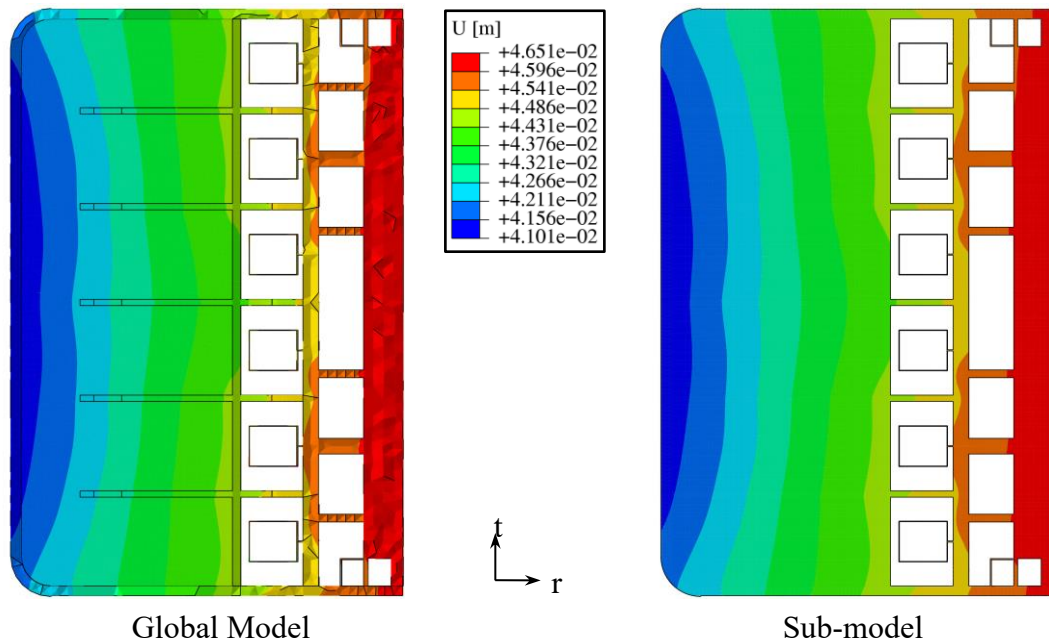


Figure 3.20 Displacement field under NO loading scenario on the upper surface of the CC in global model vs. sub-model.

3.4.2 Results

Steady state analyses have been conducted to investigate the structural response of the different COB region analysed with the sub-modelling technique, under the loads and boundary conditions characterizing three different loading scenarios: NO, OP and UVDE, the last evaluated at two different time-steps. So, the fulfilling of the design rules reported in the RCC-MRx structural code has been verified.

The Von Mises stress, shown in Figure 3.21, Figure 3.22, Figure 3.23 and Figure 3.24, and the displacement field, in Figure 3.25, Figure 3.26, Figure 3.27 and Figure 3.28, have been reported in comparison with to the global model. To this end, in each figure, the stress/displacement field calculated within each sub-model is superimposed to the analogous

field calculated from the global model. From this representation, it is possible to understand how the three regions investigated in detail show the same overall behaviour as the global model. Moreover, sub-model results allow observing details in the FW-SW region.

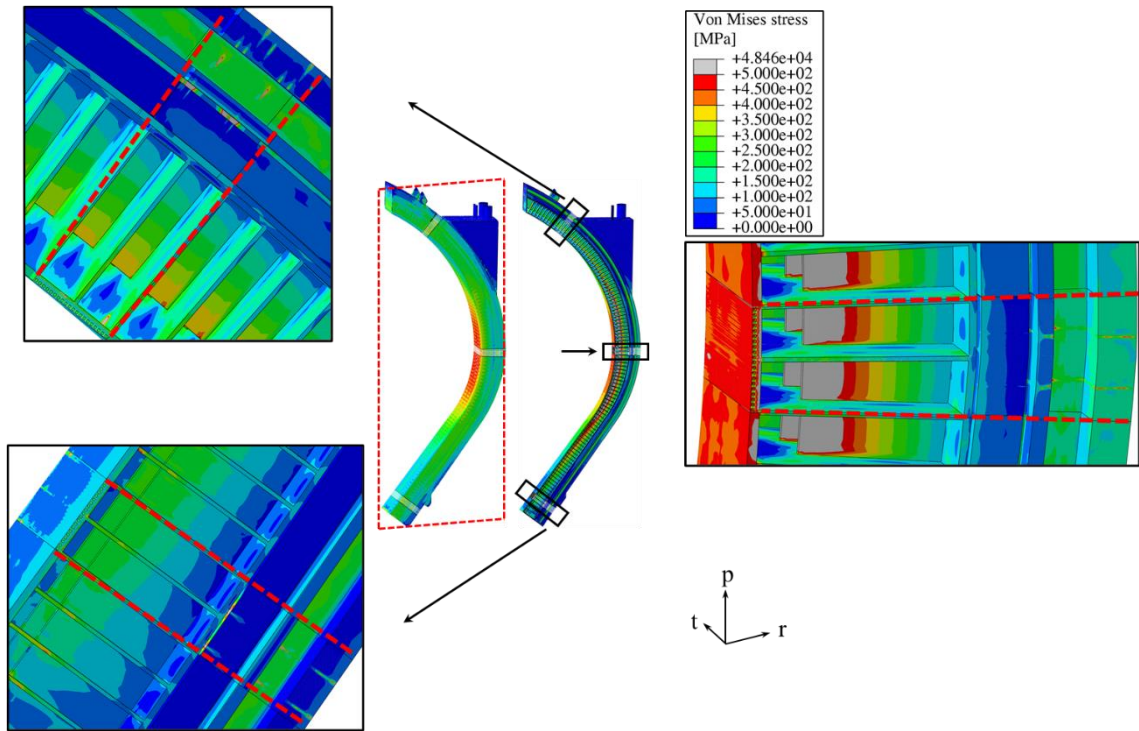


Figure 3.21 Von Mises stress field – NO on sub-models superimposed to global model.

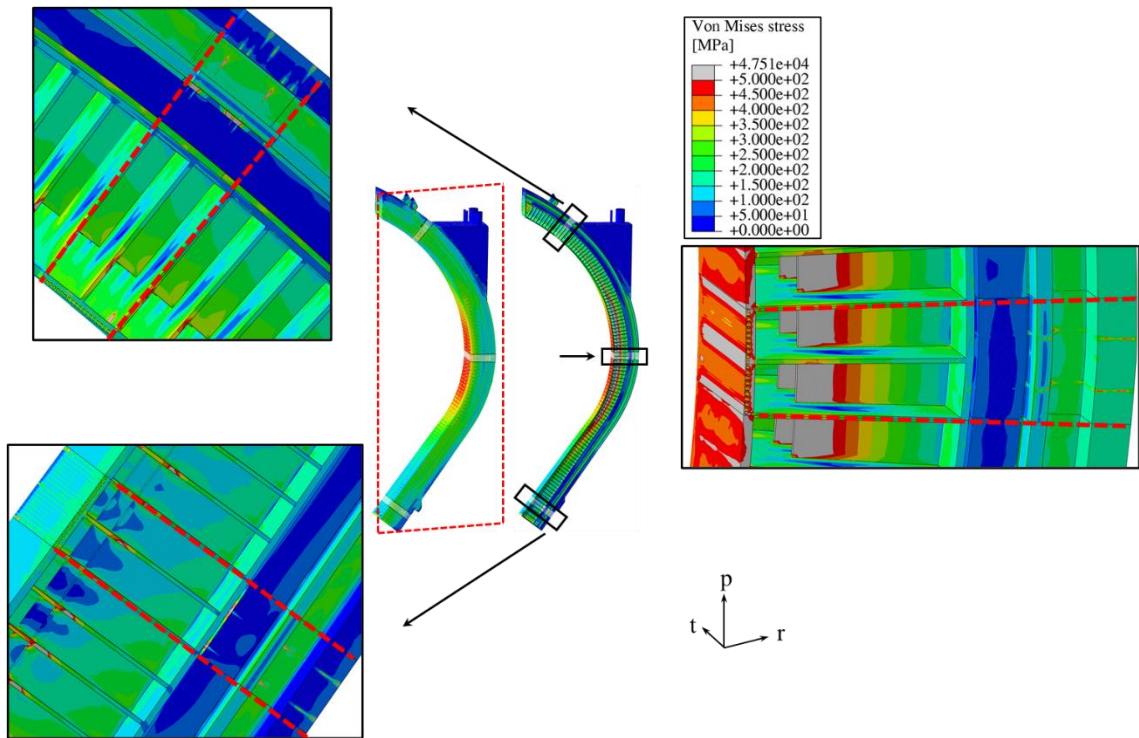


Figure 3.22 Von Mises stress field – OP on sub-models superimposed to global model.

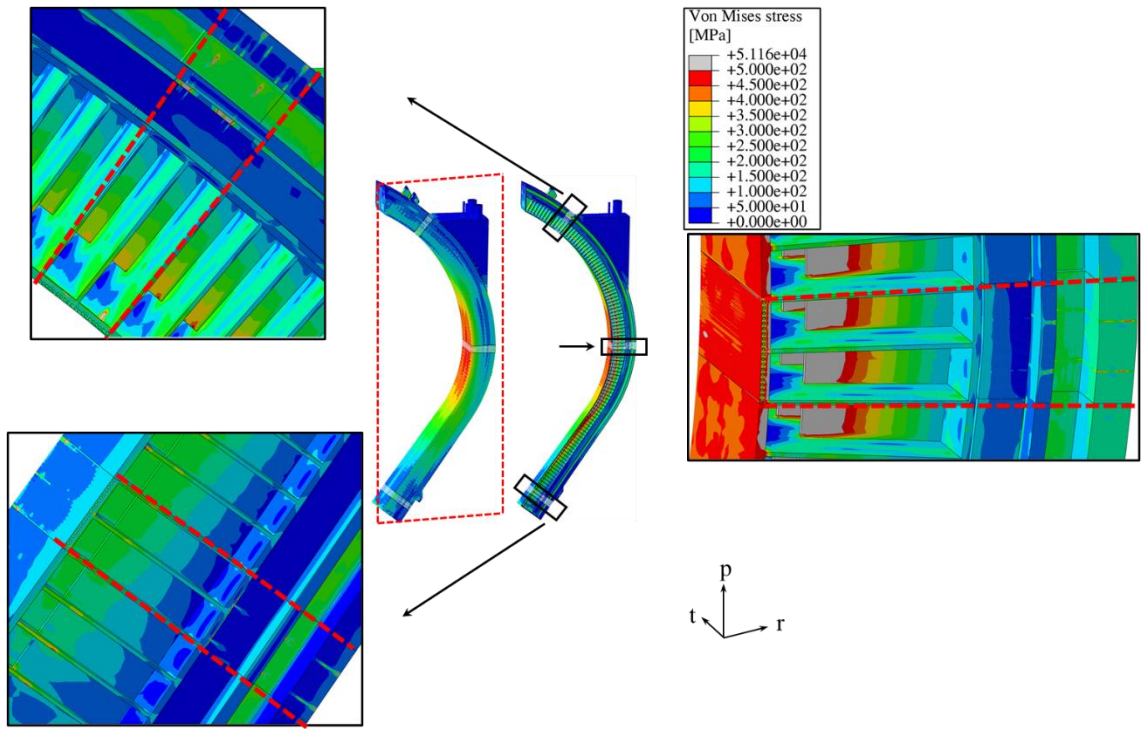


Figure 3.23 Von Mises stress field - UVDE (t=11.585 s) on sub-models superimposed to global model.

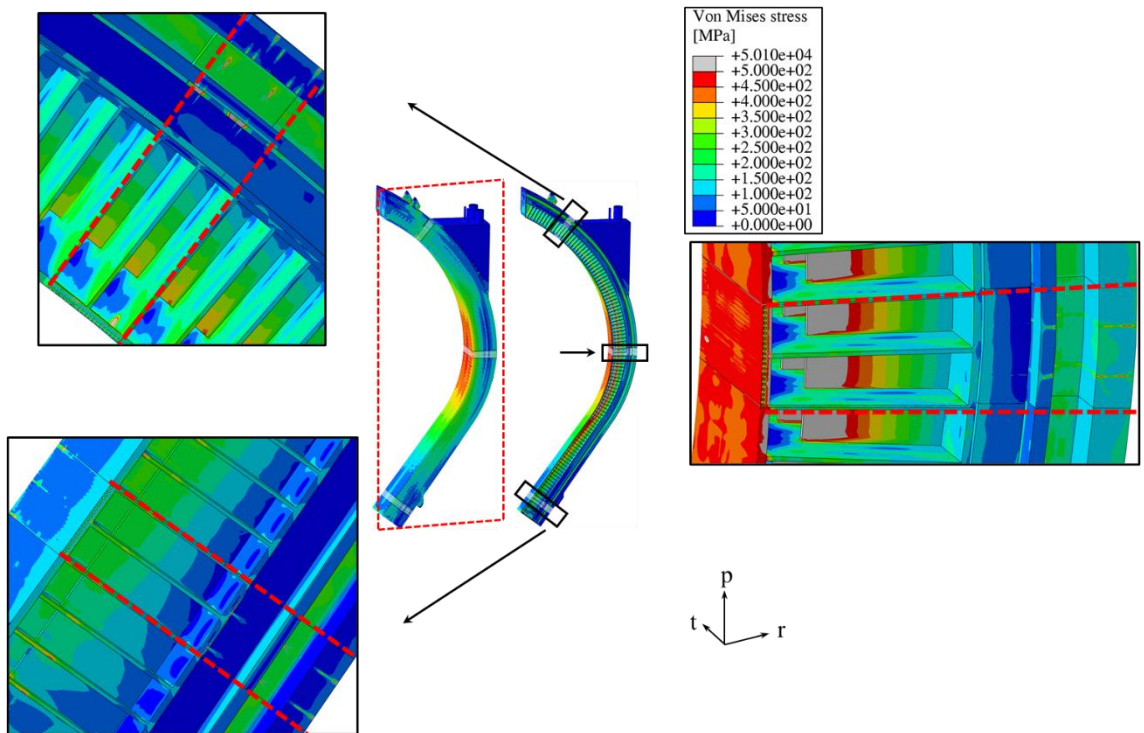


Figure 3.24 Von Mises stress field - UVDE (t=11.52 s) on sub-models superimposed to global model.

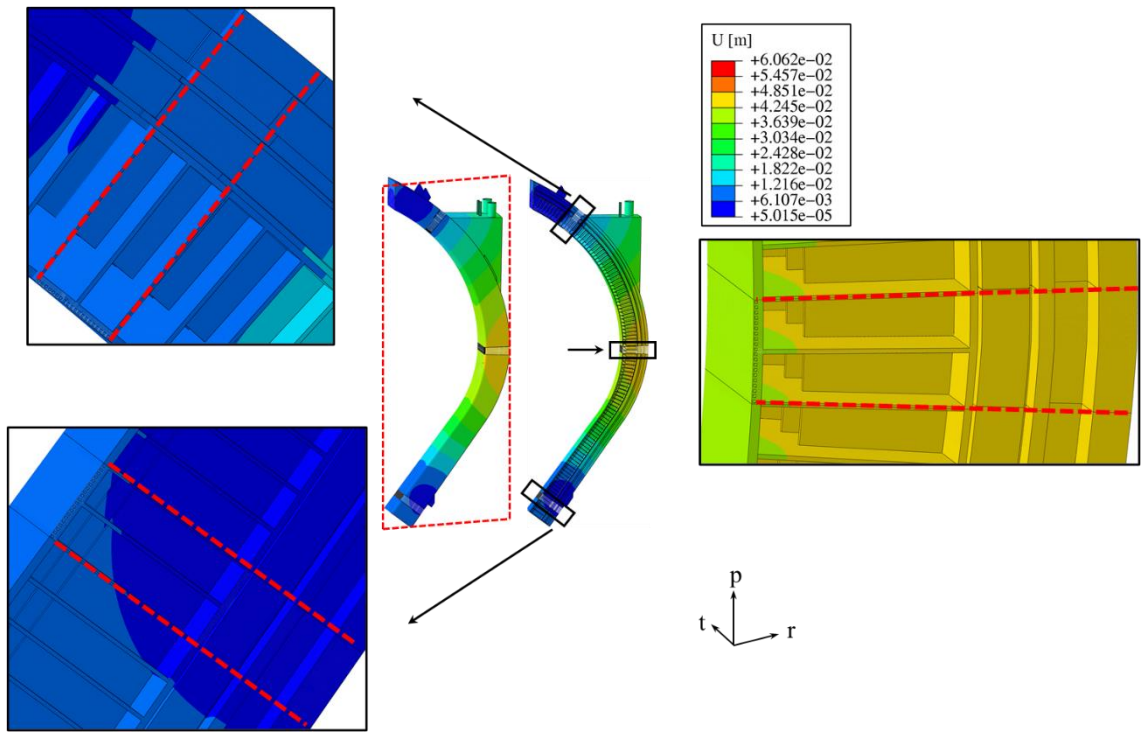


Figure 3.25 Total Displacements field – NO on sub-models superimposed to global model.

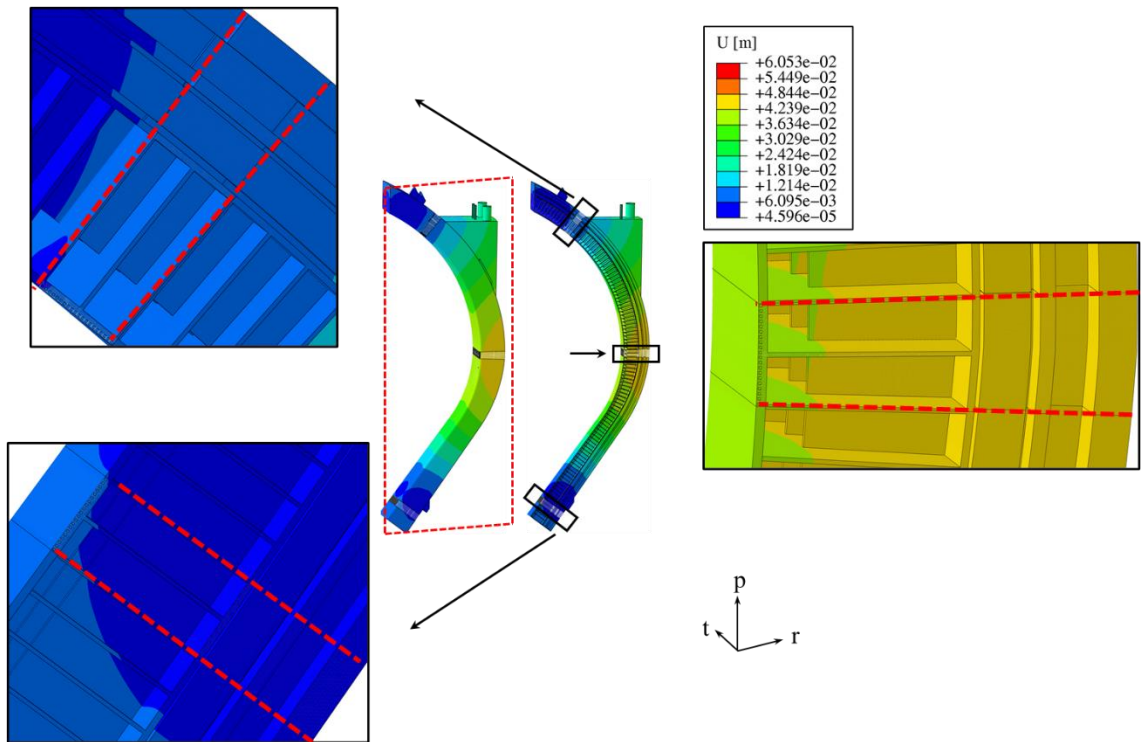


Figure 3.26 Total Displacements field – OP on sub-models superimposed to global model.

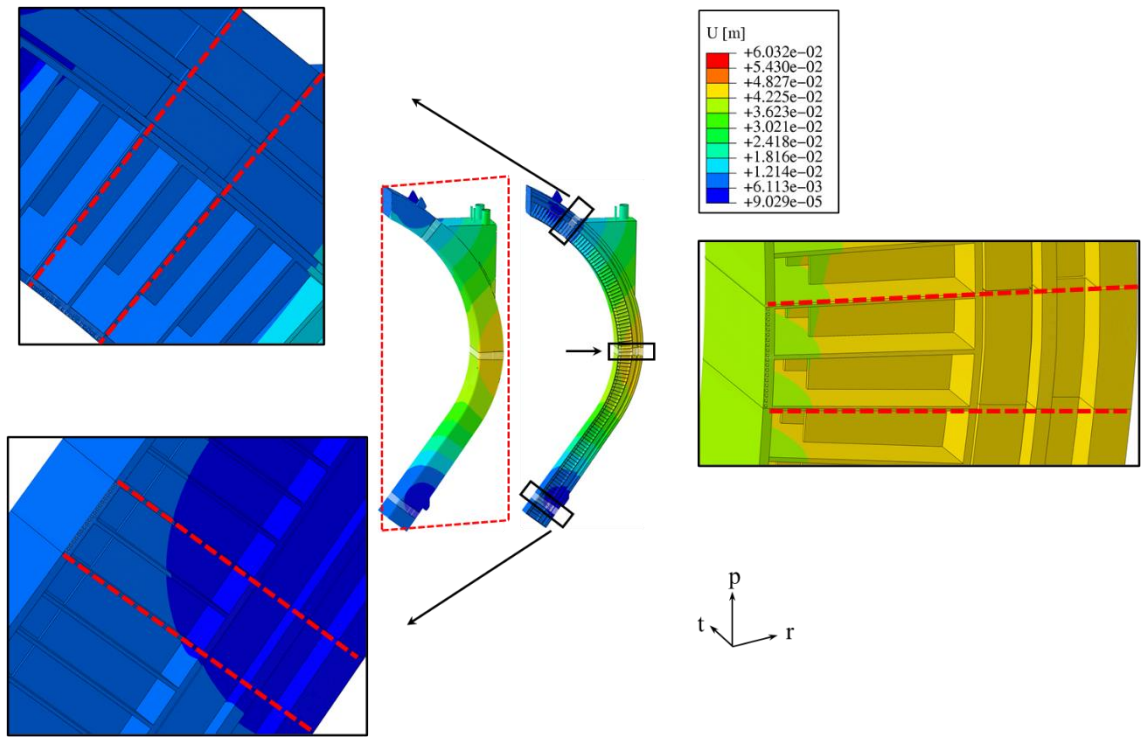


Figure 3.27 Total Displacements field - UVDE ($t=11.585$ s) on sub-models superimposed to global model.

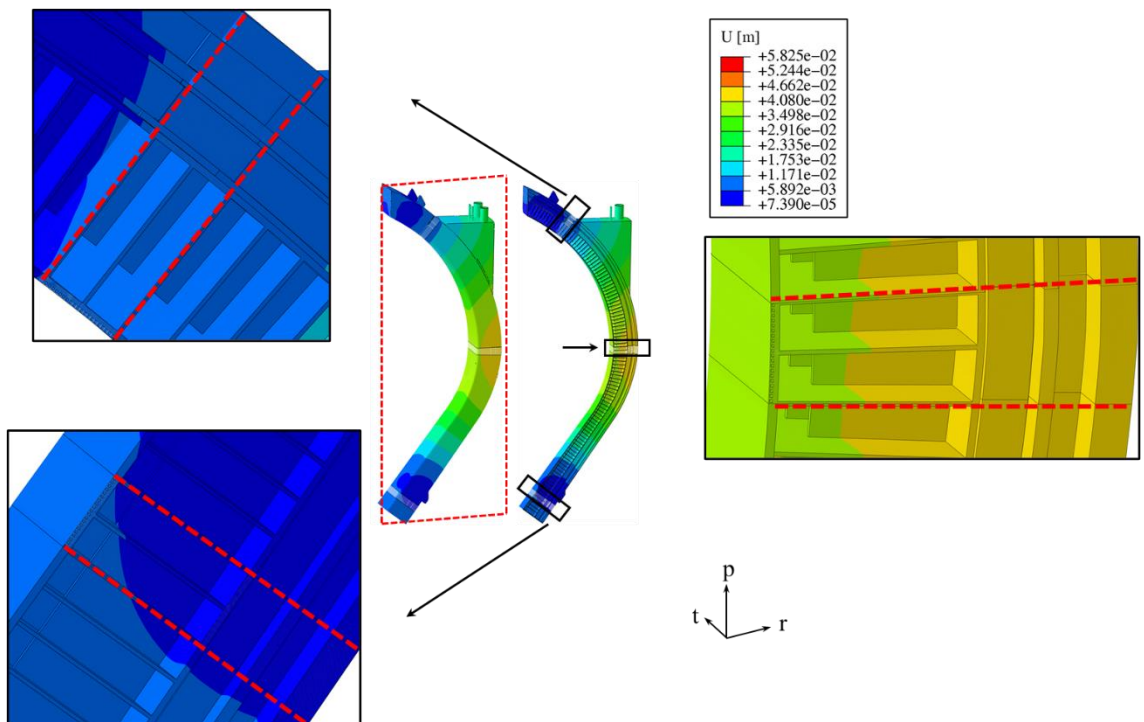


Figure 3.28 Total Displacements field - UVDE ($t=11.52$ s) on sub-models superimposed to global model.

With the aim of comparing the global model results with the sub-model results, a stress linearization procedure has been performed within two paths located on the toroidal-radial and two within poloidal-radial SPs, located in similar region as those reported in Figure 3.9.

The comparison between the stress linearization results obtained along the same paths identified in the global model and in the three sub-models are shown in Figure 3.29 to Figure 3.40, reporting the ratio between the equivalent stress value and the corresponding stress limit. Stress linearization results and the evaluation of the RCC-MRx criteria show that, in all the operative loading scenario assessed, for each path a very similar behaviour is obtained when the stresses are evaluated in the global model and in the sub-model.

The percentage errors of the ratio, previously defined, for each criterion is reported in Table 3.5, Table 3.6 and Table 3.7. Such percentage of error is calculated as the difference between the ratio value assessed within each path in the global model analysis and in the sub-models divided by the first. In particular, percentage errors are sometimes very high because the results are strongly dependent on the density of the grid used but it can be observed that the highest values of percentage error are predicted where the ratio values are the lowest. Globally, the results show that the thermo-mechanical behaviour derived by the analysis of the entire model provides a reliable response in terms of design criteria verification when compared with a more in-depth analysis performed by means of the sub-modelling technique.

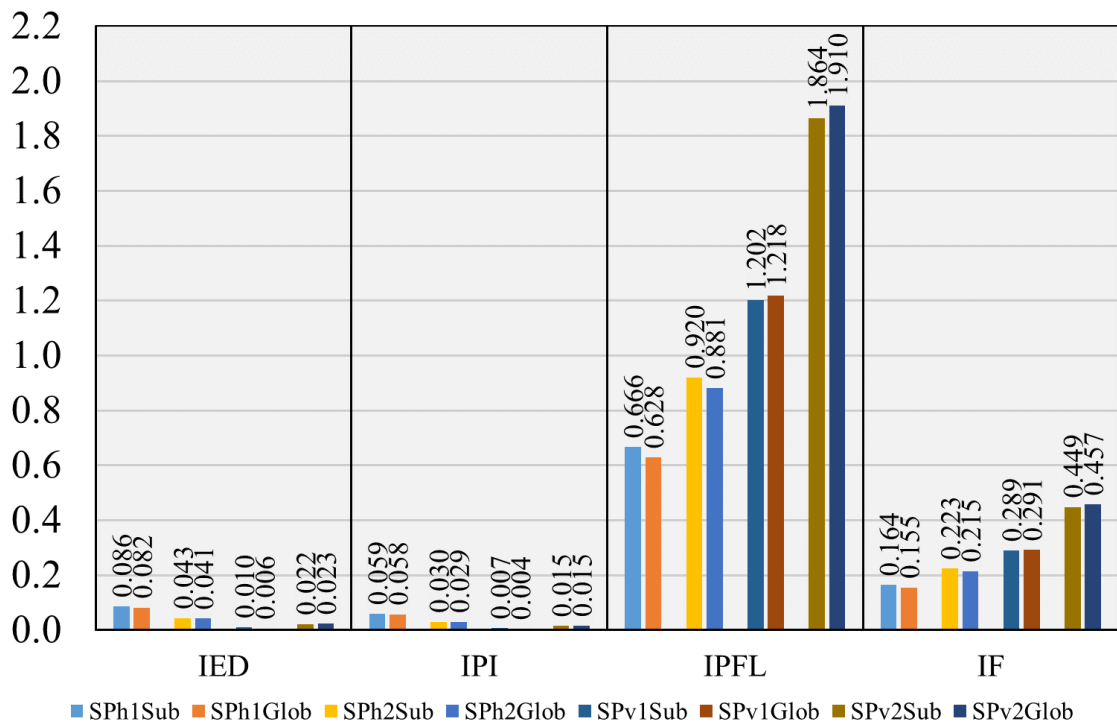


Figure 3.29 Comparison RCC-MRx criteria on CC - NO.

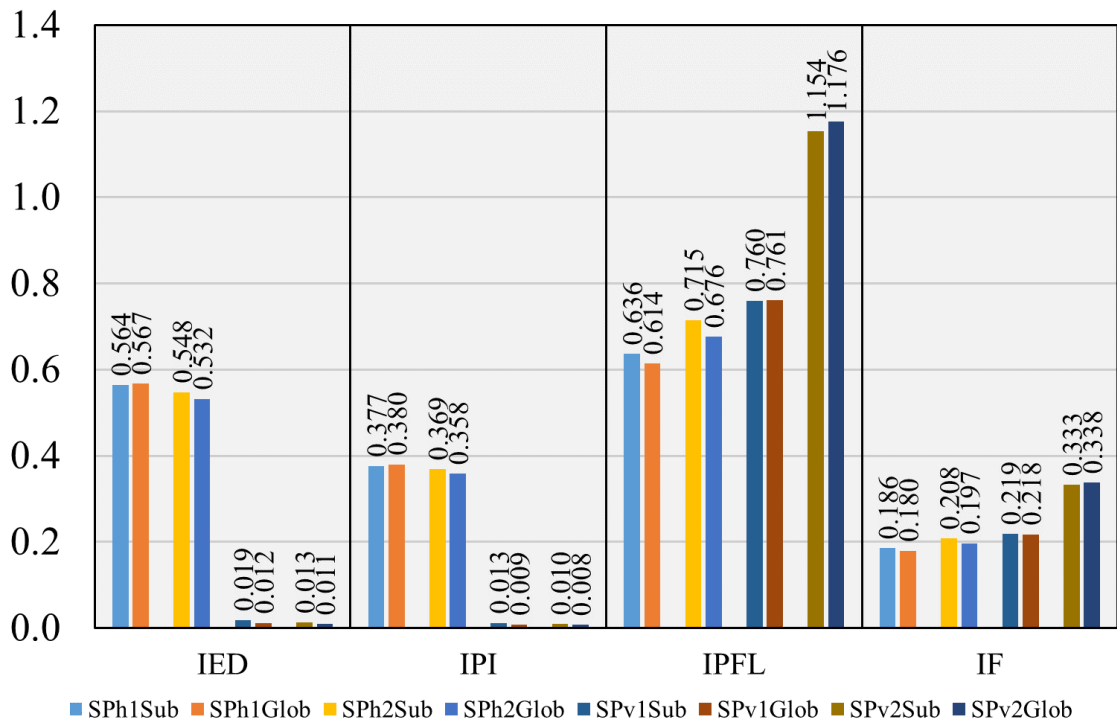


Figure 3.30 Comparison RCC-MRx criteria on CC - OP.

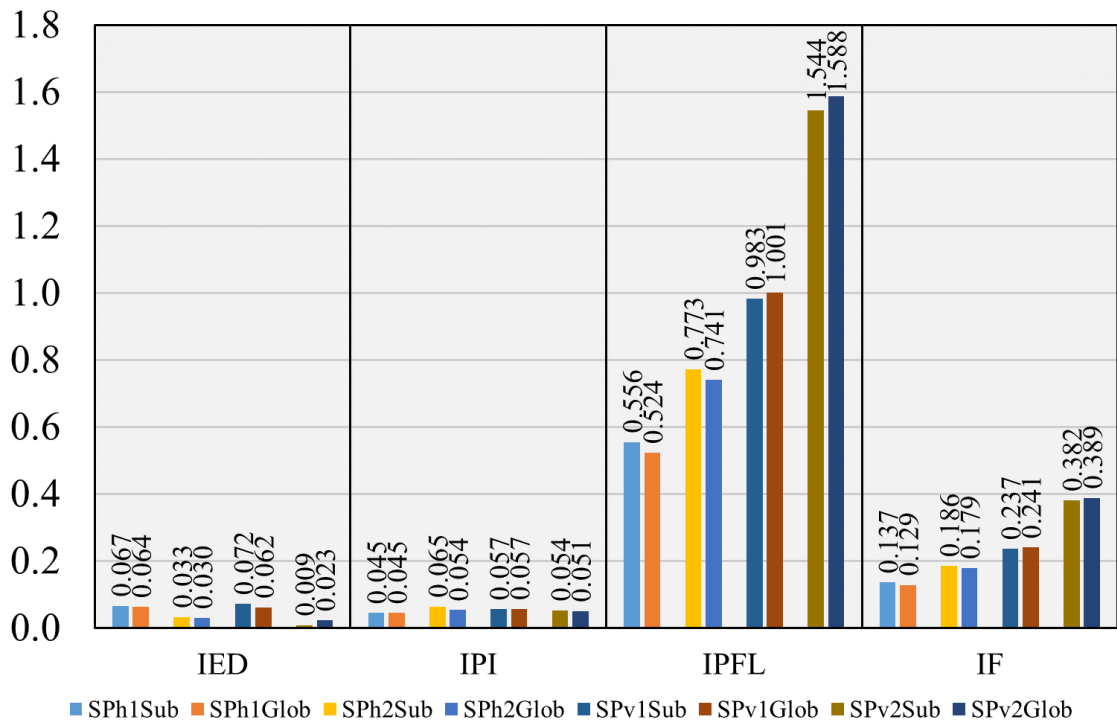


Figure 3.31 Comparison RCC-MRx criteria on CC - UVDE (t=11.585 s).

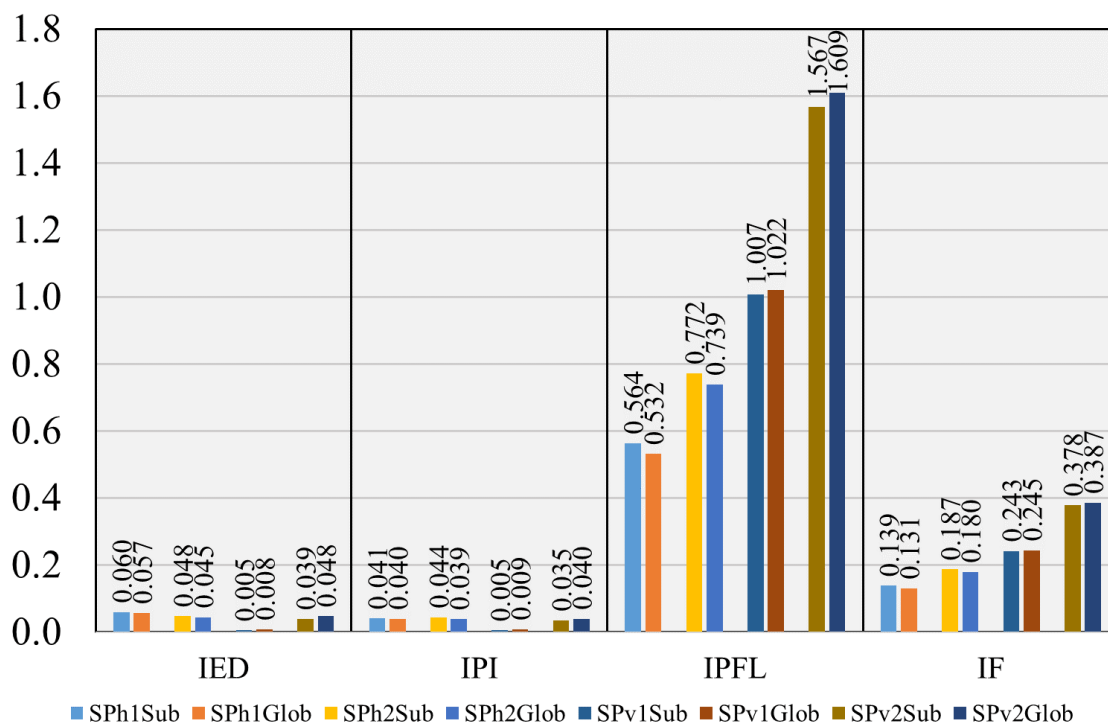


Figure 3.32 Comparison RCC-MRx criteria on CC - UVDE (t=11.52 s).

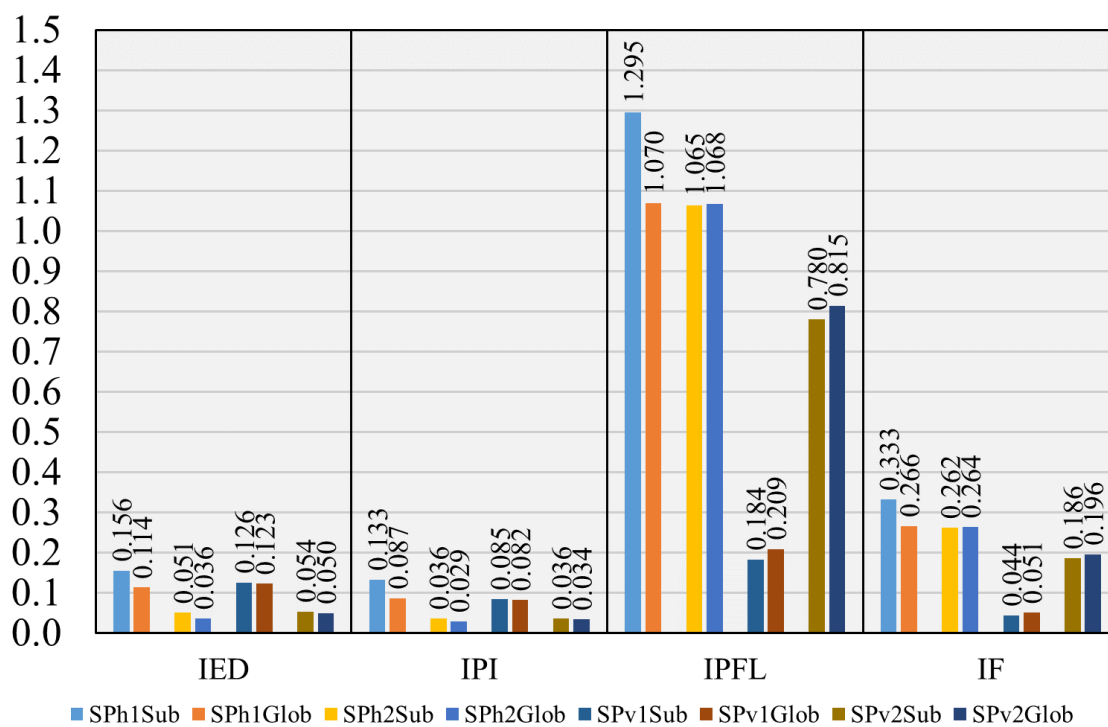


Figure 3.33 Comparison RCC-MRx criteria on BC - NO.

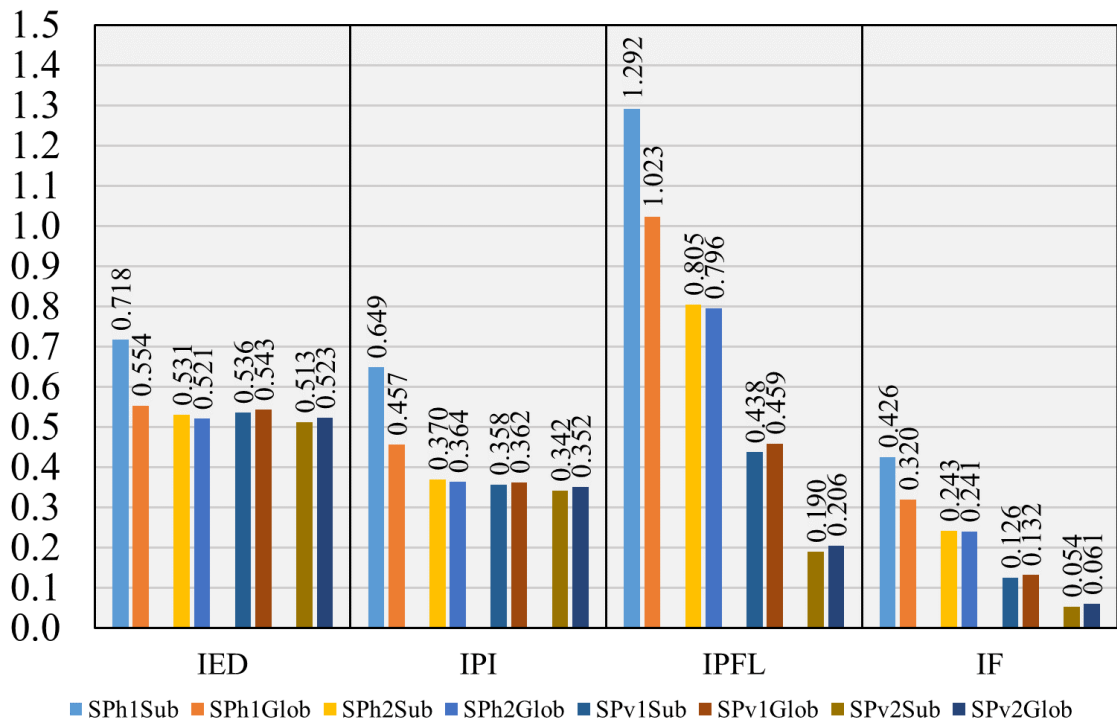


Figure 3.34 Comparison RCC-MRx criteria on BC - OP.

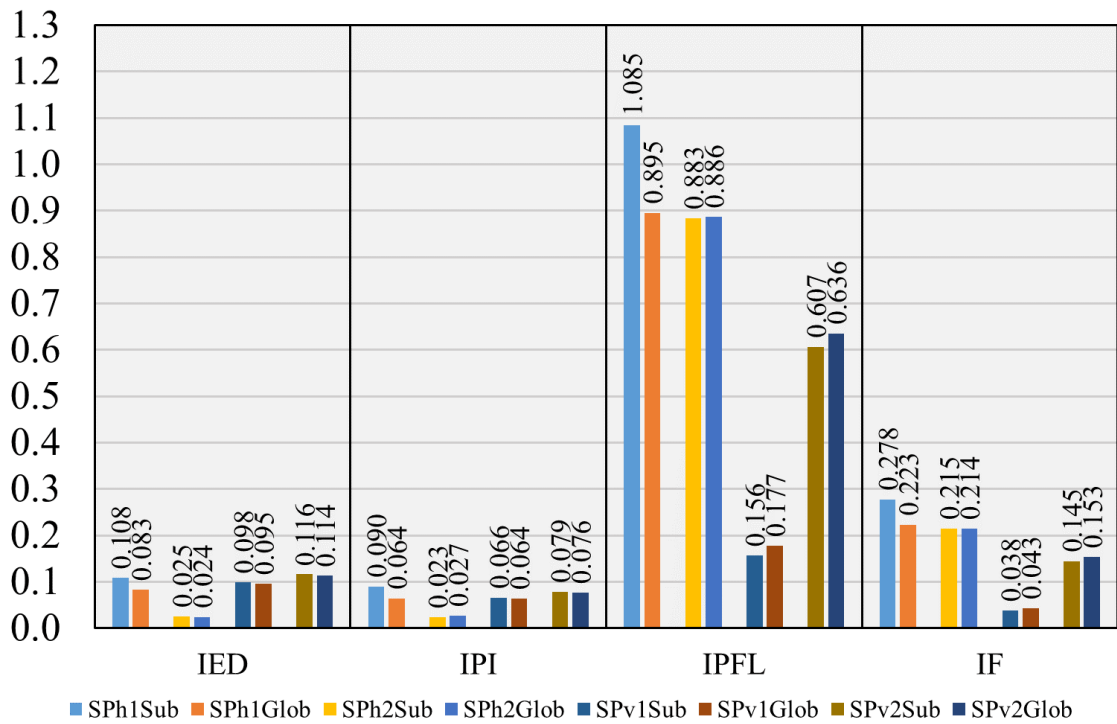


Figure 3.35 Comparison RCC-MRx criteria on BC - UVDE (t=11.585 s).

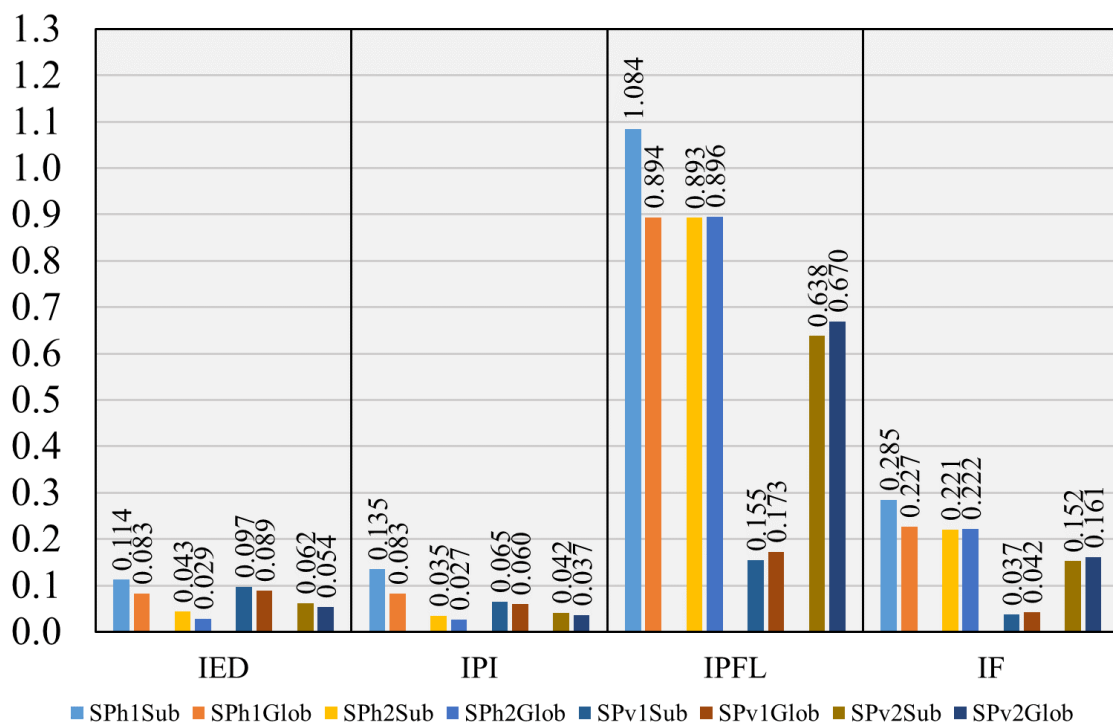


Figure 3.36 Comparison RCC-MRx criteria on BC - UVDE (t=11.52 s).

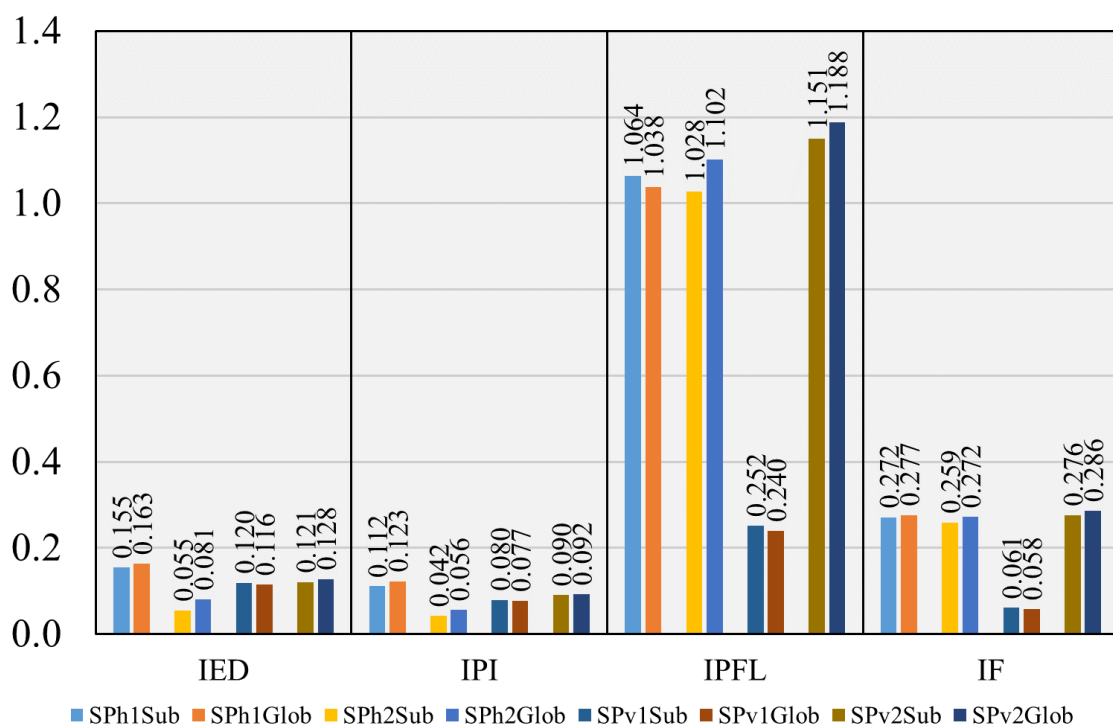


Figure 3.37 Comparison RCC-MRx criteria on TC - NO.

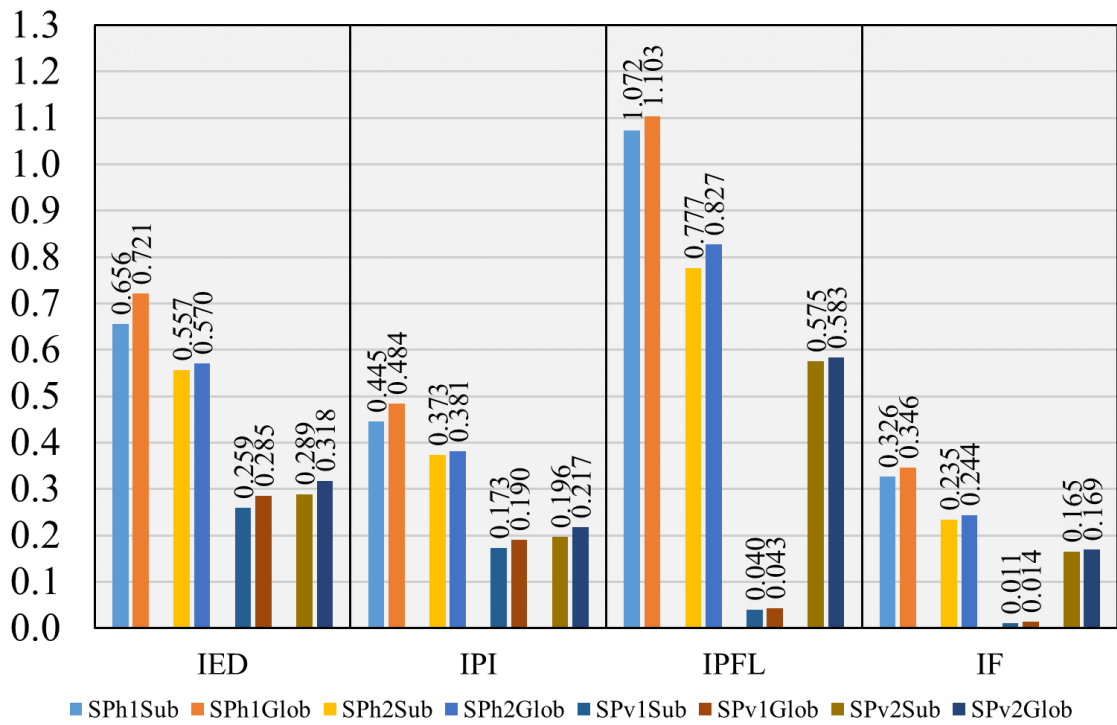


Figure 3.38 Comparison RCC-MRx criteria on TC - OP.

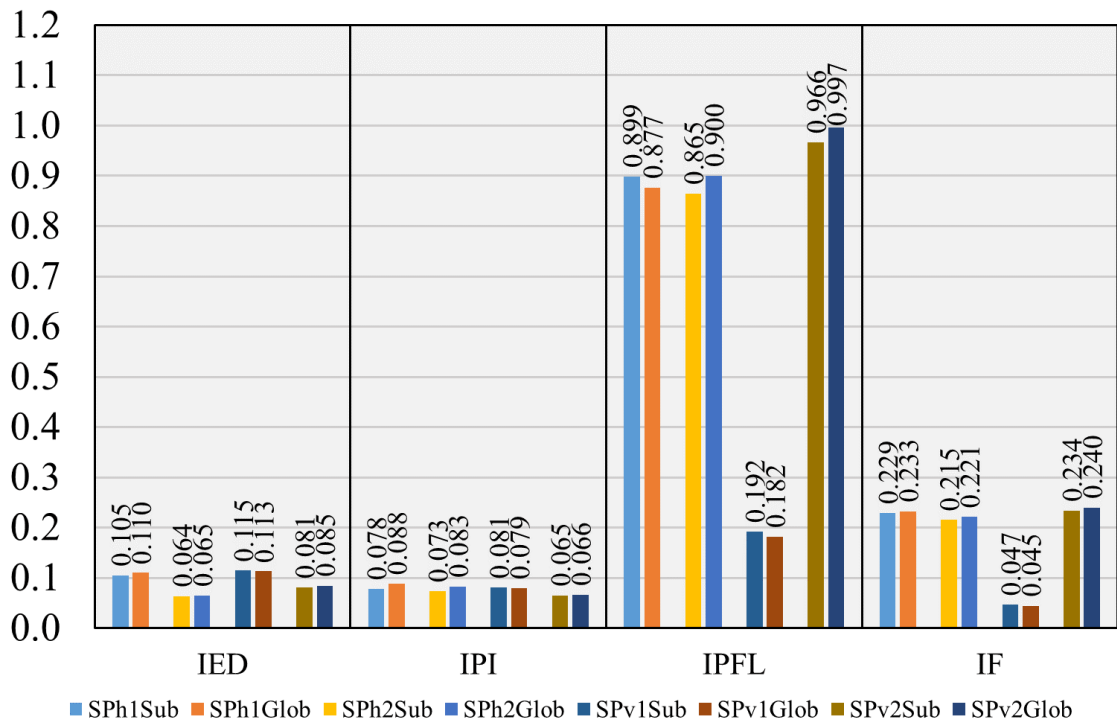


Figure 3.39 Comparison RCC-MRx criteria on TC - UVDE (t=11.585 s).

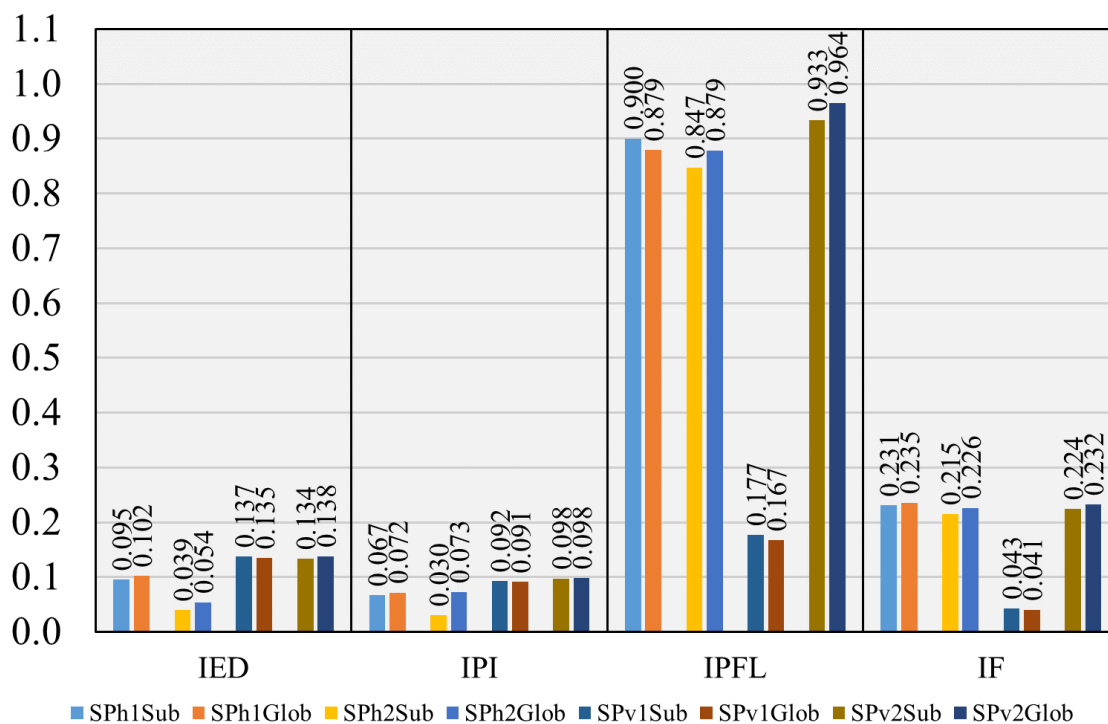


Figure 3.40 Comparison RCC-MRx criteria along on TC - UVDE (t=11.52 s).

NO				
Path	E%(IED)	E%(IPI)	E%(IPFL)	E%(IF)
SPh1	4.89%	2.17%	6.06%	5.92%
SPh2	4.85%	1.36%	4.42%	4.08%
SPv1	67.44%	60.85%	1.35%	0.79%
SPv2	5.34%	4.55%	2.39%	1.89%
OP				
Path	E%(IED)	E%(IPI)	E%(IPFL)	E%(IF)
SPh1	0.49%	1.04%	3.62%	3.26%
SPh2	2.90%	2.90%	5.68%	5.42%
SPv1	49.18%	44.84%	0.19%	0.36%
SPv2	26.15%	24.97%	1.83%	1.41%
UVDE t=11.52 S				
Path	E%(IED)	E%(IPI)	E%(IPFL)	E%(IF)
SPh1	5.33%	2.06%	5.98%	5.82%
SPh2	6.53%	13.94%	4.53%	4.04%
SPv1	40.06%	40.25%	1.44%	0.88%
SPv2	17.54%	12.13%	2.65%	2.09%
UVDE t=11.585 S				
Path	E%(IED)	E%(IPI)	E%(IPFL)	E%(IF)
SPh1	5.34%	0.20%	6.06%	5.67%
SPh2	10.48%	19.70%	4.26%	3.56%
SPv1	16.86%	1.21%	1.71%	1.59%
SPv2	59.86%	4.68%	2.75%	1.88%

Table 3.5 RCC-MRx criteria percentage errors global model vs sub-model in CC.

NO				
Path	E%(IED)	E%(IPI)	E%(IPFL)	E%(IF)
SPh1	36.49%	53.02%	21.07%	24.92%
SPh2	40.58%	25.06%	0.29%	0.58%
SPv1	2.83%	2.76%	12.32%	12.49%
SPv2	7.72%	5.75%	4.22%	4.92%
OP				
Path	E%(IED)	E%(IPI)	E%(IPFL)	E%(IF)
SPh1	29.55%	42.00%	26.36%	32.95%
SPh2	1.98%	1.82%	1.17%	0.65%
SPv1	1.31%	1.32%	4.76%	4.69%
SPv2	1.94%	2.58%	7.49%	10.65%
UVDE t=11.52 s				
Path	E%(IED)	E%(IPI)	E%(IPFL)	E%(IF)
SPh1	36.69%	63.33%	21.24%	25.65%
SPh2	50.67%	29.41%	0.32%	0.62%
SPv1	9.31%	8.97%	10.37%	10.69%
SPv2	15.67%	13.42%	4.75%	5.51%
UVDE t=11.585 s				
Path	E%(IED)	E%(IPI)	E%(IPFL)	E%(IF)
SPh1	30.77%	39.91%	21.15%	24.48%
SPh2	4.89%	13.33%	0.31%	0.10%
SPv1	3.20%	3.17%	11.91%	11.77%
SPv2	2.25%	2.87%	4.56%	5.43%

Table 3.6 RCC-MRx criteria percentage errors global model vs sub-model in BC.

Thanks to the application of the sub-modelling technique, the FW-SW region has been studied in depth, unlike the global model in which the structural behaviour of this region has not been studied because the cooling channels absence.

Therefore, a stress linearization procedure has been carried out along some paths located in the most critical FW-SW regions and the design criteria foreseen by RCC-MRx structural codes have been checked along these paths in all the assessed operative loading scenarios. In particular, Figure 3.41 shows the paths identified along FW and SW regions, nearby the cooling channels, in the Central Cells sub-model. The same criterion for the selection of the central region paths has been adopted to individuate the paths in the upper and lower regions of the COB segment.

The fulfilment of four RCC-MRx design criteria, Immediate Excessive Deformation (IED), Immediate Plastic Instability (IPI), Immediate Plastic Flow Localization (IPFL) and Immediate Fracture due to exhaustion of ductility (IF), have been selected to study the structural behaviour of the segment under the loads and boundary condition characterizing every analysed loading scenario.

NO				
Path	E%(IED)	E%(IPI)	E%(IPFL)	E%(IF)
SPh1	5.33%	9.34%	2.54%	1.84%
SPh2	31.99%	24.45%	6.76%	4.60%
SPv1	3.15%	2.98%	4.93%	5.67%
SPv2	5.11%	2.06%	3.11%	3.38%
OP				
Path	E%(IED)	E%(IPI)	E%(IPFL)	E%(IF)
SPh1	9.06%	7.93%	2.83%	5.62%
SPh2	2.35%	2.10%	6.07%	3.90%
SPv1	9.07%	9.05%	6.96%	15.63%
SPv2	9.11%	9.61%	1.26%	2.07%
UVDE t=11.52 s				
Path	E%(IED)	E%(IPI)	E%(IPFL)	E%(IF)
SPh1	6.27%	7.17%	2.43%	2.10%
SPh2	26.81%	58.46%	3.58%	5.04%
SPv1	2.06%	1.79%	5.81%	6.36%
SPv2	3.17%	0.36%	3.22%	3.44%
UVDE t=11.585 s				
Path	E%(IED)	E%(IPI)	E%(IPFL)	E%(IF)
SPh1	4.55%	11.54%	2.53%	1.62%
SPh2	1.39%	11.64%	3.91%	2.70%
SPv1	1.89%	1.60%	5.49%	4.32%
SPv2	4.54%	1.73%	3.06%	2.48%

Table 3.7 RCC-MRx criteria percentage errors global model vs sub-model in BC.

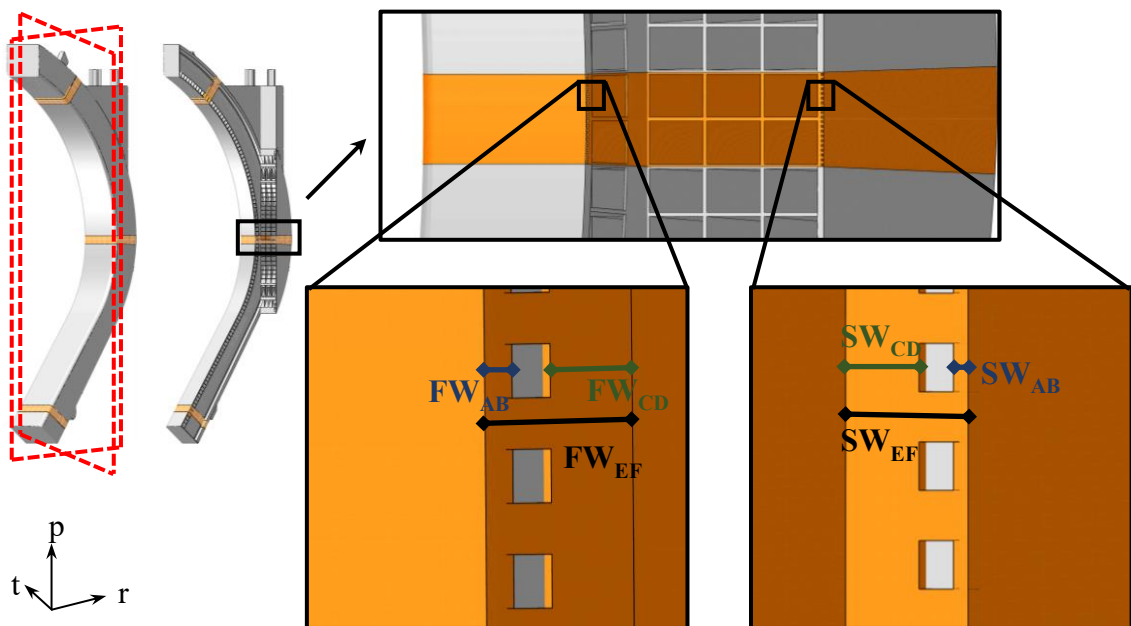


Figure 3.41 Paths within FW and SW in CC.

Mechanical results, reported in Figure 3.42, Figure 3.43, Figure 3.44 and Figure 3.45, highlight that the equatorial region of the COB is the most critical area and almost all criteria reach or exceed the stress limits values recommended by the code for the selected structural material in all the assessed scenarios along the paths located within the FW. This behaviour is attributable to the large radial displacement that the segment undergoes in the equatorial region, as seen in the global model analysis (Figure 3.5, Figure 3.6, Figure 3.7 and Figure 3.8). In particular, all paths located within the FW of the Central Cells do not fulfil the IPFL criterion, which takes into account the thermal stresses, or reach the design limit value in the best cases. On the other hand, the RCC-MRx criteria evaluated along the same paths located in TC and BC do not show critical values and are fulfilled in each operating scenario. In the OP loading scenario, representing an accidental scenario following a coolant leak, globally almost all paths fulfil the criteria, except for the paths within the FW in the equatorial region of the segment and some paths within the SWs which are close to (>0.8) or slightly exceed the critical value of the IPFL criterion. The evaluation of the RCC-MRx design criteria along the paths identified within SWs region, instead, shows that almost all the ratio values, namely the ratio between the equivalent stress value and the corresponding stress limit, remain widely below the limit of 1.

In general, it can be stated that the in-depth study of SB regions that have been simplified in the global model (i.e., the FW-SW region) is possible thanks to the sub-modelling technique, instead the thermomechanical response of the SPs is rather similar in both analyses and is therefore not strictly dependent on the mesh used. Thus, the structural behaviour of the SPs can be predicted with good accuracy already in the global model analyses and, therefore, it is not necessary to study them in detail in the sub-models' analyses. For this reason, a model with a coarser mesh within the SPs can be adopted in the sub-model, while it is possible to increase the mesh density in particular regions, as the FW-SW, in order to reduce the computational burden and, at the same time, obtain reliable results.

This results, which have a similar trend to those on the SPs, suggest a revision of the attachment system of the COB to the Vacuum Vessel to reduce the radial displacement of the COB equatorial region while reacting to the thermal deformation the segment undergoes. Moreover, further analyses aimed to investigate the COB segment with a more accurate thermal stress field must be performed. Indeed, the thermal field originated by the interpolation procedure takes origin from the thermal analysis of the only equatorial region of the WCLL COB. In principle, this procedure can be extended in order to perform thermal analysis of different regions at various poloidal positions, deriving different sets of

interpolating functions to be joined and applied together to even better describe the thermal field in the whole segment. The developed multiscale procedure presented, allowing firstly to perform local thermal assessments, then to export them on a large scale and finally to return to the local models for detailed mechanical analyses. In the next chapter, the multiscale procedure has been further refined and then applied for the thermomechanical assessment of the up-to-date geometry of the WCLL COB segment.

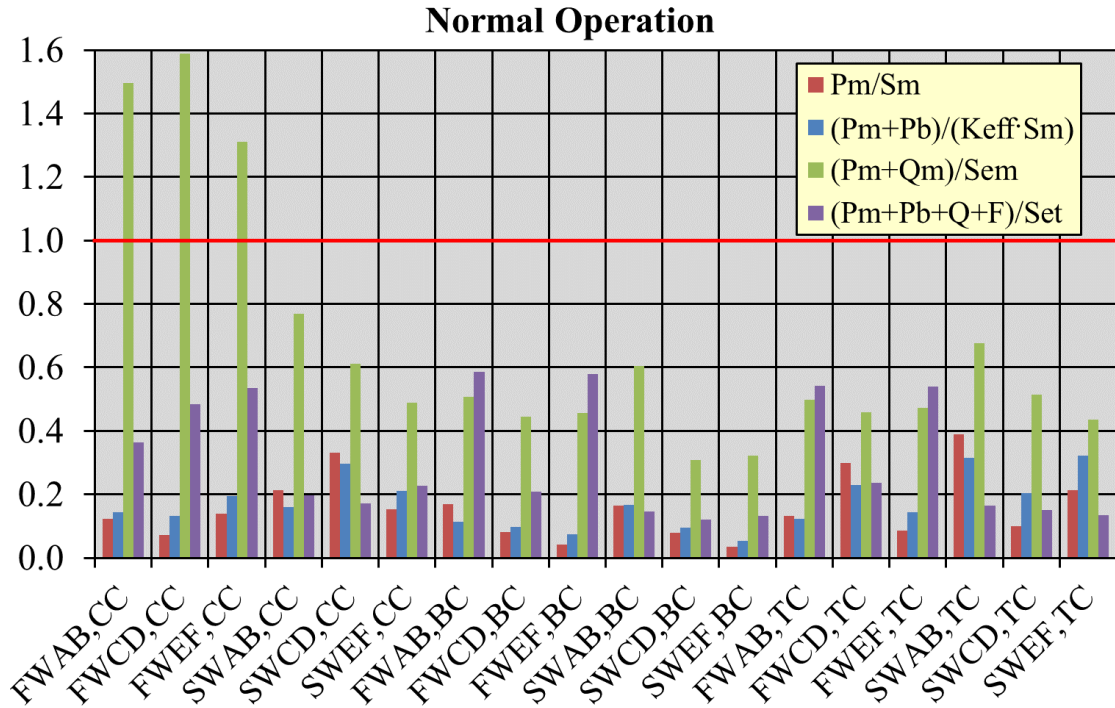


Figure 3.42 Stress linearization results under NO loading scenario.

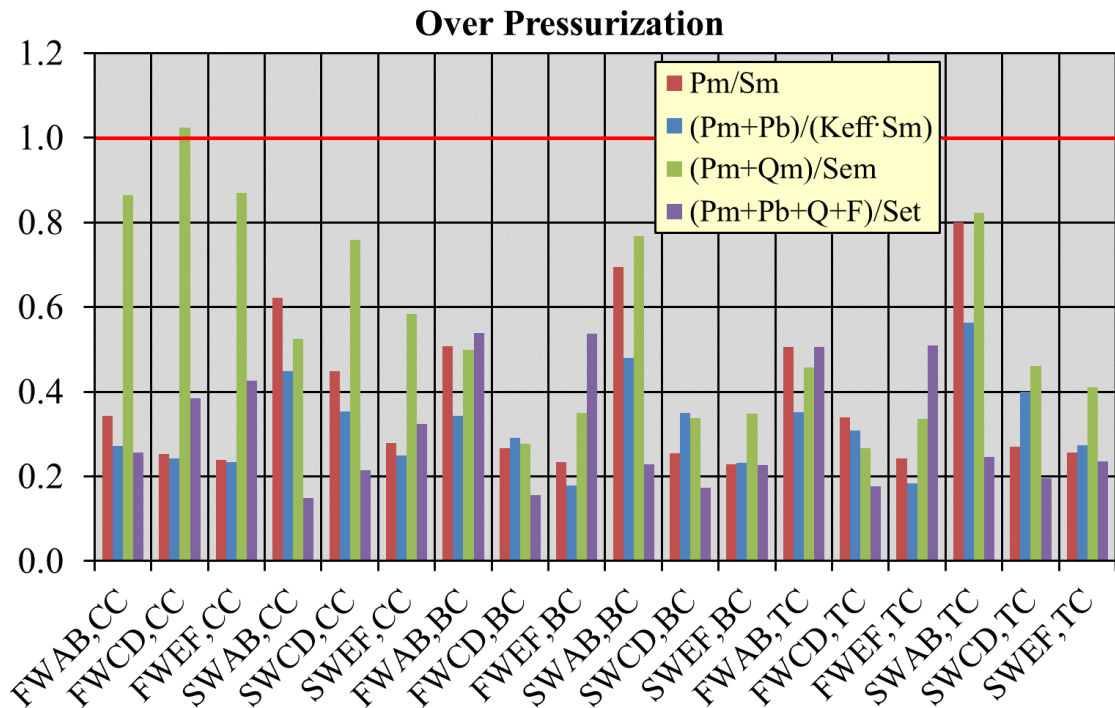


Figure 3.43 Stress linearization results under OP loading scenario.

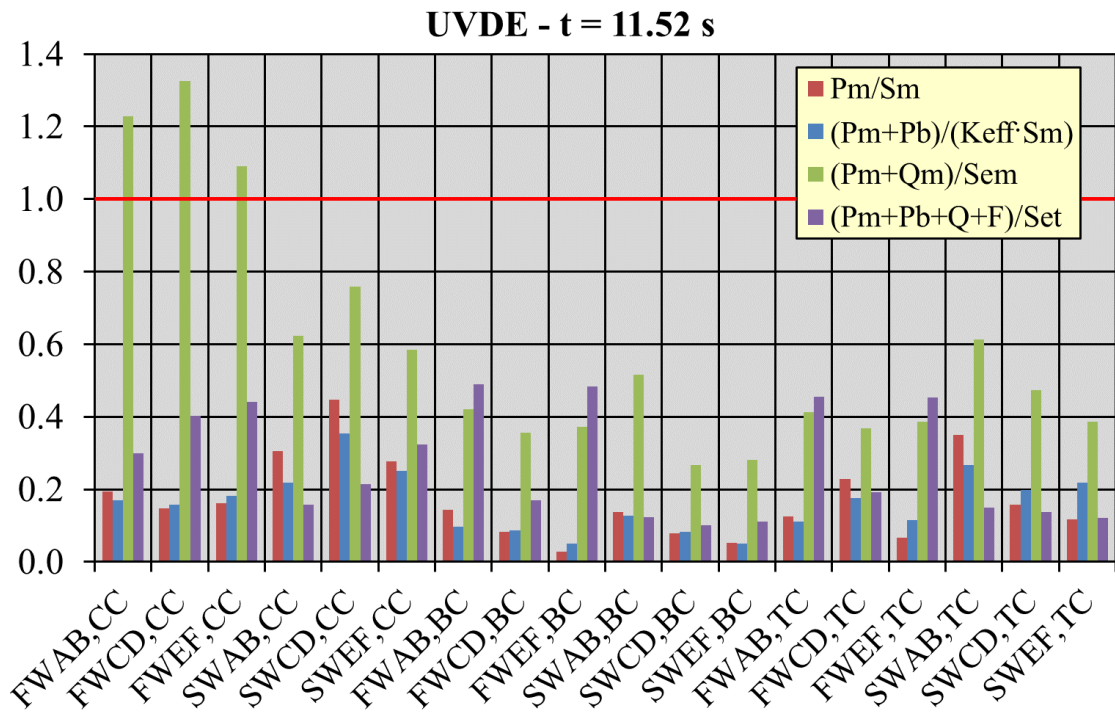


Figure 3.44 Stress linearization results under UVDE (t=11.52 s) loading scenario.

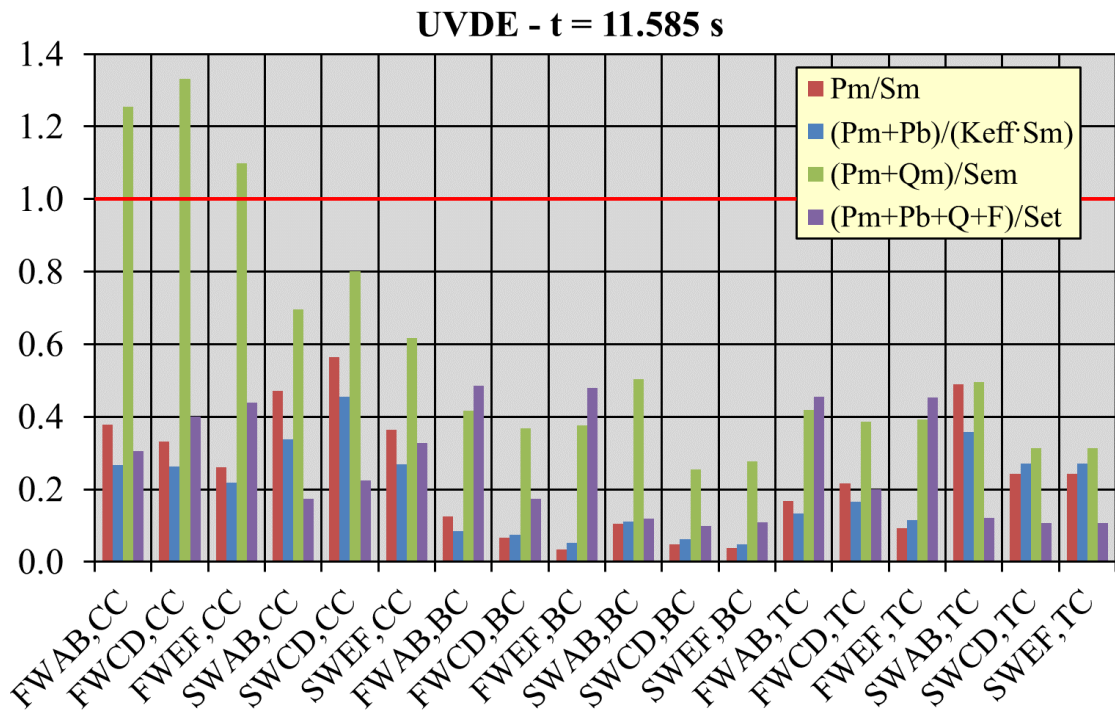


Figure 3.45 Stress linearization results under UVDE (t=11.585 s) loading scenario.

Chapter 4

4 Application of the multiscale design procedure to the thermo-mechanical assessment of the WCLL Central Outboard Segment

4.1 Introduction

The development of the multiscale procedure presented in the previous chapters, allowed obtaining a design tool capable of performing in-depth investigations of the WCLL COB segment structural performances taking into account its global behaviour. In particular, by means of the first part of the procedure, it is possible to realistically predict the thermal field of the whole segment starting from local analyses. In other words, it is possible to predict a global thermal behaviour on the basis of results coming from detailed local assessments. Afterwards, thanks to the second part of the procedure, it is possible to apply the sub-modelling technique to investigate in detail the structural response of some regions of interest, considering at the boundaries the structural influence of the rest of the segment. This means that it is possible to predict a detailed local behaviour on the basis of results coming from global assessments. Hence, the developed multiscale procedure works in a double direction, allowing to go, firstly, from the local to the global model (for thermal evaluations) and then vice-versa (for structural evaluations) in order to completely characterise the WCLL COB segment from the thermal and mechanical standpoints.

In this framework, the multiscale procedure set-up has been applied to the development of the conceptual design of the WCLL COB segment, with the aim of improving the reference design of the whole segment presented at the end of the BB pre-conceptual design phase.

Considering that the WCLL BB is subjected to thermal loads, in particular nuclear heating and a high value of heat flux on the FW surface, which vary strongly along the poloidal

direction, the COB Segment structure must change accordingly with the thermal loads in order to optimise the heat removal in each region of the segment and to reduce the poloidal thermal gradients. Moreover, it is possible to achieve a reduction in the overall amount of steel improving the tritium breeding performance of the blanket concept.

To this purpose, the developed multiscale analysis procedure has been applied performing different local thermal analyses, by subdividing the Segment into some representative region and studying each of them individually. The obtained thermal fields have been interpolated and different sets of interpolating functions have been found. Hence, by means of a proper routine, the different sets of functions have been combined and so applied to reproduce the temperature spatial distribution in the entire COB segment.

Then, a thermo-mechanical analysis of the current configuration of the COB segment has been carried out, using a complete and more realistic thermal deformation field derived from the interpolation procedure of the thermal fields raised from the thermal analyses of its different regions. Finally, applying to the sub-modelling technique, the thermo-mechanical behaviour of some interesting regions has been evaluated paying attention to those regions not directly modelled in the FEM model of the entire segment. Thanks to a stress linearization procedure, the structural response of the segment has been evaluated in view of the design rules prescribed by the French nuclear code RCC-MRx, assumed as reference for the DEMO BB structural design.

4.2 The adopted methodology

As stated in the previous section, the WCLL COB design passed through the DEMO pre-conceptual gate review was not detailed enough to allow reliable thermal-hydraulic analysis for the detailed calculation of its thermal field, since the poloidal distribution of the cooling channels and DWTs was not defined. Hence, in this work, the developed multiscale analysis procedure has been applied to get a reliable estimation of the thermal field arising within the WCLL COB segment without performing its whole thermal-hydraulic assessment, allowing the determination of the poloidal distribution of its cooling channels and tubes. Hence, the application of the multiscale procedure has allowed significantly improving the design of the WCLL COB segment along its poloidal extension moving from the pre-conceptual reference design to an up-to-date conceptual geometric layout able to better fulfil the design requirements.

To this purpose it has to be observed that each BB segment could be ideally subdivided into 7 poloidal regions [34][58], each characterized by a certain set of distributed thermal

loads (namely plasma heat flux, nuclear heating and decay heat power density) representative of the operating conditions of the considered region (Figure 4.1). Hence, for each of the seven regions in which the WCLL COB segment can be ideally divided (indicated with labels from O1 to O7 in Figure 4.1), an equatorial radial-toroidal elementary cell can be individuated as representative of the nth region (as depicted, as an example, for O5 region in Figure 4.1).

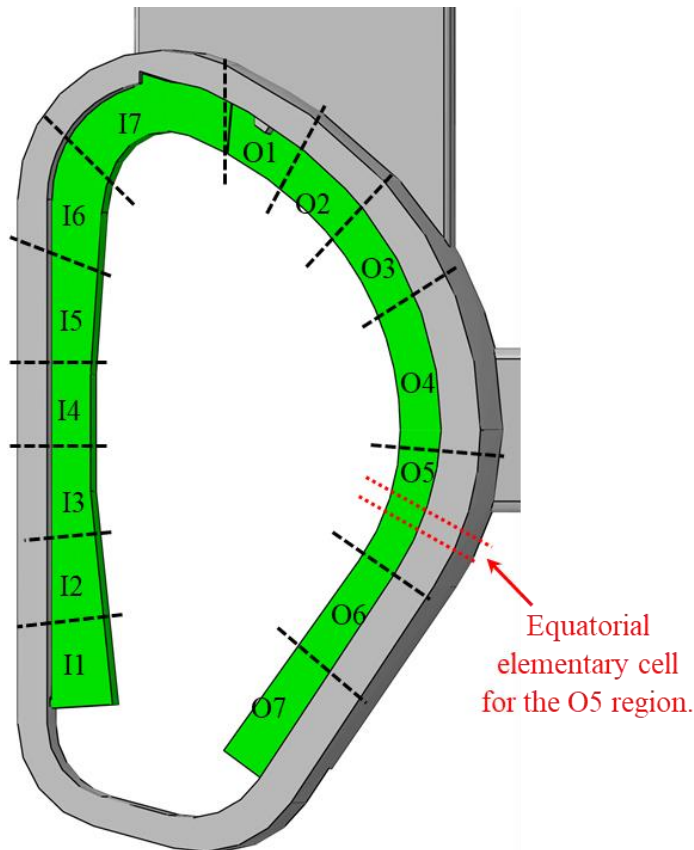


Figure 4.1 Poloidal segmentation and numbering.

Starting from that, each of the 7 equatorial radial-toroidal elementary cells belonging to the WCLL COB segment has been assessed from the thermal point of view, taking into account the 3D nature of the pertinent thermal loads and the reference pre-conceptual geometric layout, described in the following. To this purpose, considering the suggested Eurofer maximum temperature limit equal to 550 °C within the structural components [34][46], it has been found that a thermal optimization of the WCLL COB segment's cooling layout (namely Segment Box channels and breeding zone DWTs) was necessary in order to obtain, for each of the 7 equatorial cells assessed, a thermal field fulfilling the above said requirement minimizing the number of tubes. Hence, alternative geometric layouts have been conceived and assessed assuming, for each of the 7 poloidal regions, the corresponding set of thermal loads. A flowchart summarising the entire thermal optimization procedure is shown in Figure 4.2.

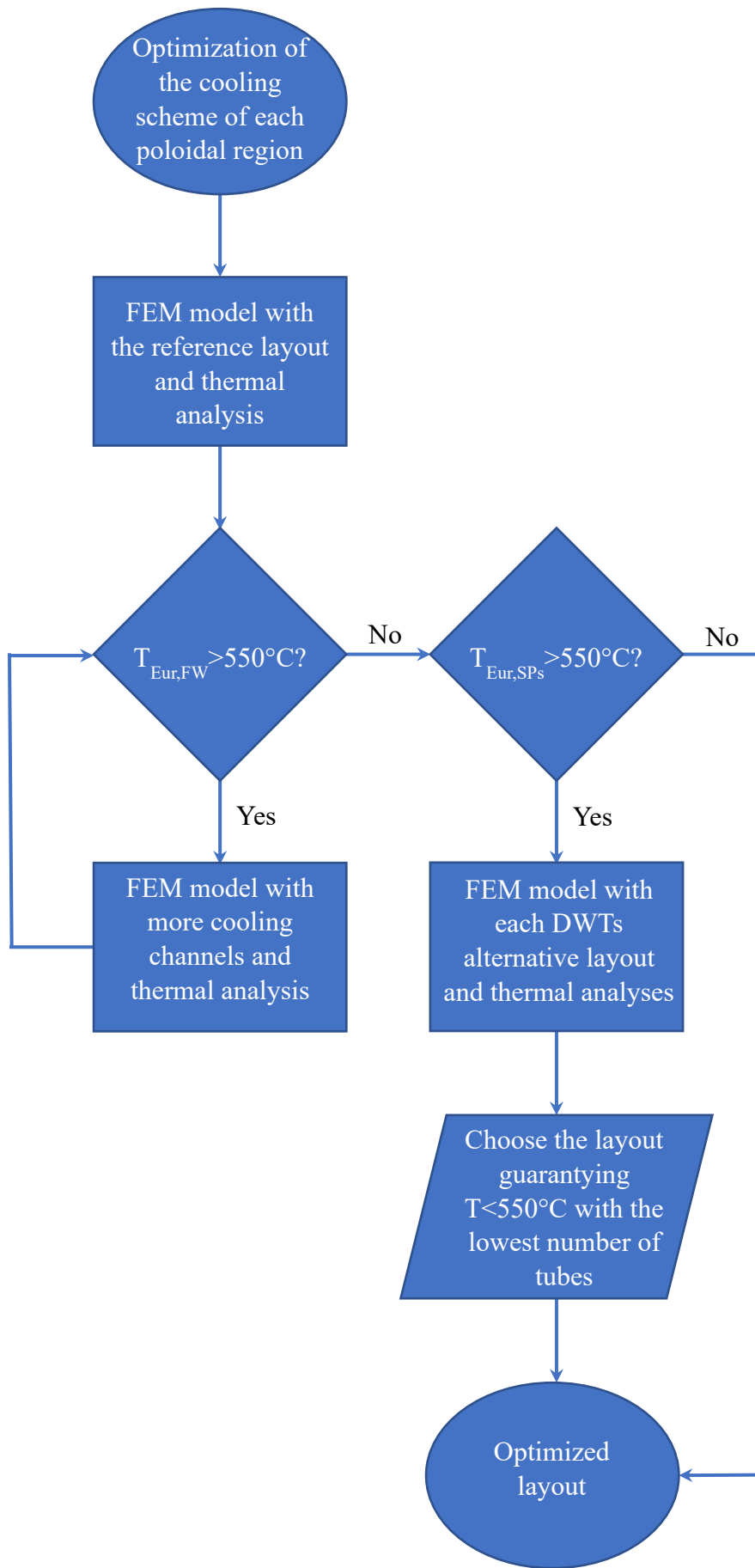


Figure 4.2 Thermal optimization procedure flowchart.

Once obtained, for each of the 7 equatorial cells assessed, an optimized cooling system geometric layout and the pertinent thermal field fulfilling the design requirement, an interpolation procedure has been performed in order to carry out 7 different sets of interpolating functions of the radial and toroidal variable capable of reproducing the calculated thermal fields with a high level of confidence. Then, the found sets of interpolating functions have been applied to the 7 poloidal regions (namely to the whole O1, O2, ..., O7 region) so to reproduce, on the whole COB segment, a detailed 3D thermal field originated by the radial-poloidal dependent thermal loads and fulfilling the prescribed design thermal requirement.

At this point, the structural assessment of the whole WCLL COB under the obtained optimized 3D thermal field has been performed, under the nominal and accidental steady state loading scenarios described in the following. The obtained results have been used to assess the displacement and Von mises equivalent stress fields and to perform a stress linearization procedure in some critical areas, so to verify the fulfilment of the structural design criteria, namely the criteria prescribed by the RCC-MRx structural design code. In the end, applying the sub-modelling technique, the local structural behaviour of some regions of interest has been assessed in detail in view of the RCC-MRx design criteria.

4.3 Thermal Analysis of the equatorial radial-toroidal cell of each of the 7 COB poloidal regions

In order to assess the thermo-mechanical performances of the WCLL COB segment, the first step has been the determination of a thermal field for the whole segment. To this purpose, the necessity to fulfil the thermal design requirement on the maximum Eurofer temperature [34] has led to optimize the WCLL COB segment's cooling scheme. In this framework, the first step has been the thermal analysis of the reference layout of the equatorial radial-toroidal elementary cell of each of the 7 COB poloidal regions (from O1 to O7, Figure 4.1), inherited from the WCCL COB segment pre-conceptual design. Afterwards, the thermal optimization of those regions not fulfilling the prescribed requirement has been performed with the aim of obtaining a thermal field characterized by the maximum Eurofer temperature within structural components lower than 550 °C [34].

The thermal analysis of the reference layout of the equatorial radial-toroidal elementary cell of each of the 7 COB poloidal regions has been performed under the steady state normal operation loading conditions foreseen for the WCLL COB.

4.3.1 The reference geometric layout

According with the Single Module Segmentation (SMS) concept, the WCLL COB Segment is composed by a single elementary cell, identified by two horizontal Stiffening Plates (SPs), that repeats along the poloidal direction from a Cap to another, which vertically close the segment. The structure, depicted in Figure 4.3, is mainly characterized by the Segment Box (SB), divisible into First Wall (FW), with the 2mm-thick of W-armor (coloured in orange in Figure 4.3), and the Side Walls (SWs) that laterally close the SB. Moreover, the structure is closed in the back by the complex of Back Plate (BP), water and breeder manifolds and the Back Supporting Structure (BSS), connected to the attachment system (coloured in grey in Figure 4.3), aimed to mechanically connect the Segment to the Vacuum Vessel (VV). The breeder flows inside the box, in the region called Breeder Zone (BZ), which is reinforced by means of the SPs. In particular, the SPs grid is composed by horizontal (or toroidal-radial) and vertical (or poloidal-radial) SPs, respectively with a thickness equal to 10 and 12 mm. A bundle of 22 cooling tubes per cell (Figure 4.4), Double Walled Tubes (DWTs), immersed in the PbLi, has the role of cooling the BZ, instead, the FW-SW-FW region is cooled by means of 7x7 m² cooling channels located into the SB.

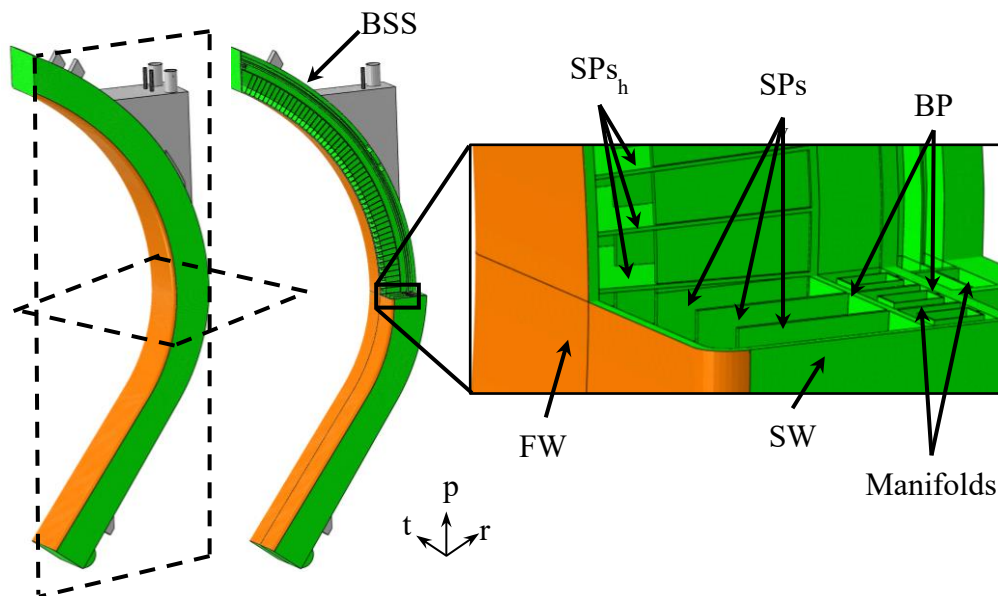


Figure 4.3 COB Segment architecture.

In order to observe the different thermal loads characterizing the poloidal extension of the segment, the number of cooling channels per cell varies along the COB segment [34], following the aforementioned poloidal segmentation. In particular, 4 channels per cell are foreseen, in the reference pre-conceptual geometric layout, for each poloidal region with exception of O7 region in which 6 channels are foreseen. Instead, only one DWTs

configuration has been selected in the pre-conceptual design for all the elementary cells along the segment. Such a design choice makes difficult following the poloidal variation of the nuclear power deposited within the breeding zone. Therefore, in this work the optimization of the DWTs poloidal layout has been performed. In particular, the reference pre-conceptual DWTs layout, named v06b as reported in [34] , consisting of 22 C-shaped double-walled tubes, with hydraulic diameter of 8 mm and an external diameter equal to 13.5 mm, each with different position and radius. In Figure 4.4 the DWTs layout in an elementary cell (namely an equatorial radial-toroidal cell) and the water path inside them (in which red arrows indicate the inlet and green the outlet), with the BZ recirculation scheme (highlighted in orange), is reported.

In the present work, two realistic 3D geometric models of a couple of elementary cells (Figure 4.5), equipped with 4 and 6 cooling channels respectively and the WCLL v06b DWTs layout, representing a portion of the whole COB segment, have been set up in order to realistically simulate the thermal behaviour of the 7 equatorial cells of the regions which the WCLL COB segment can be ideally divided in. Given that the reference DWTs layout is the same along the whole segment, the geometric model envisaging 4 FW channels represents the equatorial radial-toroidal cell of regions from O1 to O6, whereas the model with a FW equipped with 6 cooling channels represent the equatorial elementary cell of the O7 poloidal region.

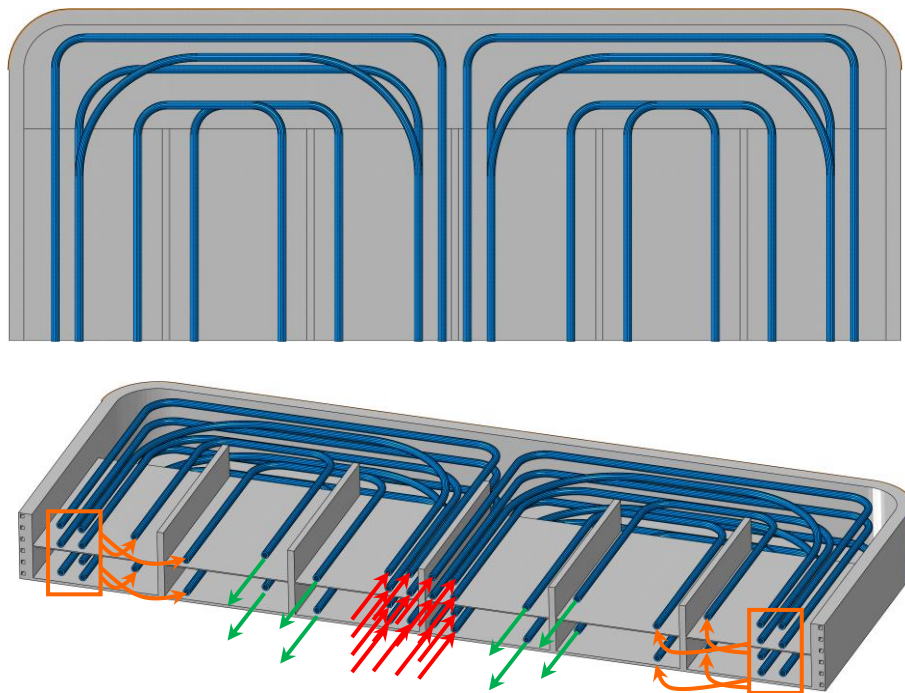


Figure 4.4 WCLL v06b DWTs layout and recirculation scheme.

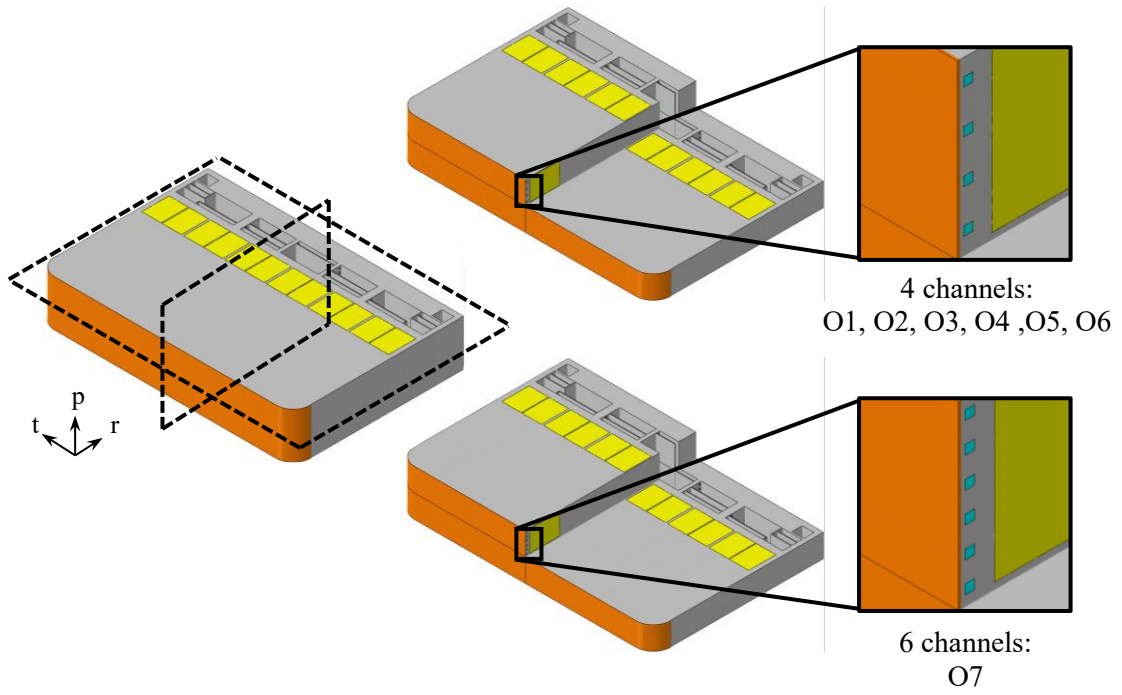


Figure 4.5 Models of the two elementary cells equipped with 4 and 6 cooling channels.

Two detailed FEM models have been set-up, each one composed of ~13M nodes connected in ~5M linear hexahedral and tetrahedral elements, including the Eurofer structure, tungsten layer, DWTs, breeder and water coolant flowing inside FW channels and DWTs.

4.3.2 Loads and Boundary Conditions

In order to perform the thermal analysis, a set of loads and boundary conditions, pertinent to the Normal Operation steady state loading scenario, has been considered for each model taken into account.

A non-uniform value of heat flux (Φ), due to particles and radiation arising from plasma, for each COB poloidal regions has been imposed onto the straight and bend FW plasma facing surface. The selected heat flux values [58], assumed at the end of flat-top, are reported in Table 4.4. In particular, the values reported in Table 4.4 have been applied onto the straight FW surface. Instead, for the bend FW surfaces a decreasing value according to a cosine-dependent law has been assumed: considering the values reported in table as maximum ones.

$$\Phi_{FWbend} = \Phi_{FW} \cdot \cos\alpha \quad (\text{Eq 4.1})$$

where Φ_{FWbend} is the value imposed to the bend FW surface, Φ_{FW} the values reported in Table 4.4 as maximum ones and α varies between 0, corresponding to the start of the bend region at the interface with the straight FW, and $\pi/2$, to the SW.

The temperature-dependent properties of materials have been considered. In particular, for Eurofer, Pb-15.7Li and Tungsten, the physical properties have been drawn from [56], [38] and [57]. For Eurofer, PbLi and Tungsten, the set of properties assumed for the analysis have been reported in Table 4.1, Table 4.2 and Table 4.3 respectively.

T [°C]	ρ [kg/m ³]	k [W/m·°C]	c_p [J/kg·°C]	α [10 ⁻⁶ /°C]	E [GPa]	ν
20	7744	28.08	449.1573	10.3	217	0.3
50	7750	28.86	//	10.5	215	
100	7740	29.78	489.9999	10.7	212	
200	7723	30.38	520.1743	11.2	207	
300	7691	30.01	545.8260	11.6	202	
400	7657	29.47	586.9650	11.9	196	
500	7625	29.58	663.6014	12.2	190	
600	7592	31.12	795.7450	//	170	
700	7559	//	1003.4060	//	162	

Table 4.1 Eurofer physical properties [56].

T [°C]	ρ [kg/m ³]	k [W/m·°C]	c_p [J/kg·°C]	α [10 ⁻⁵ /°C]
20	10172	7.69	192	11.68
300	9839	13.18	190	12.10
350	9779	14.16	189	12.18
400	9720	15.14	189	12.25
450	9661	16.12	188	12.33
500	9601	17.10	188	12.40
550	9542	18.08	187	12.48
600	9482	19.06	187	12.55
650	9423	20.04	187	12.63
700	9363	21.02	186	14.37

Table 4.2 PbLi physical properties [38].

T [°C]	ρ [kg/m ³]	k [W/m·°C]	c_p [J/kg·°C]	α [10 ⁻⁶ /°C]	E [GPa]	ν
20	19300	162.71	138.90	4.40	395.9	0.280
100		156.40	139.72	4.41	395.23	0.281
200		149.36	140.83	4.42	393.82	0.281
300		143.18	142.04	4.44	391.85	0.282
350		140.37	142.68	4.45	390.66	0.283
400		137.75	143.34	4.46	389.34	0.283
450		135.28	144.03	4.48	387.87	0.284
500		132.97	144.74	4.49	386.27	0.284
550		130.80	145.47	4.51	384.53	0.285
600		128.76	146.23	4.52	382.65	0.285
650		126.85	147.01	4.54	380.64	0.286

Table 4.3 Tungsten physical properties [57].

Moreover, a spatial distribution of volumetric density of nuclear-deposited heat power, derived from neutron transport analysis [34], has been imposed to each FEM model to simulate the distributed power deposition as a result of the neutrons, gamma photons and nuclei interactions. Moreover, differently from the previous thermal analysis carried out, also the contribution of the decay heat, caused by the activated materials, has been taken into account [59]. In particular, the decay heat power spatial distribution calculated at the shut-down has been assumed for the normal operation scenario, as it contributes to heat the structure. Globally, the decay heat power deposited within the BB during the normal operation is equal to ~2% of the power deposited by neutrons and photons.

Since, at present, the spatial distributions of nuclear power and decay heat are calculated only for the O4 region, the analogous spatial distributions for the other 6 poloidal regions have been obtained using the ratio between the Neutron Wall Loadings (NWLs) in the i-region and that in the O4 region as scaling factor. The adopted NWLs average values for each COB region [34] are reported in Table 4.4.

Moreover, in order to simulate the thermal contact of the PbLi with the SB and DWTs breeder-wetted surfaces, a pure diffusive heat transfer contact with a conservative value of thermal conductance equal to 100 [kW/m²·°C] has been assumed. The breeder, since it flows very slowly, due to the action of buoyancy and magneto-hydrodynamics forces, in fact, can

be considered as stagnant. Then, the DWTs and the SB structure are considered as a continuum concerning the thermomechanical behaviour.

	O1	O2	O3	O4	O5	O6	O7
Maximum Heat Flux [MW/m²]	0.24	0.27	0.26	0.27	0.27	0.67	0.67
Average NWL [MW/m²]	0.9834	1.1592	1.2802	1.3335	1.3287	1.1844	0.7539

Table 4.4 Total Heat Flux and average NWL poloidal distribution.

Finally, a forced convective heat transfer between coolant and water-wetted surfaces adopting a proper thermal contact model has been considered. In particular, a counter-current flow path has been imposed for the FW-SW cooling water (Figure 4.6), instead, concerning the DWTs cooling water, the path shown in Figure 4.4 has been simulated and the recirculation system has been properly modelled. To reproduce the DWTs water path, the tubes have been divided into two groups, the first, in which the water enters at 295 °C, including 14 tubes and the second, where the recirculation takes place, includes 8 tubes. In order to correctly simulate the recirculation system, the average water outlet temperature, namely mixing temperature, of the first group has been calculated and set as the water inlet temperature of the second group of tubes, by means of a proper Abaqus procedure.

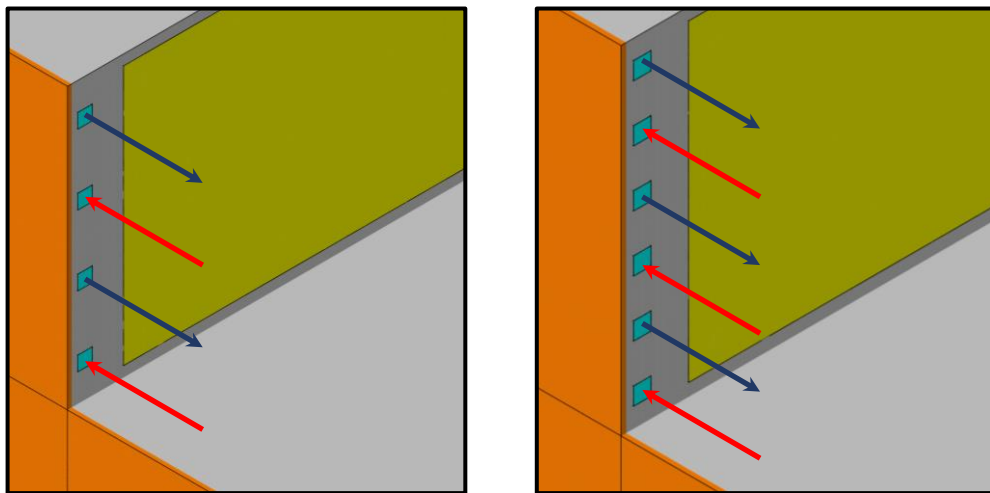


Figure 4.6 Counter-current flow path on FW-SW cooling channels.

A first attempt value of mass flow rate has been selected for each group of DWTs and channels, and a related heat transfer coefficient, calculated using the Dittus & Boelter correlation [41], has been considered. In particular, an inlet temperature (of 295 °C for the SB channels and for the first DWTs group, determined by the code for the DWTs recirculation group) and a water temperature difference (ΔT) between inlet and outlet equal to 33 °C (for each SB channel and for the whole set of DWTs) have been imposed for the

calculation. Then, adopting a “frozen field” calculation approach, it has been possible calculating the water bulk temperature along each channel/tube abscissa. In particular, the adopted procedure consists of imposing the bulk temperature and mass flow rate (i.e., mass flow per unit area) at the inlet of each cooling tubes or channels together with the heat transfer coefficient (HTC). The latter has been analytically calculated in each cooling channel or tube and does not change during the simulation. Hence, such kind of approach allows calculating the bulk temperature along the flow direction and to use it for the imposition of the convective heat transfer condition, which is characterized, in each channel or tube, by a uniform HTC and a coolant bulk temperature varying along the flow direction. The thermal analysis has been iterated [36] so to obtain a thermal rise between water inlet and outlet of 33 °C. In Table 4.5 the HTC values adopted for each poloidal region in the last iterative analysis for the complex of cooling channels and DWTs are reported, where HTC_{CC} , HTC_{DWTs} and $HTC_{DWTs,rec}$ indicate the HTC values used for the SB cooling channels, first group of DWTs and recirculation DWTs respectively.

	O1	O2	O3	O4	O5	O6	O7
HTC_{CC} [W/m ² ·K]	31368	33609	34490	35570	35518	38895	36167
HTC_{DWTs} [W/m ² ·K]	16965	19901	19258	19905	19847	20033	13576
$HTC_{DWTs,rec}$ [W/m ² ·K]	26545	31139	33530	34656	34556	31346	21243

Table 4.5 HTC values used for cooling channels and DWTs coolant.

4.3.3 Results

A steady-state thermal analysis has been performed for the equatorial cells of each of the 7 COB poloidal regions with the aim of investigating their thermal behaviour under the loads and boundary conditions they undergo. For the sake of brevity, the maximum temperature predicted in each region is reported in Table 4.6. Looking at the temperature values reached within SPs and FW, as the baffle plates do not play a structural role, only O1 and O7 regions do not overtake the Eurofer structural material limit temperature, set to 550 °C, whereas all the others exceed this value. Hence, for the latter regions, an optimization of the DWTs layout is necessary. Moreover, looking at the results reported in Table 4.6, the O6 region shows a temperature higher than the temperature limit on the FW too. This result suggests that this poloidal region must be equipped more than 4 channels. Hence, as to O6 region, a further optimization of the FW channels is necessary.

As an example, the thermal field obtained within the structural material of the O4 region, corresponding to the equatorial region of the whole COB segment, is depicted in Figure 4.7 whereas in Figure 4.8 the temperature spatial distribution within Eurofer of the O6 equatorial cells is depicted. The thermal field raised within other poloidal regions, where the temperature exceeds the suggested limit of 550°C, are not shown for the sake of brevity. In fact, these exhibit a temperature spatial distribution similar to O4 (Figure 4.7), but according on each poloidal position, the areas coloured in grey (i.e. $T > 550^\circ\text{C}$) are larger or smaller.

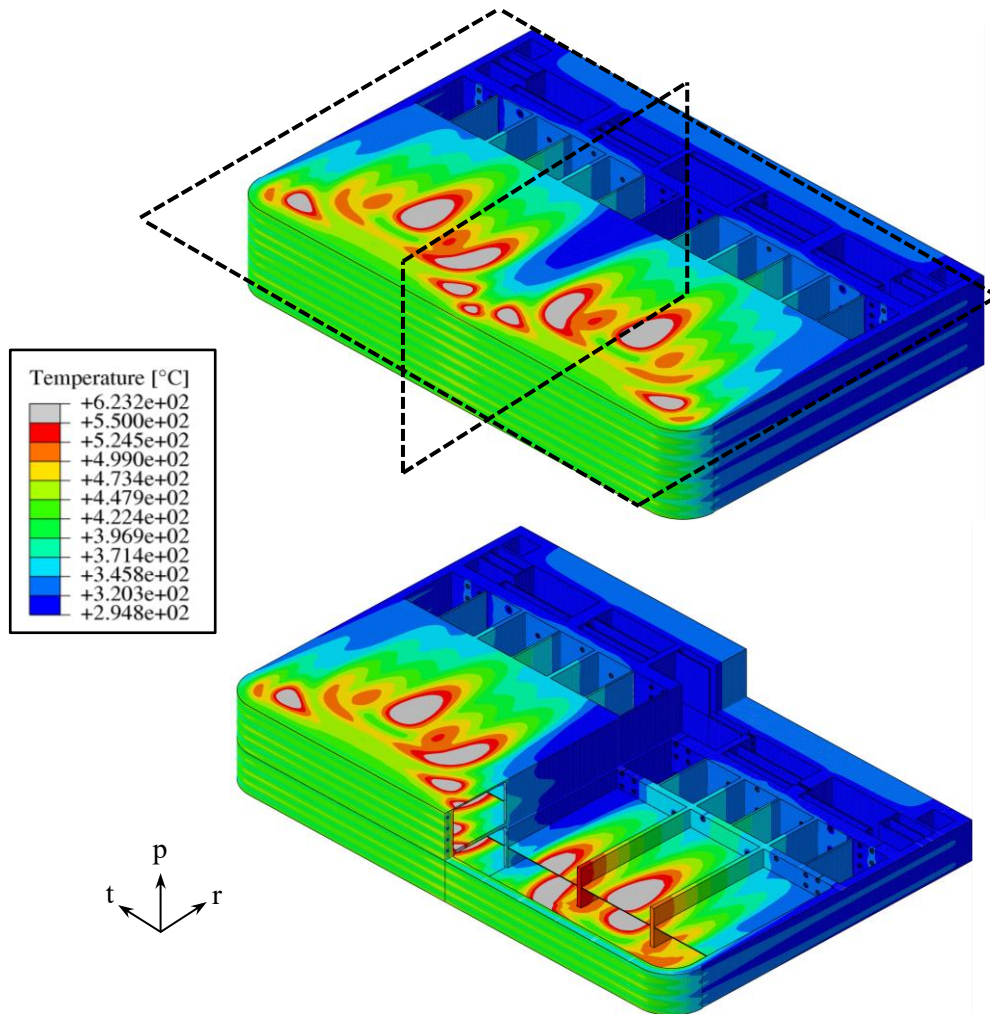


Figure 4.7 Thermal field raised within O4 region.

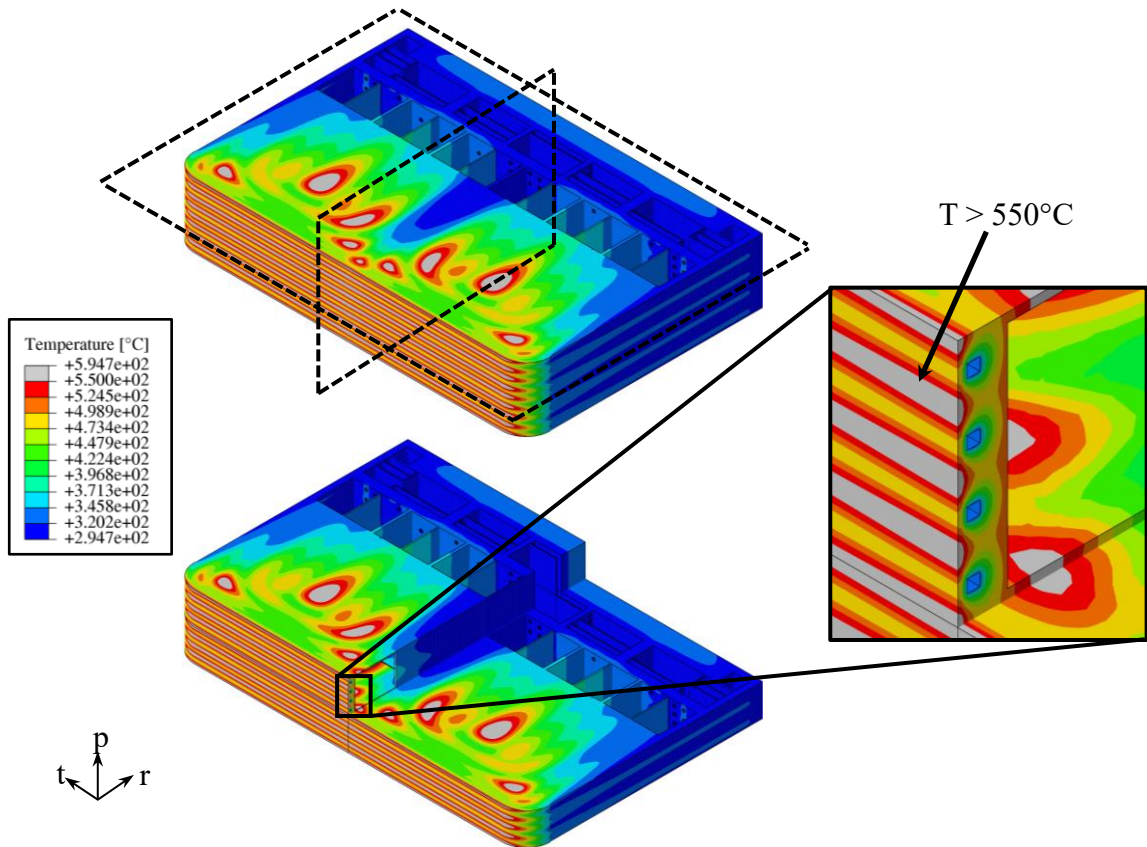


Figure 4.8 Thermal field raised within O6 region.

	O1	O2	O3	O4	O5	O6	O7
Tmax on FW [°C]	478.2	503.3	519.0	526.6	525.9	566.4	479.2
Tmax on SPs [°C]	546.7	580.5	603.1	612.9	612.1	585.2	501.0

Table 4.6 Maximum temperature values for each COB poloidal region equipped with references v06b DWTs layout.

4.4 WCLL COB thermal optimization and determination of its thermal field

The results obtained from the thermal analysis of the reference geometric layout of the equatorial elementary cell of each WCLL COB poloidal region allow concluding that, as to O2, O3, O4 and O5 region, a thermal optimization of the DWTs layout is necessary to allow fulfilling the requirement on the maximum Eurofer temperature. In addition, for O6 region, also the FW channels should be optimized since critical temperature values are predicted within both FW and SPs. Lastly, once obtained the optimized thermal field for each of the 7

poloidal regions, a thermal field for the whole WCLL COB segment can be derived repeating the interpolation procedure in each of the 7 cells assessed.

4.4.1 DWTs and FW channels thermal optimization

In order to thermally optimize the WCLL COB segment, three alternative DWTs lay-outs foreseeing 22, 24 and 26 “crossed” DWTs per elementary cell have been set-up, foreseeing the crossing of the first row of tubes to remove the temperature hotspot in the central region of the cell (Figure 4.8). In particular, these alternative DWTs configurations have been called as “cross-22”, “cross-24” and “cross-26” DWTs configurations.

Moreover, the configurations with 24 and 26 DWTs per elementary cell (namely the cross-24 and the cross-26 configurations) have been obtained moving along the radial and the toroidal directions the first two rows of tubes and adding a new row of tubes, consisting of 2 or 4 tubes respectively (Figure 4.9 and Figure 4.10). Regarding O6 region, the FW-SW has been equipped with 6 channels per cell as well.

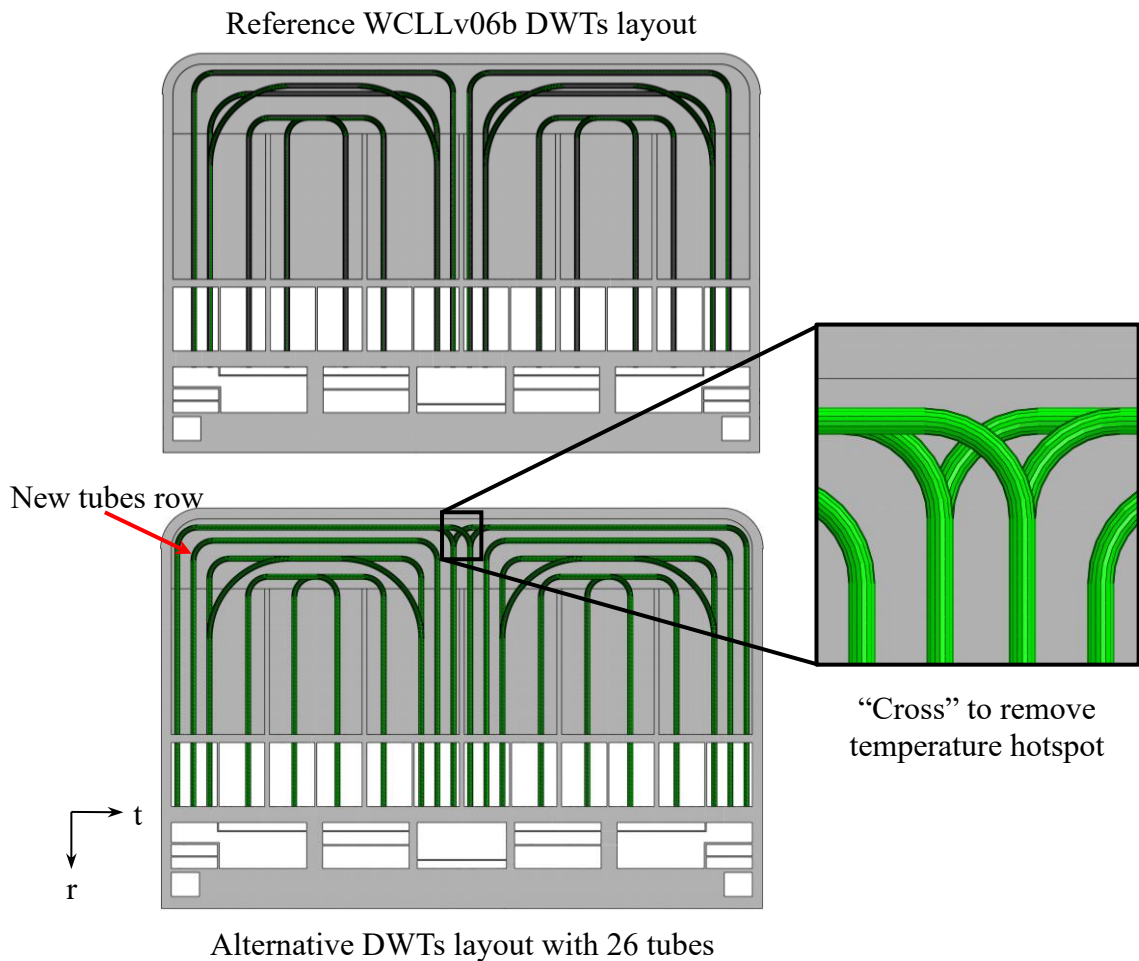


Figure 4.9 Alternative DWTs layout.

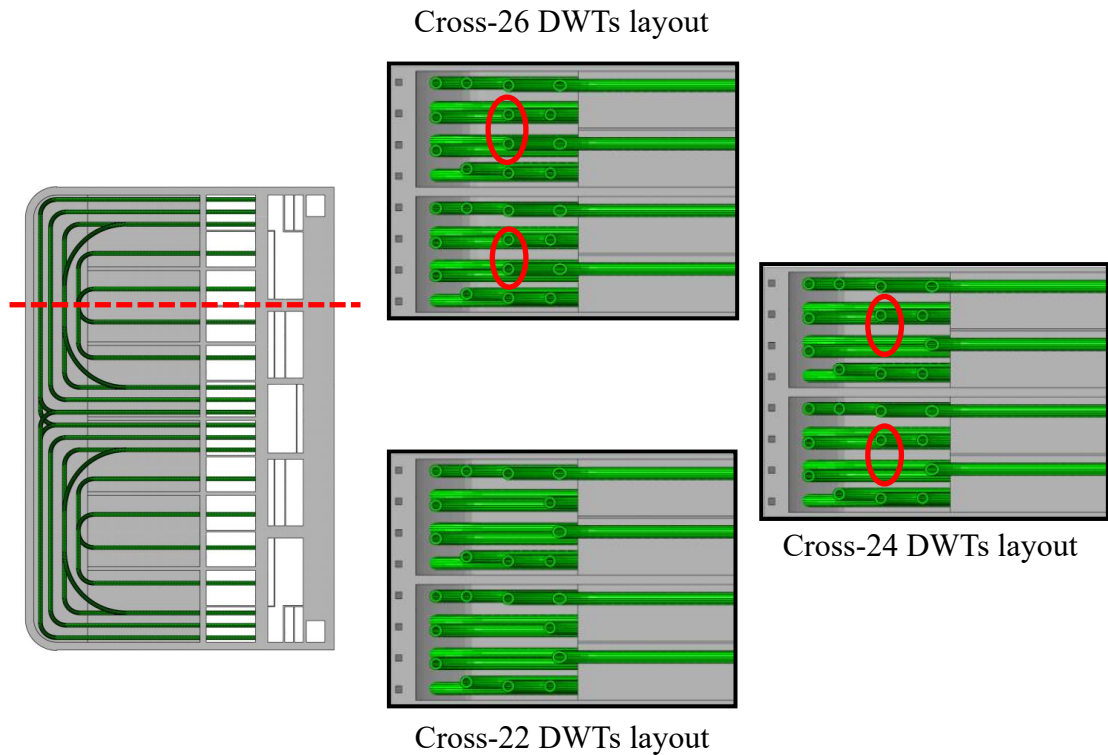


Figure 4.10 Cross-22, cross-24 and cross-26 DWTs layout.

In order to study the thermal behaviour of the three alternative DWTs configurations on each WCLL COB poloidal region to be optimized, a couple of elementary cells equipped with the cross-22, cross-24 and cross-26 DWTs configurations have been studied. Three FEM models, with a mesh composed of ~3M nodes connected in ~4M linear hexahedral and tetrahedral elements, have been set-up for each region. Then, loads and boundary conditions already discussed above have been considered. Finally, a parametric set of thermal analysis has been launched with the aim of achieving the DWTs configuration for each COB poloidal region capable of removing the heat, while keeping the temperature below 550 °C, with the minimum number of tubes.

Results are synthetically summarized in Table 4.7, where the DWTs layout configuration selected, the number of FW-SW channels for each COB region and, moreover, the corresponding maximum temperature reached on the SPs and FW is shown. As an example, the thermal fields obtained from the thermal analyses of two cells representing the O4 region equipped with the three alternative DWTs layouts are showed in Figure 4.11, Figure 4.12 and Figure 4.13. In particular, the thermal requirement has been fulfilled in both layouts equipped with 24 and 26 DWTs, so, the configuration allowing to minimize the number of tubes has been selected, namely the “cross-24”. The same approach has been followed for the other poloidal regions. The thermal field obtained from the thermal analyses of all the poloidal regions equipped with the selected optimized layout are reported in Appendix 2.

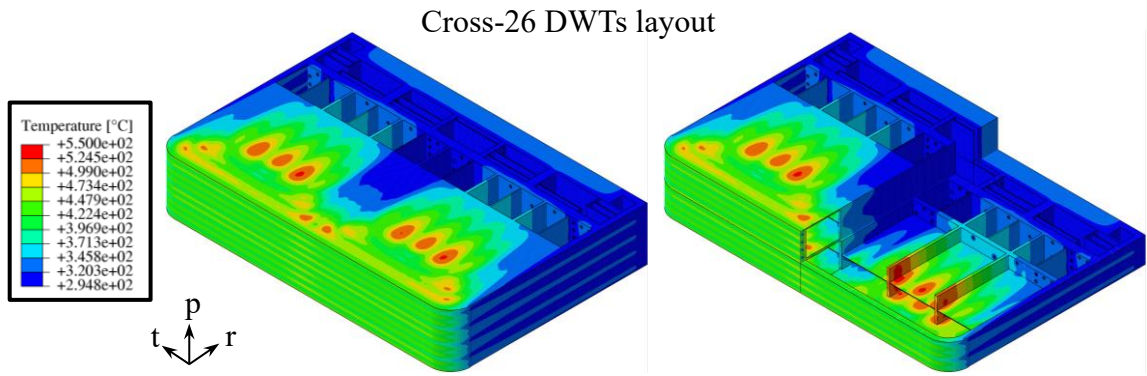


Figure 4.11 Thermal field raised in O4 with cross-26 DWTs layout.

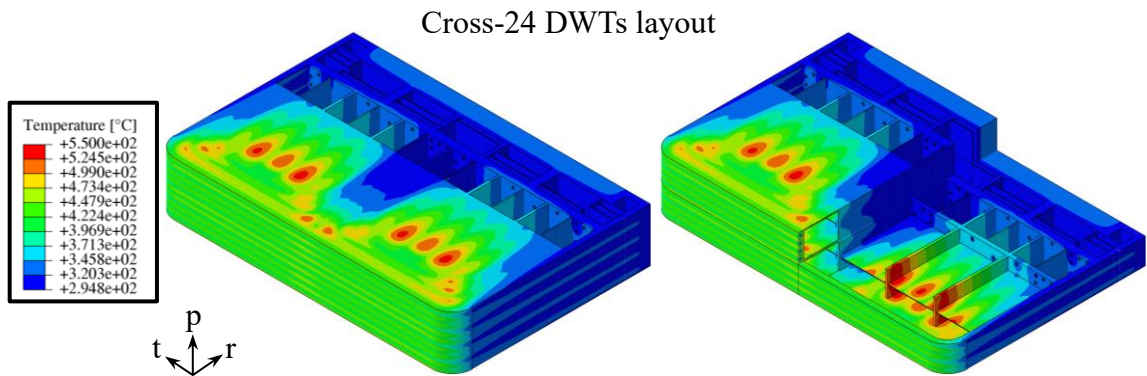


Figure 4.12 Thermal field raised in O4 with cross-24 DWTs layout.

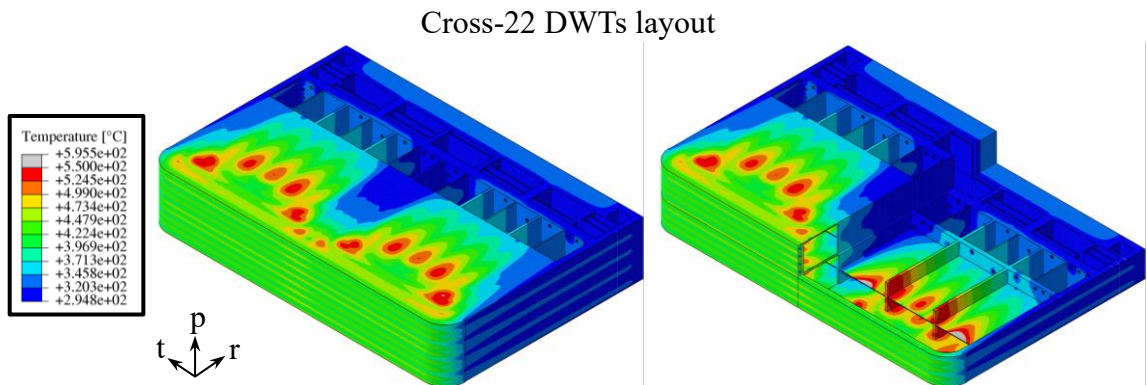


Figure 4.13 Thermal field raised in O4 with cross-22 DWTs layout.

	O1	O2	O3	O4	O5	O6	O7
n. channels	4	4	4	4	4	6	6
DWTs layout	v06b	cross-22	cross-24	cross-24	cross-24	cross-22	v06b
Tmax within SPs [°C]	546.7	534.0	531.4	538.9	538.2	539.2	501.0
Tmax within FW [°C]	478.2	484.6	497.8	504.6	504.0	474.6	479.2

Table 4.7 BZ and FW-SW cooling layout per poloidal region.

4.4.2 Determination of a thermal field for the whole WCLL COB segment

The outcomes of the previous optimization campaign have been used in order to represent in the most realistic way the thermal field arising in the whole WCLL COB segment. Indeed, starting from the optimized thermal field calculated in each of the 7 equatorial cells, an interpolation procedure has been performed to obtain 7 different set of functions of the radial and the toroidal variable. Then, a proper Fortran subroutine has been set-up to provide the poloidal dependence so to obtain a different 3D thermal field for each of the 7 WCLL COB poloidal regions. Lastly, the 7 thermal fields have been stitched together to give the 3D temperature spatial distribution for the whole WCLL COB segment.

To perform the interpolation, each equatorial cell has been divided into 13 different regions: one for the SW-FW-SW and one for the manifolds region, one for each vertical SP, for a total of 5 regions, and 6 for each horizontal SP, identified by the 5 poloidal-radial SPs, as already done in §2.3. Successively, a polynomial function of the radial and toroidal variables has been drawn for each region to represent its temperature distributions. A set of 13 polynomial functions has been then build up for each COB poloidal region to reproduce the thermal field in the most accurate way. In particular, a 14th degree polynomial function of two variables (r and t directions) has been selected for the SW-FW-SW regions, up to 9th degree polynomial function of one variable (r direction) for the manifolds, up to 10th degree polynomial functions of two variables (r and t directions) for each SP_h and up to 14th degree polynomial functions of one variable (r direction) for each SP_v. Concerning the Caps, since their cooling system has not yet been studied in detail, a polynomial function of one variable (r direction) has been obtained from the SWs region and applied to the whole plate, while, on the corresponding FW region, the same polynomial function of the nearest poloidal region (namely O1 and O7) has been used.

The obtained thermal field is depicted in Figure 4.14 with some details at different poloidal heights of the segment. Moreover, a uniform temperature value of 300°C has been considered for the supports (namely the attachment system) in charge of connecting the segment to the VV.

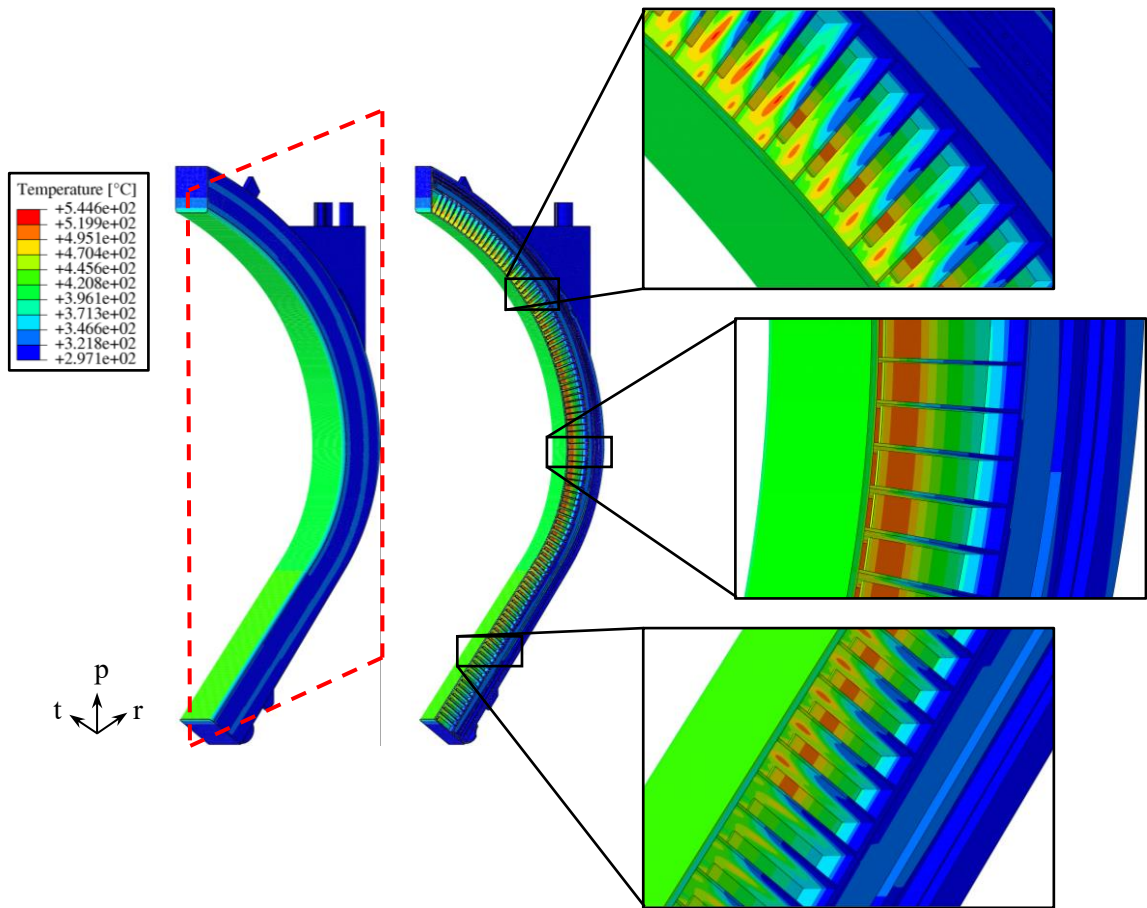


Figure 4.14 Thermal field obtained with the interpolation procedure.

Moreover, it is possible to compare node-by-node the temperature predicted from the thermal analysis of the 7 COB poloidal regions with the temperature obtained from the 7 set of polynomial functions, the so-called interpolated thermal fields, in order to evaluate their degree of accuracy. So, as an example, the contour map of the temperature error and its statistical distribution evaluated for O1 region, with its interpolated thermal field, is reported in Figure 4.15. The temperature error contour maps and statistical distributions evaluated for all the poloidal regions are reported in Appendix 3. In almost all cases, the maximum errors are located within the manifolds regions and the statistical distributions shows a peak around 0, whereas the greater values are between $\pm 10\%$ with a low value of probability.

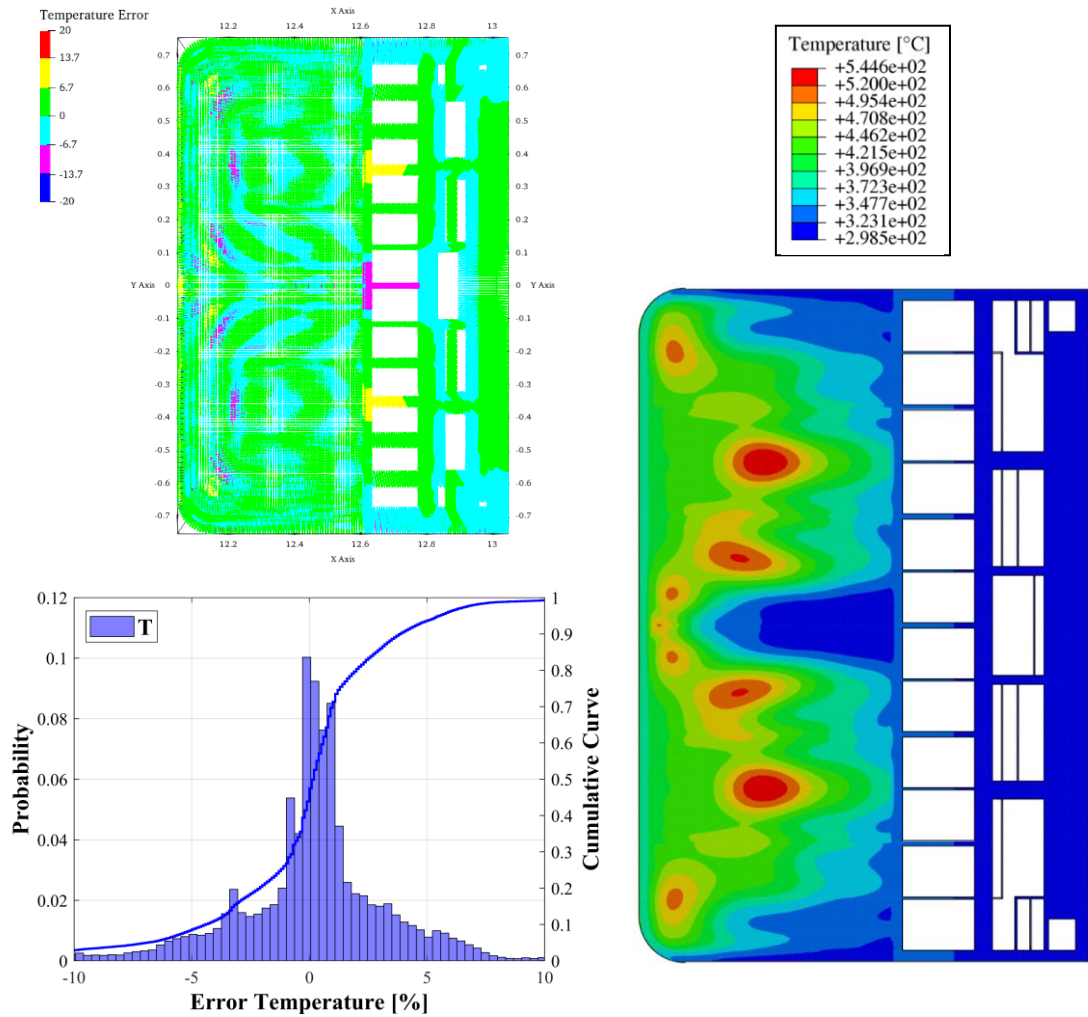


Figure 4.15 Contour map and statistical distribution of the temperature error [in %] between the calculated and interpolated thermal field and cumulative curve in O1 poloidal region.

4.5 Structural Analysis of the reference COB segment

Once obtained a reliable and detailed thermal field of the whole WCLL COB segment, its structural performances under different steady state loading scenarios have been assessed. To this end, since Baffle Plates and DWTs have no significant structural role, they are not been considered in the pertinent FEM model, in order to reduce the computational burden. Therefore, a FEM model has been created on Abaqus and a mesh composed of ~ 3.2 M nodes connected in ~ 8.7 M tetrahedral and hexahedral elements has been set up.

4.5.1 Loads and Boundary Conditions

The thermo-mechanical behaviour of the reference WCLL COB segment has been evaluated under purposely selected steady state loading scenarios. In particular, the loading

scenarios considered are: the Normal Operation (NO), the Over-Pressurization (OP) and the Upper Vertical Displacement Event (UVDE). The first takes into account the thermomechanical loads arising under the nominal conditions and it is classified as Level A scenario in RCC-MRx structural design code. Instead, the OP scenario refers to a severe accidental condition, related to the occurrence of an in-box LOCA leading to the loss of the component. It is classified under the Level D in RCC-MRx structural design code. Lastly, the UVDE scenario have been considered. It refers to an off-normal event due to an uncontrolled vertical plasma disruption, being classified as Level C.

In order to predict the structural response of the COB segment, a set of loads and boundary conditions has been assumed to reproduce the three assessed loading scenarios [49].

- internal pressure distribution according to the considered loading scenario;
- mechanical restraints;
- gravity load;
- non-uniform deformation thermal field;
- electro-magnetic loads.

Since neither breeder nor water have been modelled, in order to reproduce their mechanical effect, a uniform pressure value has been imposed to all the wetted surfaces. In particular, the design pressure value, calculated as the nominal one times a safety factor equal to 1.15 [49], has been imposed onto both breeder-wetted and water-wetted surfaces. So, for NO and UVDE loading scenario, a pressure equals to 17.825 MPa has been considered for all the water-wetted surfaces, instead a value equal to 0.575 has been applied to the surfaces wetted by the PbLi. Instead, an equal value of 17.825 has been considered for all the internal wetted surfaces in the OP loading scenario.

Additionally, the reference attachment system consists in a set of supports aimed at fixing the blanket segments to the VV and, at the same time, withstanding very large electro-magnetic loads, thermal deformations and maintaining a good alignment of the FW. The supports are located at the bottom and at the top part of the segment and each face of these supports works along a particular direction, thus ensuring the segment connection with the VV [42]. These contacts are simulated by means of springs, particular Abaqus element, in correspondence of each surface, as reported in §2.6. So, each of the springs is assigned a specific value of elastic constant.

The gravitational load has been also applied onto the whole model. However, since liquid metal breeder and coolant have not been modelled, their contribution has been taken into account using an Eurofer equivalent density, as already done in previous analyses. The equivalent density value has been obtained assuming that the percentage of steel, water and

breeder are equal to that calculated for the equatorial region. So, temperature-dependent properties of Tungsten and Eurofer structural steel [56][57] have been taken into account and implemented in the model, properly modify the Eurofer density values.

As to the non-uniform deformation thermal field, it arises within the structure as effect of the imposed temperature spatial distribution (Figure 4.14) and the volumetric expansion coefficient.

Finally, the electro-magnetic loads have also been considered for all the assessed steady state loading scenarios. In fact, their action during normal and off-normal operation cannot be neglected and must be included during the investigation of the COB structural response [51][52]. Since steady state analyses have been performed, the EM loads considered and used are relative to a specific instant of time, i.e., time step. During both NO and OP loading scenario, as prescribed by [48][49], the same EM loads have been considered. In particular, only the ferromagnetic loads contribution is considered, since the Lorentz's forces one is negligible. Instead, this assumption cannot be done for the UVDE loading scenario and the Lorentz's forces needs to be taken into account. So, as already done in §3.2, the EM loads related to two different time steps have been considered for the thermo-mechanical evaluation under the UVDE loading scenario: the time steps corresponding to the maximum of the radial forces and moment, $t=11.52$ s and $t=11.585$ s respectively. Thanks to a purposely developed computational procedure, the EM loads, calculated separately through a dedicated electro-magnetic analysis, have been applied onto the node mesh of the COB segment model. In particular, this procedure allows matching the cloud of points on which the EM forces are calculated to the structural analysis mesh. Since the former is much coarser than the latter, the developed procedure is capable of assigning the EM forces calculated at the point x, y, z to the closest node of the structural analysis mesh. Since the EM model take into account the presence of breeder and DWTs, which are absent in the COB segment FEM model, the EM values in that regions have been allocated to the nearby Eurofer portion in order to conservatively consider their effects.

4.5.2 Results

Steady state analyses of the reference COB segment under different loading scenarios have been performed with the aim of evaluating its structural behaviour, as well as verifying that the design criteria of the RCC-MRx for the structural material are fulfilled.

So, the Von Mises equivalent stress fields obtained for each different loading scenario are reported in Figure 4.16 and Figure 4.17, in which only the Eurofer structural material is

displayed. The deformed vs. undeformed shapes are likewise depicted in in Figure 4.18 and Figure 4.19, also with the displacement fields for each assessed scenario. In particular, the deformed shapes are showed with an isotropic amplification factor equal to 20. Looking at the displacement fields, in each operating scenario analysed, the maximum displacement occurs along the radial direction, as well as, looking the Von Mises stress fields, the equatorial region being the particularly stressed one. In Table 4.8 the maximum and minimum values of displacement along all directions for all the assessed scenarios are reported, where U_r , U_t and U_p indicates the displacements along the radial, toroidal and poloidal direction respectively. The values obtained show the same trend and the largest displacement occurs in all the assessed scenarios along the radial direction, with the highest value raised in the OP loading scenario. Moreover, in the UVDE scenario, when the EM loads are considered at the time step of 11.585 s (maximum of radial moments), a larger displacement in toroidal direction than in the other scenarios can be highlighted.

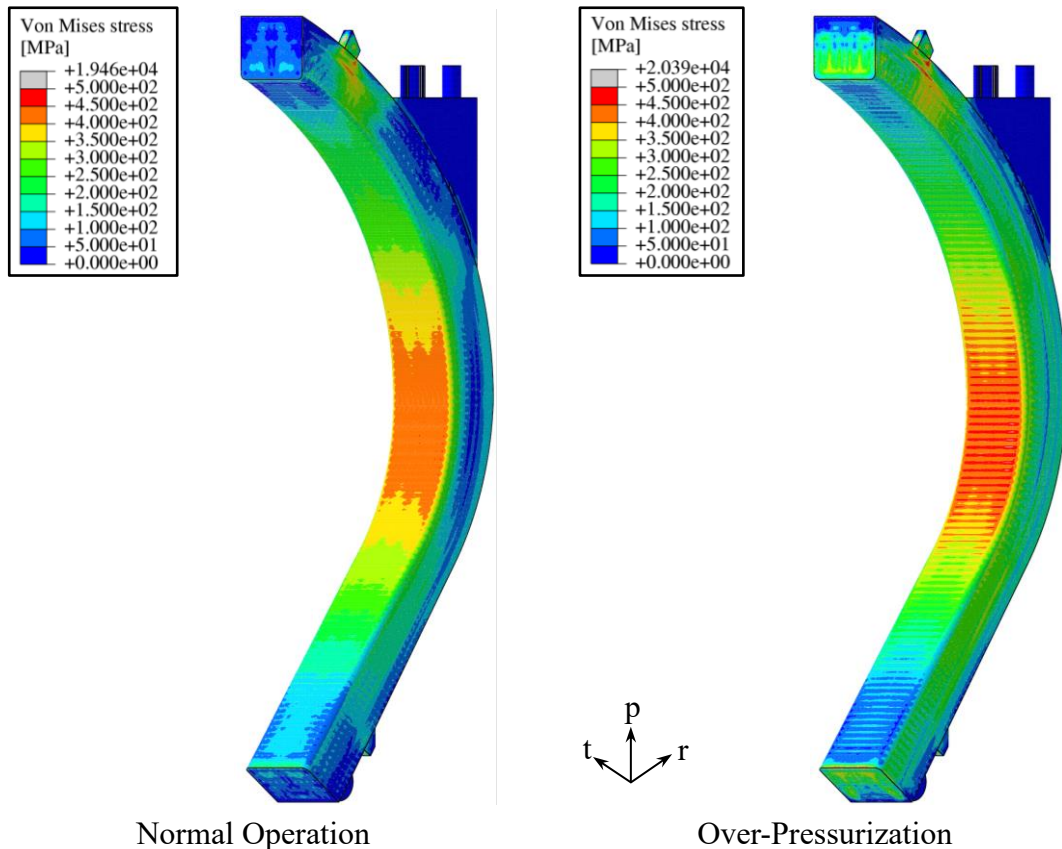


Figure 4.16 Von Mises stress field under NO e OP loading scenarios.

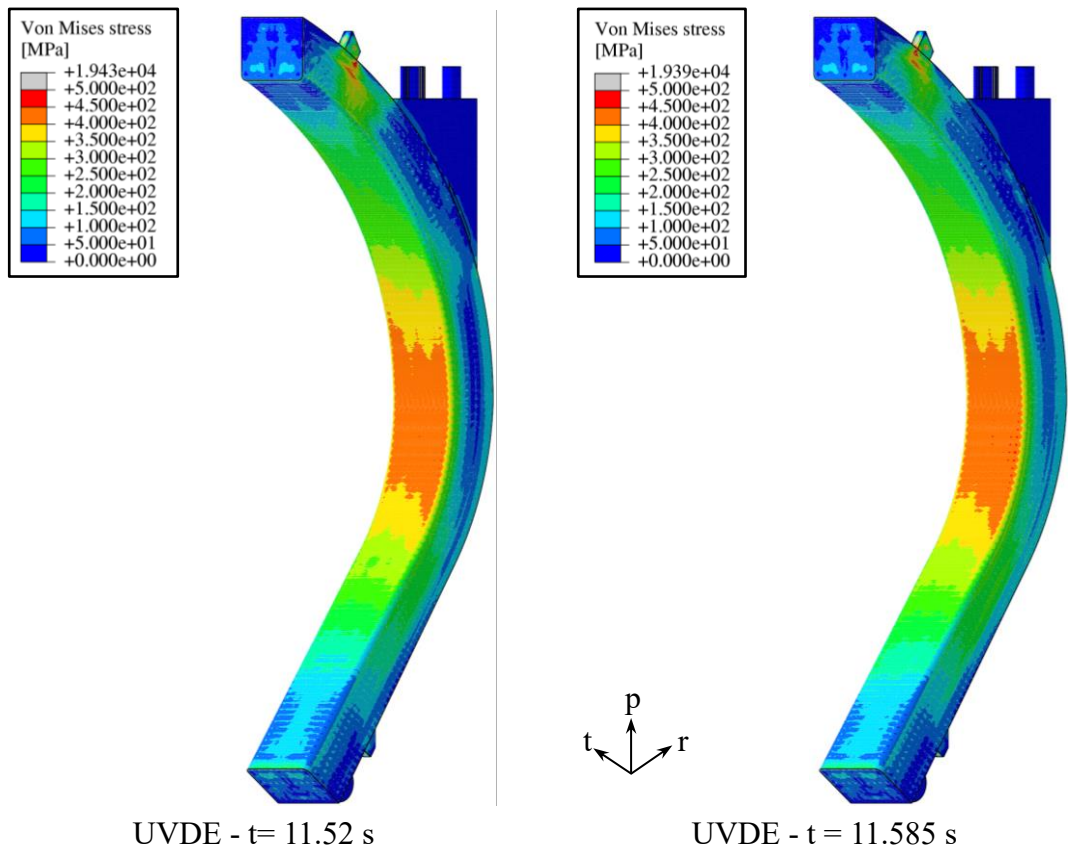


Figure 4.17 Von Mises stress field under UVDE ($t=11.52$ s and $t=11.585$ s) loading scenario.

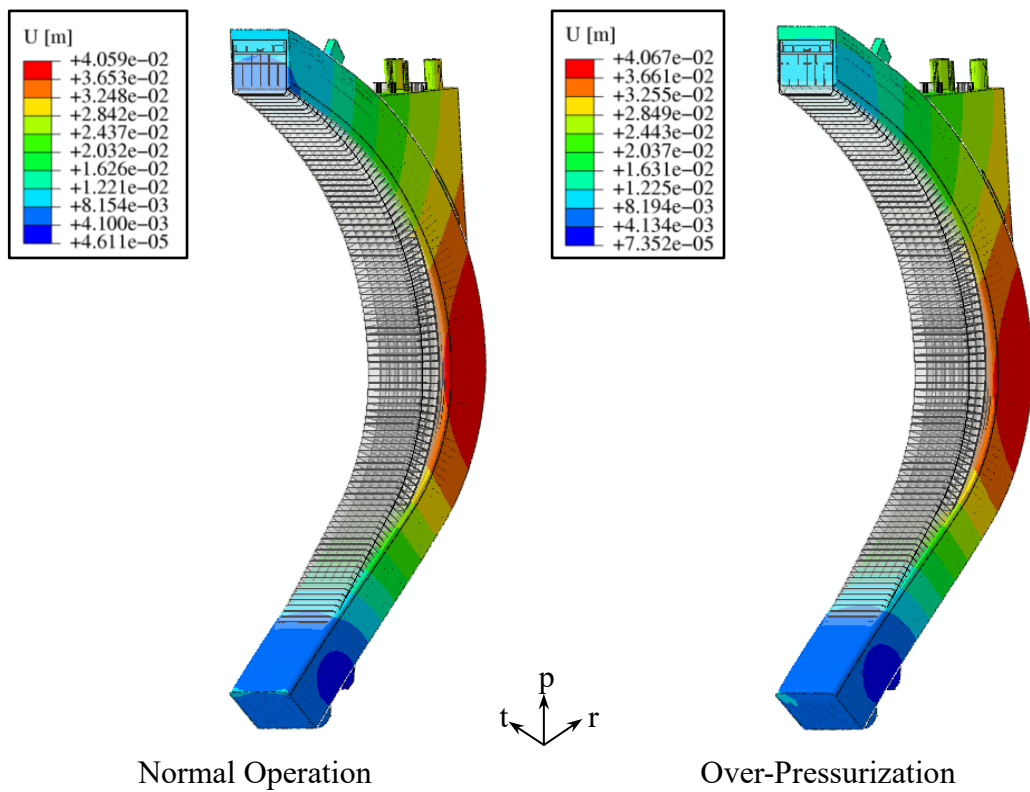


Figure 4.18 Deformed vs. Undeformed shapes under NO and OP loading scenarios.

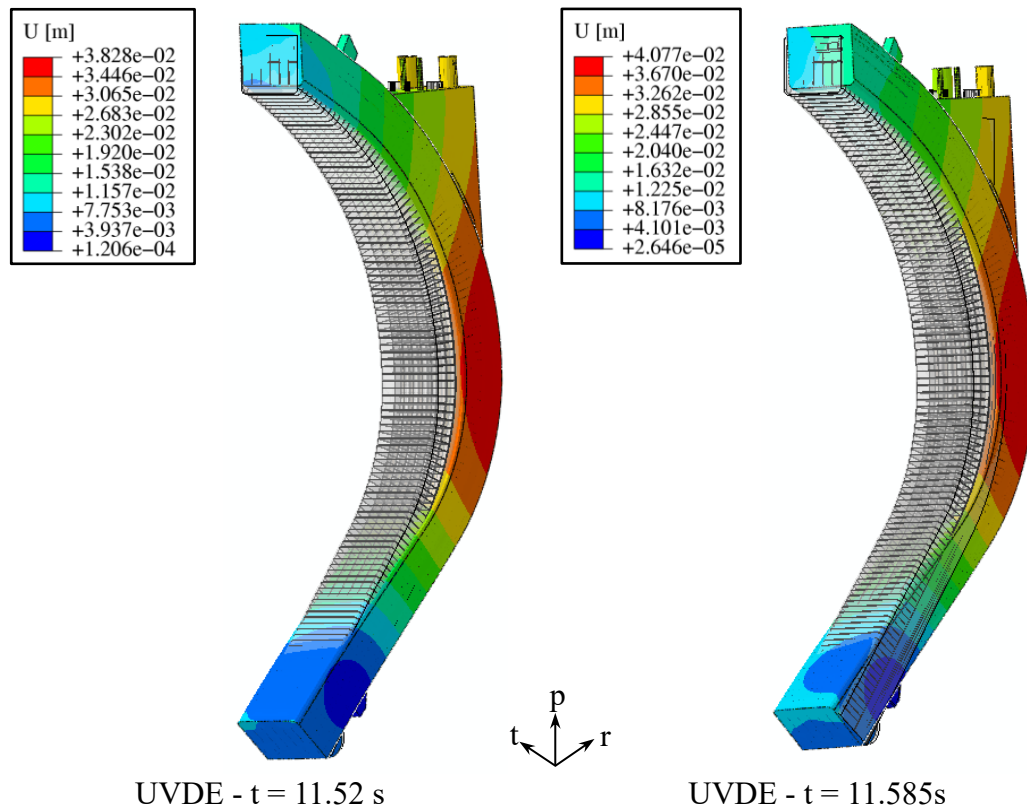


Figure 4.19 Deformed vs. Undeformed shapes under UVDE ($t=11.52$ s and $t=11.585$ s) loading scenario.

	NO	OP	UVDE T=11.52 s	UVDE T=11.585 s
Ur, max [mm]	40.3461	40.5314	37.9137	40.3827
Ur, min [mm]	-9.71531	-9.59273	-9.58886	-9.56706
Ut, max [mm]	5.46014	5.59649	6.19565	7.99158
Ut, min [mm]	-5.0945	-4.82734	-5.11112	-12.4684
Up, max [mm]	23.7326	23.5357	23.9653	23.9025
Up, min [mm]	-5.01018	5.88849	-4.63463	-5.45198

Table 4.8 Maximum and minimum displacements values obtained.

In the end, a stress linearization procedure has been performed along some significant paths located within the most stressed regions of the structure and, then, the fulfilment of Level A, C and D criteria, namely for the NO, UVDE and OP loading scenario respectively, prescribed by the RCC-MRx design code along them has been checked. In particular, four criteria have been taken into account for the structural evaluation: Immediate Excessive Deformation (IED), Immediate Plastic Instability (IPI), Immediate Plastic Flow Localization (IPFL) and Immediate Fracture due to exhaustion of ductility (IF), as reported in Table 3.3. While the first two criteria only consider the primary stresses, the others also take into account secondary stresses occurring along the analysed path. For each criterion, the stress

limit values have been calculated, for the service level (A, C or D) to which each loading scenario analysed relates, in accordance with the structural material and the average path temperature. Therefore, since the cooling channels located within the FW-SW region have not been modelled to reduce the computational burden, only the SPs grid has been considered from the mechanical point of view and some paths lying on the poloidal-radial and toroidal-radial SPs (Figure 4.20), at three different poloidal height, highlighted in red and blue in Figure 4.20, have been individuated.

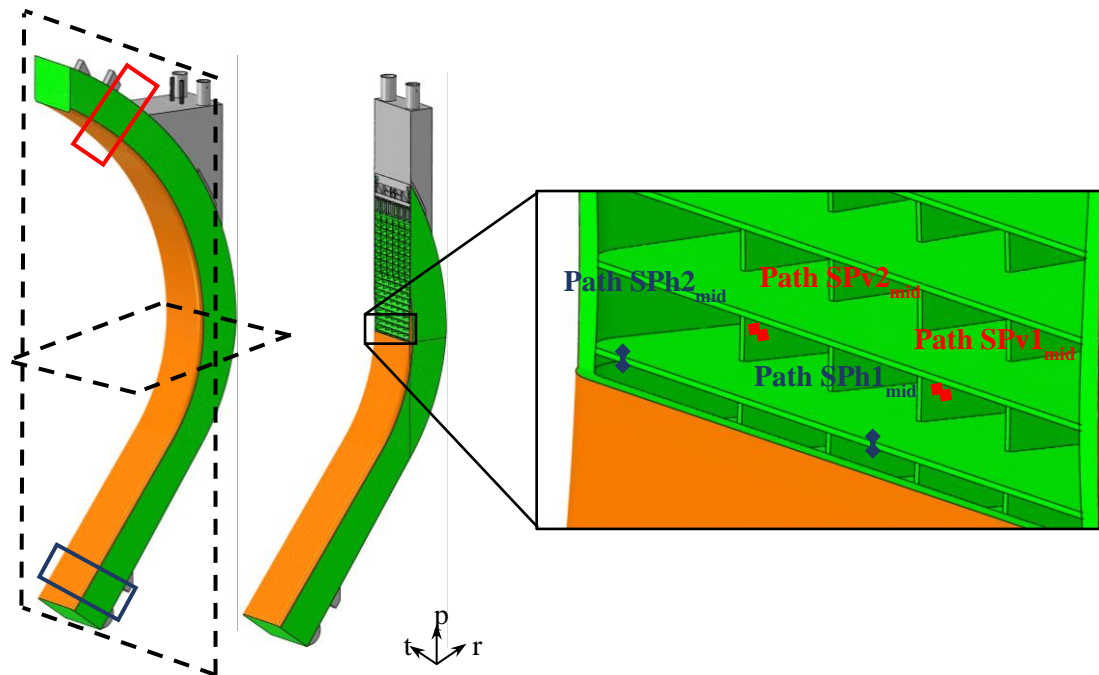


Figure 4.20 Paths within SPs grid in the equatorial region.

The obtained results are reported in Figure 4.21, Figure 4.22, Figure 4.23 and Figure 4.24. For each criterion, the ratio between the equivalent stress value and the corresponding stress limit is reported in the figures and values greater than 1 are highlighted in red, indicating that the criterion is not fulfilled within the selected path. The evaluation of the results of the RCC-MRx criteria, indicates that the vertical SPs are particularly stressed, in particular the path named SPv2, in the three poloidal heights of the Segment. In each considered loading scenario, these paths do not totally fulfil the criteria against the immediate plastic flow localization, namely the $(P_m+Q_m)/S_{em}$, unlike the path within the central poloidal-radial SP which, due to its lower average temperature, verifies this criterion in every operating scenario and at every segment height considered. Moreover, also the path SPH1, located in the central part of a horizontal SP, in the upper region does not fulfil the IPFL criterion, taken into account the secondary stresses, in the NO loading scenario. In any cases, in the other loading scenarios considered, the IPFL criterion evaluated along the “SPH1,top” path

reaches high value (>0.8). Globally, average temperatures are higher in the regions in which the criterion against the Immediate Plastic Flow Localization is not verified, as reported in Table 4.9. Therefore, high temperatures, together with the action of the selected attachment system, could contribute to the non-verification of these RCC-MRx criteria.

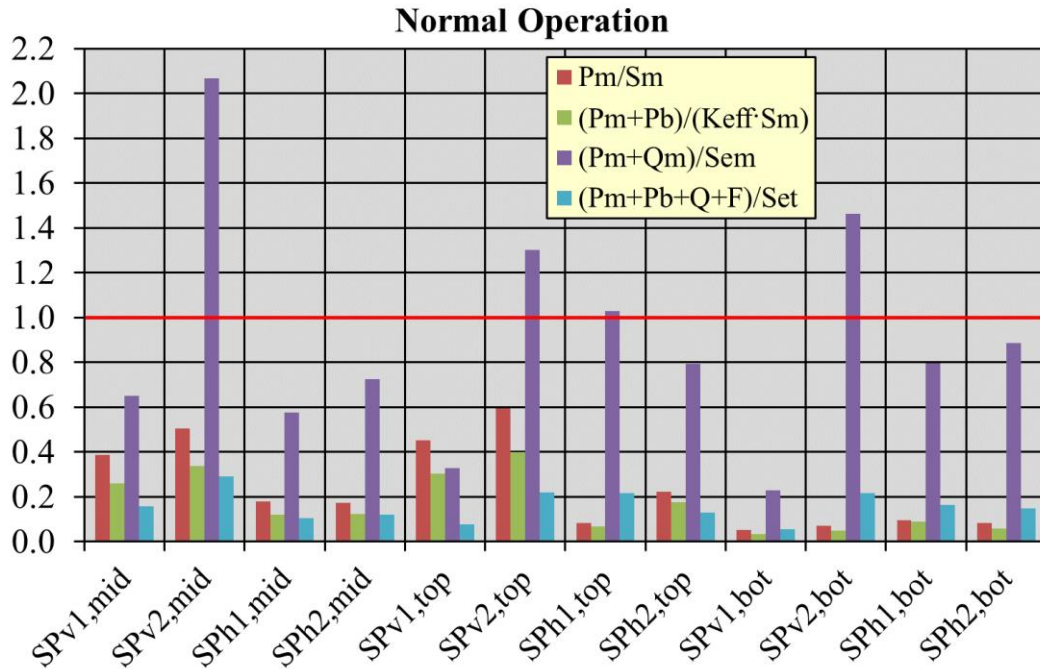


Figure 4.21 Verification of RCC-MRx criteria under NO loading scenario.

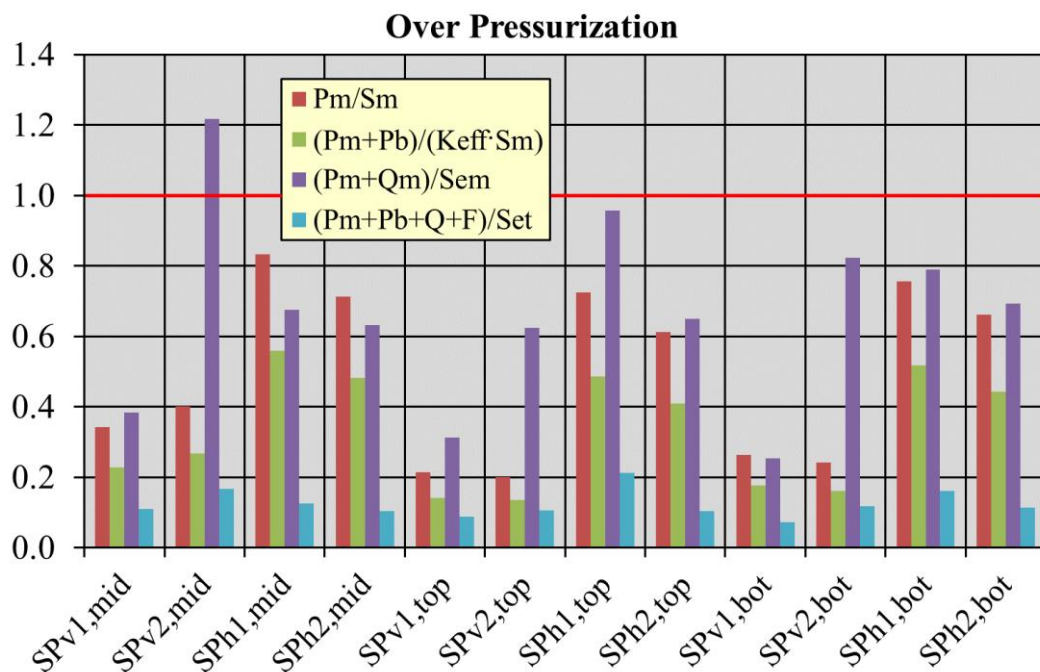


Figure 4.22 Verification of RCC-MRx criteria under OP loading scenario.

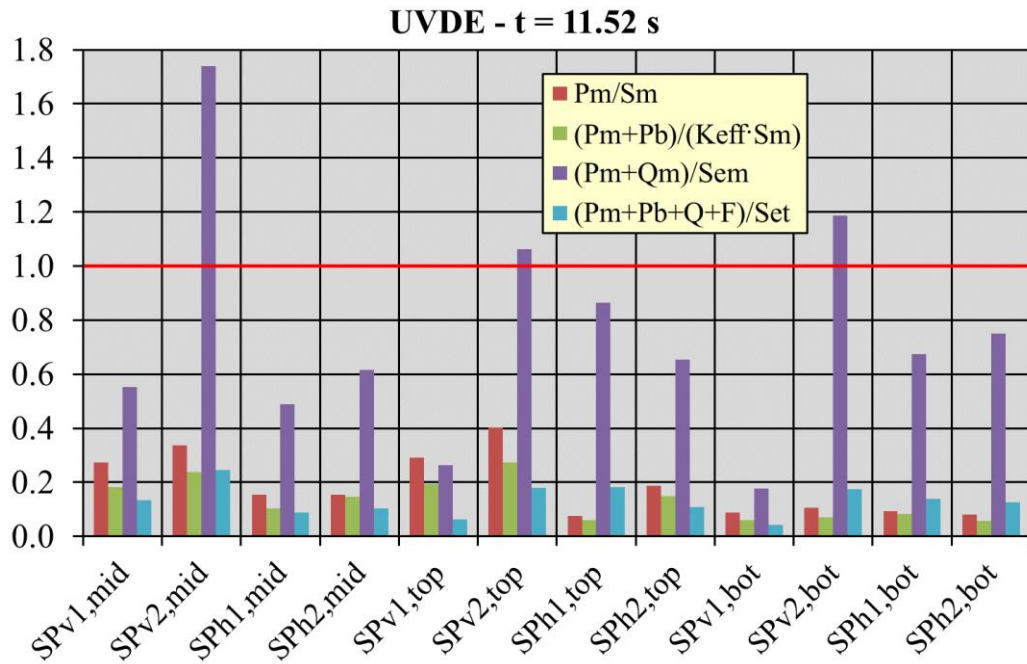


Figure 4.23 Verification of RCC-MRx criteria under UVDE - t=11.52 s loading scenario.

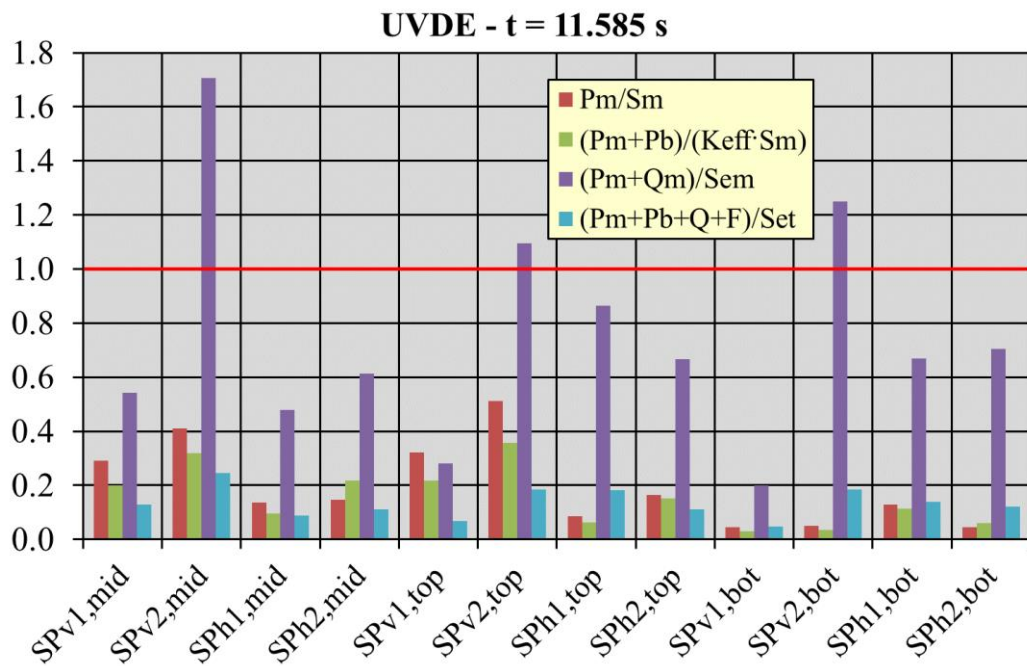


Figure 4.24 Verification of RCC-MRx criteria under UVDE - t=11.585 s loading scenario.

Path	SPh1 _{mid}	SPh2 _{mid}	SPv1 _{mid}	SPv2 _{mid}
T _{ave} [°C]	435.6	473.0	346.0	519.3
Path	SPh1 _{top}	SPh2 _{top}	SPv1 _{top}	SPv2 _{top}
T _{ave} [°C]	400.6	485.8	325.4	462.6
Path	SPh1 _{bot}	SPh2 _{bot}	SPv1 _{bot}	SPv2 _{bot}
T _{ave} [°C]	430.0	478.1	339.2	503.7

Table 4.9 Average temperature within the paths.

4.6 Thermo-mechanical analysis adopting the sub-modelling technique of some WCLL COB segment critical regions

Once investigated the overall structural behaviour of the WCLL COB segment under nominal and accidental loading scenarios, the sub-modelling technique has been adopted to assess in detail the structural performances of some regions of interest of the segment. Thanks to this approach, it is possible to assess the local thermo-mechanical behaviour of some regions of the segment imposing, as boundary conditions, the displacement field previously calculated in the analysis of the whole segment. In this way, it is possible to assign at the border of the local models a set of boundary conditions directly drawn for the segment global analysis, so to take realistically into account the deformative effect deriving from the rest of the segment on the investigated region. In this case, it is possible to perform a detailed analysis of the structural behaviour of the FW-SWs region. Indeed, in the whole segment geometric model considered in this work, the FW-SWs region is not equipped with cooling channels and, therefore, its structural performances cannot be assessed in view of RCC-MRx criteria. Using the sub-modelling technique, it is then possible to assess in detail the stress level arising within a local FW-SWs region equipped with purposely designed cooling channels, also taking into account the effect of the rest of the segment in addition to the proper loads acting on it. Moreover, the local analysis can rely on a finer mesh, allowing to increase the level of reliability of the results.

4.6.1 The FEM models

In order to investigate the structural behaviour of the COB segment more in detail, since some details are absent in the global model analysis, the sub-modelling technique has been used to analyse certain regions at different poloidal heights of the segment. In particular, a set of three elementary cells has been individuated within the upper, middle and lower part of the segment (highlighted in red in Figure 4.25), corresponding to O1, O4 and O7 region according to the ideal poloidal segmentation showed in Figure 4.1. Each model has been equipped with the cooling channel into the SW-FW-SW region, on the basis of the region they belong to: 4 channels for the upper and middle regions and 6 channels for the lower one. Neither Baffle Plates nor DWTs have been modelled because of their no significant structural role, as aforementioned. The cells triplets have been obtained by cutting the whole COB model by means of plane passing through the middle of the upper and lower toroidal-radial SPs of each region, in order to apply the sub-modelling technique in Abaqus. So, three FEM models of ~2.5M nodes connected in ~2M hexahedral elements have been set up.

Comparing the mesh set-up in the sub-models with that of the global model in the analogous poloidal positions (Figure 4.26), the increased level of detail of such a kind of analysis become immediately clear.

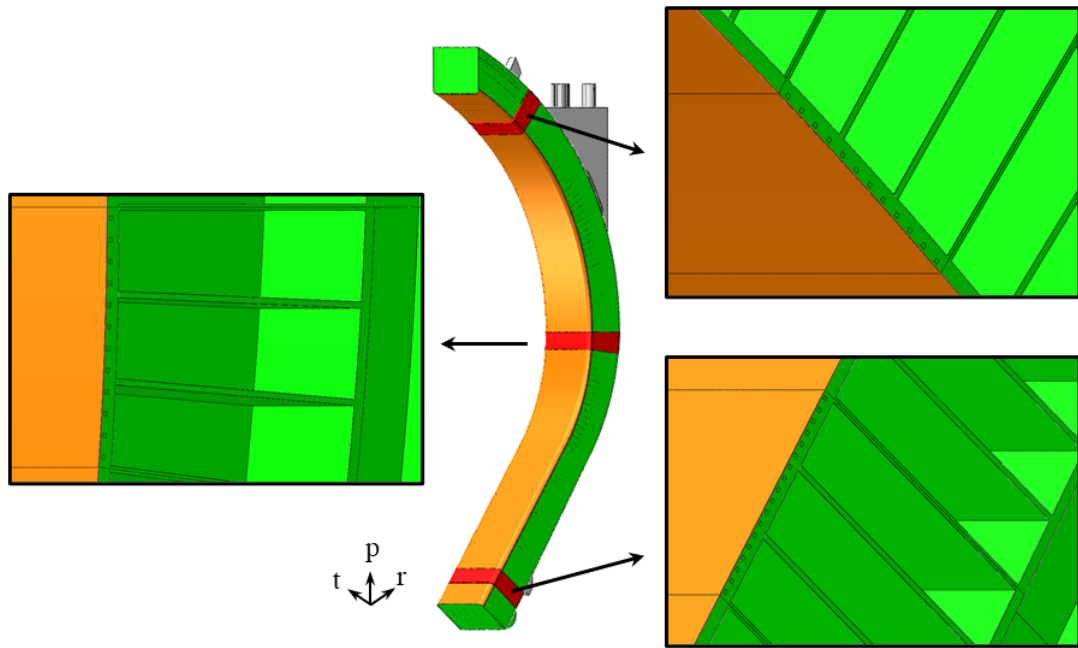


Figure 4.25 Models of Top, Central and Bottom cells

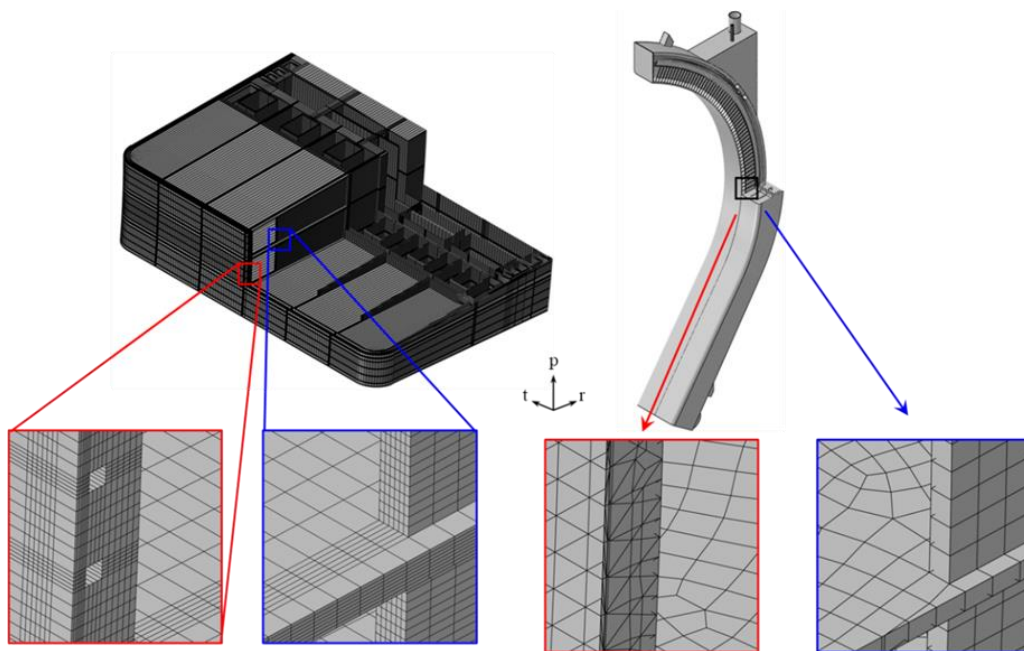


Figure 4.26 Mesh of the sub-model vs mesh of the global model in the equatorial region.

4.6.2 Loads and Boundary Conditions

The three models representing the upper, middle and lower region of the COB segment have been studied under NO, OP and UVDE (considering two different time steps) steady

state loading scenarios, as already done for the entire segment analysis. In order to correctly reproduce these scenarios, the following loads and boundary conditions have been considered:

- Thermal deformation field;
- Gravity load;
- Internal pressure distribution;
- Electro-magnetic loads;
- Mechanical restraints.

The thermal deformation fields arising as consequence of the non-uniform interpolated temperature distribution, obtained from the cooling layout optimization of each poloidal region and the following “multi-regions” interpolation, have been applied onto the three models with respect of the belonging region (Figure 4.27).

The weight force has been taken into account imposing the gravity load to each model. Moreover, the structural material Eurofer has been considered, and the temperature dependent property have been adopted [56]. The density values have been properly modified in order to take into account the presence of breeder and water by means of a purposely calculated temperature-dependent equivalent density.

With regard to the internal pressure, to simulate the presence of the breeder and the coolant, in NO and UVDE loading scenarios a pressure of 17.825 MPa has been imposed within every cooling channel inside the SW-FW-SW region, instead a pressure of 0.575 MPa has been considered for all the internal SB surfaces wetted by the breeder. During the OP loading scenario, as it represents a coolant leak event (LOCA accident), a pressure of 17.825 MPa has been applied onto both water and breeder-wetted surfaces.

The EM loads related to the NO, OP and UVDE scenarios have been taken into account. In NO and OP scenarios, only the ferromagnetic loads contribution is considered. Instead, as already done for the whole segment analysis, the EM loads of two different time steps have been considered for the UVDE scenario, in particular for $t=11.52$ s and $t=11.585$ s, relative to the maximum of the radial forces and moment respectively. Hence, the accidental EM loads have been added to the ferromagnetic ones.

Finally, the sub-model technique in Abaqus consists in applying the displacements values along the three directions (u_r , u_t and u_p) in the respective regions of the global model to the nodes of the two cutting (i.e., boundary) surfaces of each sub-model. So, thanks to this technique, the cells triplets analysed take into account the thermo-mechanical response of the entire segment. Of course, the proper displacement spatial distribution has been applied depending on the loading scenario considered. As an example, in Figure 4.28 and Figure

4.29 the displacement field applied onto upper and lower surfaces in NO scenario for the central cells sub-model is depicted.

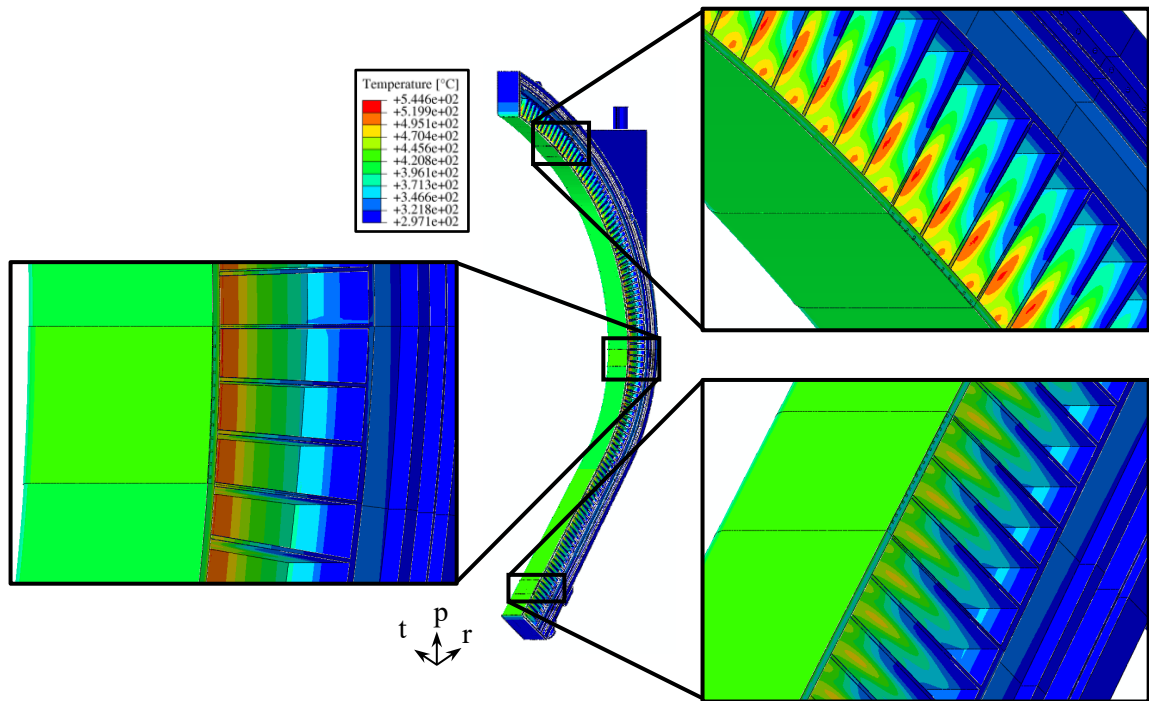


Figure 4.27 Temperature field onto Top, Central and Bottom models superimposed to the global model.

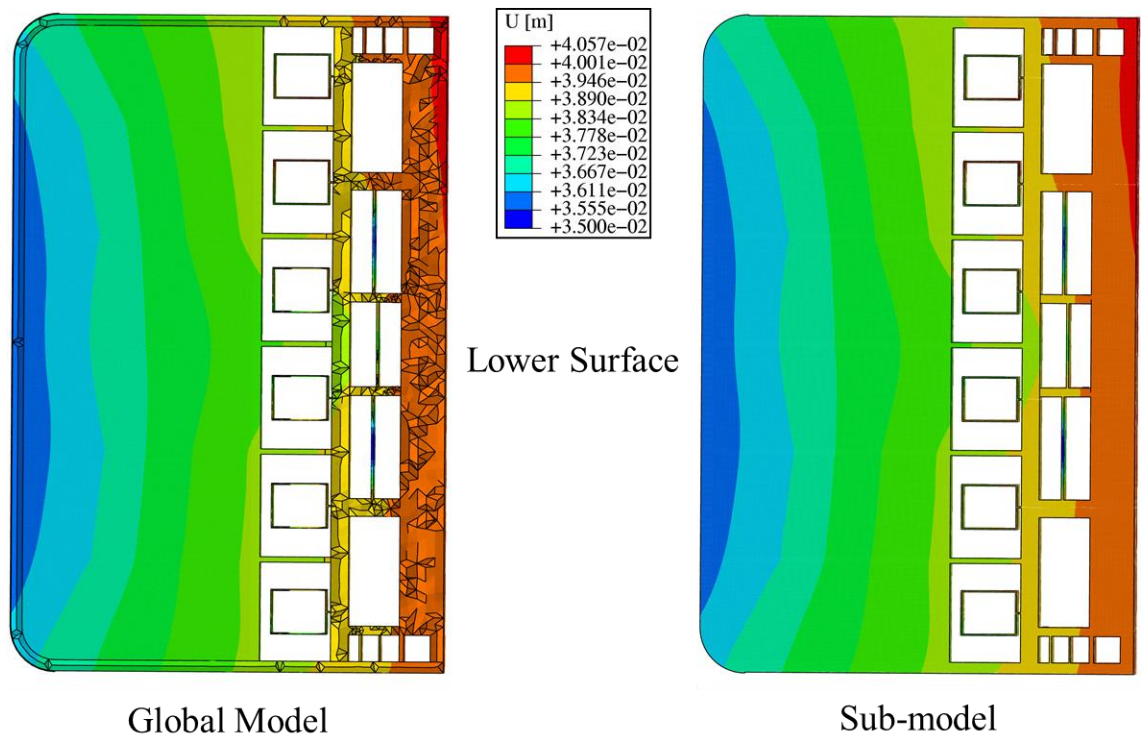


Figure 4.28 Displacement field in global model and sub-model applied in NO scenario to the lower boundary of the central cells sub-model.

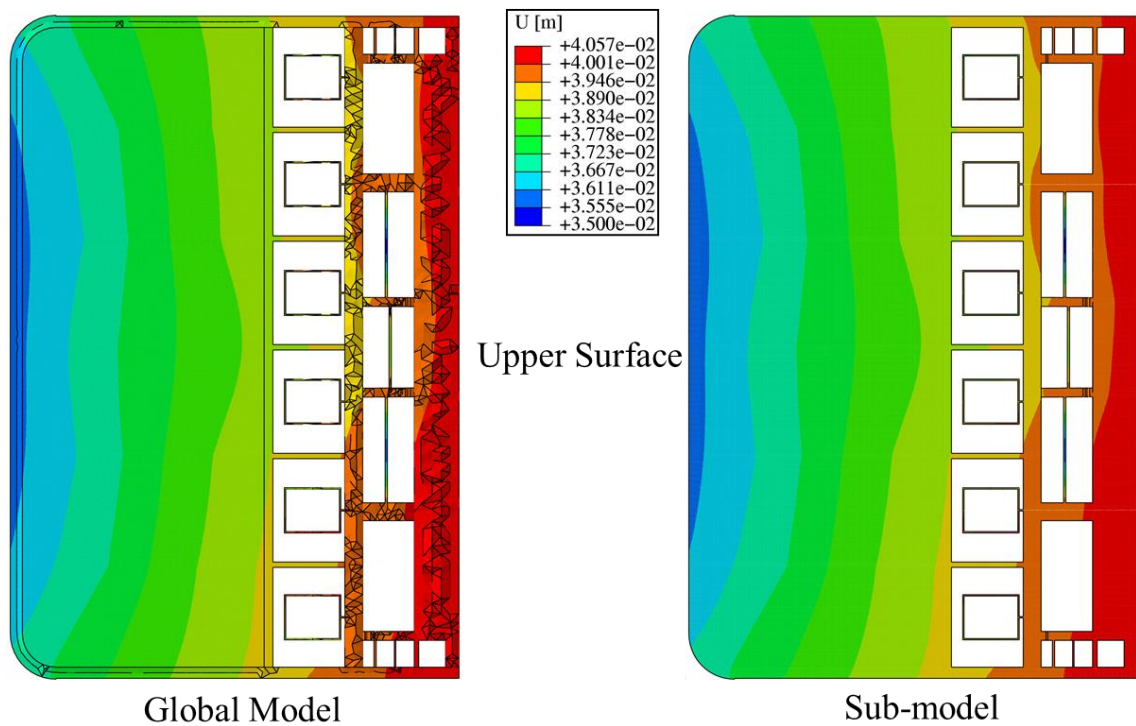


Figure 4.29 Displacement field in global model and sub-model applied in NO scenario to the upper boundary of the central cells sub-model.

4.6.3 Results

Steady state analyses have been run in order to assess the thermo-mechanical behaviour of three regions of interest of the WCLL COB segment under the selected NO, UVDE and OP loading scenarios, related to Level A, C and D service of level of RCC-MRx structural design code, respectively. In Figure 4.30, Figure 4.31, Figure 4.32 and Figure 4.33 the Von Mises equivalent stress field of the three regions analysed, namely Top, Central and Bottom cells, superimposed to the entire COB model response (calculated from the whole segment analysis previously reported), are depicted.

The obtained results have been analysed and a stress linearization procedure has been performed in order to verify the fulfilment of the RCC-MRx design criteria corresponding to the Level A, Level C and Level D. Therefore, a proper set of paths has been selected, looking at the Von Mises equivalent stress field spatial distribution, in correspondence of the most stressed region of each model. In particular, localised peaks of Von Mises equivalent stress value occur at the points of application of the electromagnetic forces and should not be taken into account for the evaluation of the RCC-MRx design criteria. As reported in Figure 4.34, showing the paths selected in the Central Cells (CC) model, six

paths have been selected within the FW and SW region. The same set of paths has been considered in the Top and Bottom Cells (TC and BC, respectively) models.

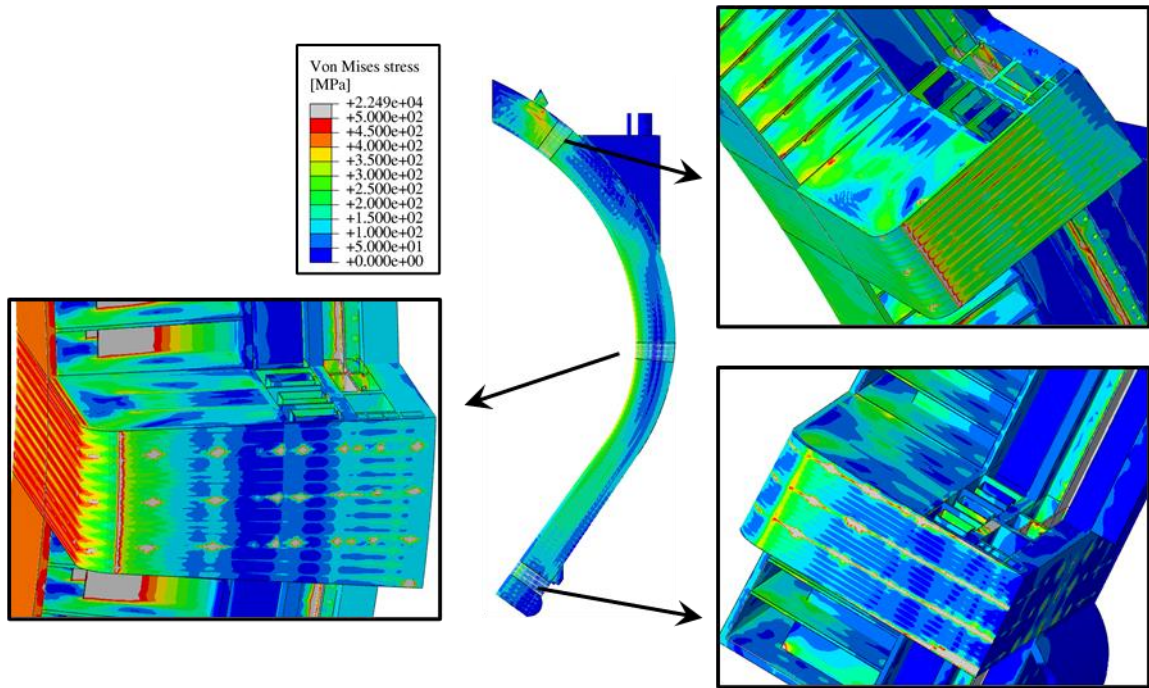


Figure 4.30 Von Mises stress field onto Top, Central and Bottom models in NO superimposed to the global model.

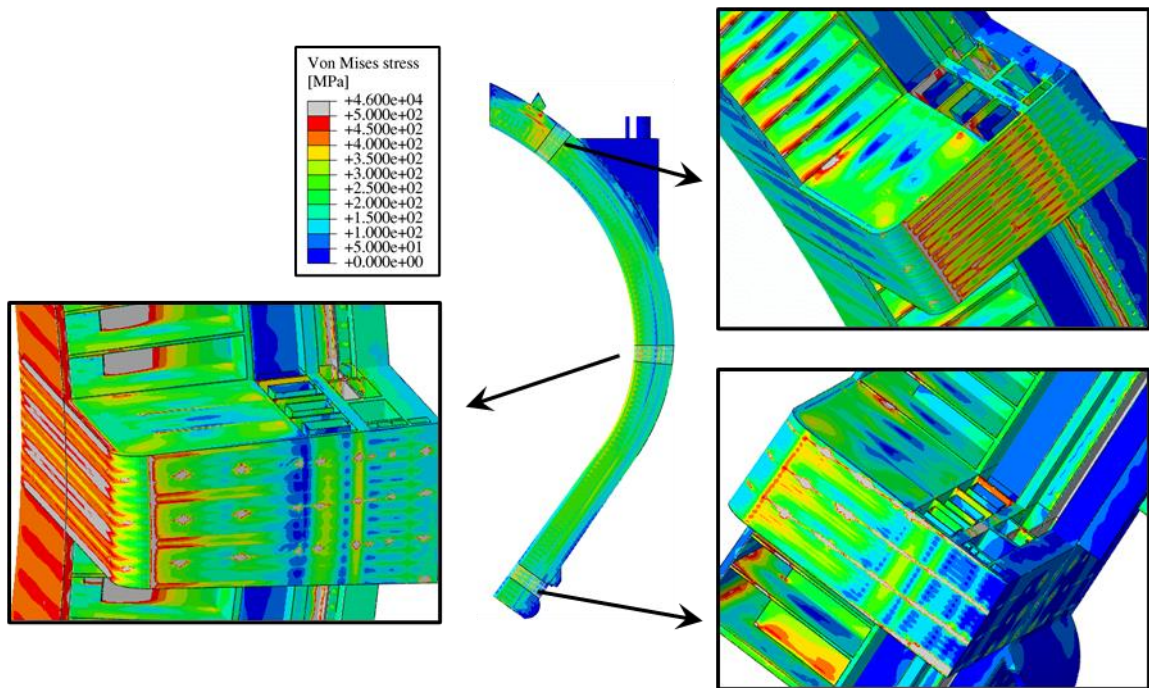


Figure 4.31 Von Mises stress field onto Top, Central and Bottom models in OP superimposed to the global model.

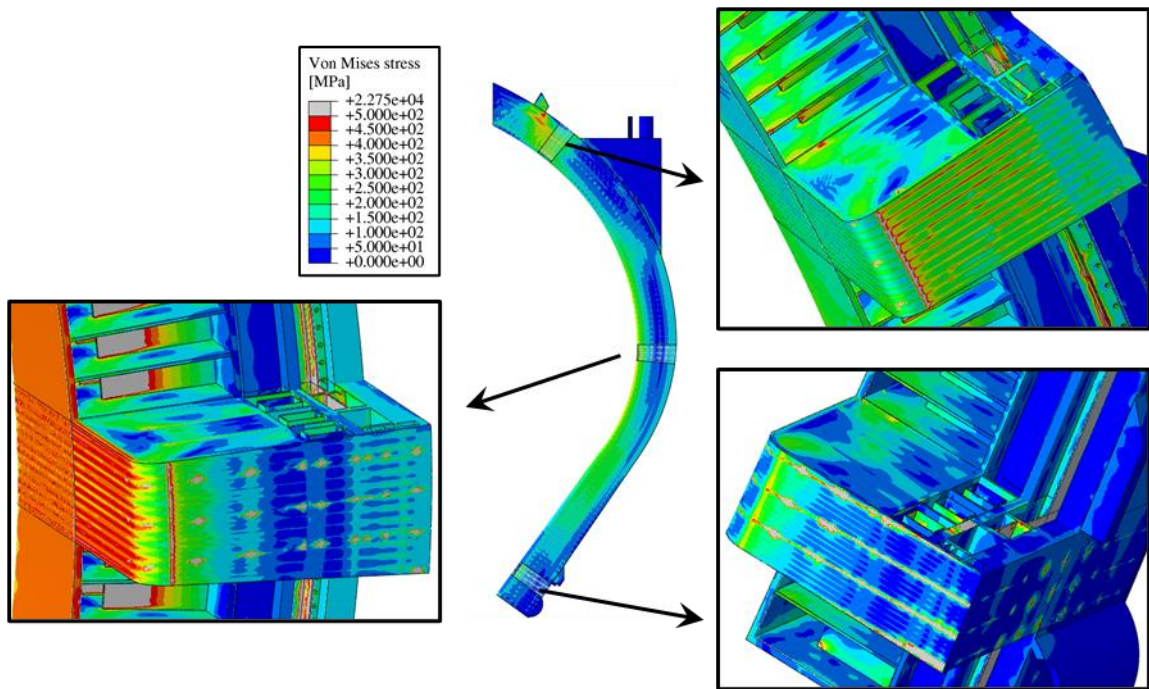


Figure 4.32 Von Mises stress field onto Top, Central and Bottom models in UVDE (t=11.52 s) superimposed to the global model.

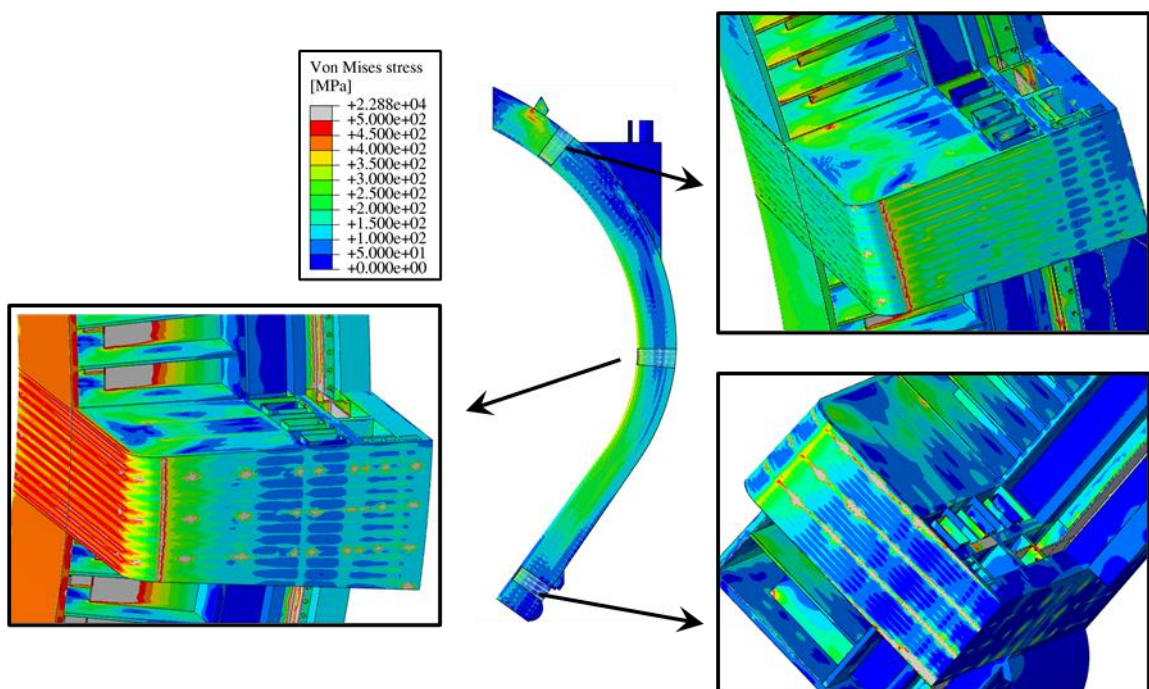


Figure 4.33 Von Mises stress field onto Top, Central and Bottom models in UVDE (t=11.585 s) superimposed to the global model.

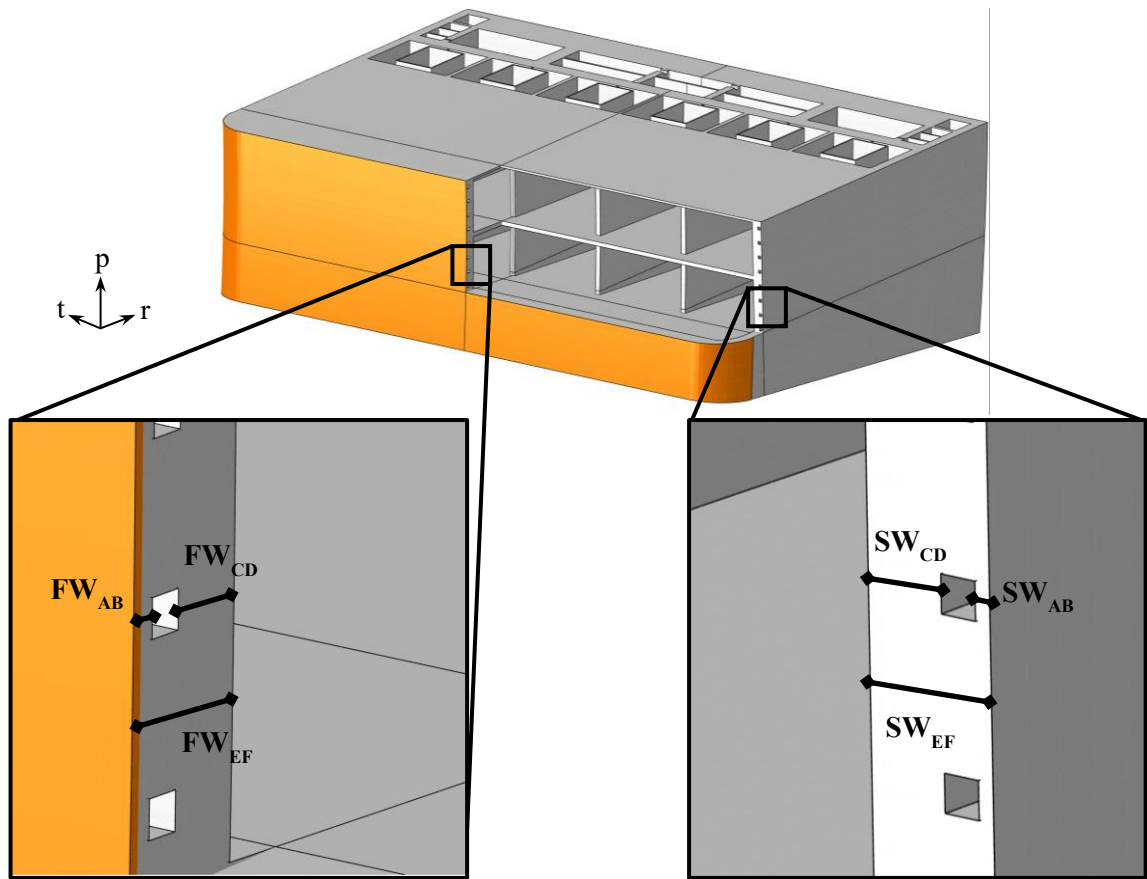


Figure 4.34 Paths selected within FW-SW region in TC model.

A stress linearization procedure has been performed and the equivalent stress value obtained within each path has been compared to the stress limits prescribed by the RCC-MRx design criteria. As already done, four criteria have been taken into account for the evaluation: Immediate Excessive Deformation (IED), Immediate Plastic Instability (IPI), Immediate Plastic Flow Localization (IPFL) and Immediate Fracture due to exhaustion of ductility (IF). The obtained results have been summarized in Figure 4.35, Figure 4.36, Figure 4.37 and Figure 4.38, reporting the ratio between the equivalent stress values and the corresponding stress limits for each criterion.

Results show that all the paths within the TC and BC models fulfil the selected criteria but two paths (namely SW_{AB} and SW_{CD}) in which the ratio $(P_m+Q_m)/S_{em}$ come close to (>0.9) and exceed the limit. In particular, the IPFL criterion evaluated within the SW_{AB} path within the upper region of the segment is not fulfilled in NO, OP and UVDE ($t=11.52s$) loading scenario, far exceeding the limit. Beyond these exceptions, all of the selected criteria of the RCC-MRx design code evaluated along the other paths identified along the SW region are largely verified. Moreover, all the paths selected within the CC model fulfil the IED, IPI and IF criteria, instead all the paths on the FW region do not verify the criteria against the

immediate plastic flow localization, taking into account the secondary stresses, reaching high values of the ratio.

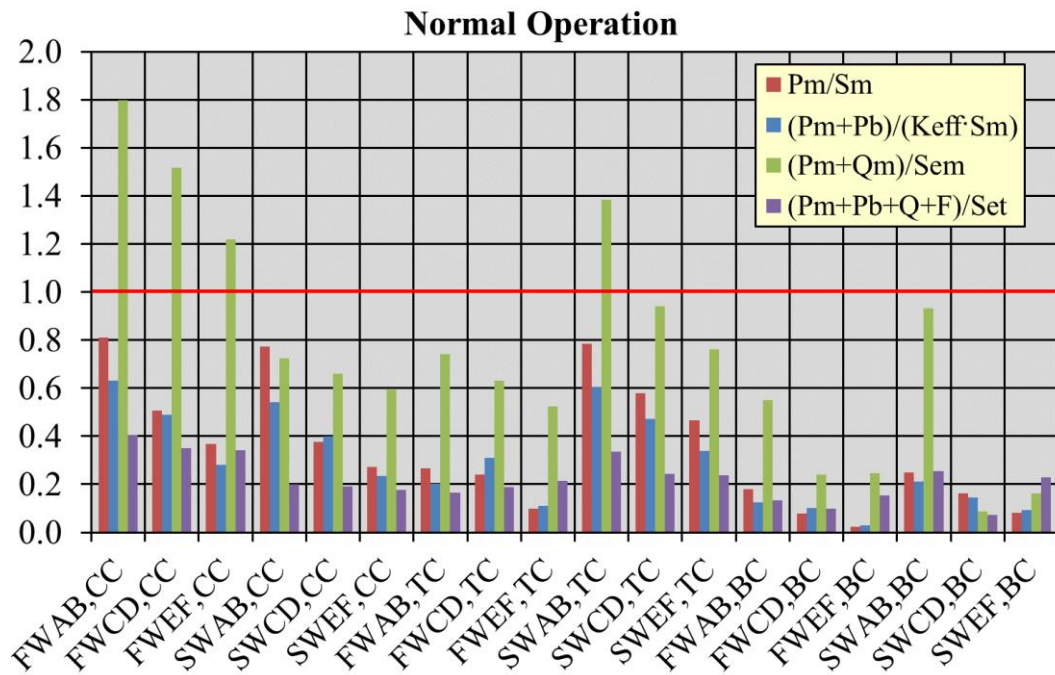


Figure 4.35 RCC-MRx criteria verification in NO loading scenario.

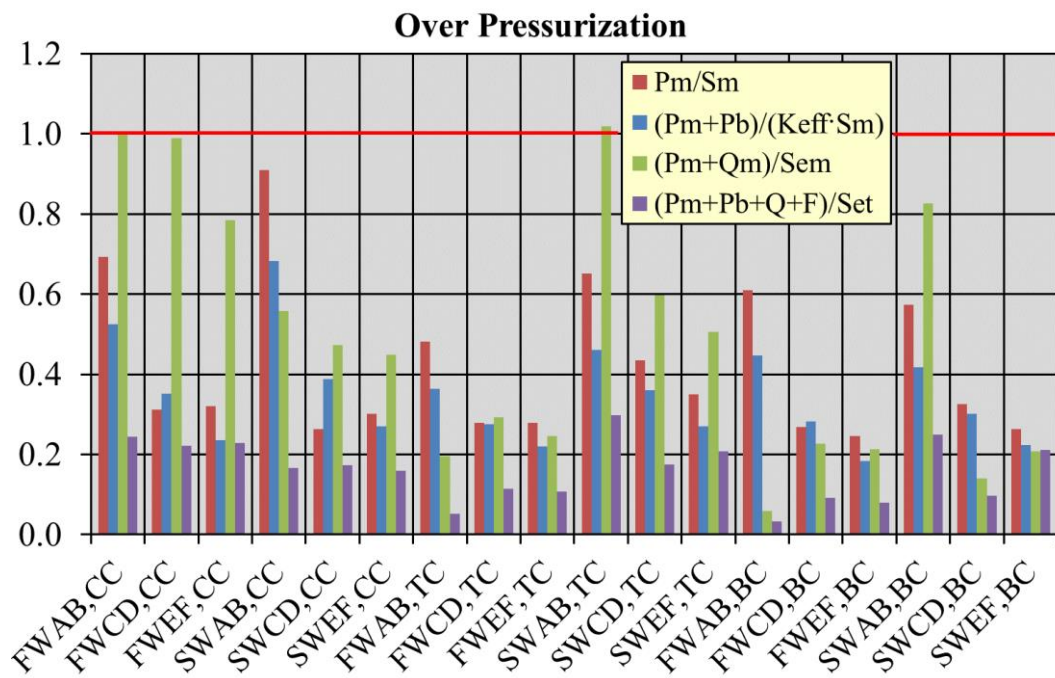


Figure 4.36 RCC-MRx criteria verification in OP loading scenario.

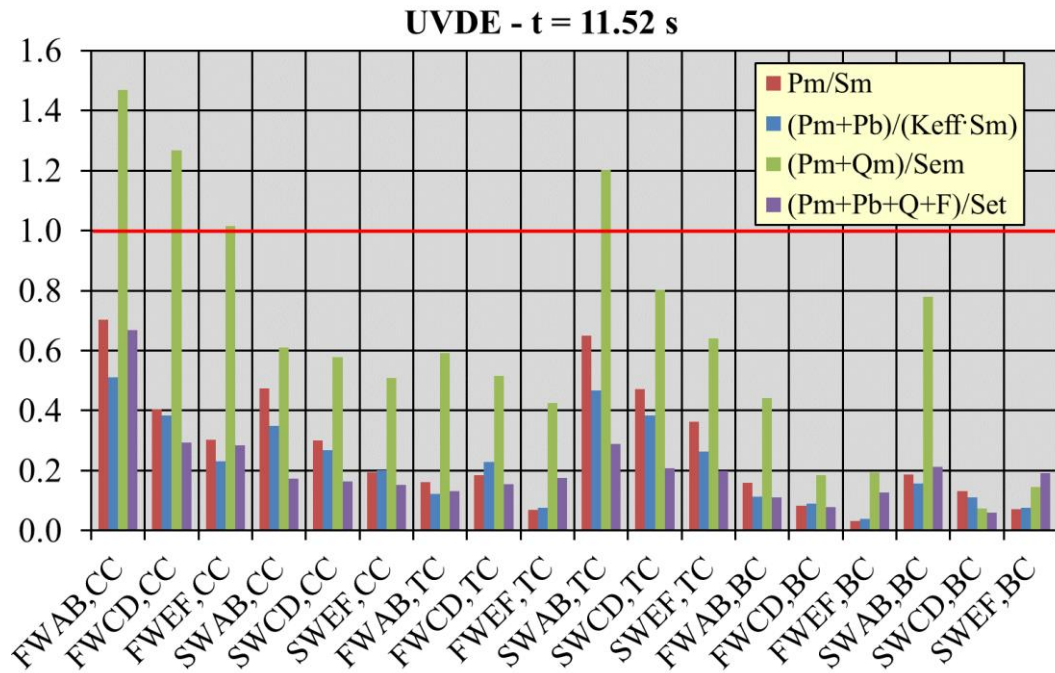


Figure 4.37 RCC-MRx criteria verification in UVDE (t=11.52 s) loading scenario.

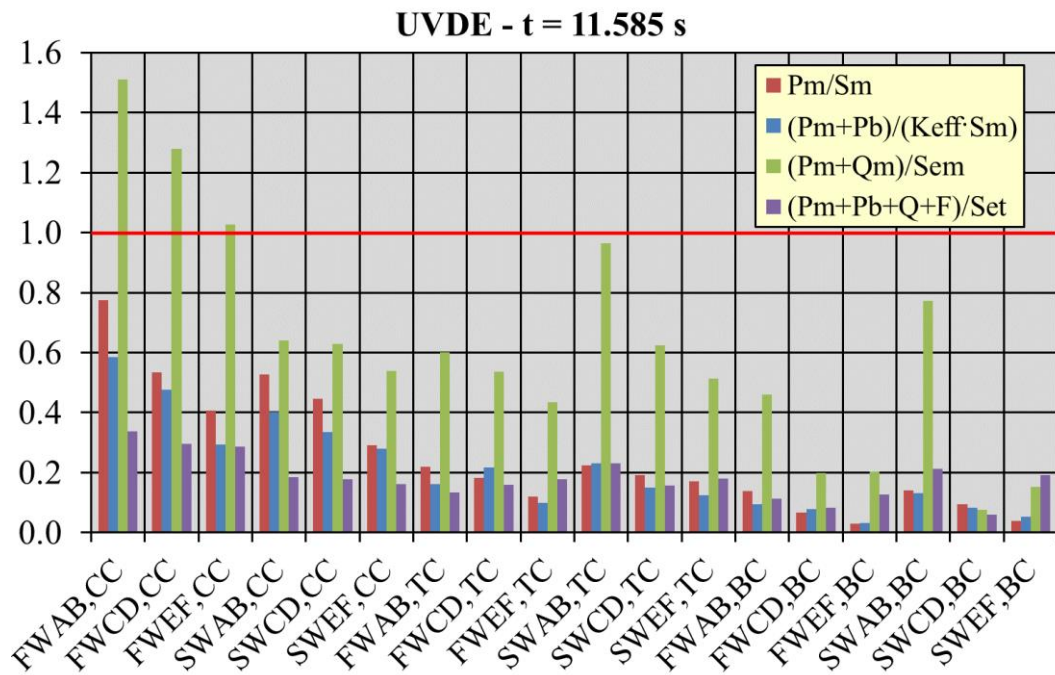


Figure 4.38 RCC-MRx criteria verification in UVDE (t=11.585 s) loading scenario.

In the previous chapter, in which the multiscale procedure has been presented, it was observed that comparing the results of the stress linearization and the evaluation of the RCC-MRx design criteria obtained along the same SPs paths, when the stresses are evaluated in the global and in the sub-models, show a very similar behaviour. Since the same behaviour is observed applying the multiscale procedure to the conceptual design of the WCLL COB segment, the results of those comparison are not reported for brevity. Hence, this allow

concluding that, in the sub-modelling analysis, the attention and the modelling effort can be focussed on the FW-SWs region since the global analysis already give reliable results concerning the SPs domain.

The verification of the RCC-MRx criteria has allowed confirming the results obtained from the global analysis on the whole segment. In fact, the most critical region is still the equatorial one, where a remarkable radial deformation arises due to the geometric layout of the attachment system. In the other regions, the predicted structural behaviour seems to be promising. Hence, a deep revision of the geometric configuration of the attachments seems to be helpful in order to reduce the stress level within the WCLL COB segment, not only within SPs but also within the FW-SWs regions.

In conclusion, in this chapter, the multiscale procedure has been applied for the conceptual design of the WCLL COB segment. This alternative procedure permits to obtain a complete and detailed response of the thermomechanical behaviour of the segment. On the one hand, the thermal field of the entire segment has been obtained by means of local thermal analysis of its portions, while, on the other hand, particular and critical regions of the segment have been studied by using reliable loads and boundary conditions.

Conclusion

The research activity carried out during the XXXIV cycle of Ph.D. course in Energy and Information Technologies – nuclear engineering and applied physics curriculum held at the Department of Engineering (DI) of the University of Palermo has been framed within the design activities concerning the DEMO nuclear fusion reactor, focussing on the development of a multiscale design procedure in support of the WCLL BB conceptual design. The research activity reported in this Thesis has been carried out under the umbrella of the EUROfusion consortium, supported by the European research programmes Horizon2020 and Horizon Europe. In fact, the University of Palermo is fully involved in the EUROfusion consortium, being one of the ENEA's affiliated entities.

In particular, the work has been focussed on the study of the thermal and thermo-mechanical behaviour of the Central Outboard Blanket (COB) Segment of the DEMO Water Cooled Lithium Lead Breeding Blanket (WCLL BB), purposely developing and adopting a multiscale analysis procedure able to overcome the design limitations due to lack of maturity of the reference pre-conceptual design and allowing significantly to evolve the design toward the conceptual stage.

The first part of the research activity carried out during the Ph.D. course has been focussed on the development of the above said multiscale procedure, allowing to predict a 3D temperature spatial distribution in the whole segment starting from thermal analysis on local regions, evaluating the global structural response of the segment and then assessing in detail some local regions to investigate their structural performances taking into account, at their boundaries, the mechanical effect of the whole segment. In other words, the developed multiscale procedure is able to work in double direction, going from local to global models and vice-versa to fully characterise, from the thermal and thermo-mechanical standpoints, the assessed WCLL COB segment.

In particular, once carried out the 3D thermal field that arises in one elementary cell of the WCLL COB, an interpolation procedure capable of reproducing with a high level of confidence the calculated 3D temperature distribution has been set-up, dividing the assessed domain in a certain number of regions and obtaining, within each region, an interpolating

function of the radial and toroidal variable. Then, statistical assessments have allowed checking the error amount in the temperature and secondary stress prediction using the set of interpolating functions. Once verified that the error between the calculated temperature and secondary stress 3D fields and the analogous fields coming from the interpolation procedure (as to the stress fields, it is calculated imposing the interpolated thermal field) can be considered acceptable, the dependence on the poloidal coordinate has been introduced and the interpolating functions have been used to impose a thermal field to the whole WCLL COB segment. Then, the structural analysis under different steady state loading scenarios of the segment has been performed and, in the end, thanks to the application of the sub-modelling technique, the in-depth investigation of the thermo-mechanical performances of some local regions of interest, imposing at their boundaries the displacement field calculated in the global structural analysis, has been performed comparing the results with the reference RCC-MRx design criteria.

In the second part of the research activity carried out during the Ph.D. course, the developed multiscale analysis procedure has been applied to the design of the WCLL COB segment, starting from its pre-conceptual reference layout and improving it toward the achievement of the conceptual stage. To this purpose, considering the ideal subdivision of the segment in 7 poloidal regions in order to consider the poloidal variation of the thermal loads (i. e. heat flux onto the SB, nuclear power density and decay heat power density), 7 elementary cells (each one at a different poloidal position) have been assessed from the thermal point of view. Once verified that the pre-conceptual design was not able to fully withstand the poloidal-dependent thermal loads fulfilling the suggested thermal requirement (i. e. maximum Eurofer temperature in structural components lower than 550 °C), an optimization procedure has been performed in order to find alternative layouts for the Segments Box cooling channels (whether necessary) and the Breeding Zone cooling tubes able to fulfil the above said requirement. To this end, alternative DWTs spatial arrangements have been introduced in the design to cope with the poloidal variation of the thermal loads as well as the number of SB channels per elementary slice have been slightly increased in the segment's lower region. Then, once thermally optimized the 7 elementary cells (each representative of the 7 WCLL COB poloidal regions), the resulting thermal fields have been used to derive 7 sets of interpolating functions which have been stitched together to assign a 3D thermal field to the WCLL COB segment. Afterwards, the structural analysis of the segment under selected steady state loading scenarios have been performed and, in the end, applying the sub-modelling technique, the in-depth investigation of the thermo-mechanical performances of some regions of interest has been carried out, allowing to highlight some

criticalities to be faced in the follow up of the conceptual design activities. In particular, it has been found that the attachment system devoted to connecting the BB to the vacuum vessel should be re-designed in order to avoid an excessive deformation in the equatorial region, which mainly results in the not-fulfilment of the RCC-MRx design criteria in that region.

In conclusion, the research activity performed in the Ph.D. course in Energy and Information Technologies has allowed improving the thermo-mechanical performances of the WCLL COB segment reference design configuration, contributing to the development of a sound geometric layout able to withstand the prescribed design criteria and requirements and moving from the pre-conceptual layout toward the achievement of the conceptual design stage. Moreover, the developed multiscale procedure gave a great contribution in the framework of the DEMO WCLL BB research activities and, furthermore, could be applied to other segments of the BB or other blankets concepts, as already done (in a separate work, here not reported for the sake of brevity) for the WCLL Left Outboard Blanket segment. In fact, the developed procedure allows to realistically predict the thermal field for an entire BB segment without performing a full and detailed thermal-hydraulic assessment (often not possible due to lack of maturity of the segment design), evaluate its thermo-mechanical performances to be used as boundary conditions to assess in-depth some local regions (which can be modelled more in detail than the segment due to their limited extension). In such a way, the research campaigns aimed at the design of the BB can take into account a higher number of alternatives and/or variants, proceeding more rapidly toward the completion of the conceptual design phase.

References

- [1] https://www.euro-fusion.org/fileadmin/user_upload/EUROfusion/Documents/2018_Research_roadmap_long_version_01.pdf
- [2] L. Barucca et al., Pre-conceptual design of EU DEMO balance of plant systems: Objectives and challenges, *Fusion Engineering and Design*, (169) 2021, 112504, DOI: 10.1016/j.fusengdes.2021.112504
- [3] https://commons.wikimedia.org/wiki/Image:Binding_energy_curve_-_common_isotopes.svg?uselang=it
- [4] T. Dolan, *Fusion Research: principles, experiments and technology*, Pergamon Press, 1982
- [5] A.A. Harms, K. F. Schoepf, G. H. Miley, D. R. Kingdon, *Principles of Fusion Energy*, World Scientific Publishing Co, 2002
- [6] M. Rubel, Fusion Neutrons: Tritium Breeding and Impact on Wall Materials and Components of Diagnostic Systems, *Journal of Fusion Energy*, (38) 315–329 (2019), DOI: 10.1007/s10894-018-0182-1
- [7] https://inis.iaea.org/collection/NCLCollectionStore/_Public/33/001/33001691.pdf
- [8] C. Bachmann et al., Initial DEMO tokamak design configuration studies, *Fusion Engineering and Design*, 98-99 (2015), 1423-1426, DOI: 10.1016/j.fusengdes.2015.05.027
- [9] T. Klinger et al., Overview of first Wendelstein 7-X high-performance operation, *Nuclear Fusion*, 59 (2019), 112004, DOI: 10.1088/1741-4326/ab03a7
- [10] A. Iiyoshi et al., Overview of the Large Helical Device project, *Nuclear Fusion*, 39 (1999), 1245, DOI: doi.org/10.1088/0029-5515/39/9Y/313
- [11] F. Romanelli, *Fusion electricity, a roadmap to the realization of fusion energy*, European Fusion Development Agreement, EFDA, November 2012, ISBN 978-3-00-040720-)

- [12] F. Giannetti et al., BOP-2.2-T034-D001, WCLL PHTS&BOP with Small ESS Design Overview (Direct Coupling Option), IDM Ref. EFDA_D_2N995W v1.0, April 2020
- [13] V. Narcisi et al., Analysis of the EU-DEMO WCLL Power Conversion System in Two Relevant Balance of Plant Configurations: Direct Coupling with Auxiliary Boiler and Indirect Coupling, *Sustainability* (2022), 14 (10), 5779, DOI: 10.3390/su14105779
- [14] C. Bachmann, Plant Description Document, IDM Ref. EFDA_D_2KVVQZ, 2018
- [15] I. Moscato et. al., Tokamak cooling systems and power conversion system options, *Fusion Engineering and Design*, (178) 2022, 113093, DOI: 10.1016/j.fusengdes.2022.113093
- [16] F.A. Hernández et al., Consolidated design of the HCPB Breeding Blanket for the pre-Conceptual Design Phase of the EU DEMO and harmonization with the ITER HCPB TBM program, *Fusion Engineering and Design*, (157) 2020, 111614, DOI: 10.1016/j.fusengdes.2020.111614
- [17] A. Del Nevo, P. Arena, BB.WCLL-JUS-2-CD1-BB WCLL Design Description Document (DDD), IDM Ref. EFDA_D_2NGB4U, 2020
- [18] J. Aubert, G. Aiello, A. Li Puma, A. Morin, A. Tincani, R. Giammusso, P.A. di Maio, Preliminary design a Water Cooled Lithium Lead blanket concept for DEMO reactor, IDM Ref. EFDA_D_2L7HFV, 2013.
- [19] R. Wenninger, G. Federici, DEMO1 Reference Design - 2015 April ("EU DEMO1 2015"), IDM Ref. EFDA_D_2LBJRY, 2015.
- [20] G. Bongiovì et al., Multi-Module vs. Single-Module concept: Comparison of thermomechanical performances for the DEMO Water-Cooled Lithium Lead breeding blanket, *Fusion Engineering and Design*, 136 (2018) 1472-1478, doi: 10.1016/j.fusengdes.2018.05.037.
- [21] R. Wenninger, DEMO1 Reference Design - 2017 March ("EU DEMO1 2017"), IDM Ref. EFDA_D_2NE9JA, 19 June 2017.
- [22] R. Forte et al., Preliminary design of the top cap of DEMO Water-Cooled Lithium Lead breeding blanket segments, *Fusion Engineering and Design*, (161) 2020, 111884, DOI: 10.1016/j.fusengdes.2020.111884
- [23] A.F. Tavassoli et al. *Journal of Nuclear Materials* 329–333 (2004) 257–262
- [24] D. Stork et al., Materials R&D for a timely DEMO: Key findings and recommendations of the EU Roadmap Materials Assessment Group, *Fusion*

- Engineering and Design, (89) 2014 1586-1594, DOI: 10.1016/j.fusengdes.2013.11.007
- [25] G. Yu et al., Thermal creep behaviour of the EUROFER 97 RAFM steel and two European ODS EUROFER 97 steels, *Fusion Engineering and Design*, (75-79) 2005, 1037-1041, DOI: 10.1016/j.fusengdes.2005.06.311
- [26] A.F. Tavassoli et al., Current status and research achievements in ferritic7martensitic steels, *Journal of Nuclear Materials* (455) 2014, 269-276, DOI: 10.1016/j.jnucmat.2014.06.017
- [27] E. Gaganidze, J.Aktaa, Assessment of neutron irradiation effects on RAFM steels, *Fusion Engineering and Design*, (88) 2013, 118–128, DOI: 10.1016/j.fusengdes.2012.11.020
- [28] P. Marmy, Low Cycle fatigue and creep-fatigue of Eurofer 97, EFDA Technology Work programme, 2003
- [29] <https://www.sciencedirect.com/topics/engineering/elasticity-theory>
- [30] Abaqus Analysis User's Guide: Online Documentation. Version 6.14-2, Providence, RI, Simulia, Dassault System
- [31] RCC-MRx, Design and Construction Rules for Mechanical Components in high-temperature structures, experimental reactors and fusion reactors, Tome 1 Sect. III Subsect. B, AFCEN, 2012.
- [32] The American Society of Mechanical Engineers (ASME), Boiler and Pressure Vessel Code, 2015 Edition
- [33] S. D'Amico et al., Preliminary thermal-hydraulic analysis of the EU-DEMO Helium-Cooled Pebble Bed fusion reactor by using the RELAP5-3D system code, *Fusion Engineering and Design*, Vol. 162, 2021, pp. 112111, <https://doi.org/10.1016/j.fusengdes.2020.112111>.
- [34] P. Arena et al., The DEMO Water-Cooled Lead-Lithium Breeding Blanket: design status at the end of the Pre-Conceptual Design Phase, *Applied Sciences*, 11 (24), 11592, 2021, <https://doi.org/10.3390/app112411592>.
- [35] R. Forte et al., On the effects of the Double-Walled Tubes lay-out on the DEMO WCLL breeding blanket module thermal behaviour, *Fusion Engineering and Design*, vol. 146 part A, 2019, 883-886M, <https://doi.org/10.1016/j.fusengdes.2019.01.105>.
- [36] P.A. Di Maio et al., On the thermo-mechanical behaviour of the DEMO Water Cooled Lithium Lead equatorial outboard blanket module, *Fusion Engineering and Design*, vol. 124, 725-729, 2017, DOI: 10.1016/j.fusengdes.2017.05.051.

- [37] Material Property Handbook pilot project on Eurofer97 (MTA EK, KIT), IDM Ref. EFDA_D_2MRP77, 24/02/2016
- [38] D. Martelli, A. Venturini, M. Utili, Literature review of lead-lithium thermophysical properties, *Fusion Engineering and Design*, (138) 2018, 183-195, DOI: 10.1016/j.fusengdes.2018.11.028
- [39] Goodfellow, Metals, Alloys, Compounds, Ceramics, Polymers, Composites. Catalogue 1993/94
- [40] F. Maviglia, DEMO PFC Heat Load Specification, IDM Ref. EFDA_D_2NFPNU v1.1, 2019
- [41] F. P. Incropera et al, Principles of heat and mass transfer, 7th edition
- [42] C. Bachmann et al., IDD - Blanket Mechanical Supports, IDM Ref. EFDA_D_2NHC86, January 2019.
- [43] A. Tassone, et al., Recent Progress in the WCLL Breeding Blanket Design for the DEMO Fusion Reactor. *IEEE Transactions on Plasma Science*, 46 (5), pp. 1446-1457, 2018, DOI: 10.1109/TPS.2017.2786046.
- [44] P.A. Di Maio et al., On the effect of stiffening plates configuration on the DEMO Water Cooled Lithium Lead Breeding Blanket module thermo-mechanical behaviour, *Fusion Eng. Des.*, 146, Part B, 2247-2250, 2019, DOI: 10.1016/j.fusengdes.2019.03.163
- [45] A. Del Nevo et al., Internal Deliverable BB-3.2.1-T003-D001: Design engineering for WCLL – 2016 activities, Final Report (2016), EFDA IDM Ref. EFDA_D_2MTZP6.
- [46] A. Del Nevo et al., Internal Deliverable BB-3.2.1-T006-D001: WCLL BB design and Integration studies 2019 activities, Final Report (2020), EFDA IDM Ref. EFDA_D_2P5NE5.
- [47] I. Catanzaro et al., Parametric study of the influence of double-walled tubes layout on the DEMO WCLL breeding blanket thermal performances, *Fusion Engineering and Design*, 161 (2020), 111893, doi: 10.1016/j.fusengdes.2020.111893
- [48] G. Bongiovì et al., BB.WCLL-DEF-2-CD1-BB WCLL Load Specifications Document, Final Report on Deliverable (2020), EFDA IDM Ref. EFDA_D_2P6MJG.
- [49] G. A. Spagnuolo et al., Development of load specifications for the design of the breeding blanket system, *Fusion Engineering and Design*, 157, 111657, 2020
- [50] C. Bachmann et al., Initial definition of structural load conditions in DEMO, *Fusion Engineering and Design*, 124 (2017), 633-637, DOI: 10.1016/j.fusengdes.2017.02.061

- [51] I. A. Maione et al., Assessment of EM results – 2018, Final Report on Deliverable (2019), EFDA IDM Ref. EFDA_D_2NUFTN.
- [52] I.A. Maione et al., Analysis of EM loads on DEMO WCLL Breeding Blanket during VDE-up, Fusion Engineering and Design, 136 (2018), 1523-1528.
- [53] G. Zhou et al., Preliminary structural analysis of the new HCPB blanket for EU DEMO reactor, International Journal of Hydrogen Energy 41 (2016) 7053-7058.
- [54] A. Del Nevo et al., Internal Deliverable BB-3.2.1-T007-D001: WCLL BB design and Integration studies 2020 activities, Final Report (2020), EFDA IDM Ref. EFDA_D_2NTP7J.
- [55] F. Maviglia, Z. Vizvary, M.L. Richiusa, J. Gerardin, M. Firdaouss, DEMO PFC Surface Heat Load Specifications (2020), EFDA IDM Ref. EFDA_D_2P985Q.
- [56] E. Gaganidze, Material Properties Handbook – EUROFER97 (2020), EFDA IDM Ref. EFDA_D_2NZHBS
- [57] E. Gaganidze, F. Schoofs, Material Properties Handbook – Tungsten (2020), EFDA IDM Ref. EFDA_D_2P3SPL
- [58] F. Maviglia, DEMO PFC Surface Heat Load Specification (2020), EFDA IDM Ref. EFDA_D_2P985Q
- [59] T. Berry, T. Eade, Activation analysis and evaluation of inventories, decay heat, for important components – Activity 2019 – CCFE contribution (Calculation of decay heat in PbLi for entire WCLL reactor), EFDA IDM Ref. EFDA_D_2NQL5P

5 Appendix 1

Further details of the mesh independence assessment

In this appendix, all the outcomes derived from the comparison between the calculated and the interpolated thermal field for each of the mechanical models analysed (i.e. coarse mesh 2, coarse mesh 3 and coarse mesh 4), which have not been reported in §2.5 for the sake of brevity, are given in Figure 5.1, Figure 5.2 and Figure 5.3. As already explained in the chapter, after testing the predictive ability of the thermal field interpolating functions in terms of both temperature and secondary stresses, a mesh independence procedure has been performed to verify the applicability of the above-mentioned interpolating procedure even when the meshes are coarser.

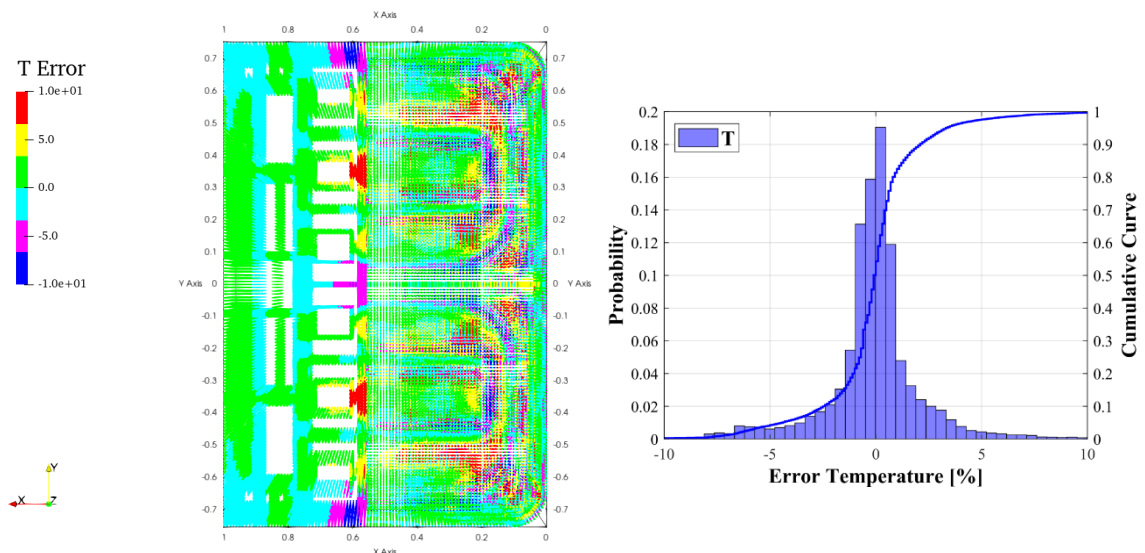


Figure 5.1 Error on temperature prediction for the coarser mesh 2.

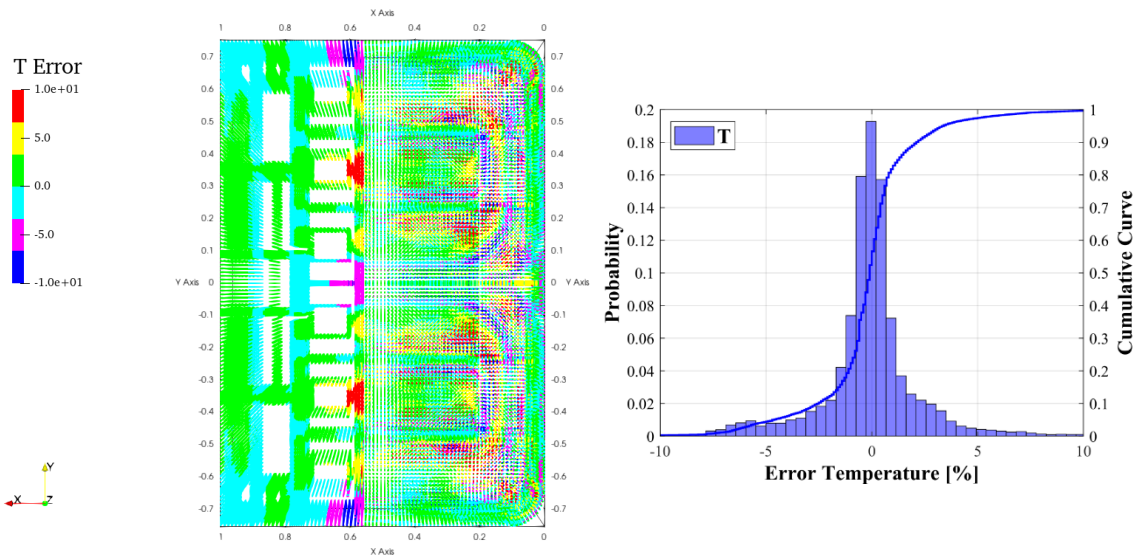


Figure 5.2 Error on temperature prediction for the coarser mesh 3.

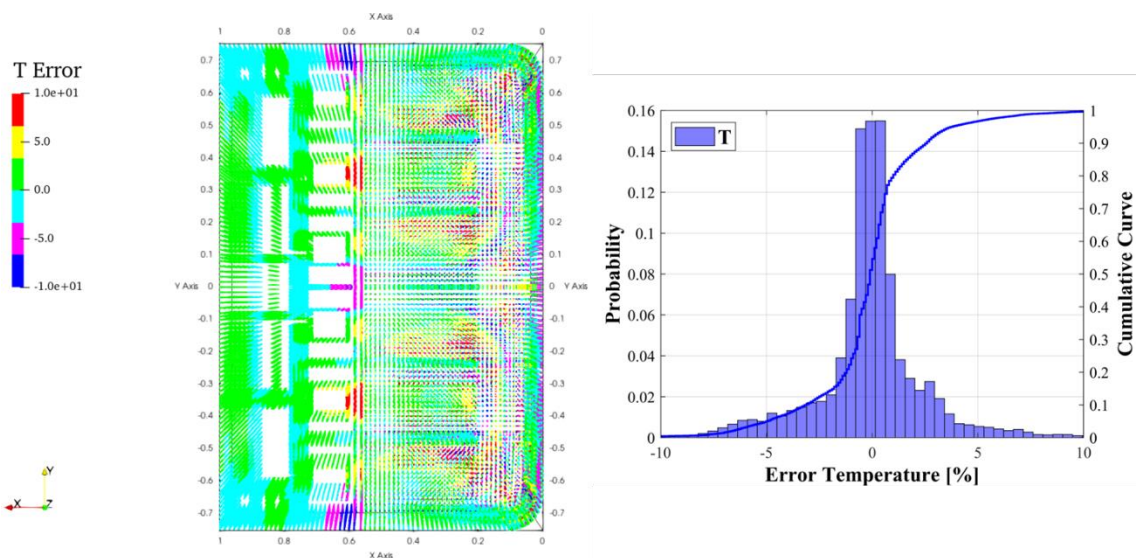


Figure 5.3 Error on temperature prediction for the coarser mesh 4.

Moreover, different regions of the structure have been selected to extract and compare the temperature value, in particular, three paths located in the same position near the cooling channels within FW and SW, as reported in Figure 5.4, and FW bend (Figure 5.5), three on the vertical SPs and three on the horizontal SPs (Figure 5.5). The comparison between the temperature values obtained in the aforementioned paths located in the different FE models is shown in Figure 5.6 to Figure 5.20. Looking at the figures below it may be noted that the percentage error compared to the original model remains below 3% and the maximum values are within the toroidal-radial SPs in Coarse 4 and Coarse 5. Such low percentage error values indicate that the obtained set of interpolating functions also fits well even used on FE models with different parameters and coarser meshes, further confirming previous statements and results.

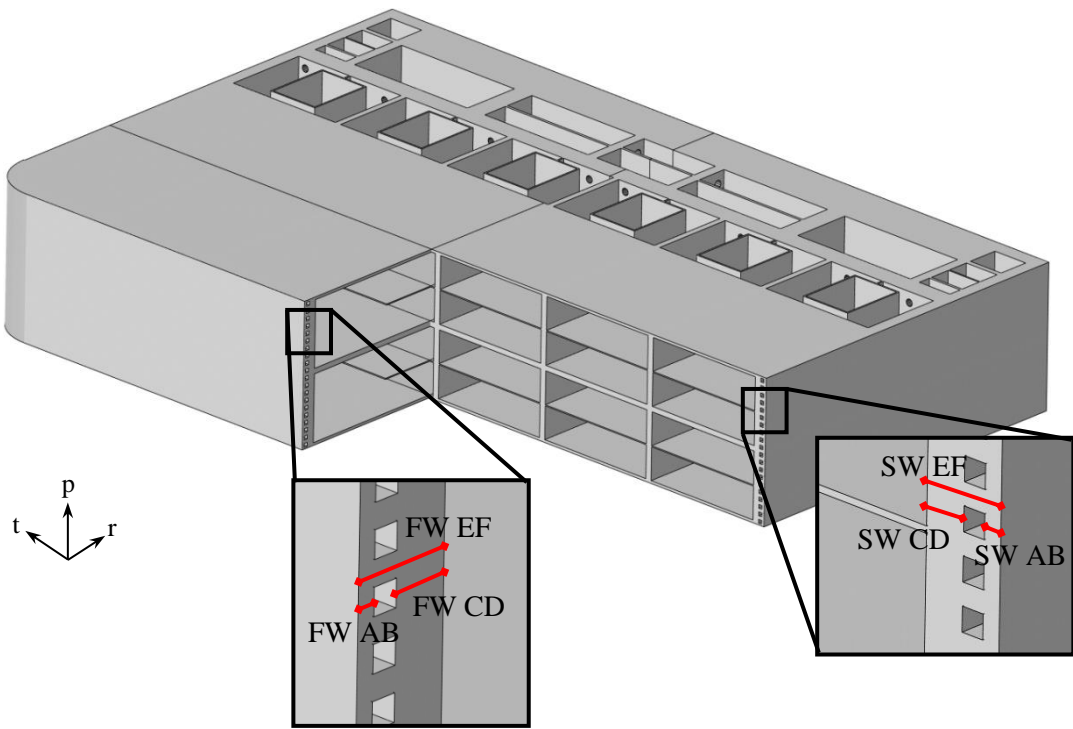


Figure 5.4 Paths within FW and SWs.

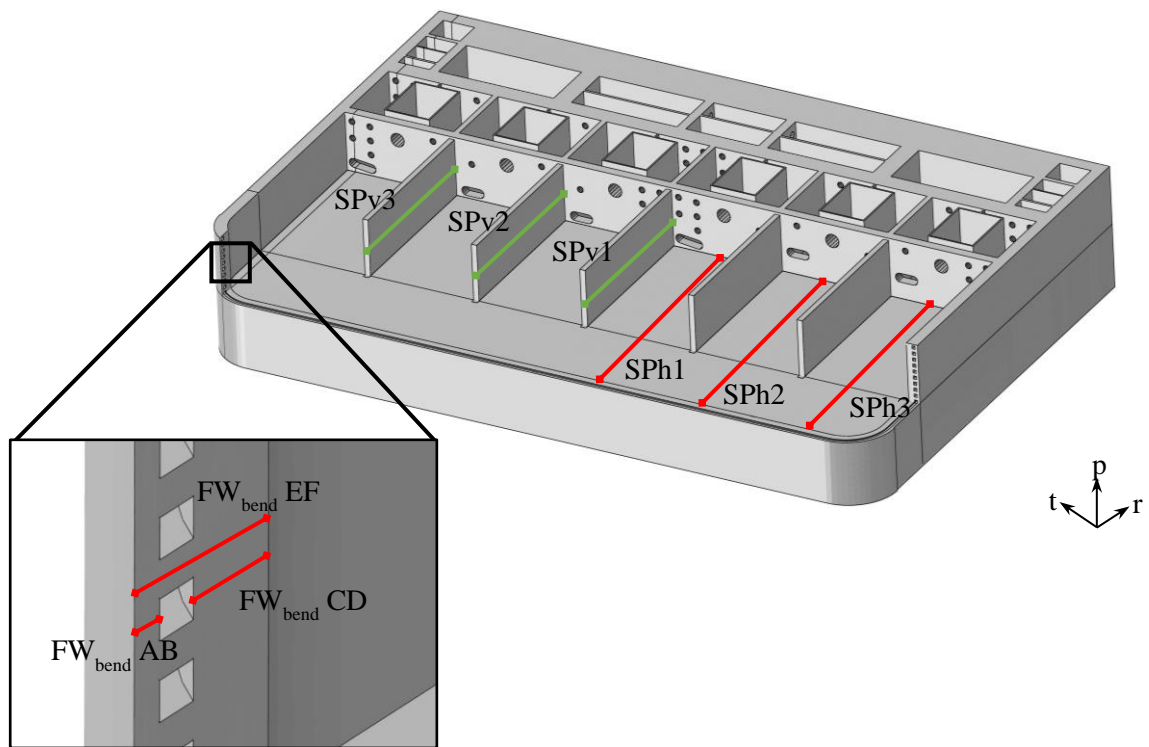


Figure 5.5 Paths within horizontal and vertical SPs and FW bend.

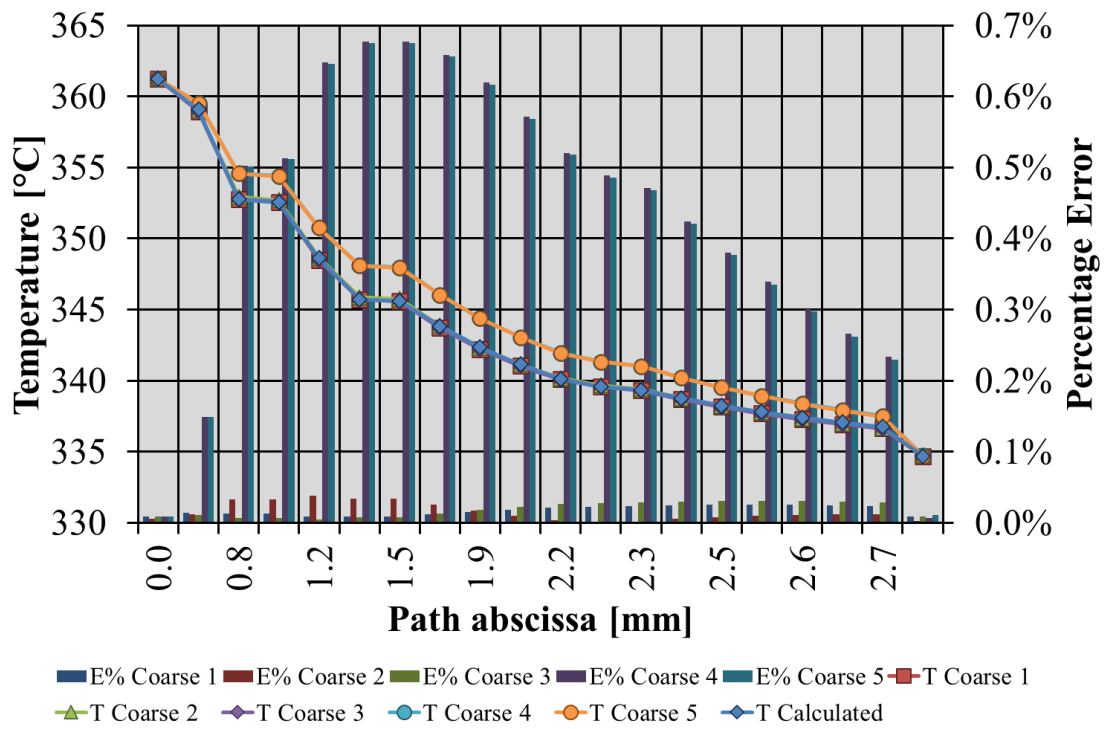


Figure 5.6 Path FW AB temperature comparison.

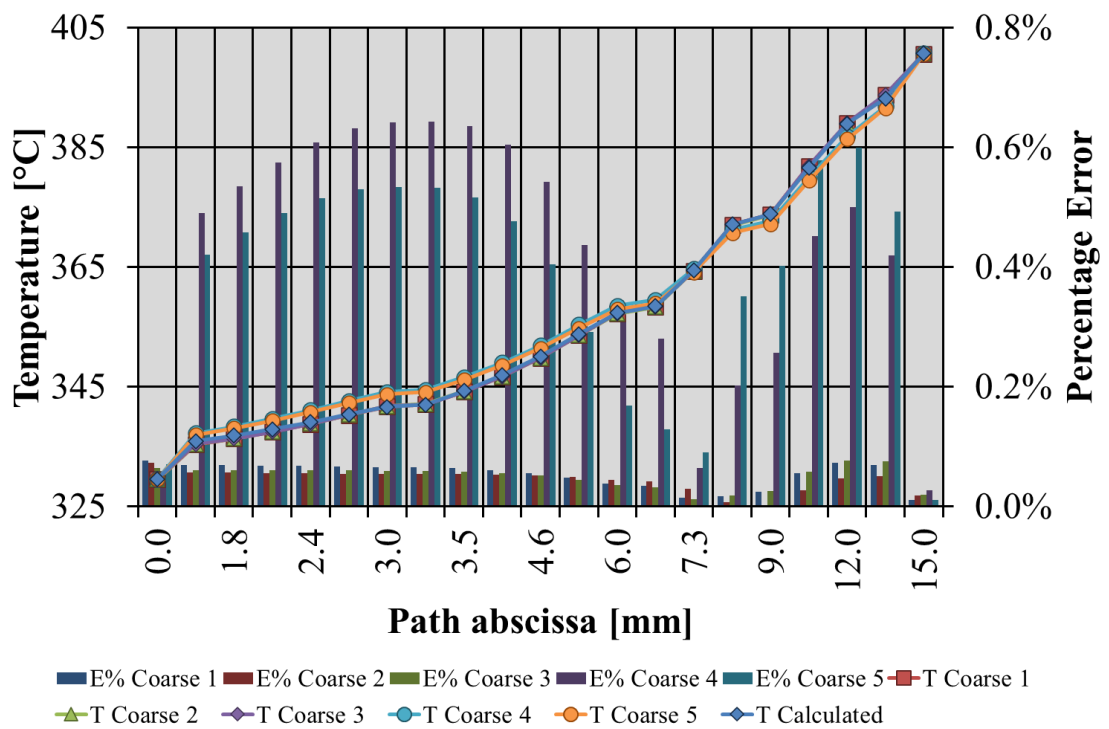


Figure 5.7 Path FW CD temperature comparison.

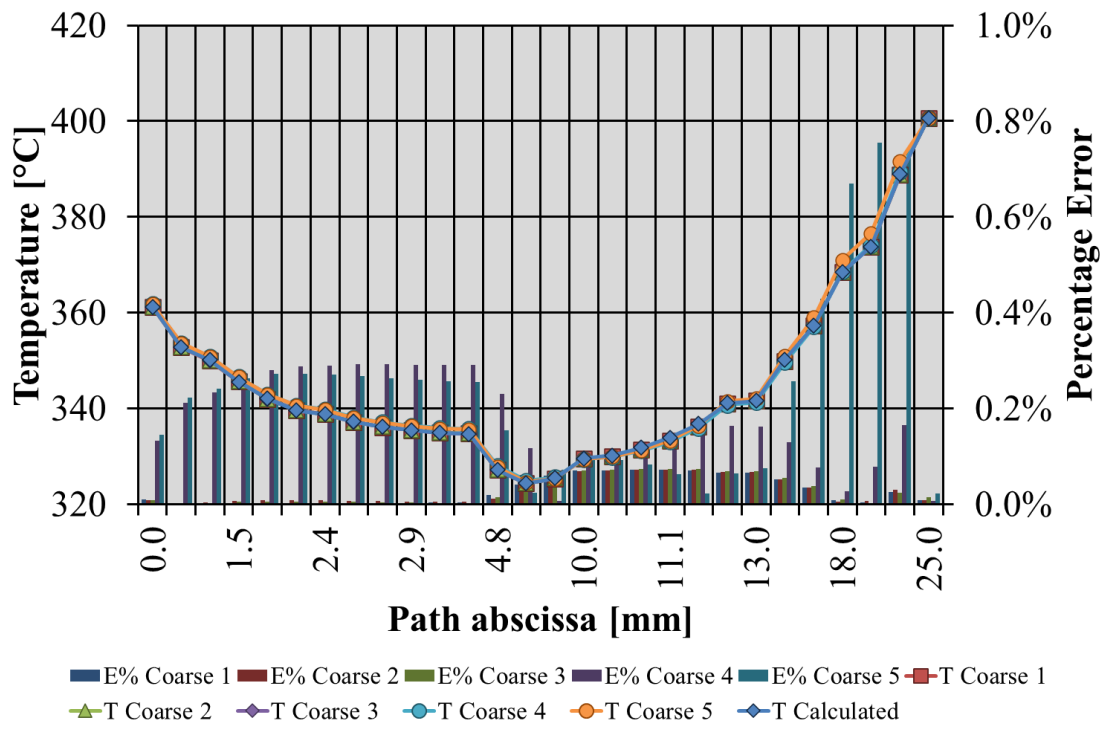


Figure 5.8 Path FW EF temperature comparison.

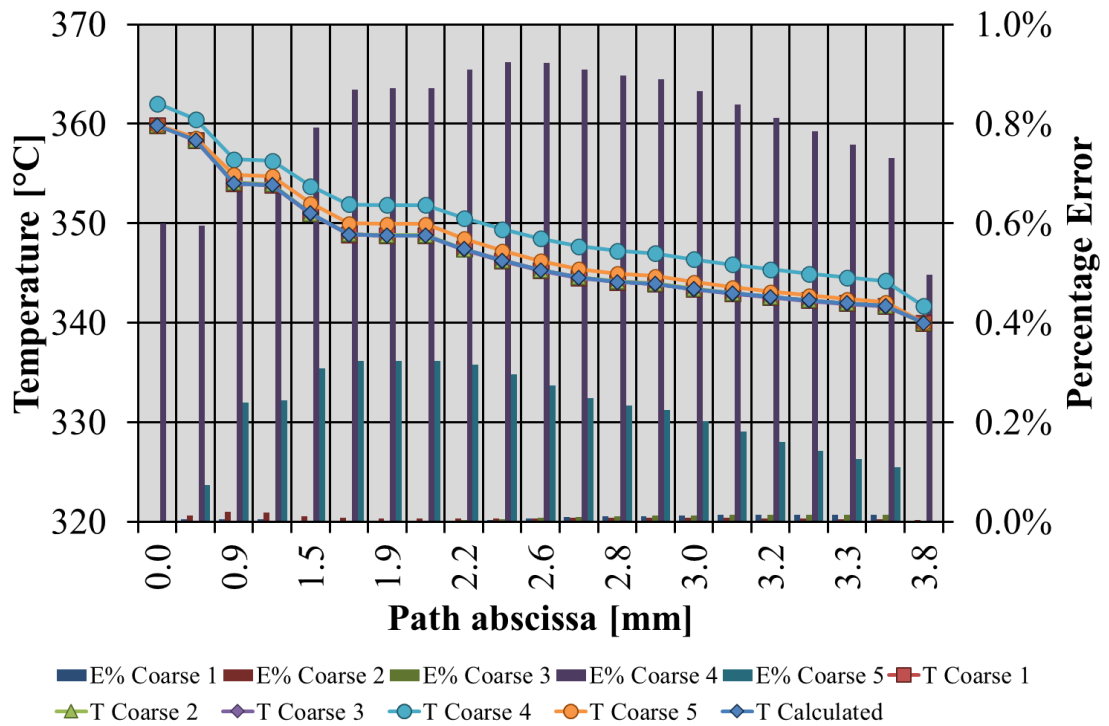


Figure 5.9 Path FW Bend AB temperature comparison.

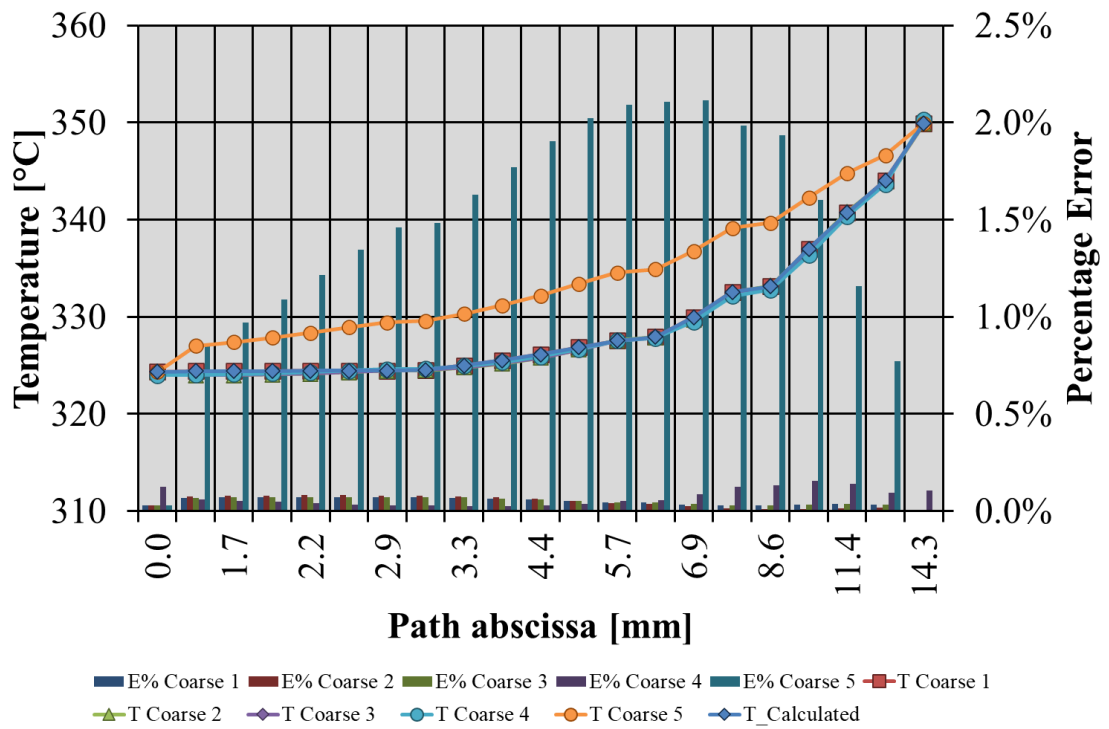


Figure 5.10 Path FW Bend CD temperature comparison.

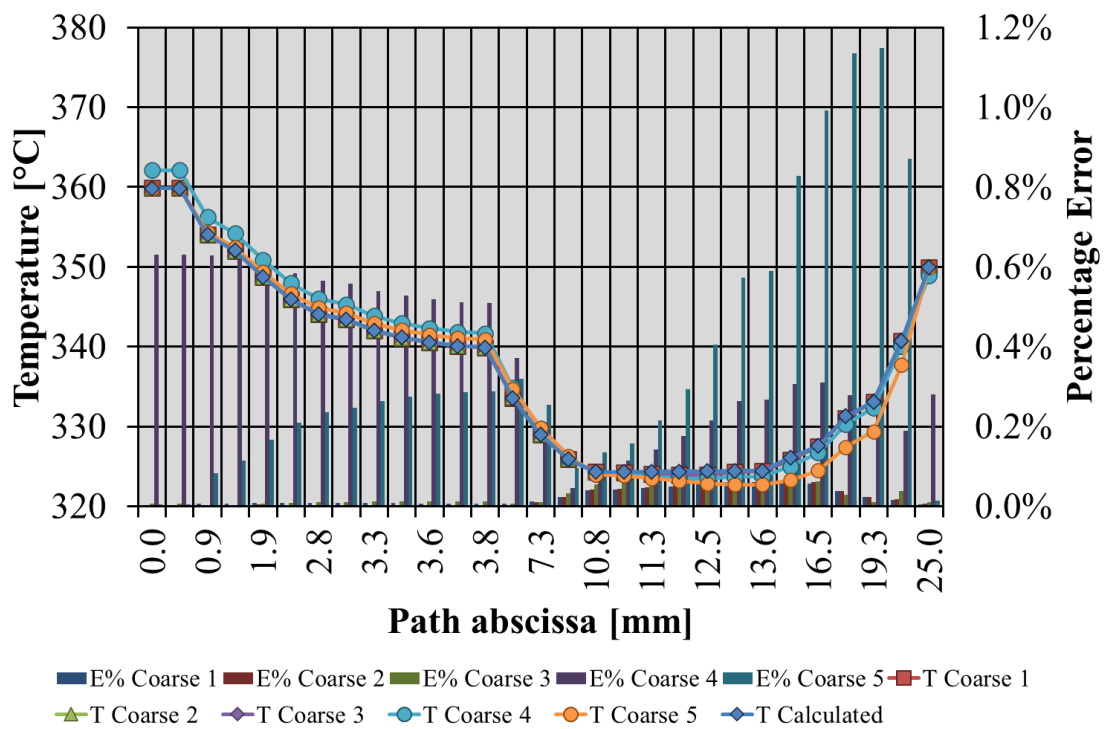


Figure 5.11 Path FW Bend EF temperature comparison.

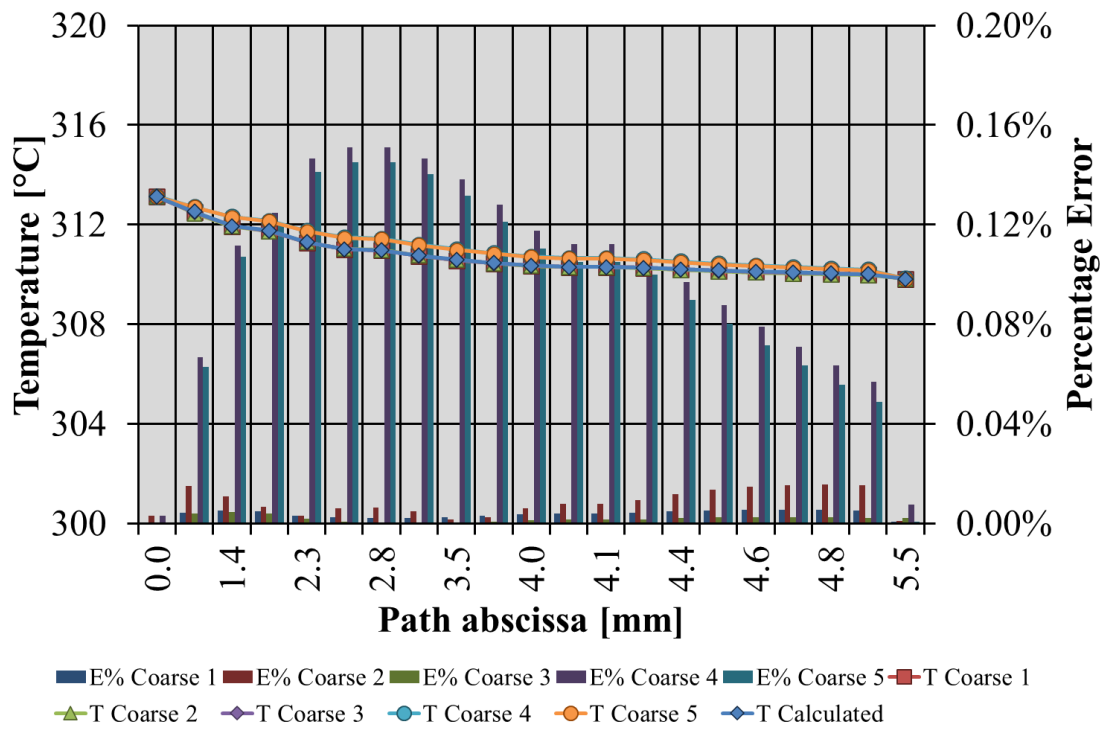


Figure 5.12 Path SW AB temperature comparison.

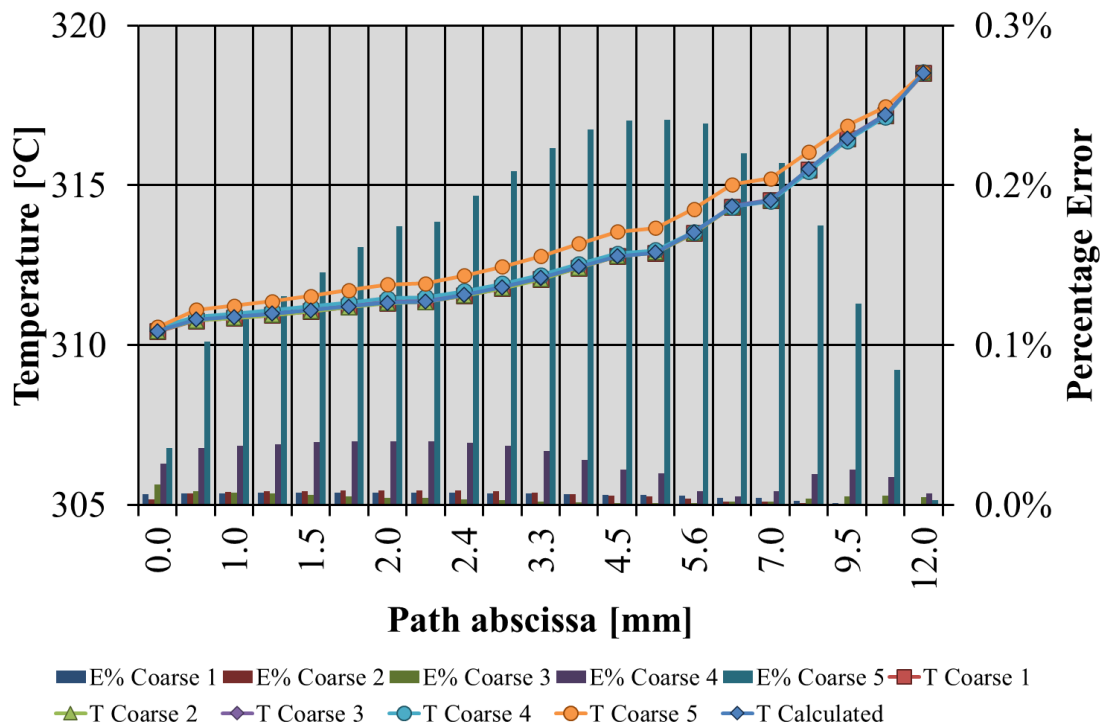


Figure 5.13 Path SW CD temperature comparison.

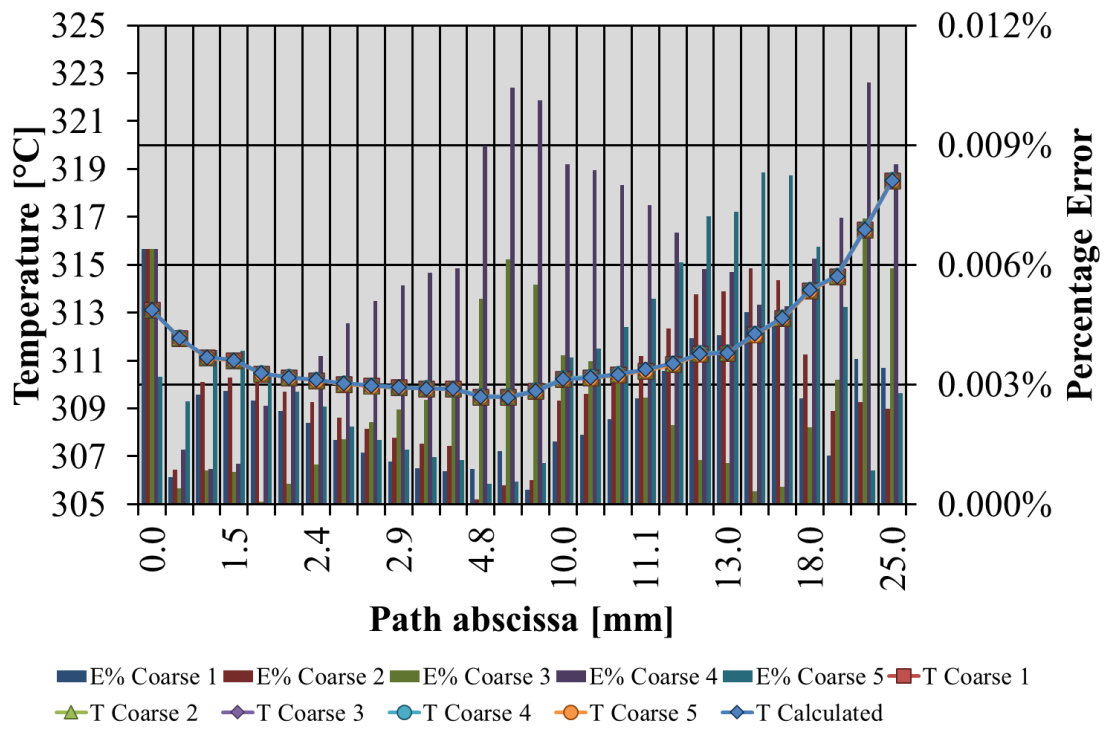


Figure 5.14 Path SW EF temperature comparison.

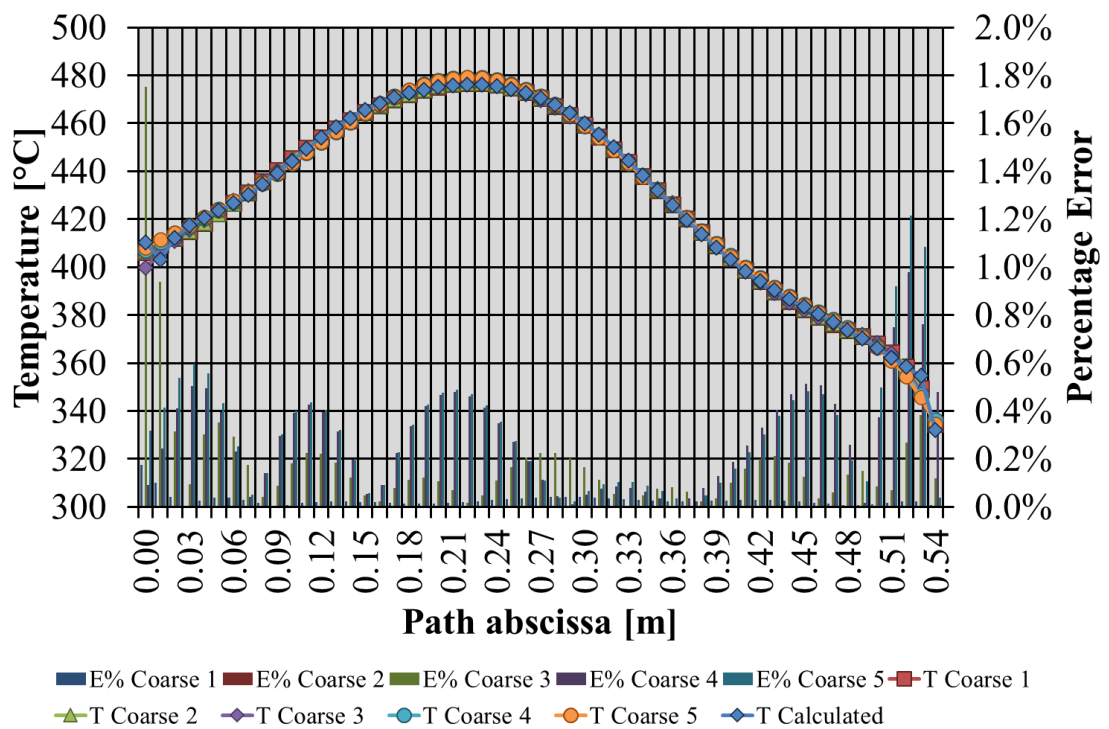


Figure 5.15 Path SPh1 temperature comparison.

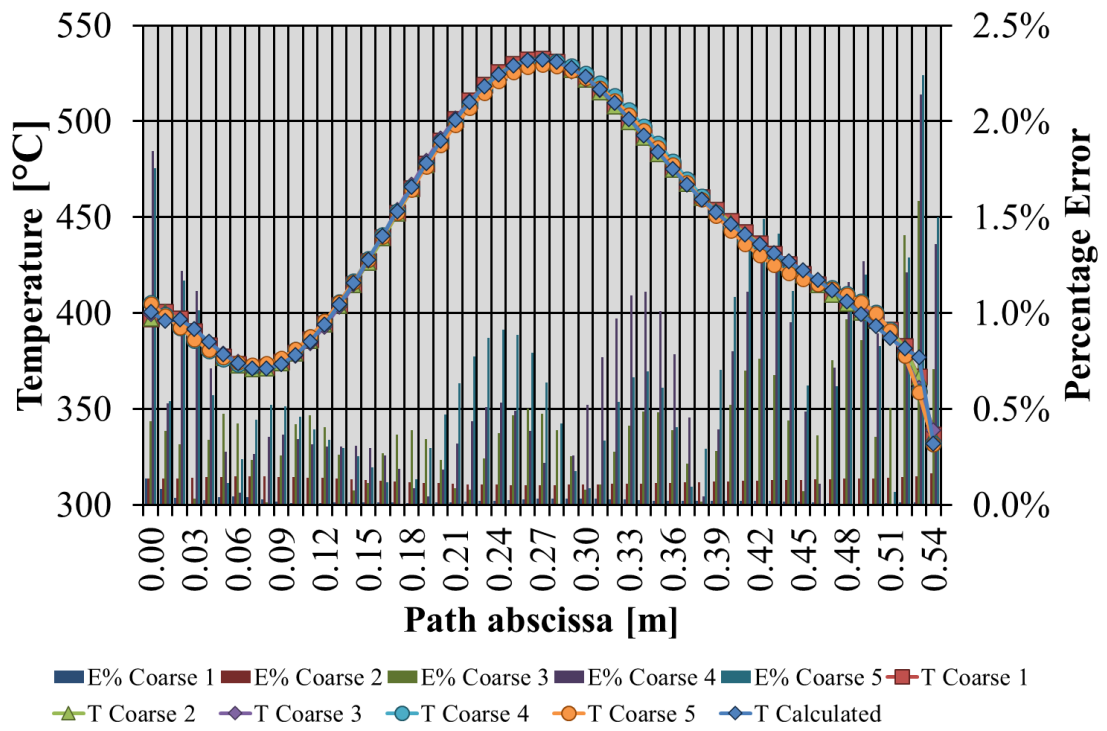


Figure 5.16 Path SPh2 temperature comparison.

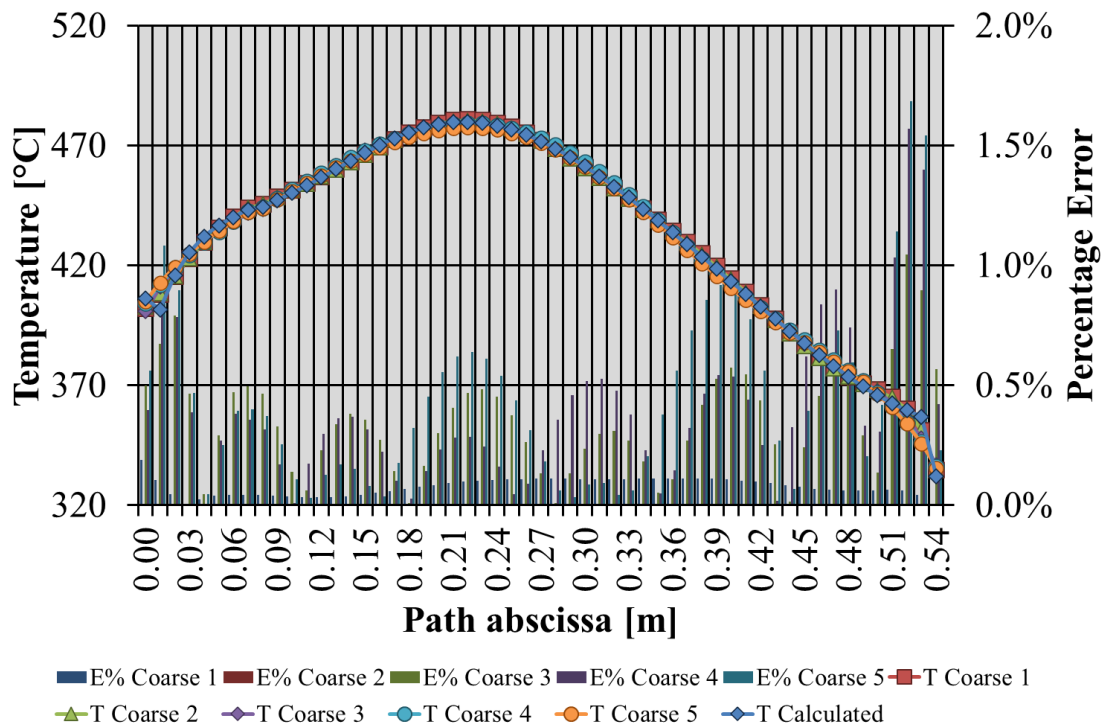


Figure 5.17 Path SPh3 temperature comparison.

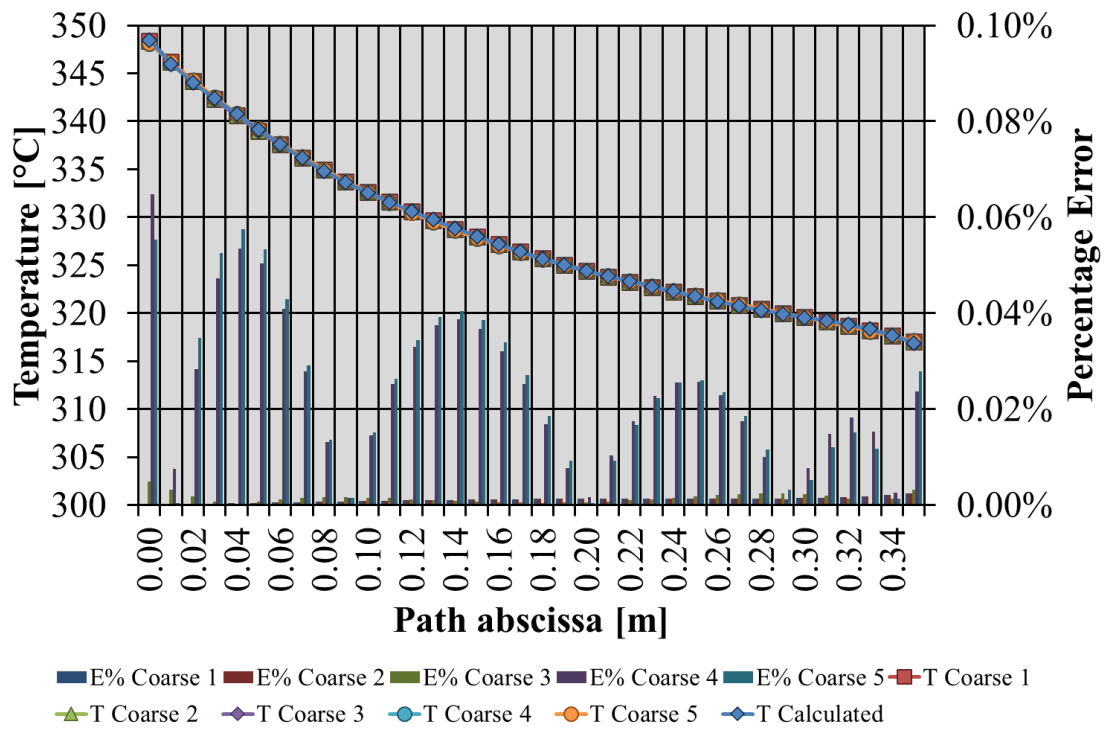


Figure 5.18 Path SPv1 temperature comparison.

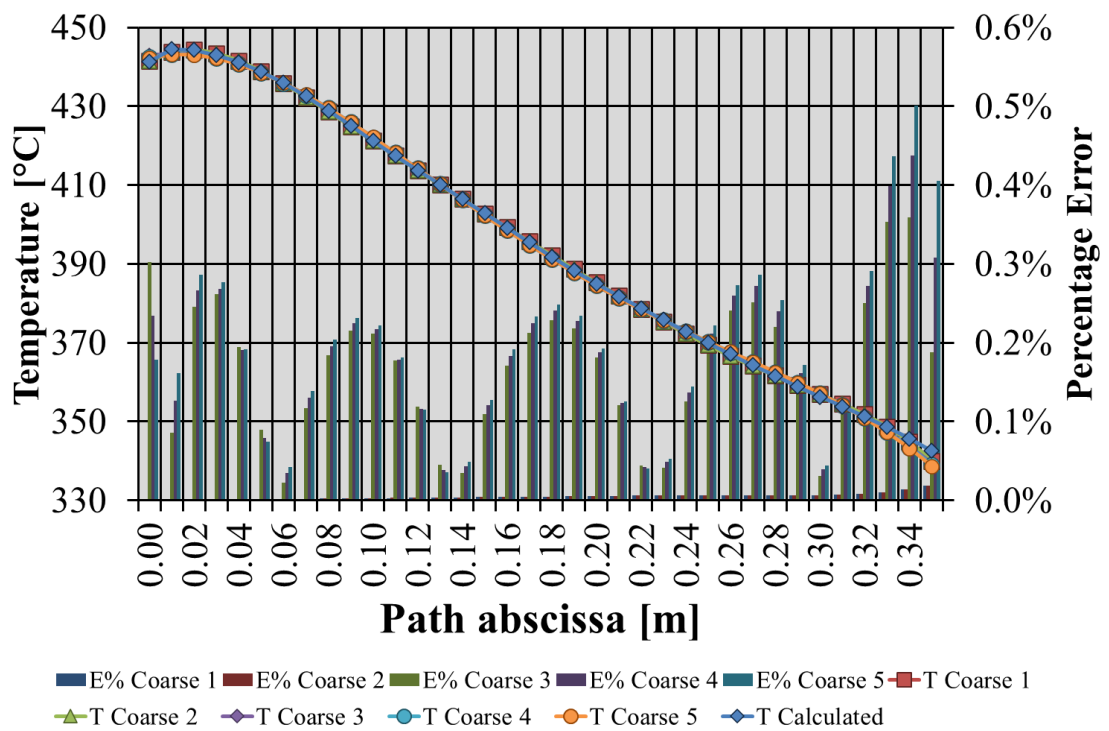


Figure 5.19 Path SPv2 temperature comparison.

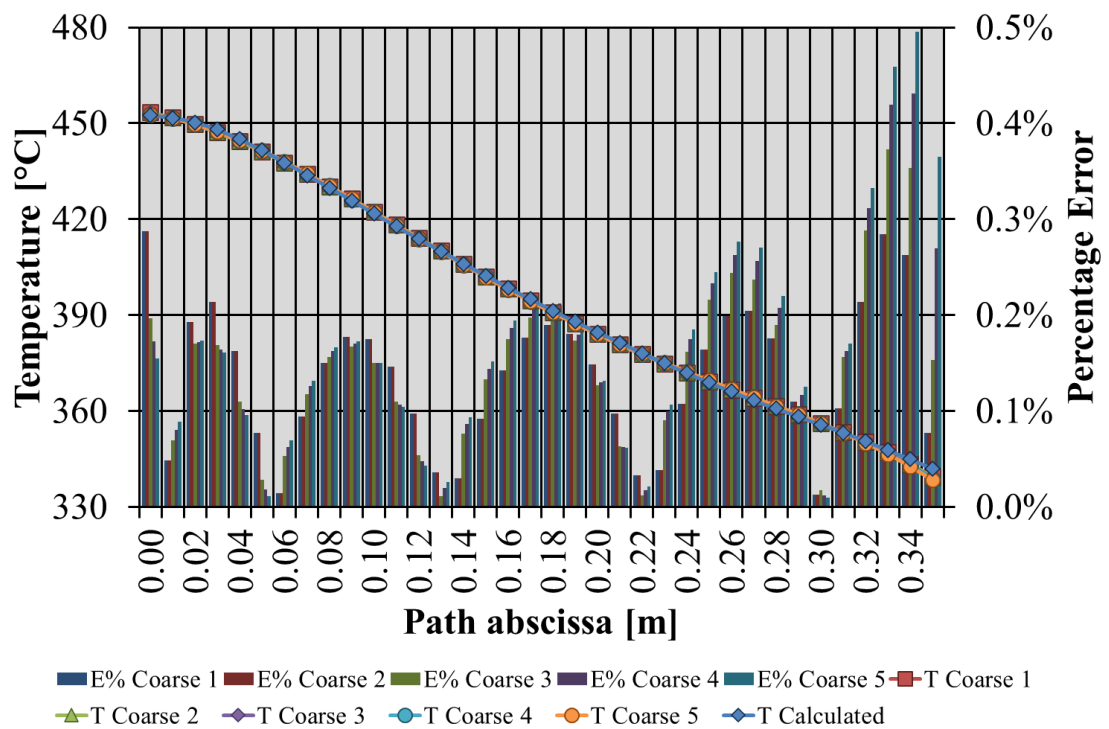


Figure 5.20 Path SPv3 temperature comparison.

Regarding the comparison between the secondary stress fields deriving from the calculated thermal field and the interpolated one, in §2.5 only the results for the “coarse Mesh 5” are reported for the sake of brevity. In the following the results of that comparison for the coarse 1, 2, 3 and 4 are reported in Figure 5.21 to Figure 5.48. In all the examined cases the highest percentage error resulting from the comparison between the calculated thermal stress and that coming from the interpolated temperature arise where the stresses are the lowest. Moreover, the error statistical distributions and the associated cumulative curves show a similar behaviour for each FE model. In particular, the most of the error values (about 80 %) remain within the range $\pm 50\%$ with peaks in between $\pm 20\%$, allowing to state that the procedure is reliable for coarser meshes.

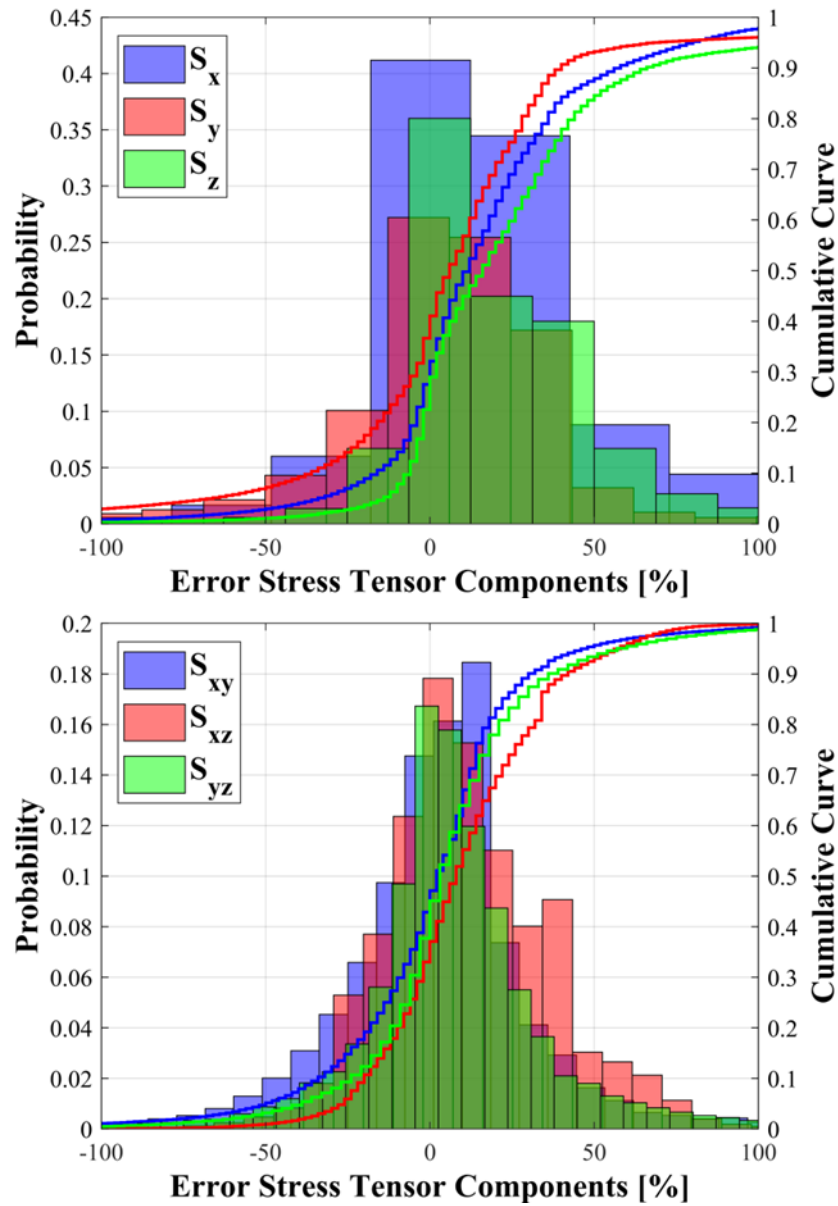


Figure 5.21 Statistical distribution of the error on S_{ij} between the calculated thermal field and the “multi-region” interpolation (histograms) and cumulative curves for the “coarse Mesh 1”.

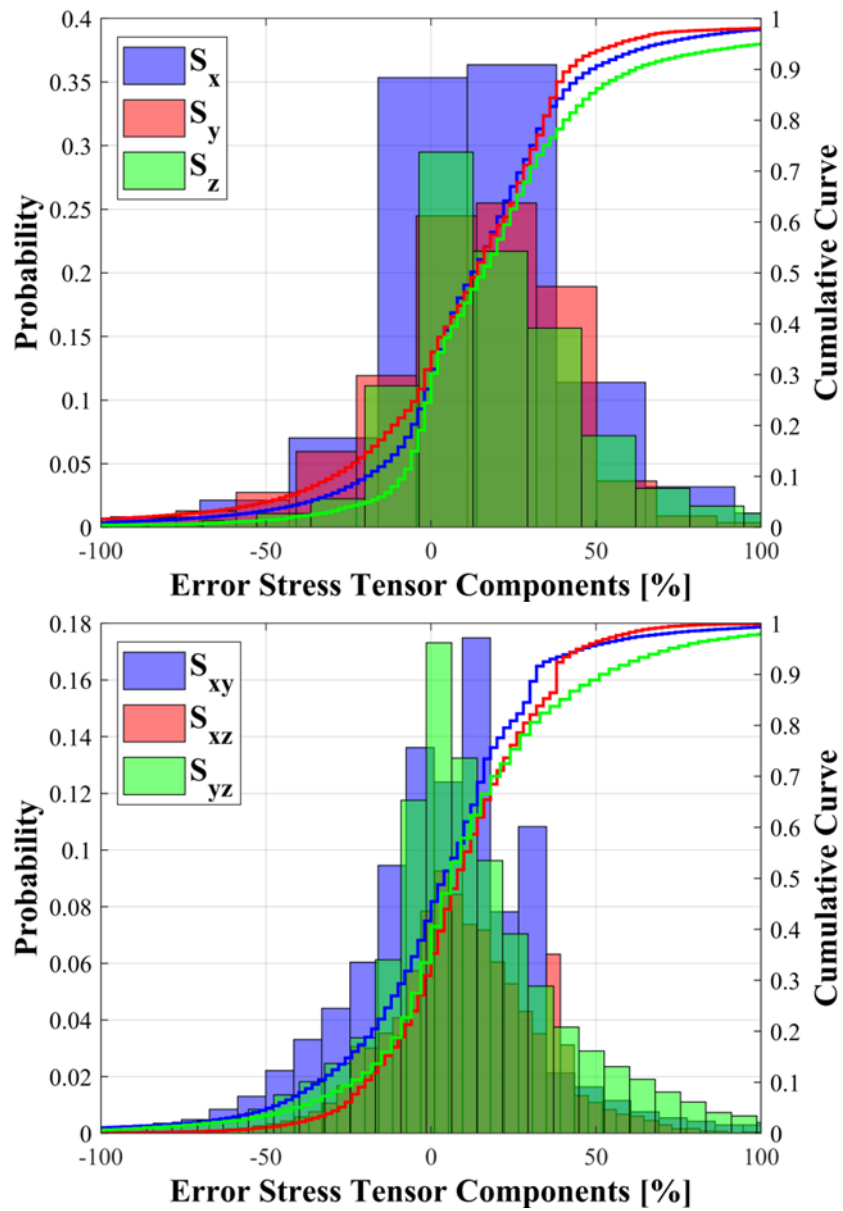


Figure 5.22 Statistical distribution of the error on S_{ij} between the calculated thermal field and the “multi-region” interpolation (histograms) and cumulative curves for the “coarse Mesh 2”.

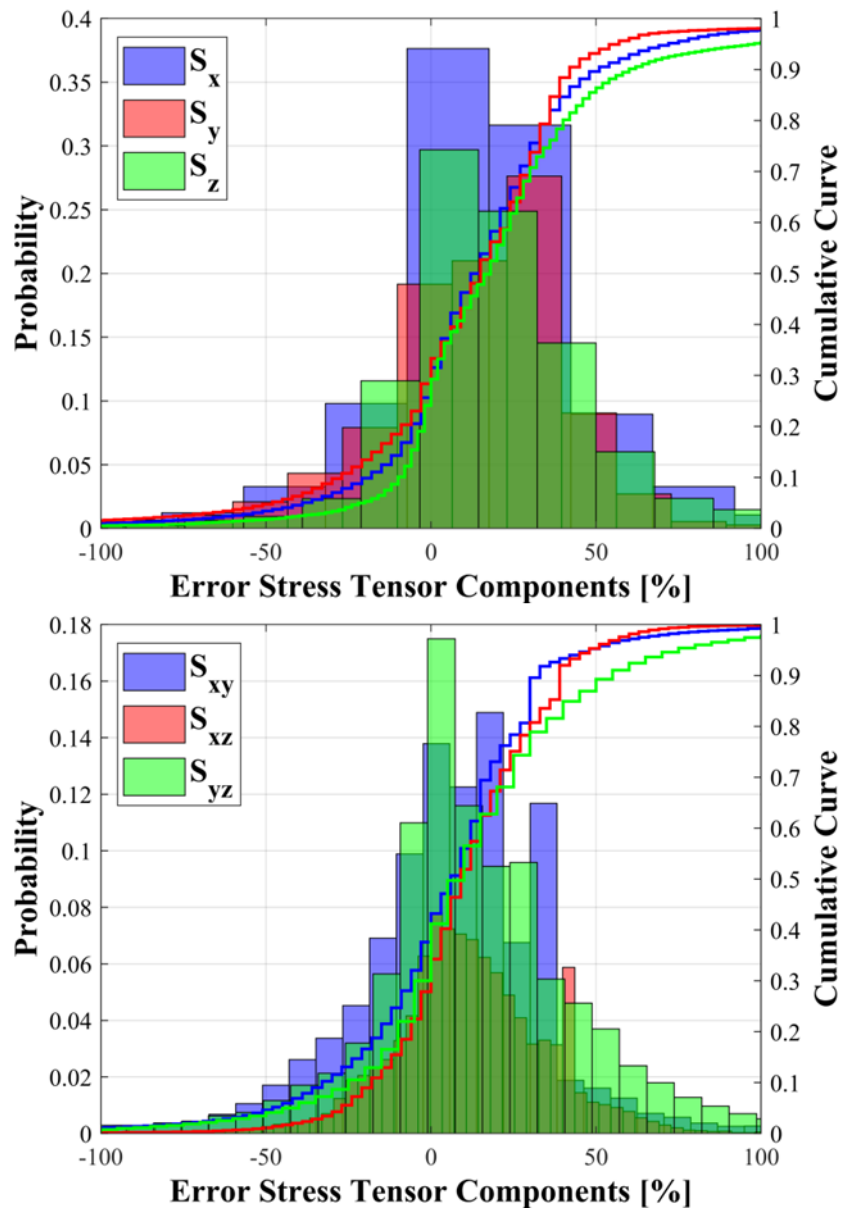


Figure 5.23 Statistical distribution of the error on S_{ij} between the calculated thermal field and the “multi-region” interpolation (histograms) and cumulative curves for the “coarse Mesh 3”.

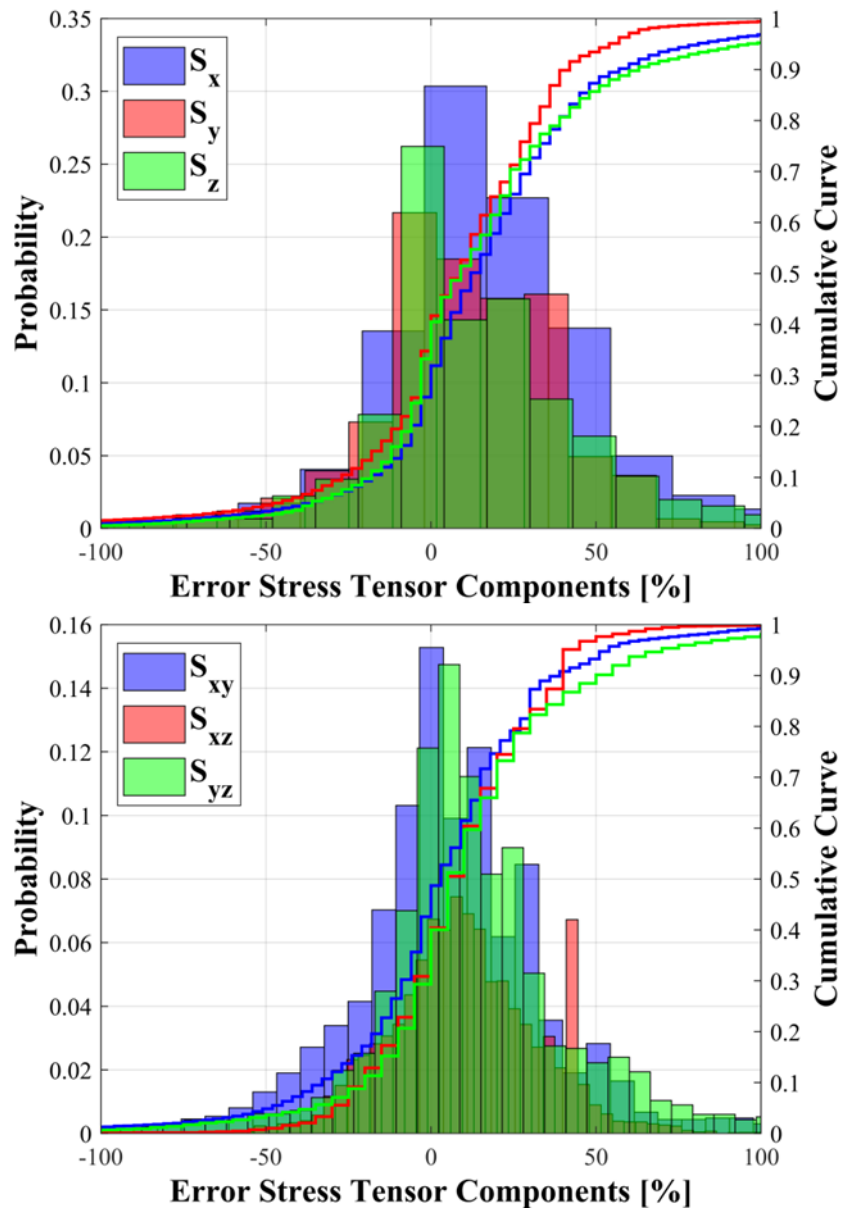


Figure 5.24 Statistical distribution of the error on S_{ij} between the calculated thermal field and the “multi-region” interpolation (histograms) and cumulative curves for the “coarse Mesh 4”.

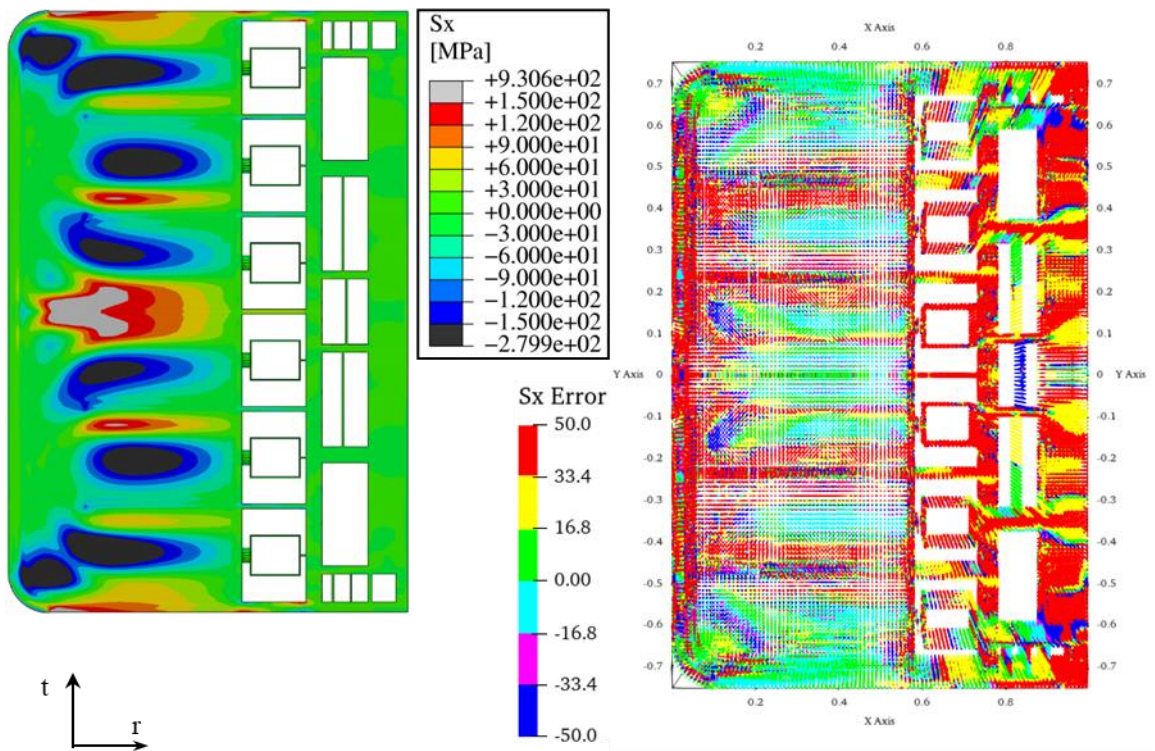


Figure 5.25 S_x spatial distribution from calculated thermal field (left) and relative error contour map (right) when compared with S_x from interpolated thermal field for the "coarse Mesh 1".

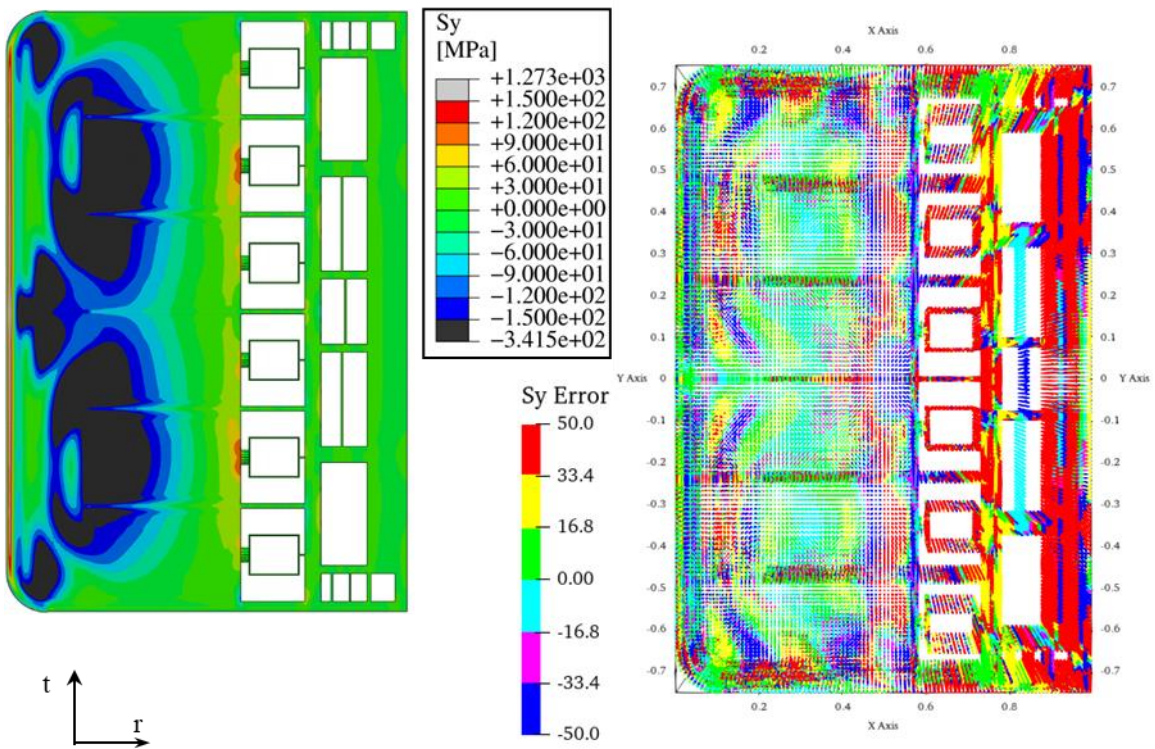


Figure 5.26 S_y spatial distribution from calculated thermal field (left) and relative error contour map (right) when compared with S_y from interpolated thermal field for the "coarse Mesh 1".

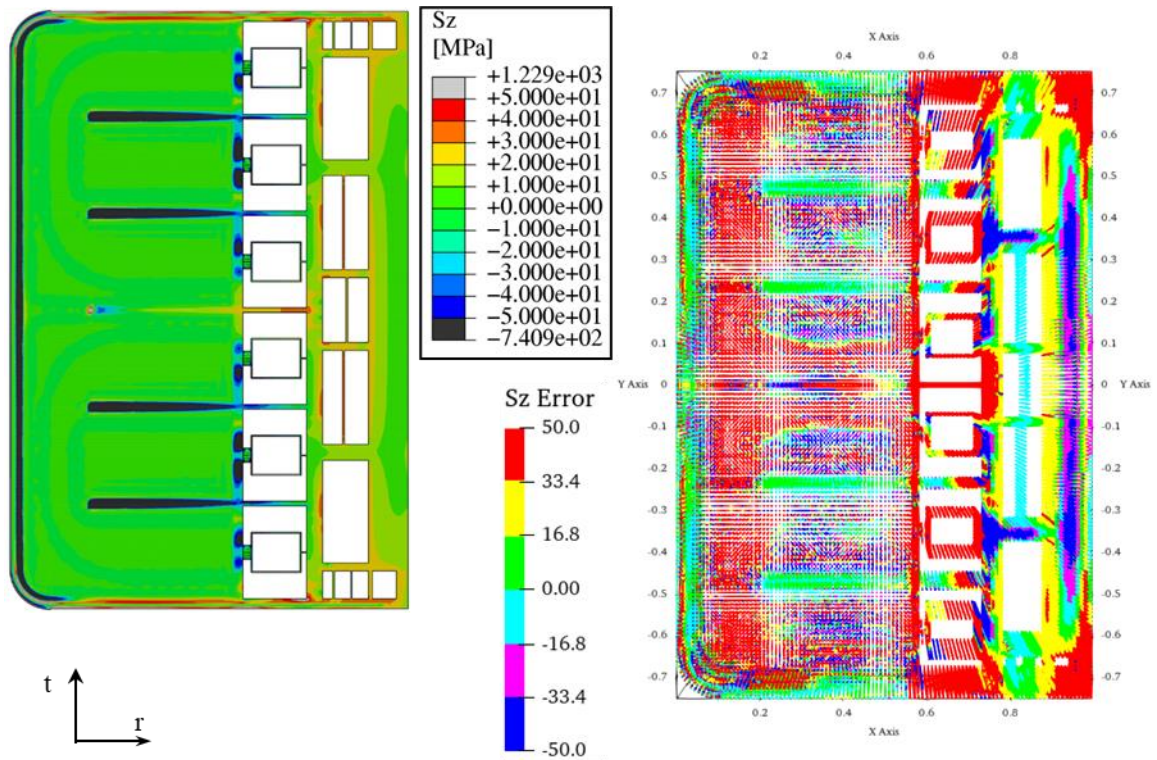


Figure 5.27 Sz spatial distribution from calculated thermal field (left) and relative error contour map (right) when compared with Sx from interpolated thermal field for the “coarse Mesh 1”.

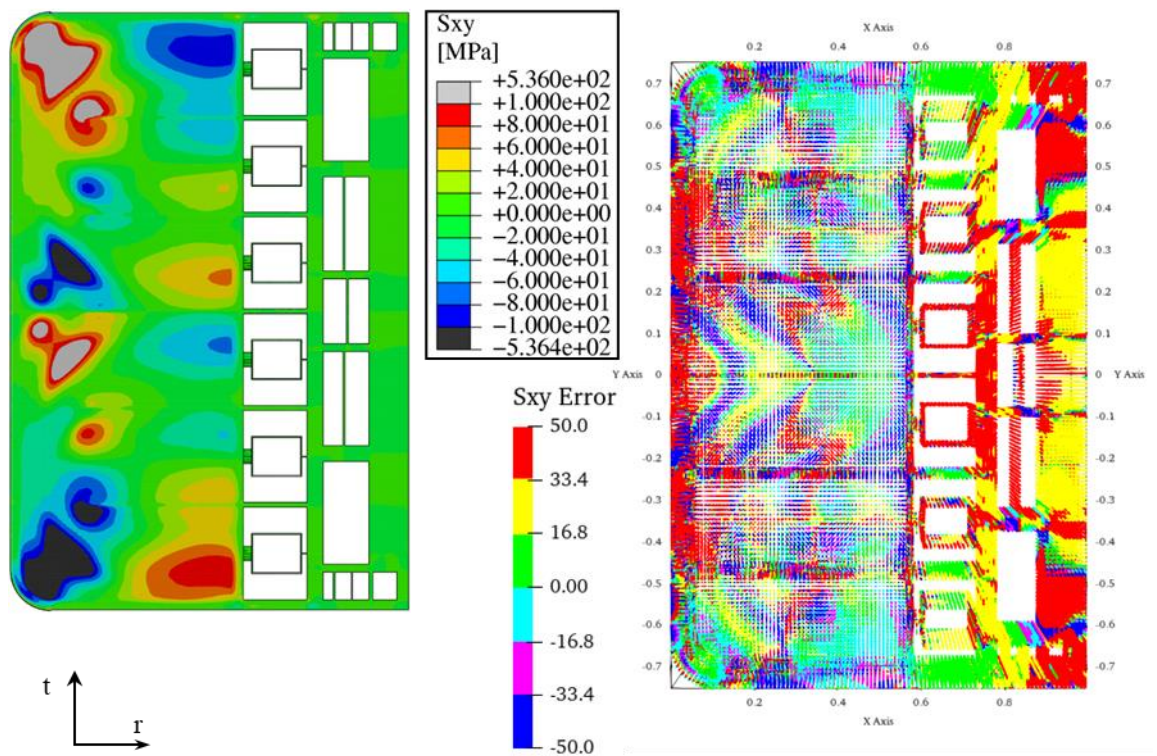


Figure 5.28 Sxy spatial distribution from calculated thermal field (left) and relative error contour map (right) when compared with Sx from interpolated thermal field for the “coarse Mesh 1”.

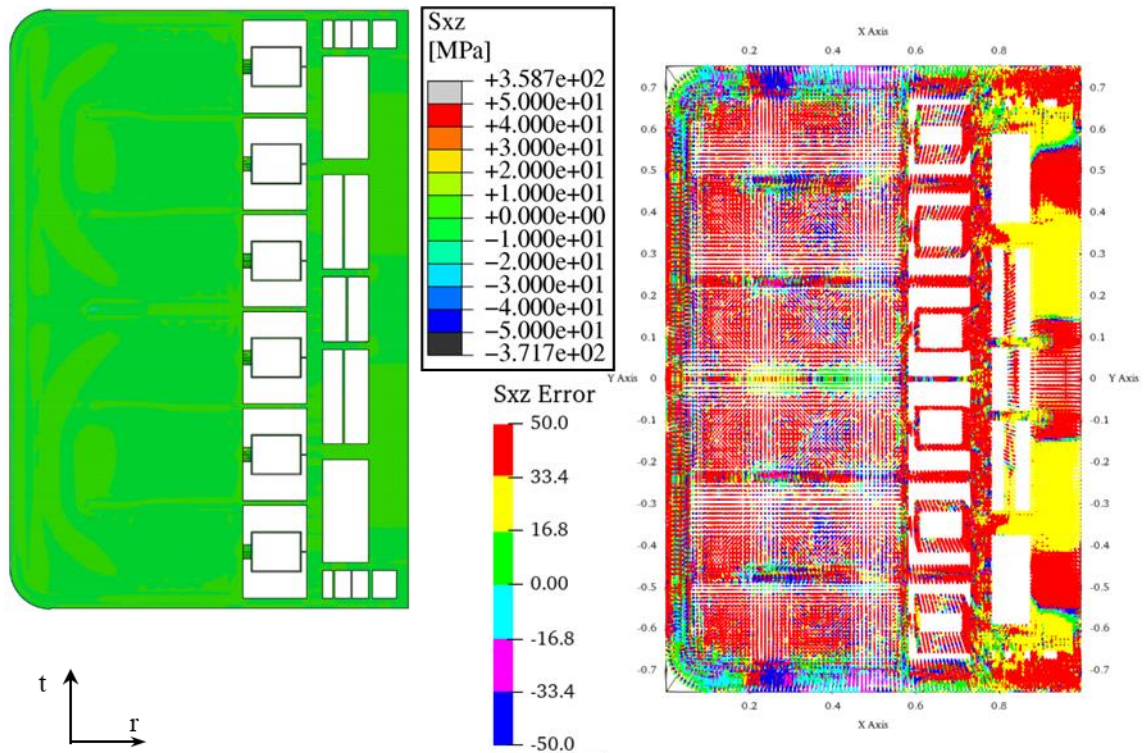


Figure 5.29 S_{xz} spatial distribution from calculated thermal field (left) and relative error contour map (right) when compared with S_x from interpolated thermal field for the “coarse Mesh 1”.

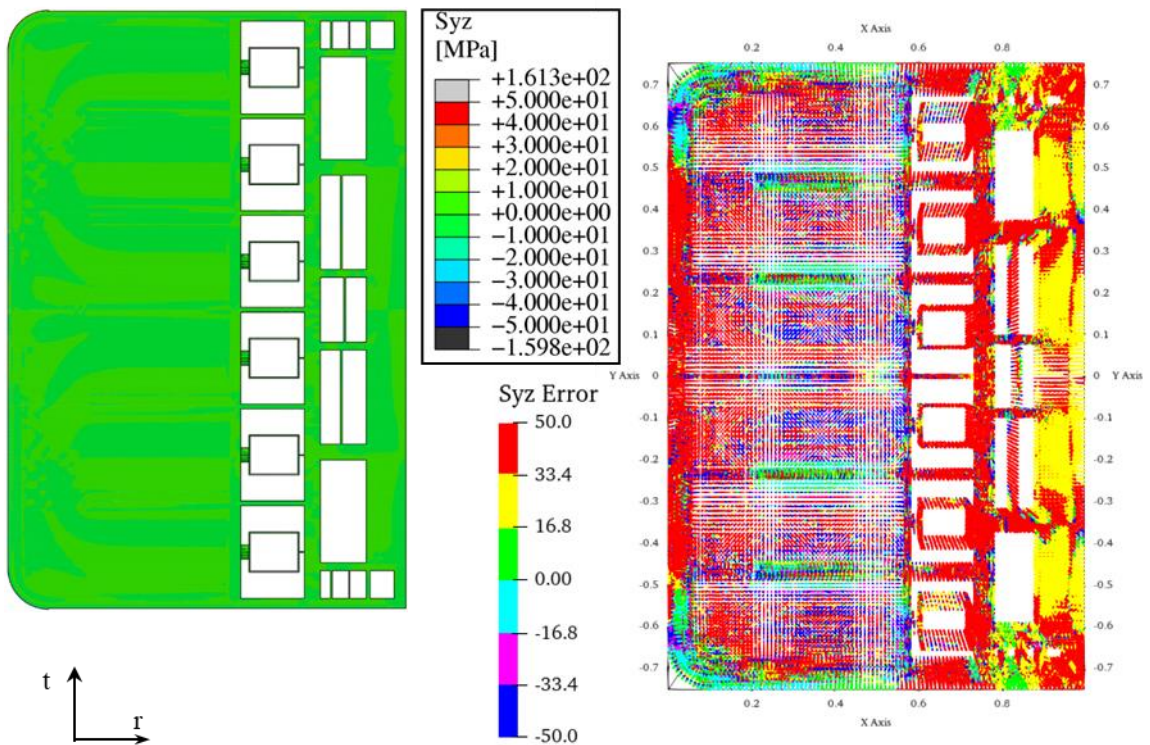


Figure 5.30 S_{yz} spatial distribution from calculated thermal field (left) and relative error contour map (right) when compared with S_x from interpolated thermal field for the “coarse Mesh 1”.

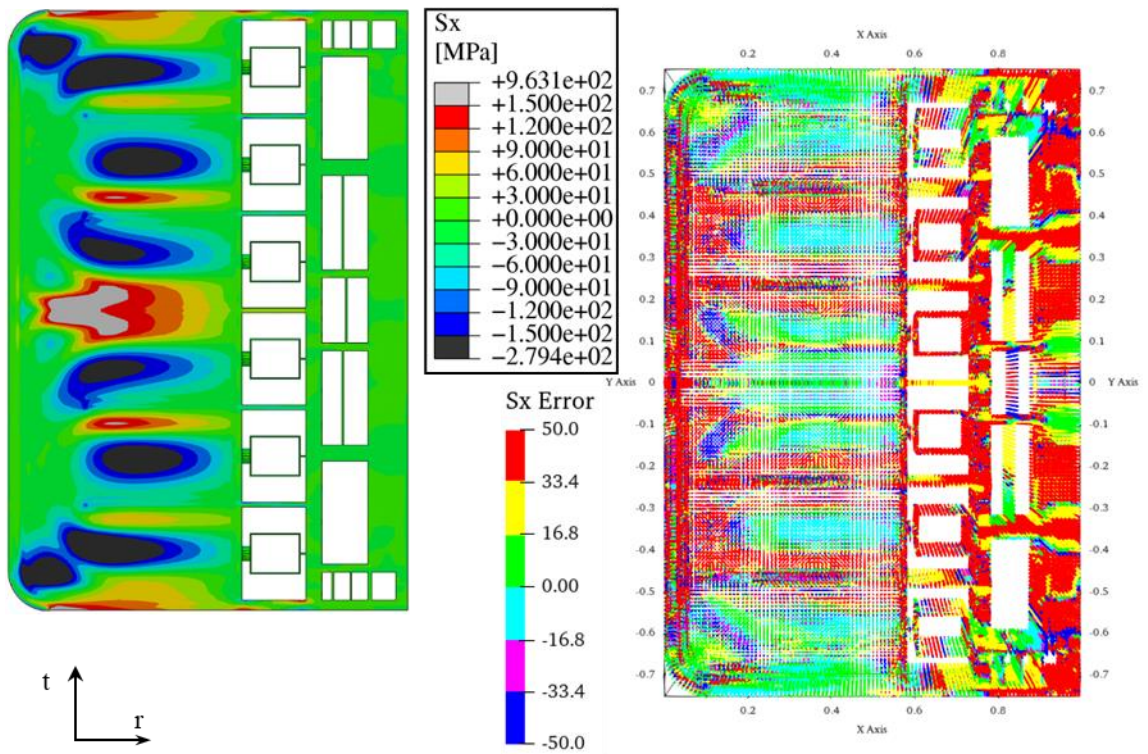


Figure 5.31 S_x spatial distribution from calculated thermal field (left) and relative error contour map (right) when compared with S_x from interpolated thermal field for the “coarse Mesh 2”.

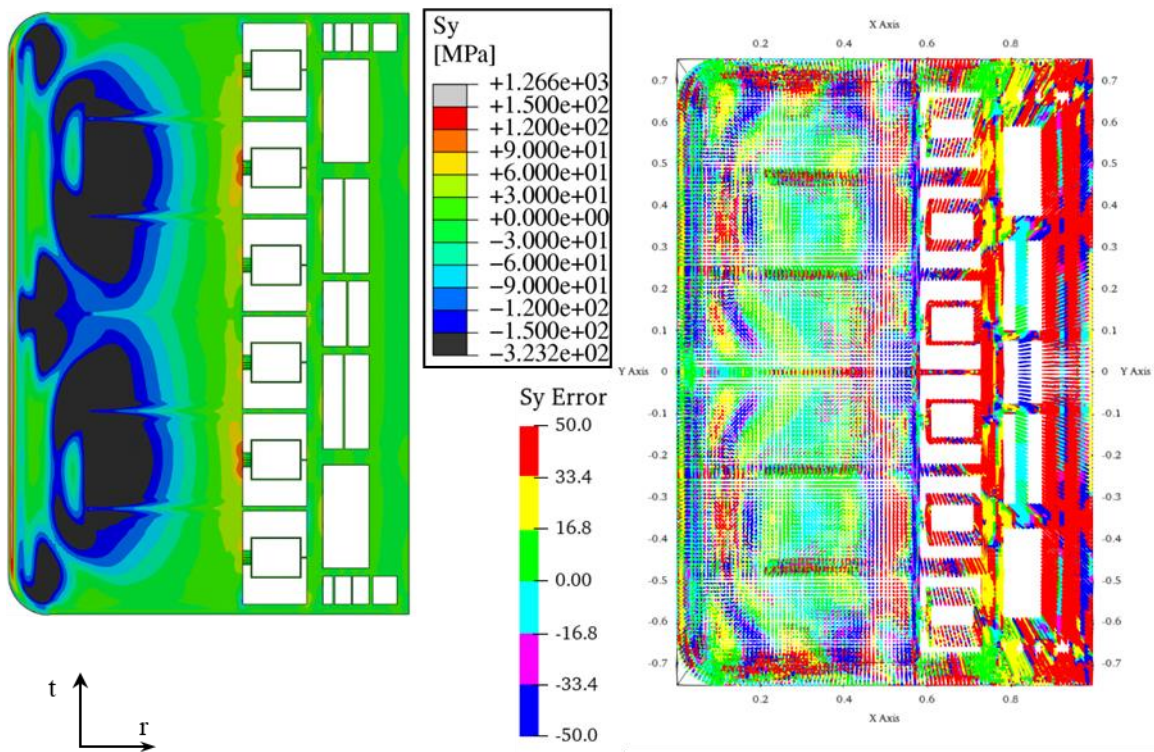


Figure 5.32 S_y spatial distribution from calculated thermal field (left) and relative error contour map (right) when compared with S_y from interpolated thermal field for the “coarse Mesh 2”.

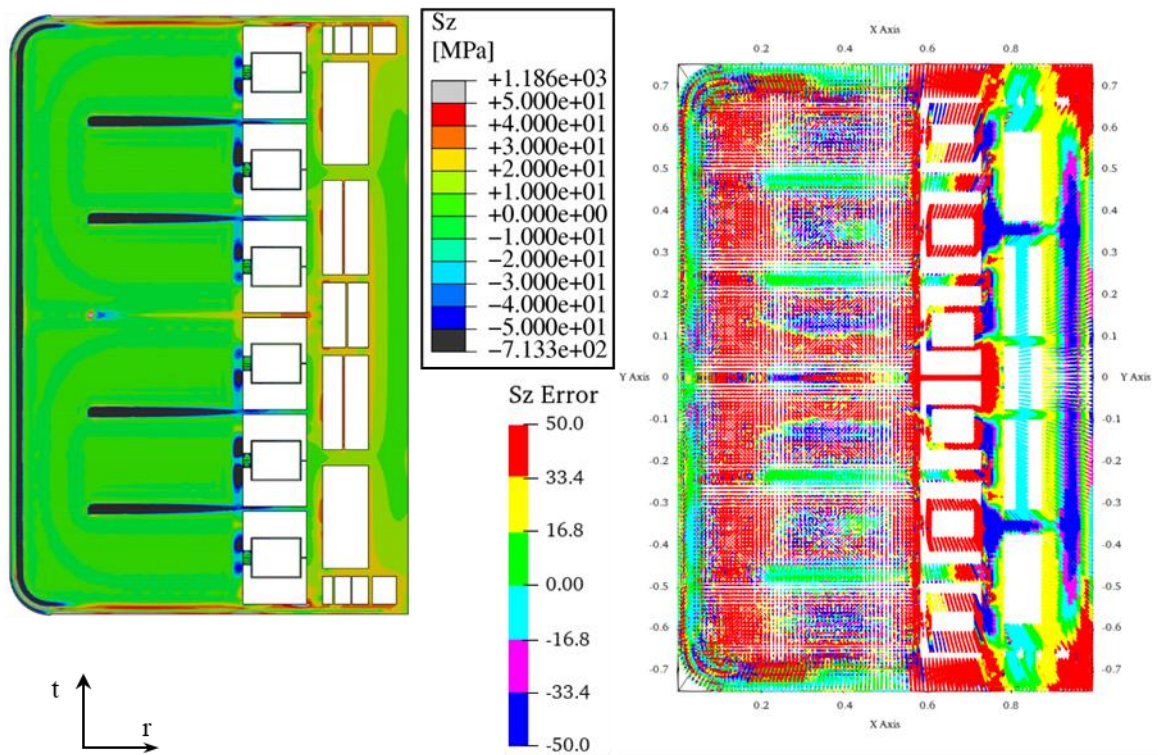


Figure 5.33 Sz spatial distribution from calculated thermal field (left) and relative error contour map (right) when compared with Sx from interpolated thermal field for the “coarse Mesh 2”.

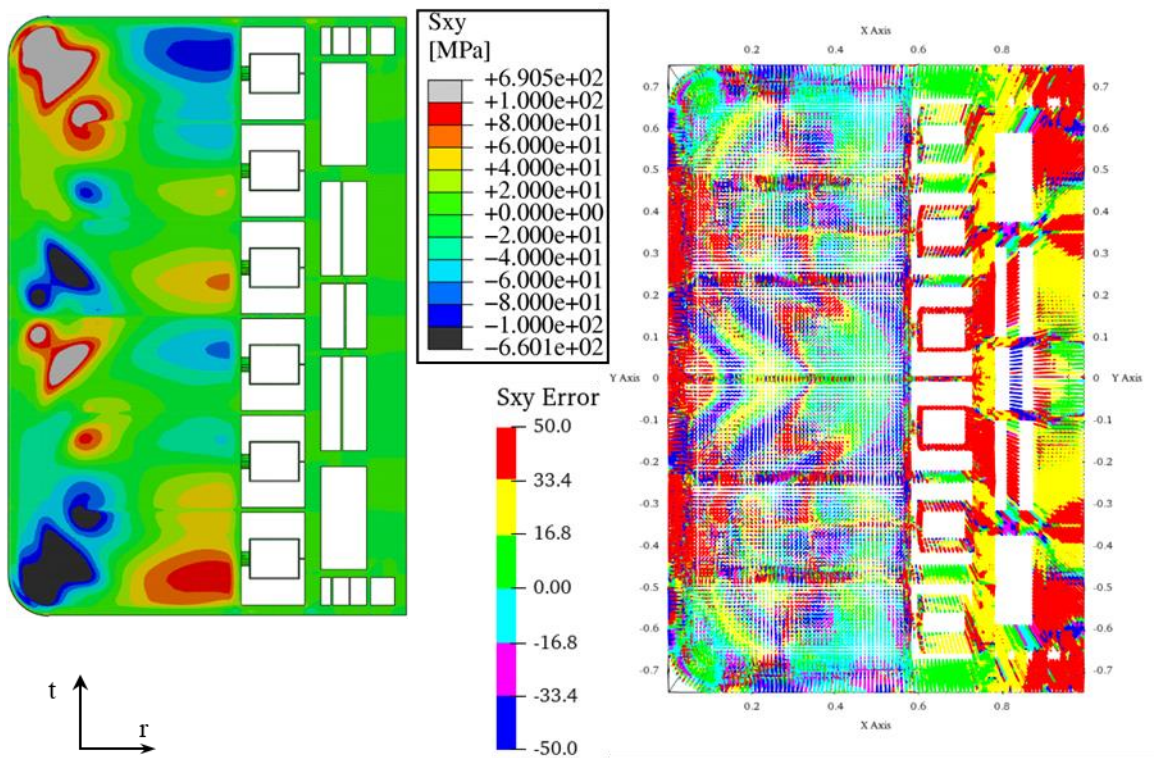


Figure 5.34 Sxy spatial distribution from calculated thermal field (left) and relative error contour map (right) when compared with Sx from interpolated thermal field for the “coarse Mesh 2”.

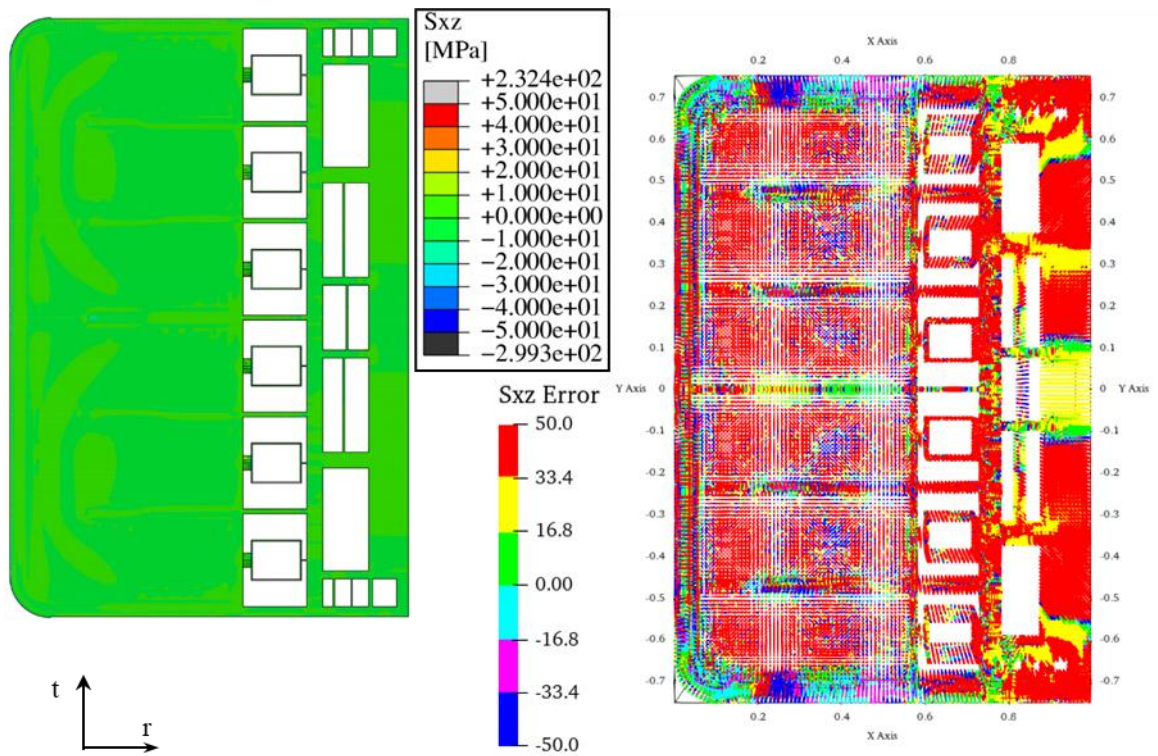


Figure 5.35 S_{xz} spatial distribution from calculated thermal field (left) and relative error contour map (right) when compared with S_x from interpolated thermal field for the “coarse Mesh 2”.

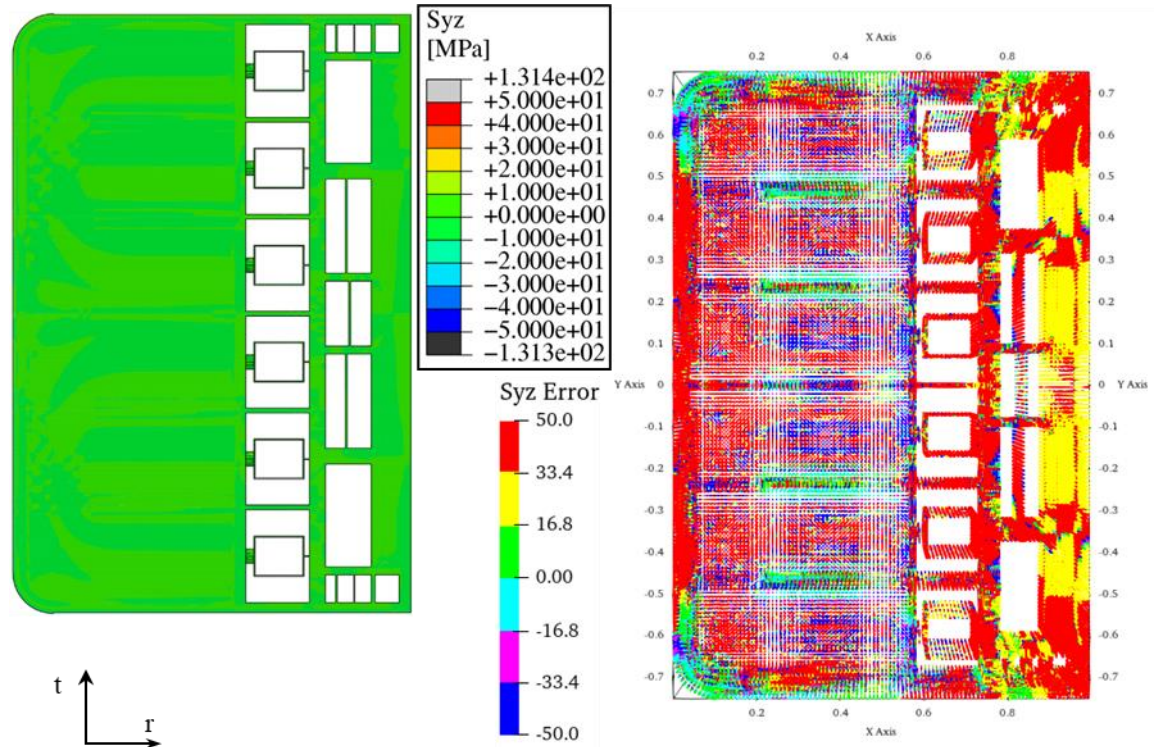


Figure 5.36 S_{yz} spatial distribution from calculated thermal field (left) and relative error contour map (right) when compared with S_x from interpolated thermal field for the “coarse Mesh 2”.

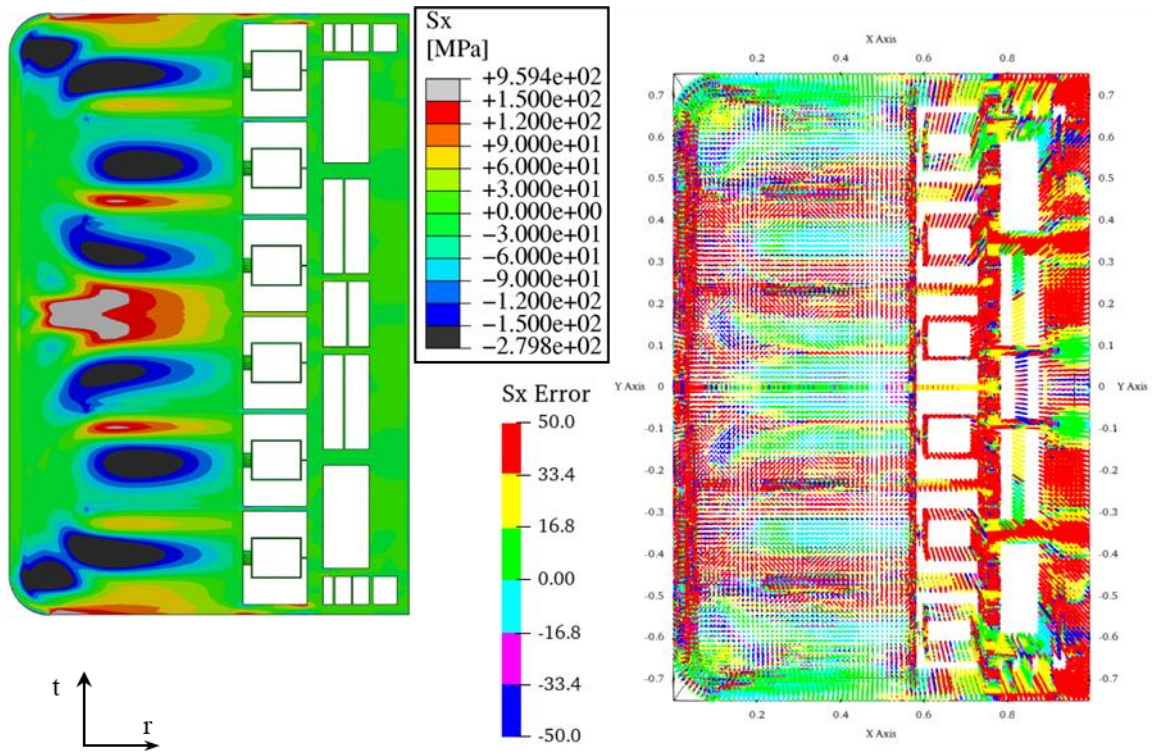


Figure 5.37 S_x spatial distribution from calculated thermal field (left) and relative error contour map (right) when compared with S_x from interpolated thermal field for the “coarse Mesh 3”.

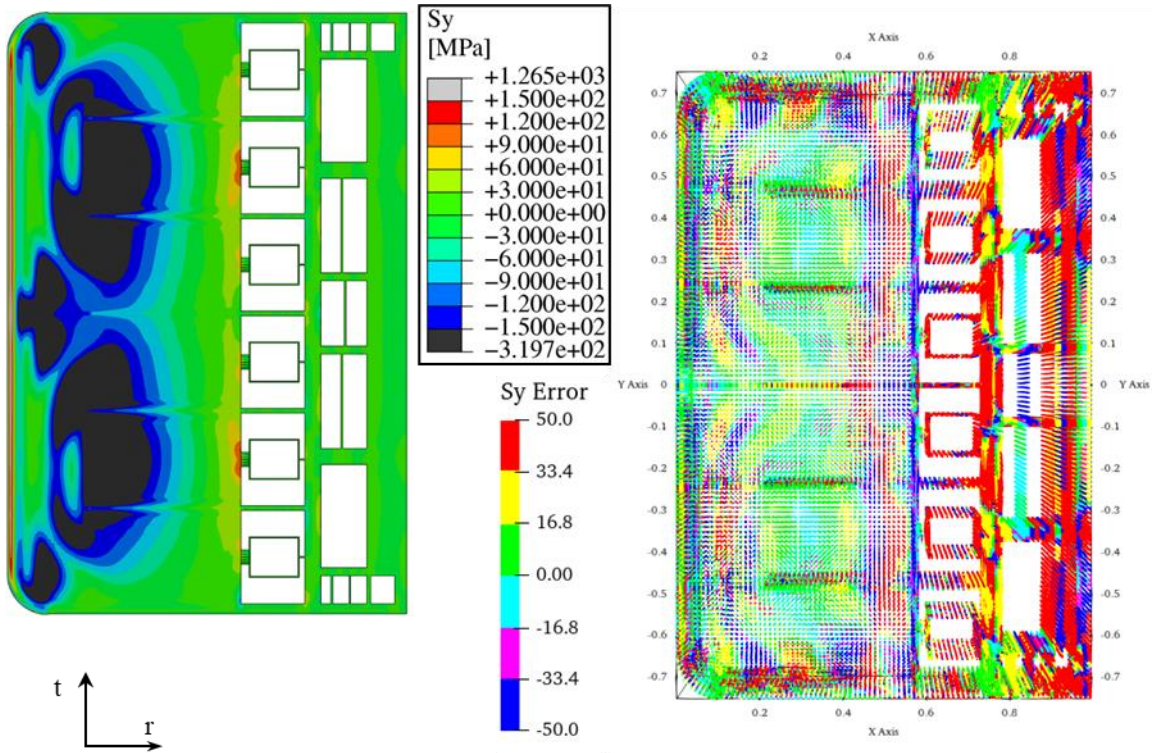


Figure 5.38 S_y spatial distribution from calculated thermal field (left) and relative error contour map (right) when compared with S_x from interpolated thermal field for the “coarse Mesh 3”.

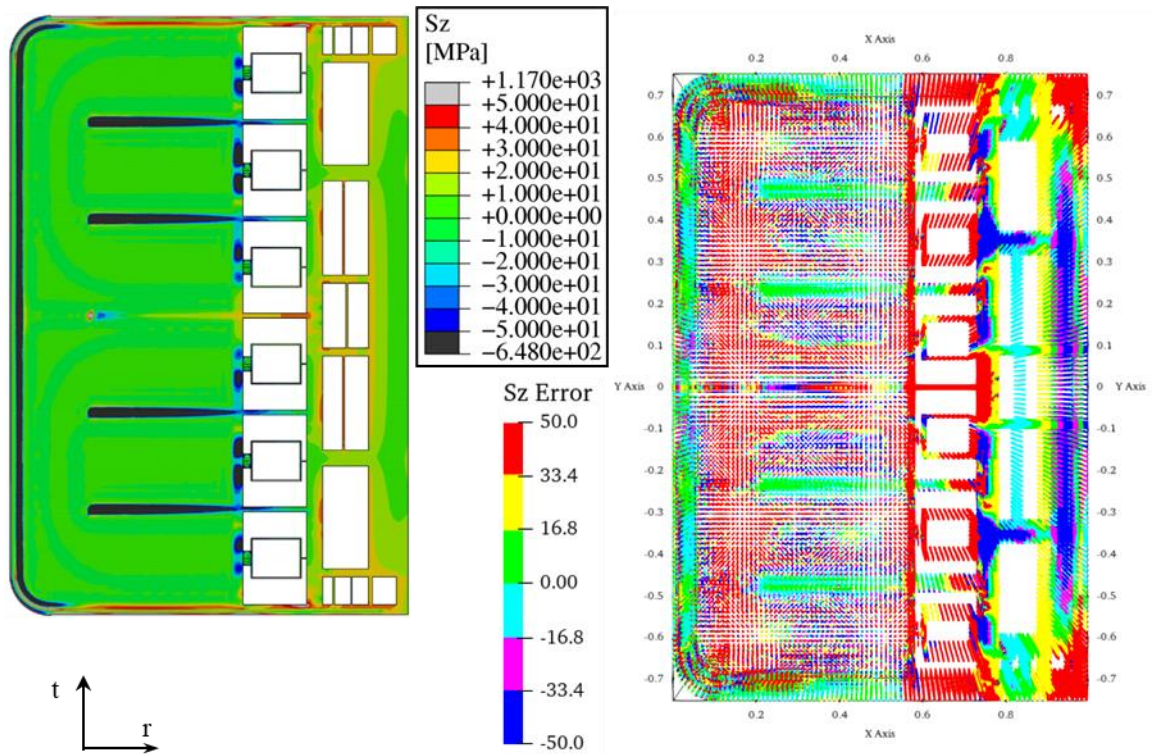


Figure 5.39 Sz spatial distribution from calculated thermal field (left) and relative error contour map (right) when compared with Sx from interpolated thermal field for the “coarse Mesh 3”.

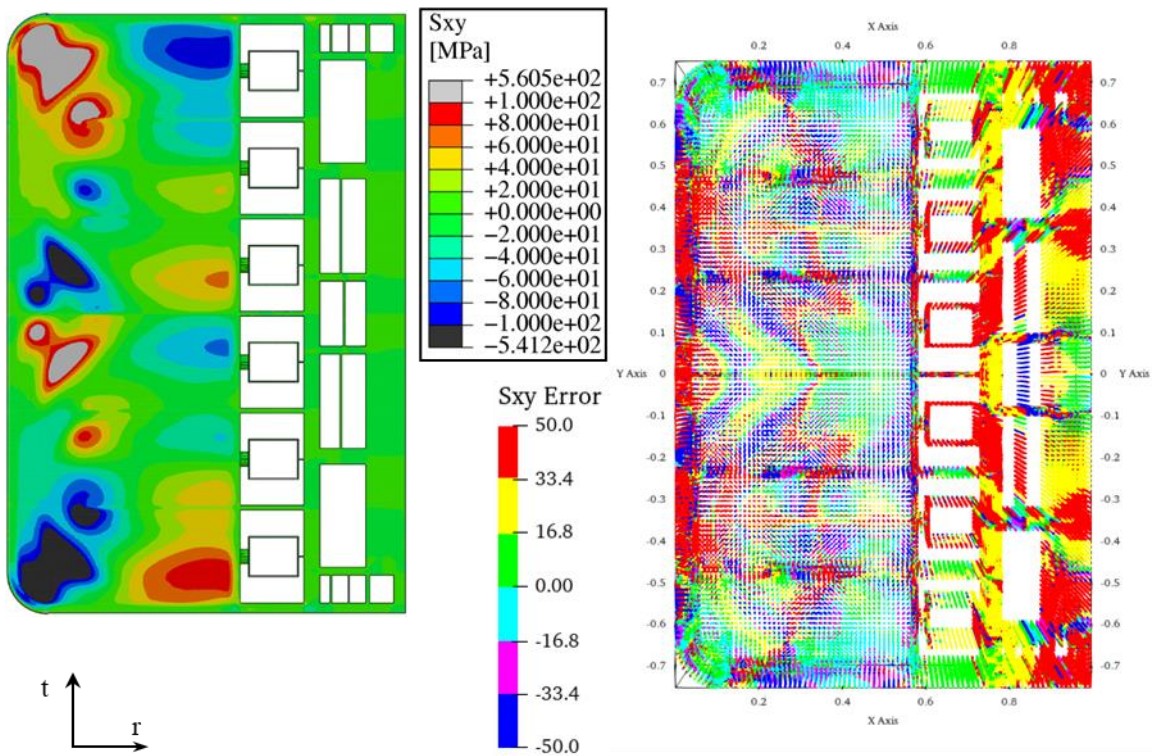


Figure 5.40 Sxy spatial distribution from calculated thermal field (left) and relative error contour map (right) when compared with Sx from interpolated thermal field for the “coarse Mesh 3”.

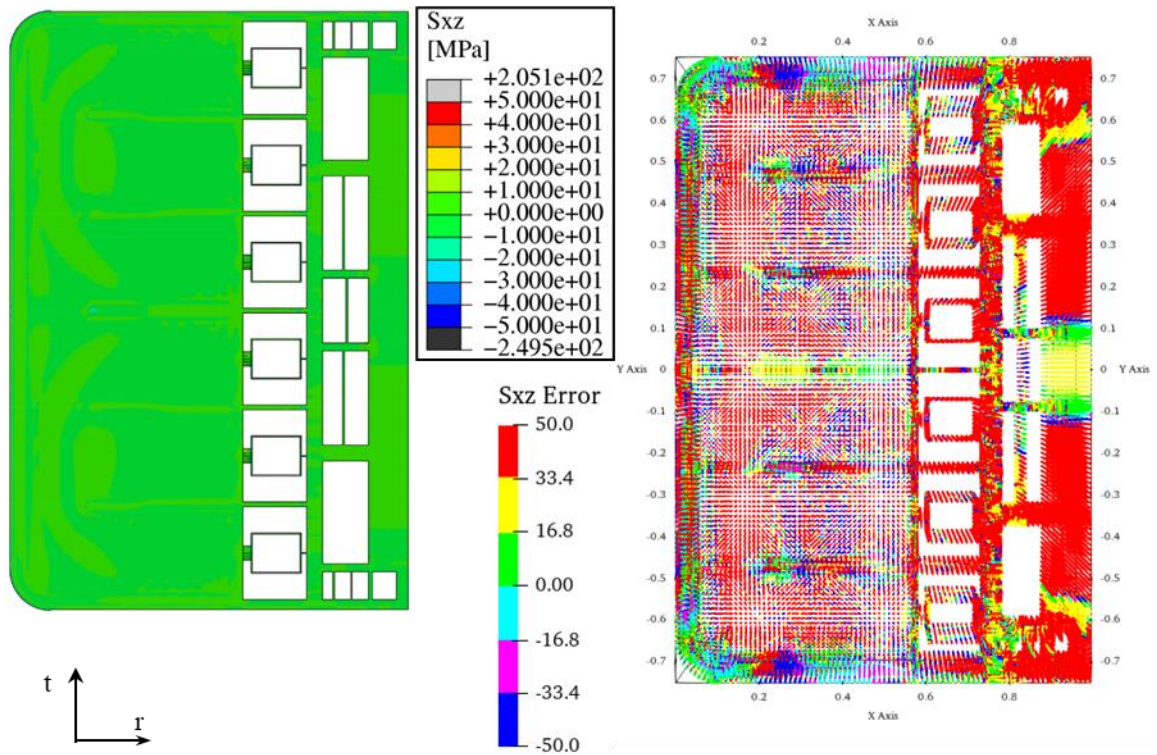


Figure 5.41 S_{xz} spatial distribution from calculated thermal field (left) and relative error contour map (right) when compared with S_x from interpolated thermal field for the “coarse Mesh 3”.

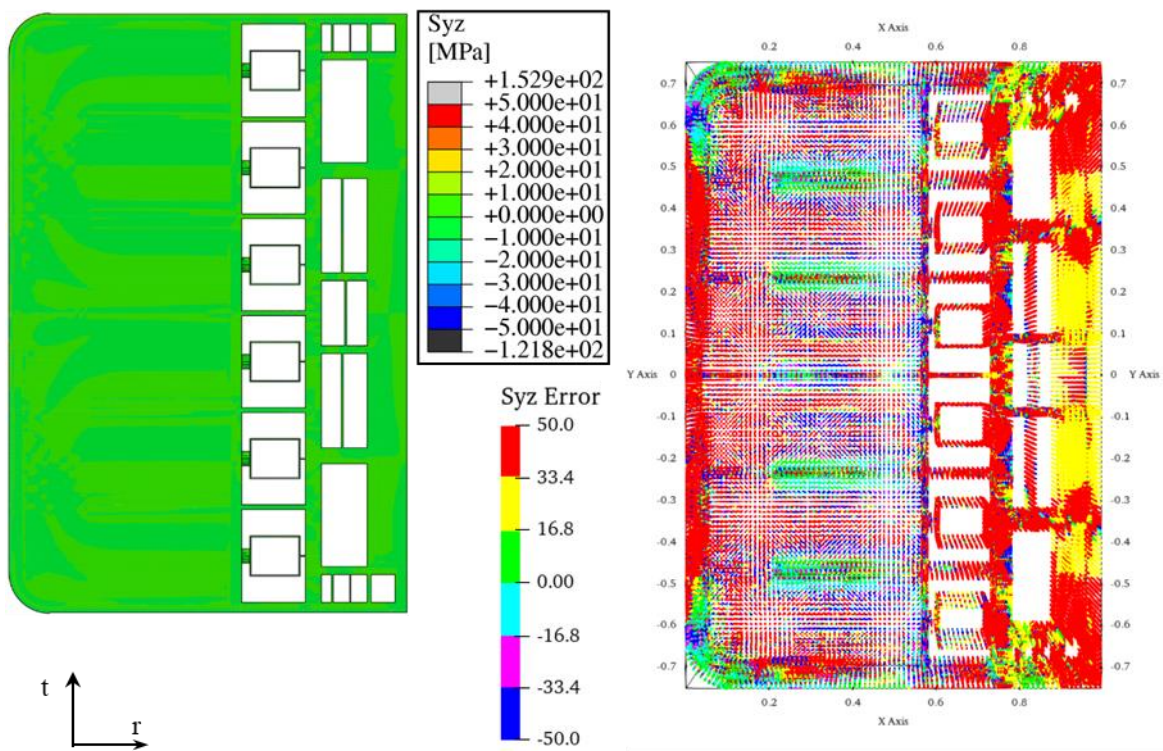


Figure 5.42 S_{yz} spatial distribution from calculated thermal field (left) and relative error contour map (right) when compared with S_x from interpolated thermal field for the “coarse Mesh 3”.

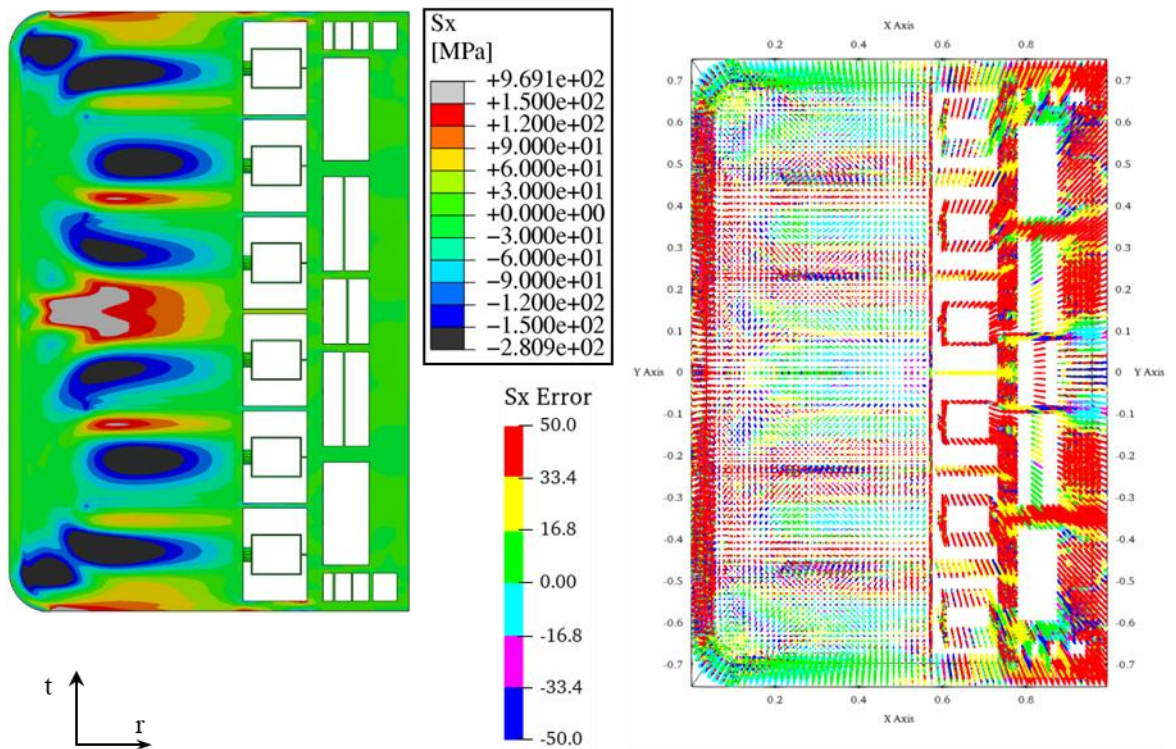


Figure 5.43 S_x spatial distribution from calculated thermal field (left) and relative error contour map (right) when compared with S_x from interpolated thermal field for the "coarse Mesh 4".

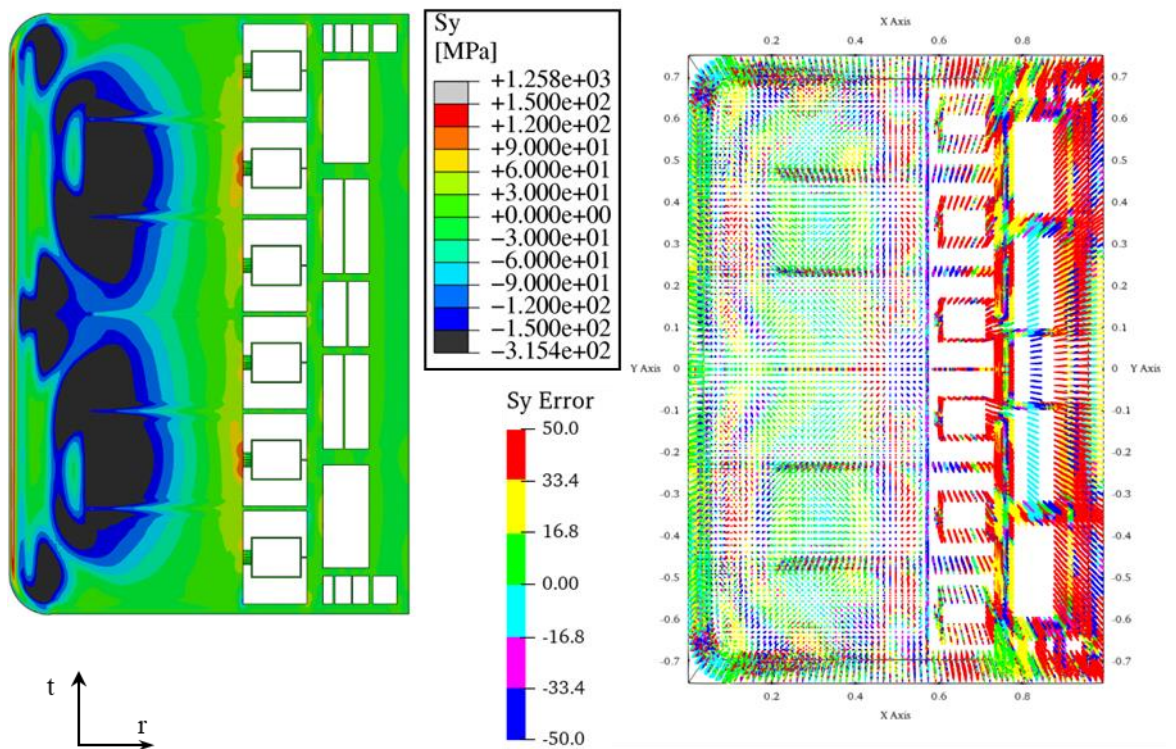


Figure 5.44 S_y spatial distribution from calculated thermal field (left) and relative error contour map (right) when compared with S_y from interpolated thermal field for the "coarse Mesh 4".

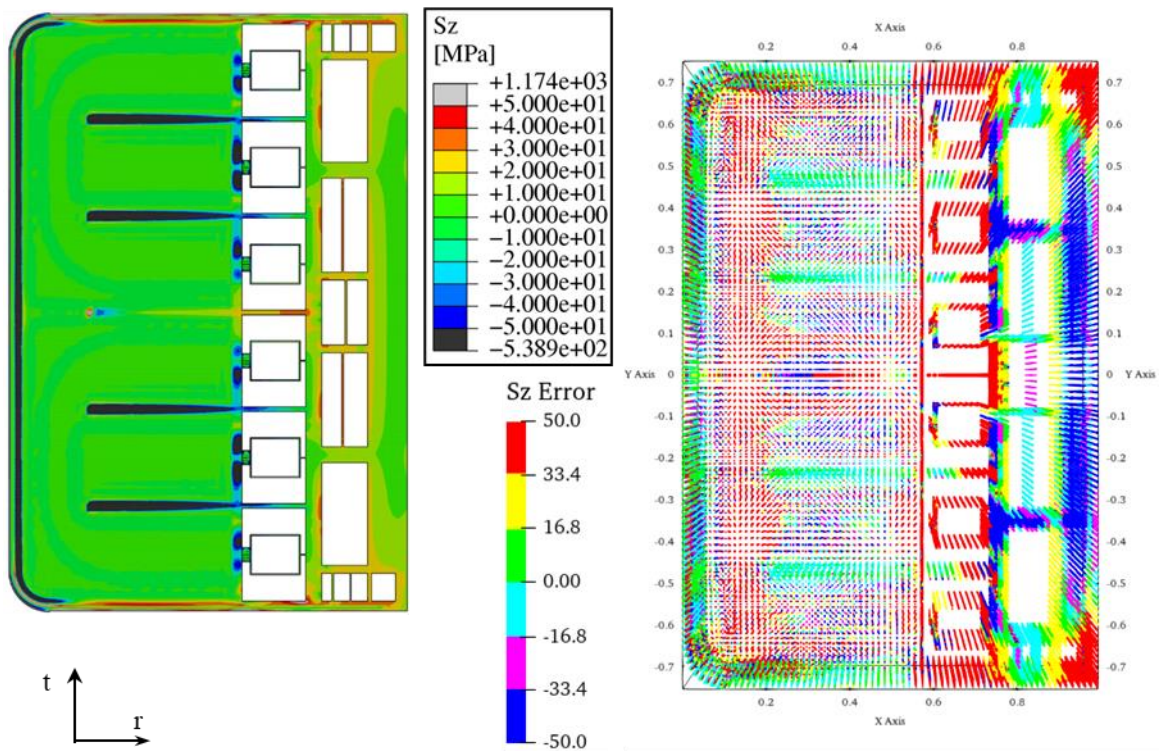


Figure 5.45 S_z spatial distribution from calculated thermal field (left) and relative error contour map (right) when compared with S_x from interpolated thermal field for the “coarse Mesh 4”.

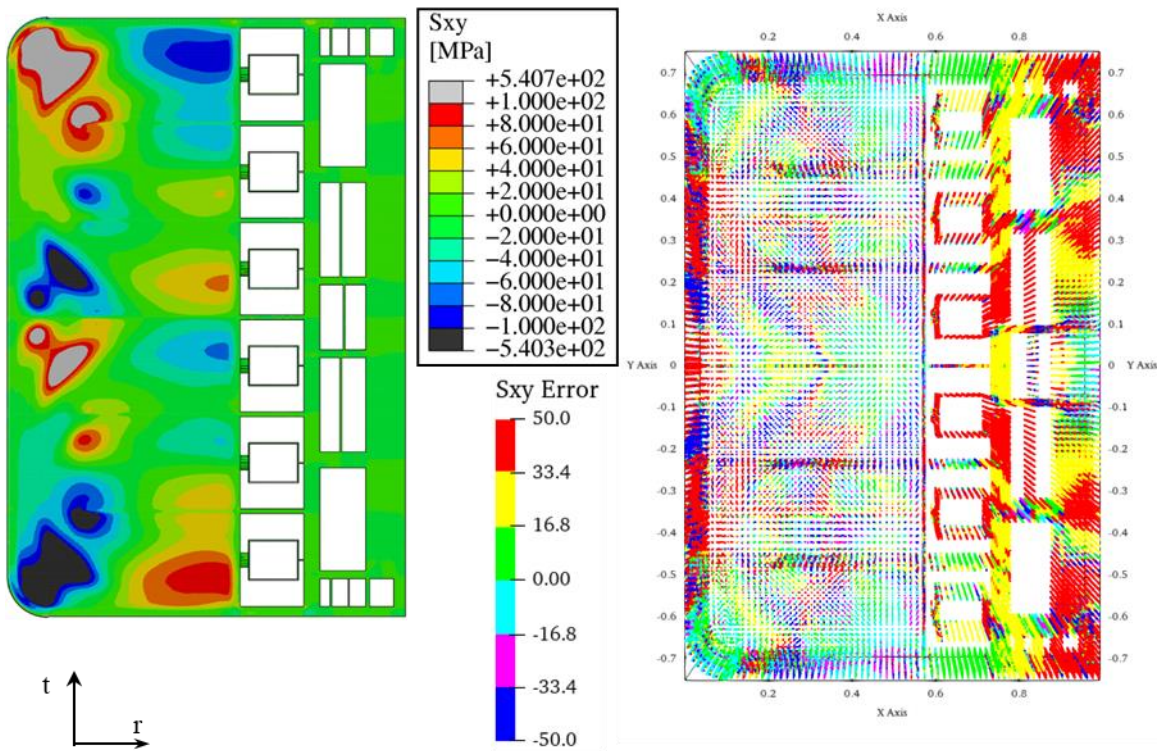


Figure 5.46 S_{xy} spatial distribution from calculated thermal field (left) and relative error contour map (right) when compared with S_x from interpolated thermal field for the “coarse Mesh 4”.

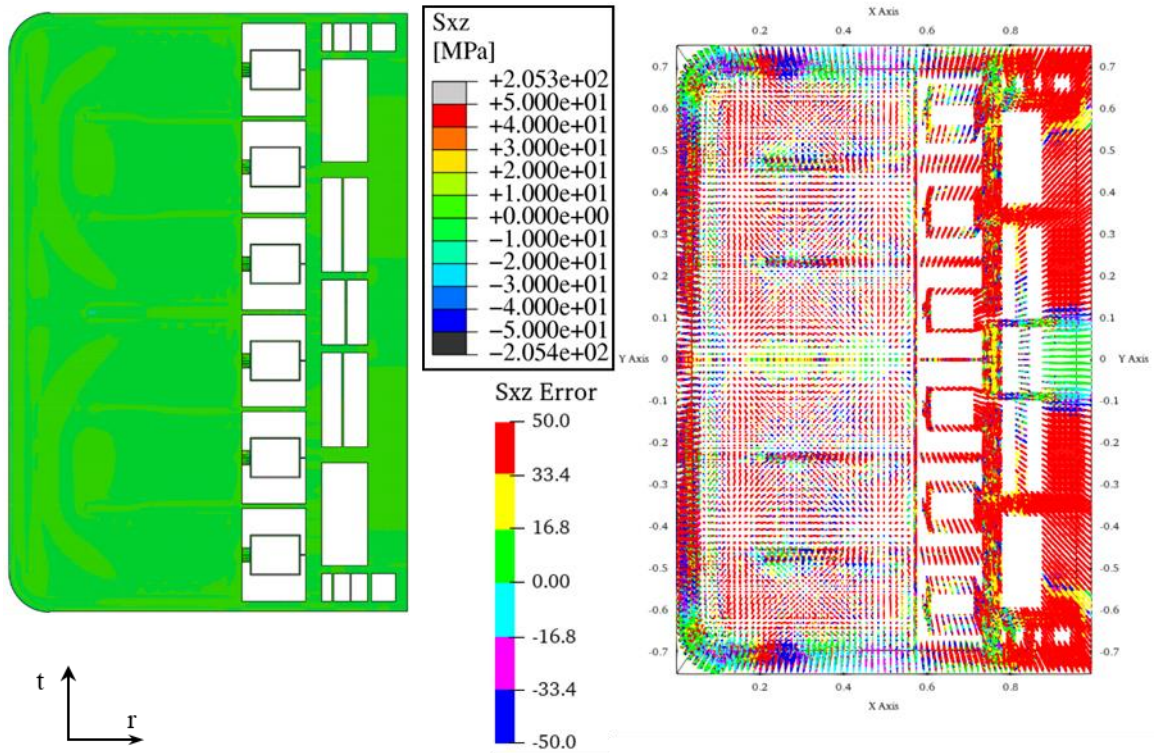


Figure 5.47 S_{xz} spatial distribution from calculated thermal field (left) and relative error contour map (right) when compared with S_x from interpolated thermal field for the “coarse Mesh 4”.

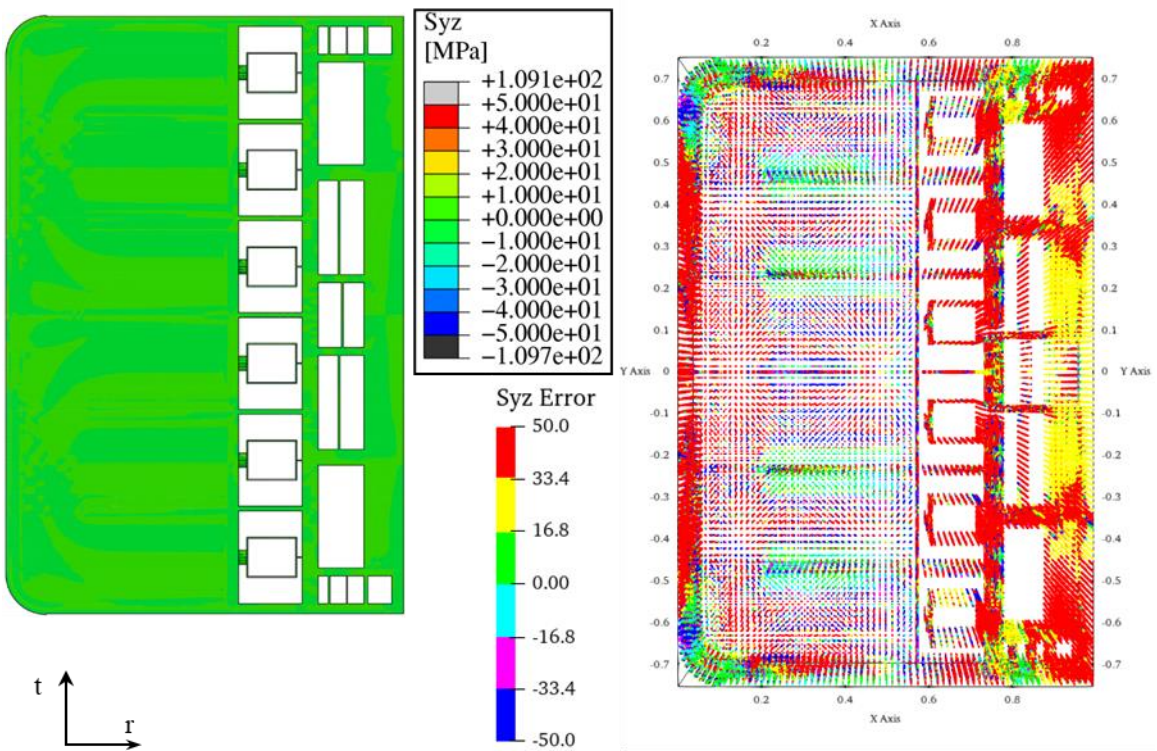


Figure 5.48 S_{yz} spatial distribution from calculated thermal field (left) and relative error contour map (right) when compared with S_x from interpolated thermal field for the “coarse Mesh 4”.

6 Appendix 2

Further details of the WCLL COB poloidal regions optimized layout

In this appendix, the thermal field obtained from the thermal analysis of all the WCLL COB poloidal regions equipped with the corresponding selected DWTs and cooling channels layout, not shown for brevity in §4.4.1, are reported in Figure 6.1 to Figure 6.7. The cooling channels number and DWTs configuration selected for each region is capable of removing the heat while keeping the temperature below the suggested limit for the structural material, namely 550°C, with the minimum number of tubes.

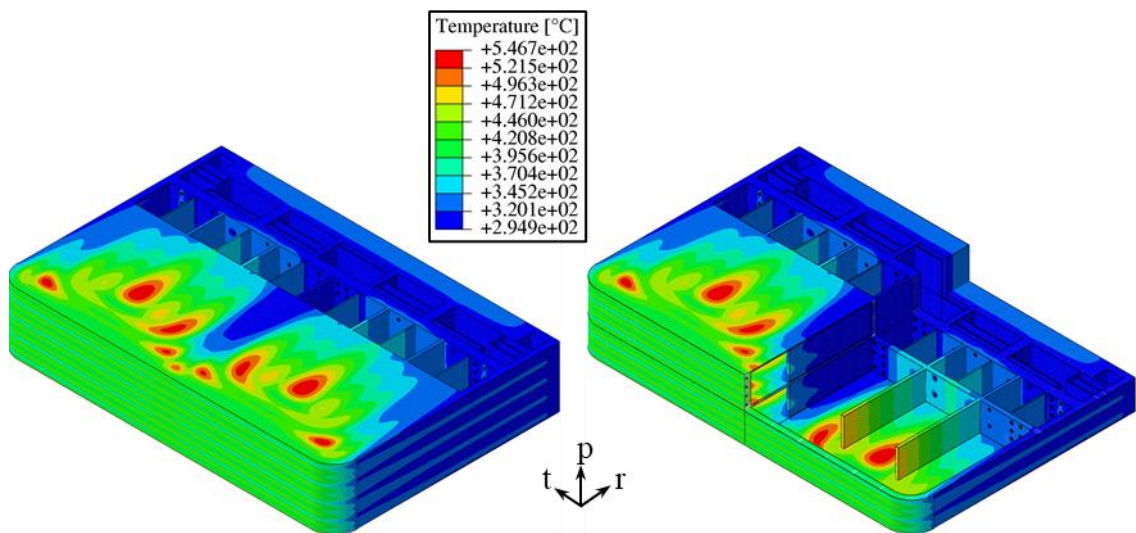


Figure 6.1 Thermal field raised within O1.

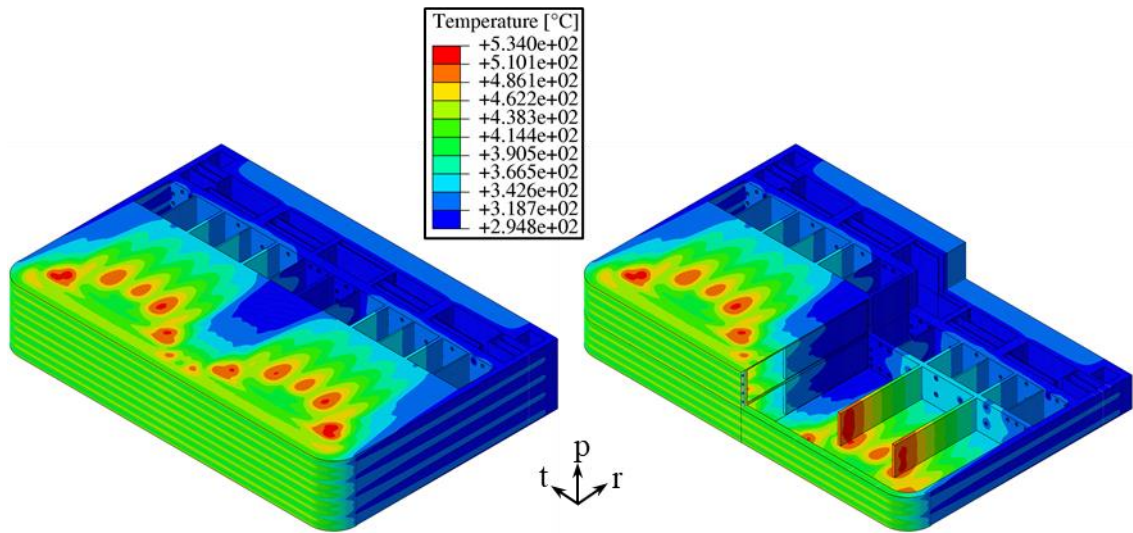


Figure 6.2 Thermal field raised within O2.

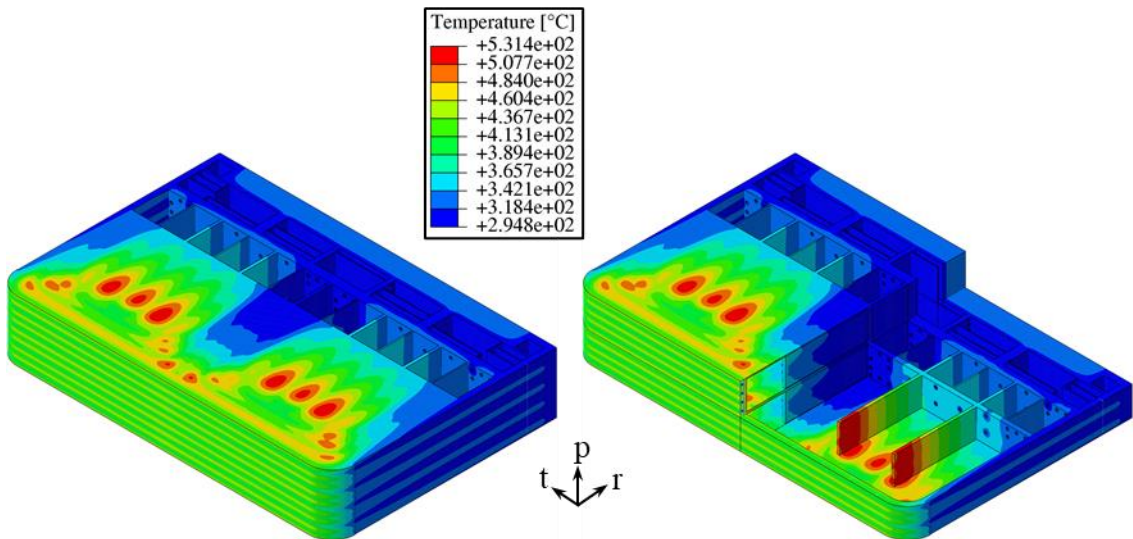


Figure 6.3 Thermal field raised within O3.

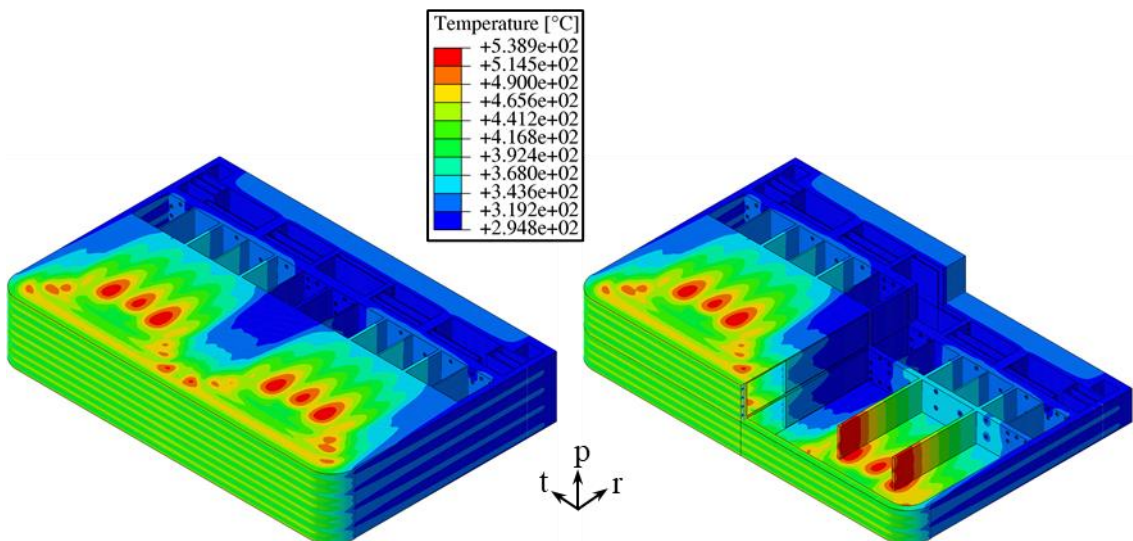


Figure 6.4 Thermal field raised within O4.

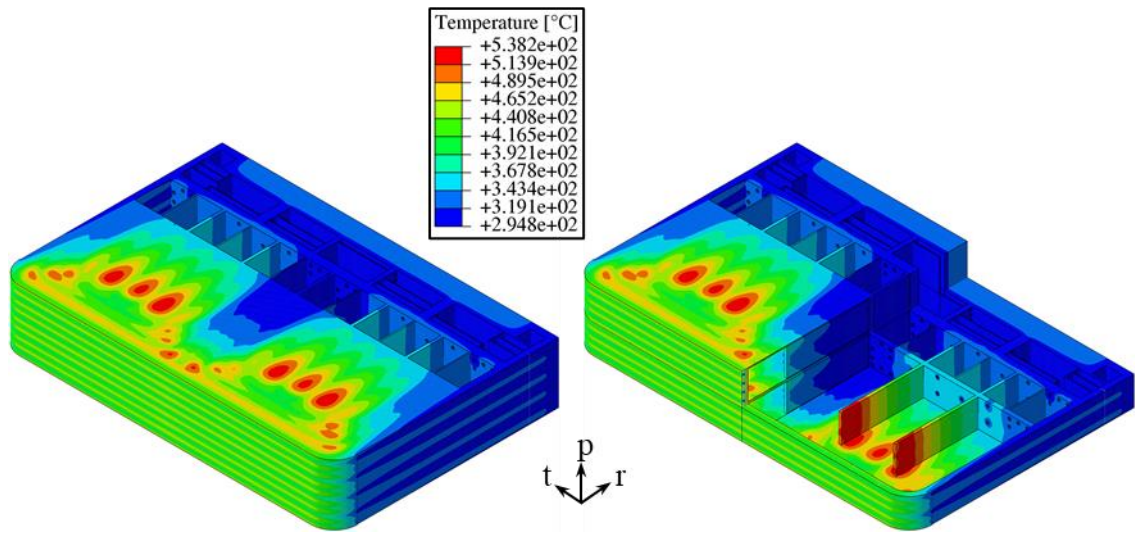


Figure 6.5 Thermal field raised within O5.

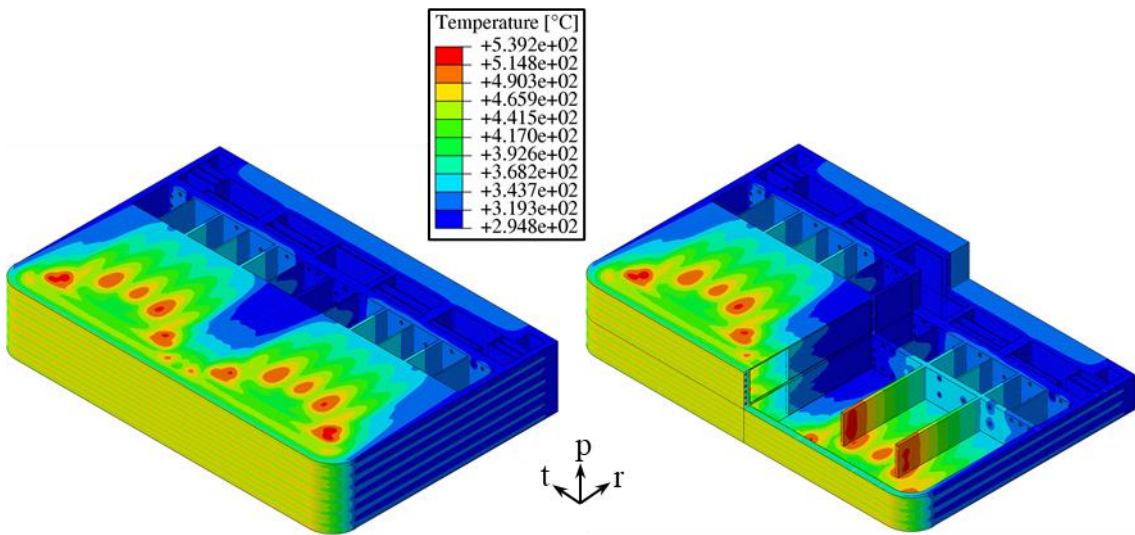


Figure 6.6 Thermal field raised within O6.

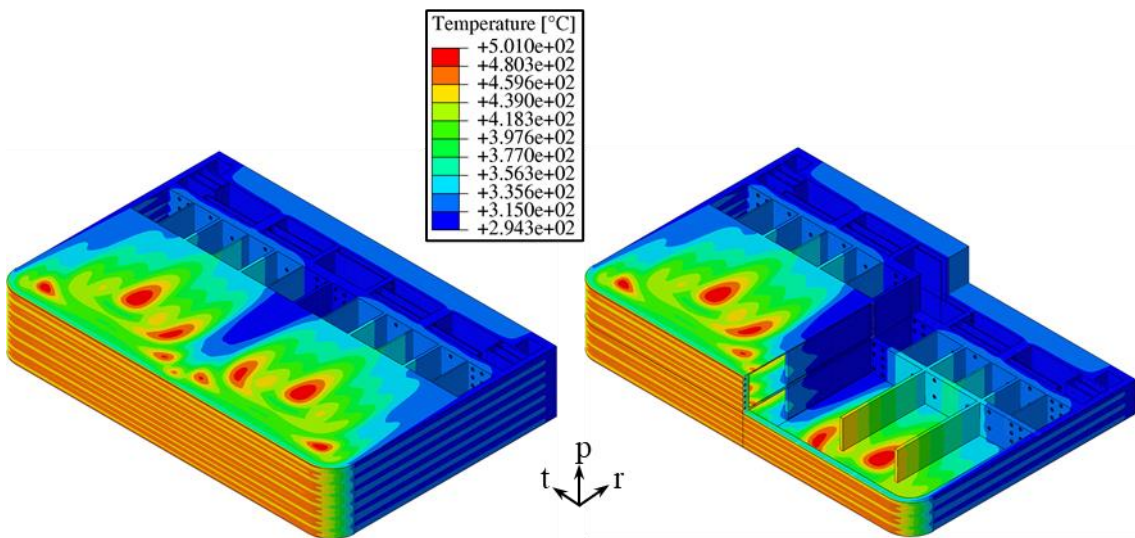


Figure 6.7 Thermal field raised within O7.

7 Appendix 3

Further details of the multi-region interpolation procedure for the WCLL COB poloidal regions

In this appendix, the quantitative comparison between the calculated thermal field and that interpolated by the “multi-region” strategy for the WCLL COB poloidal region (from O2 to O7), not shown for brevity in §4.4.2 is reported. So, the contour map of the relative error, defined as the difference between the calculated temperature and the interpolated one divided by the calculated value, together with the respective relative error statistical distribution, the associated cumulative curve and the corresponding interpolated thermal field, are depicted in Figure 7.1 to Figure 7.6.

All seven poloidal regions show a similar behaviour, in particular, the highest relative error occurs where the temperature reaches lower values, in correspondence of the manifolds region, or nearby the DWTs, where the three-dimensionality of the model is more manifest.

Looking at the figures, the statistical distributions of the calculated relative error show that the most of the error values stays within the range $\pm 4\%$, with a peak around 0. Indeed, looking at the cumulative curve, about the 90 % of the relative error values stay within this range.

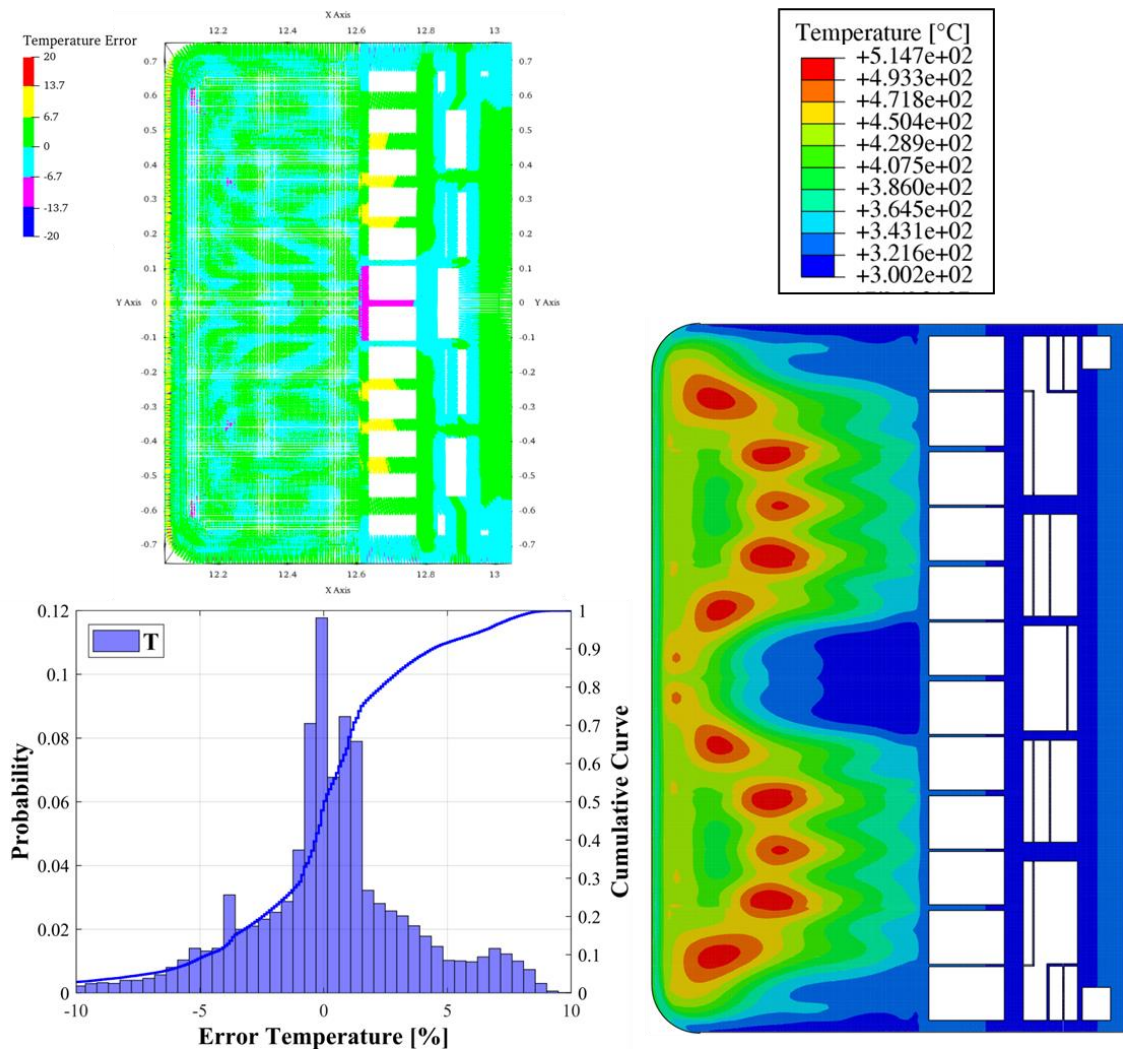


Figure 7.1 Contour map and statistical distribution of the temperature error [in %] between the calculated and interpolated thermal field and cumulative curve in O2 poloidal region.

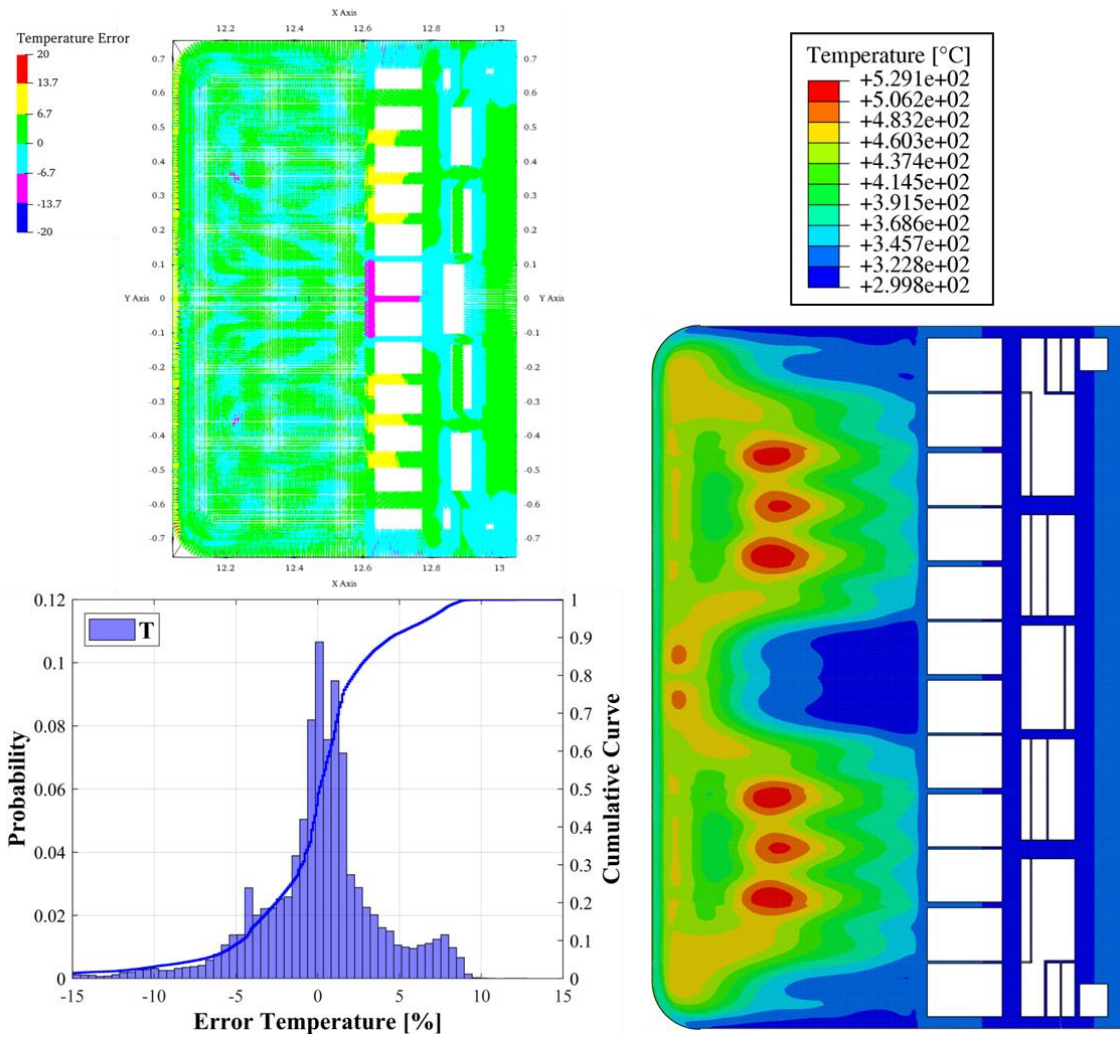


Figure 7.2 Contour map and statistical distribution of the temperature error [in %] between the calculated and interpolated thermal field and cumulative curve in O3 poloidal region.

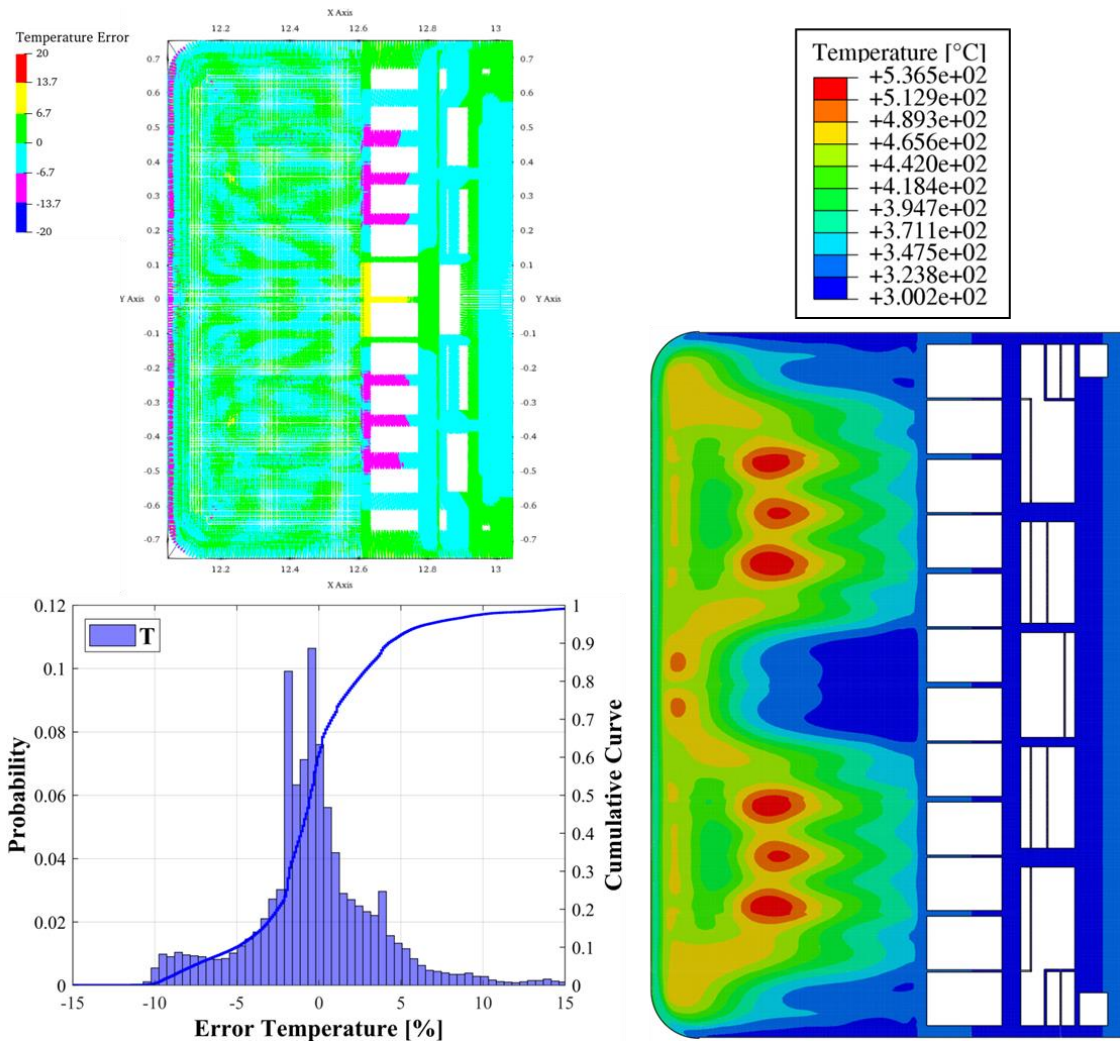


Figure 7.3 Contour map and statistical distribution of the temperature error [in %] between the calculated and interpolated thermal field and cumulative curve in O4 poloidal region.

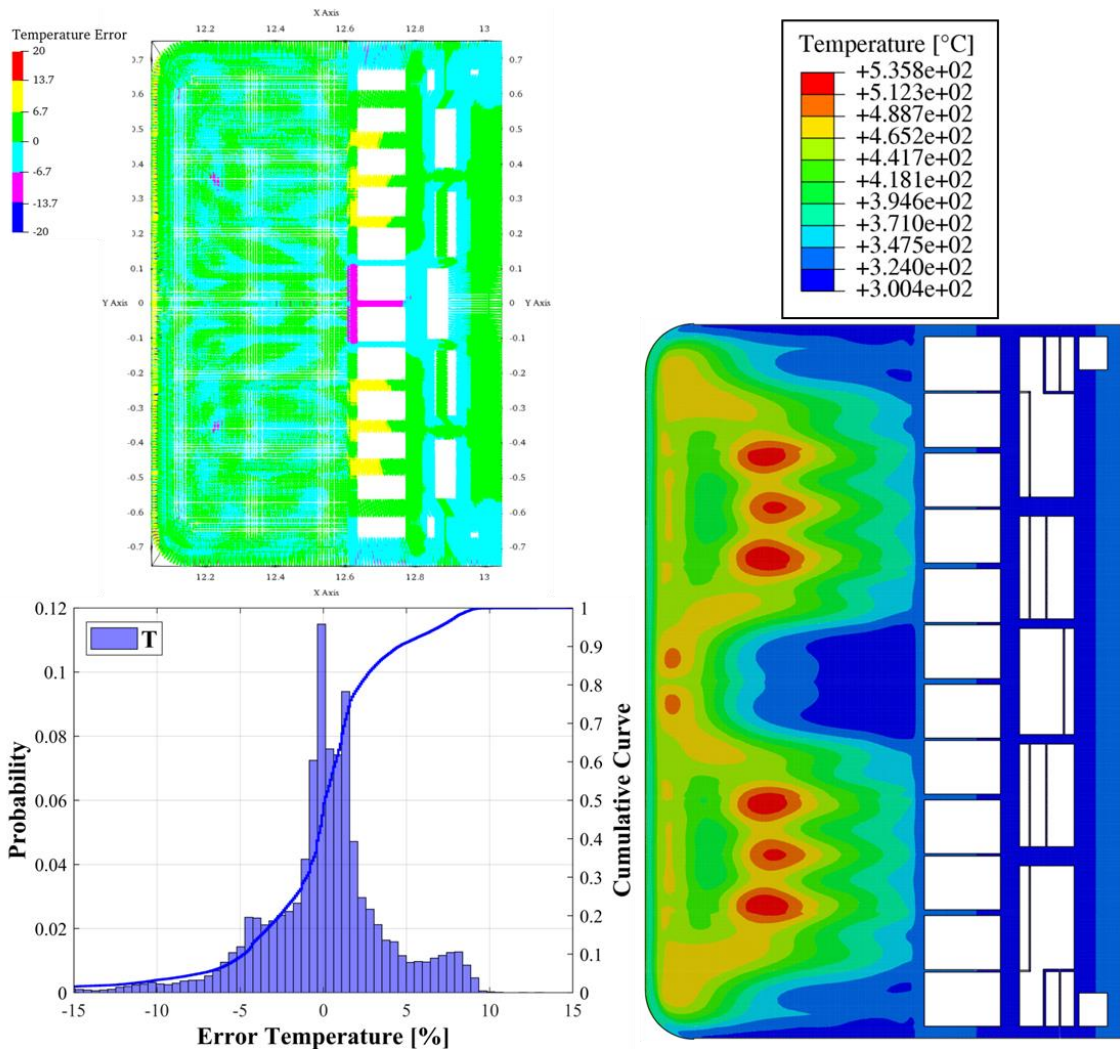


Figure 7.4 Contour map and statistical distribution of the temperature error [in %] between the calculated and interpolated thermal field and cumulative curve in O5 poloidal region.

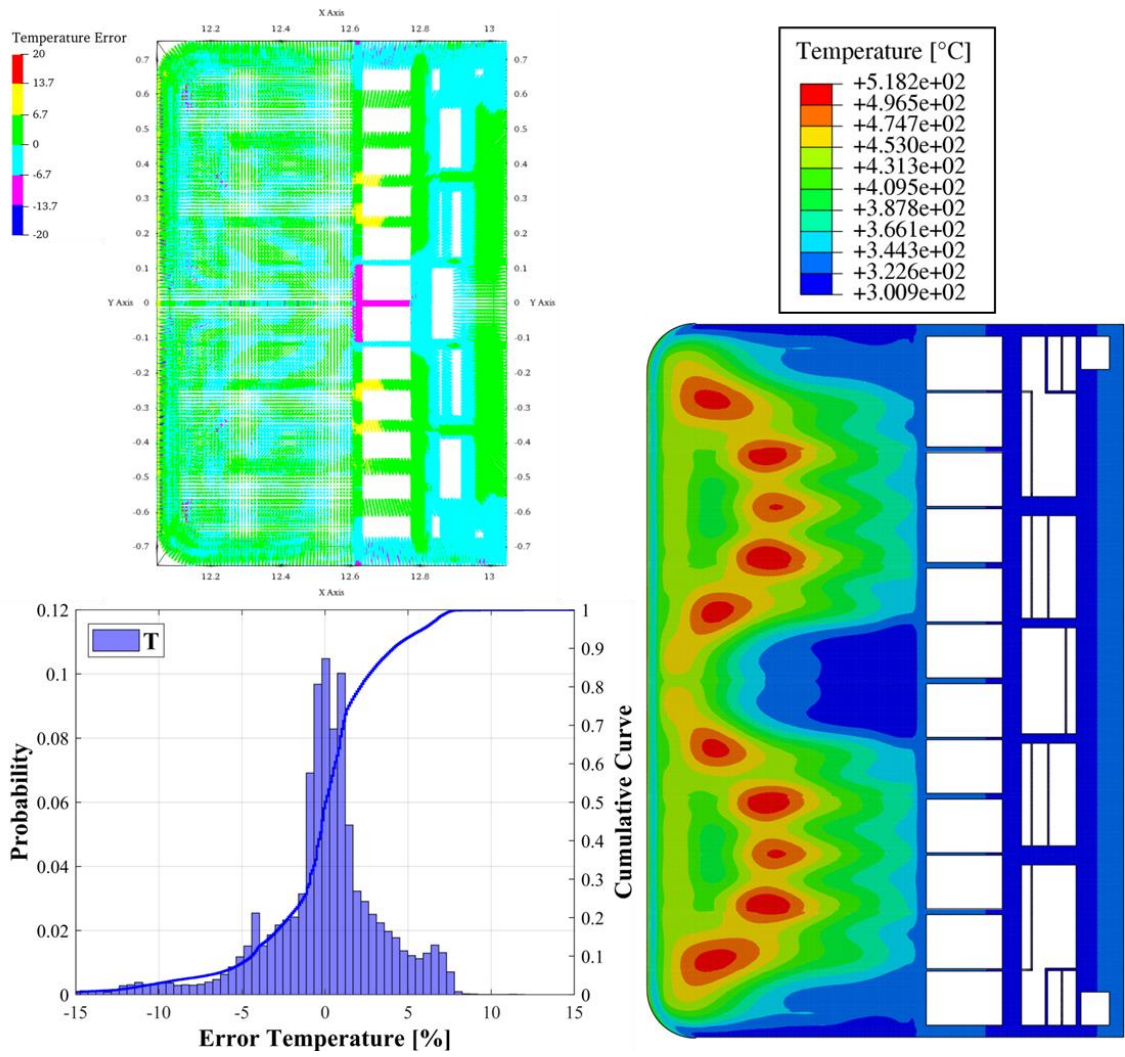


Figure 7.5 Contour map and statistical distribution of the temperature error [in %] between the calculated and interpolated thermal field and cumulative curve in O6 poloidal region.

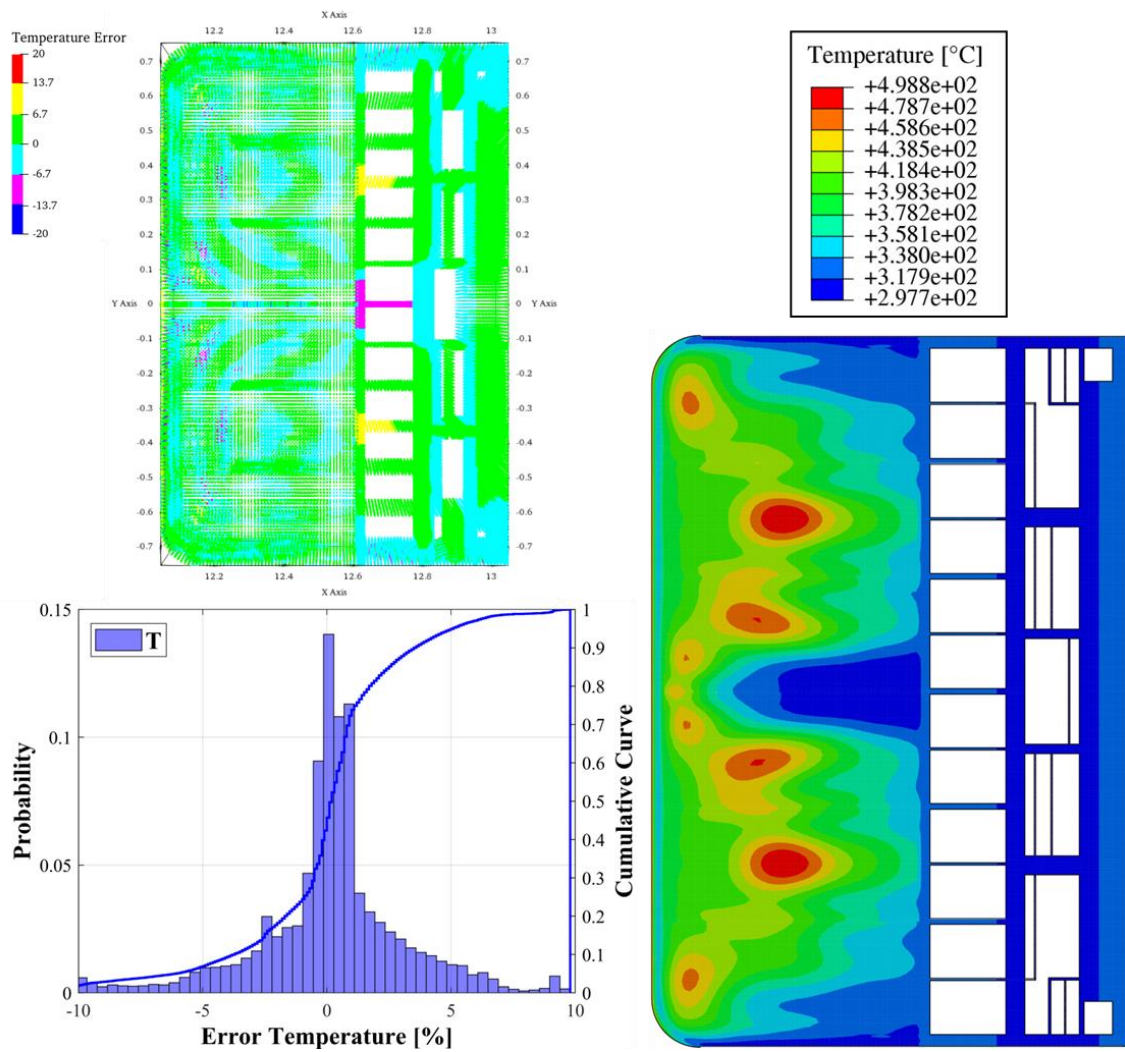


Figure 7.6 Contour map and statistical distribution of the temperature error [in %] between the calculated and interpolated thermal field and cumulative curve in O7 poloidal region.